STRUCTURAL STUDIES OF BLOCK COPOLYMER AND BLOCK COPOLYMER/ALUMINOSILICATE MATERIALS

A Dissertation

Presented to the Faculty of the Graduate School

of Cornell University

in Partial Fulfillment of the Requirements for the Degree of

Doctor of Philosophy

by

Gilman Ewan Stephen Toombes

August 2007

STRUCTURAL STUDIES OF BLOCK COPOLYMER AND BLOCK COPOLYMER/ALUMINOSILICATE MATERIALS

Gilman Ewan Stephen Toombes, Ph. D.

Cornell University 2007

Block copolymers consist of two or more chemically distinct polymer chains (blocks) linked by covalent bonds. These blocks can micro-phase separate into nanometer-sized domains whose structure depends upon the size and interactions of the blocks. Block copolymers can also control the ordering of inorganic precursors that selectively associate with one block. This thesis describes structural studies of block copolymer and block copolymer/aluminosilicate materials.

First, the structure of a bicontinuous poly(isoprene-block-ethylene oxide) (PI-b-PEO) copolymer/aluminosilicate material was studied via Small Angle X-ray Scattering (SAXS) and Transmission Electron Microscopy (TEM). The material was synthesized via a solvent casting process that distorted the continuous network of channels formed by the PI minority phase (volume fraction 0.36). This deformation was studied using elastic, constant-curvature and constant-thickness models of the double gyroid structure. SAXS and TEM data from the material were compared to models of several types of network structure and were found to be most consistent with a distorted double gyroid structure.

Second, a set of three poly(ethylene-alt-propylene-block-ethylene oxide-block-n-hexyl methacrylate) (PEP-b-PEO-b-PHMA) copolymers were used to study the phase behavior of ABC triblock copolymers with a small, strongly incompatible B block and roughly equivalent A and C blocks. The A and C blocks formed lamellar domains while reduction of the B domain volume fraction caused the B block to transform from sheets to rods to balls. A strong segregation limit analysis of these

morphologies suggests this sequence of transitions is quite general.

Finally, two morphologies were examined in PEP-b-PEO-b-PHMA copolymer/aluminosilicate materials. Compounds with B and C domains of roughly equal volume and a small A block (~ 0.10) formed a hexagonally patterned lamellae morphology consistent with the proposed "pillared-lamellae" ABC copolymer structure. However, for a compound with a larger A block (~ 0.2), the individual B domains formed zigzag shaped strands. These strands were arranged in a four-layer woodpile structure in which strands in successive layers ran in alternate directions and the third and fourth layers of strands were offset. This unusual, woodpile stacking may be stabilized by the presence of A and C domains along the outside of each strand.

BIOGRAPHICAL SKETCH

Gil Toombes was born in Brisbane, Australia on July 27, 1977. He attended Jindalee Primary School (1983-1989), Brisbane Grammar School (1990-1994) and the University of Queensland (1995-1997) where he completed a Bachelor of Science degree in Physics. He commenced his studies in the Department of Physics at Cornell University in August, 1998.

ACKNOWLEDGMENTS

Over the past eight years I have greatly benefited from the constant guidance, support and encouragement of my advisor, Sol Gruner. Sol has been a great advisor and I owe him a tremendous debt of gratitude for encouraging me with his boundless curiosity and keeping me gainfully employed. I thank Professors Carl Franck and Neil Ashcroft for generously giving their time to serve on my thesis committee. This text was greatly improved by Sol, Carl and Neil's detailed comments and corrections. The numerous, remaining errors are solely my fault for which I ask the reader's forgiveness. (Please employ the general rule that if something seems wrong to you, it probably is.)

This thesis describes work performed in collaboration with the group of Professor Uli Wiesner in the Department of Materials Science. I thank Uli for sharing his great enthusiasm for block copolymers. Much of the work described in Chapter 2 was done with Adam Finnefrock and I thank Adam for being so generous with his time and advice. I am also grateful for the chance to work with Surbhi Mahajan, who synthesized all of the materials in Chapters 3, 4, 5 and 6, did a lot of the characterization work and was fun to collaborate with. I thank Mick Thomas and Matt Weyland for their skillful electron microscopy reported in Chapters 5 and 6. Finally, I thank Anurag Jain, BK Cho, Phong Du, Marleen Kamperman, Scott Warren and Andrew Burns for considerable help with synthesis and characterization.

A number of other groups have helped me during my studies. I owe a great debt to Olaf Andersen who graciously welcomed me into his laboratory at the Cornell Medical School. Many thanks to Olaf, Aung Kyaw Chi, Shobana Sundaram and Michael Bruno for showing me how to patch-clamp and involving me in their research on lipids and ion channels. I am grateful to Ian Berke in Rod MacKinnon's lab for

showing me how to purify and reconstitute MthK channels. I also thank Anne McNeil, David Collum and Lara Liou in the Department of Chemistry for letting me be a part of their fun lithium NMR experiments.

In Sol's lab I have been very fortunate to learn from Mark Tate and Marty Novak. Mark spent many hours teaching me and helping me fix equipment I had broken and I am thankful for his guidance throughout my time at Cornell. Marty built much of the equipment used in this thesis and I benefited many times from his amazing ability to turn rough sketches into beautiful devices. Marty and Mark both provided considerable help developing experiments and activities for kids to learn and enjoy science and I will greatly miss them.

I have also been fortunate to have many great colleagues in the lab and I thank Paul Urayama, Adam Finnefrock, Lois Pollack, Matt Renzi, Cayce Butler, Marcus Collins, Raphael Kapfer, Alper Ercan, Xuefa Li, Pascale Chenevier, Peter Abbamonte, Jochen Gutmann, Dag Arneson, Dan Schuette, Nozomi Ando, Buz Barstow, Gideon Alon, Joe Zinter, Jamie Chung, Peter Busch, Chae Un Kim, Lucas Koerner, Darol Chamberlain, Hugh Philipp, Darren Southworth, Yi-fan Chen, Tom Caswell, Elizabeth Landrum and Marianne Pouchet for their friendship and help. Special thanks are due to Paul, Adam, Dan and Lucas for administering the lab's computer system, Marty and Ann Marie Novak for inviting the entire lab to their house every summer for the annual "Marty Party" extravaganza and Matt, Lisa Kwok and Thalia Mills for the hikes, tightly-contested rounds of miniature golf and countless other weekend adventures.

I wish to thank the many people in the physics department who have helped me, including Greg Werner, Harald Pfeiffer, Karen Daniels, Jonathan Wrubel, Eileen Tan, Andrew Perrella, Michael Berninger, Tom Glickman, Harsh Vishwasrao, Kat Cicak, Richard Yeh, Bjoern Lange, Lauren Hsu, Anjali Gopalakrishnan, K Narayan,

Nilay Pradhan, Abhay Pasupathy, Mandar Deshkmuth, Chris Deufel, Shaffique Adam, Jeandrew Brink, Eric Ryan and Allie King, Luke Donev, Robin Smith, Curry Taylor, Greg Stiesberg, Carl Franck, Monica Plisch, Don Holcomb, Persis Drell, Mike Teter, Dan Ralph, Viet Elser, Rob Thorne, Eric Smith, Phil Krasicky, Vince Kotmel, Judy Wilson, Rosemary French, Lisa Margosian and Deb Hatfield. Thank you also to thank Nev Singhota, Kevin Dilley, Jane Earle, Juliane Bauer-Hutchinson and the other members of the Cornell Center for Materials Research Outreach program.

While in Ithaca I have greatly appreciated the fellowship at Cornell Protestant Cooperative Ministries lead by the Reverend Taryn Mattice and I am deeply indebted to Taryn and many members of the PCM congregation including Ed Chan, Dan Plafcan, Pauline Kusiak, Nathan Edwards, Amy Heusinkveld, David Baer, Robert Mann-Thompson, Andrew North, Scott Bellen, Jill Wason, John Glauber, Clark Smith, Julie Gosse, Sam Hess, Danny Fredrickson, Carolyn Stedinger, Nikki Kalbing, Meg Richards and Chris Magnano.

I also must thank Dorothy, Dan and Henri Schuette and Taryn, Terry and Noah Mattice for sharing the joy of seeing the world through young eyes.

Thank you to Leanne Duffy, Howard Wiseman, Sara Schneider, Kate Eltham, Andrew and Angela Rae and my brother Spencer, and his wife, Kay, for visiting Ithaca, my brother, Luke, for traveling around Utah, Rod Jory for hosting visits to Canada and England and Thalia for visiting my family in Australia.

Finally, I thank my parents, Ewan and Judith, and my siblings Spencer, Luke and Ngaio for their continual love and support.

TABLE OF CONTENTS

LIST OF FIGURES

LIST OF TABLES

LIST OF ABBREVIATIONS

2-D	two dimensional
3-D	three dimensional
AFM	Atomic Force Microscopy
°C	degrees Celcius
CCD	Charge Coupled Detector
cm	centimeter
CuK_α	K_α X-rays from Copper (wavelength 0.154nm)
EM	Electron Microscopy
FWHM	Full Width Half Maximum
GLYMO	3-(glycidyloxypropyl) trimethoxysilane
HAADF	High Angle Annular Dark Field (detector)
IDL	Interactive Data Language (software)
K	Kelvin (Temperature)
kV	kiloVolt
Li-triflate	Lithium trifluoromethanesulfonate
log	Natural Logarithm
mA	milliAmpere
mg	milligram
μL	microliter
mm	millimeter
nm	nanometer
Pa	Pascals
PB	poly(butadiene)
PEELS	Parallel Electron Energy Loss Spectroscopy
PEO	poly(ethylene oxide)
PEP	poly(ethylene-alt-propylene)
PEP-b-PEO-b-PHMA	poly(ethylene-alt-propylene-block-ethylene oxide-block-n-hexyl methacrylate)
PHMA	poly(n-hexyl methacrylate)
PMMA	poly(methyl methacrylate)
PI	poly(isoprene)
PI-b-PEO	poly(isoprene-block-ethylene oxide)
PS	poly(styrene)
SAXS	Small Angle X-ray Scattering
SCMFT	Self Consistent Mean Field Theory
S/cm	Siemens per centimeter
SEM	Scanning Electron Microscopy
SIRT	Simultaneous Iterative Reconstruction Technique
SSL	Strong Segregation Limit
STEM	Scanning Transmission Electron Microscopy
TEM	Transmission Electron Microscopy
μm	micro-meter
WAXS	Wide Angle X-ray Scattering
WSL	Weak Segregation Limit

LIST OF SYMBOLS

$\boldsymbol{a_1}$, $\boldsymbol{a_2}$, $\boldsymbol{a_3}$	Real Space Lattice Vectors (Ch. 1, 2, 3, 6)
$A_{\text{ball}}(\varepsilon)$	Ratio of Surface Area to In-Plane Area for a Ball-Shaped Domain with aspect ratio ε (height/width). (Ch. 4)
$A_{\text{cyl}}(s_x, s_y)$	Fourier transform of a rod in rods-at-lamellae structure (Ch. 3)
A_{ij}	Area per unit cell of domain interfaces between blocks i and j. (Ch. 4)
A_j^m	Fourier amplitude describing elastic distortion of material (Ch. 2)
A^p	2×3 matrix of $\boldsymbol{a_1}$, $\boldsymbol{a_2}$ and $\boldsymbol{a_3}$ projected into the x-y plane (Ch. 2)
$A_{\text{perf}}(\varepsilon,\phi_a)$	Ratio of Surface Area to In-Plane Area for a perforation in a lamellae with aspect ratio ε and in-plane area fraction ϕ_a (Ch. 4)
$A_{\text{ring}}(\varepsilon_1,\varepsilon_2)$	Ratio of Surface Area to In-Plane Area for a toroidal domain with aspect ratio ε_1 and ratio of toroidal to axial radii of ε_2. (Ch. 4)
$A_{\text{rod}}(\varepsilon)$	Ratio of Surface Area to In-Plane Area for a Rod-Shaped Domain with aspect ratio ε (height/width). (Ch. 4)
$A_{\text{sph}}(s_x,s_{yz})$	Fourier transform of a ball in the balls-at-lamellae structure (Ch. 3)
$A_u(q_j)$	Fourier Amplitude for Wave-Vector q_j
α_j	Rotation axis for crystallite (Ch. 2)
$\boldsymbol{b_1}$, $\boldsymbol{b_2}$, $\boldsymbol{b_3}$	Reciprocal Space Lattice Vectors (Ch. 1, 2)
B	Intensity of background scattering around a Bragg Peak (Ch. 2)
B_k	Coefficients describing background scattering in powder pattern (Ch. 3)
B_{jk}	3×3 matrix of reciprocal lattice vectors $\boldsymbol{b_1}$, $\boldsymbol{b_2}$ and $\boldsymbol{b_3}$ (Ch. 2)
C	Constant coefficient (Ch. 1).
C_{int}	Coefficient describing the Interfacial Energy per copolymer. (Ch. 4)
C_{stretch}	Coefficient describing the Stretching Energy per copolymer. (Ch. 4)
χ_{ij}	Flory-Huggins Segment-Segment Interaction Parameter for Species X and Y (dimensionless; Ch. 1)
d	Characteristic size of block copolymer structure generally taken to be one of the lattice constants. (Ch. 4)
d	Cubic unit cell size (Ch. 2)
d_A	Thickness of A domain (Ch. 1)
d_{AC}	Diameter of the cylindrical AC interface in the rings-at-lamellae structure (Ch. 4)
d_{box}	B-domain height when approximated by a box-shaped profile (Ch. 4)
d_B	Average thickness of B-domain (Ch. 1, 4)
d_{BB}	PHMA Backbone-Backbone Repeat Spacing (Ch. 3, 5 and 6)
d_c	Distance between rods in the rods-at-lamellae structure (Ch. 3)
d_{CC}	Side chain-side chain repeat spacing (Ch. 3, 5 and 6)
d_{cyl}	Diameter of cylinders in the AB or ABA cylinder phase and rings-at-cylinder structure. (Ch. 4)
d_{i}	In-plane spacing between domains (Ch. 4)
d_{ip}	Spacing Between Concertinas in plane (Ch. 6)
d_l	Lamellar repeat spacing (Ch. 2, 3 and 4)

d_r	In-Plane Row Spacing (Ch. 5)
d_s	Distance between adjacent balls at the AC interface in the balls-at-lamellae structures (Ch. 3)
d_{SOL}	Sol-Sol particle repeat spacing (Ch. 6)
d_w	Concertina Wiggle Period (Ch. 6)
d_x	Height of B-domains (Ch. 3, 4)
d_y	In-plane width of B domains (Ch. 3, 4)
δ_i	Hildebrand Solubility Parameter (Ch. 1, 3, 4, 5 and 6)
δ_{ij}	Kronecker Delta Matrix (Ch. 2)
$e_{jk}(x_l)$	Strain field at point $X_j(x_k)$ (Ch. 2)
e^m_{jk}	Fourier amplitudes of strain field (Ch. 2)
ε	Ellipse eccentricity (Ch. 2)
ε	Aspect ratio of rod, ball or perforation (Ch. 4)
ε	Fractional Contraction (Ch. 6)
ε_{jkl}	Anti-symmetric tensor (Ch. 2)
$E(x)$	Complete Elliptic Integral of Second Kind (Ch. 4)
f_X	Volume Fraction of Block/Phase X (Ch. 1-6)
F_{hkl}	Fourier Coefficient for reciprocal lattice vector (*hkl)* (Ch. 1)
$F^u(q_j)/F^c(q_j)$	Fourier amplitude for wave vector q_j in the uncompressed/compressed structure (Ch. 2)
F_h^{TL}	Fourier coefficient of the slab model of the triple-lamellae structure for the *h*-th harmonic (Ch. 3)
F_h^{DL}	Fourier coefficient of the slab model of the double-lamellae structure for the *h*-th harmonic (Ch. 3)
F_{hk}^{rods}	Fourier coefficient for (*h,k*) reciprocal lattice vector in the rods-at-lamellae structure (Ch. 3)
F_{hkl}^{balls}	Fourier coefficient for (*h,k,l*) reciprocal lattice vector in the balls-at-lamellae structure (Ch. 3)
ϕ	Sample Rotation angle (Ch. 2)
ϕ	Angle at which concertina strands cross (Ch. 6)
ϕ_a	Fraction of plane of AC interface occupied by B-domains (Ch. 4)
ϕ_A	Fraction of B-domain on A side of AC interface (Ch. 3, 4)
ϕ_C	Fraction of B-domain on C side of AC interface (Ch. 3, 4)
$\phi_{cyl}(x,y)$	Fourier transform for a half-cylinder (Ch. 3)
ϕ_i	Ratio of B-domain in-plane spacing to lamellar repeat spacing. (Ch. 4)
ϕ_n	Azimuth of film normal in the un-rotated sample (Ch. 2)
$\phi_{sph}(x, y)$	Fourier transform of a half-ellipsoid (Ch. 3)
G	Gibbs free energy per copolymer (Ch. 4)
G_{int}	Component of Gibbs free energy per copolymer from enthalpy of mixing at domain interfaces (Ch. 4).
$G_{stretch}$	Component of Gibbs free energy per copolymer from stretching of chains into domain interiors. (Ch. 4)
$\Delta G[\rho_i]$	Change in Free Energy per copolymer relative to disordered state. (Ch. 1)
γ	Crystallite mosaicity (radians; Ch. 2)

γ_{ij}	$\gamma_{ij} \times k_B T$ is the Enthalpy of mixing per unit area (surface tension) between blocks i and j (Ch. 3, 4)
(h,k,l)	Reciprocal lattice vector (Ch. 1)
$\{h,k,l\}$	Set of symmetry-related reciprocal lattice vectors (Ch. 1)
$h(y)$	Function describing B-domain interface shape (Ch. 4)
$H_{n,cyl}$	Integrated moments of domain profile (Ch. 4)
$\Delta H_{segment}(\boldsymbol{x})$	Enthalpy of Mixing per segment at point $\boldsymbol{x}$ (Ch. 1)
$\Delta H[\rho_i]$	Average mixing enthalpy per copolymer (Ch. 1)
$\eta_{A/C}$	Mean squared path length of block A/C relative to mean squared end-to-end length of block A/C in triple-lamellar structure with same lattice size. (Ch. 4)
η_B	Mean squared path length of chains in the block B relative to a lamellar B domain of the same average thickness. (Ch. 4)
I, $I(s)$, $I(s_x,s_y)$	Scattering intensity per steradian (Ch. 1, 2, 3, 5 and 6)
$\langle I_{\{hkl\}} \rangle$	Average intensity of Bragg Reflections {hkl} (Ch. 2)
$I_{AVG}(s)$	Average Scattering intensity per steradian (Ch. 2)
$I_{back}(s)$	Intensity of background scattering in powder pattern (Ch. 3)
I_0	Integrated intensity of Bragg spot (Ch. 2)
I_j	Integrated intensity of scattering peak in powder pattern (Ch. 3)
φ	Rotation angle (Ch. 2)
φ_{AC}	Coefficient relating area of AC interface to area of AB/BC interfaces in triple-lamellar structure. (Ch. 4)
φ_{AB}	Ratio of AB interfacial area to area of AB interface projected into the plane of the AC interface. (Ch. 4)
φ_{BC}	Ratio of BC interfacial area to area of BC interface projected into the plane of the AC interface. (Ch. 4)
k_B	Boltzmann's Constant (Ch. 1, 4)
$\boldsymbol{k}_{incident}$	Wave-vector of the incident X-ray (Ch. 1)
$\boldsymbol{k}_{scattered}$	Wave-vector of the scattered X-ray (Ch. 1)
L	Distance between sample and detector in SAXS beam line (Ch. 1)
L_X	Root mean squared end-to-end length of a polymer chain of type X in a homopolymer melt (Ch.1, 3, 4, 5 and 6)
λ	X-ray Wavelength (Ch. 1)
$\lambda(x_l)$	Second Lame elastic coefficient at point x_l (Ch. 2)
λ^m	Fourier coefficients of second Lame elastic coefficient (Ch. 2)
M_{jk}	3*3 Transformation Matrix describing sample compression (Ch. 2)
M_i	Molecular Weight of a copolymer (Ch. 1)
M_n	Number Average Molecular Weight (Ch.1-6)
M_w	Weight Average Molecular Weight (Ch. 1-6)
M_X	Molecular Weight of X (Ch. 1)
$\mu(x_l)$	First Lame elastic coefficient at point x_l. (Ch. 2)
μ^m	Fourier coefficients of first Lame elastic coefficient (Ch. 2)
N	Average Number of segments in a copolymer. (Ch. 1-6)
N_X	Average Number of segments of type X in copolymer (Ch. 1)
n_i	Number of molecules (Ch. 1)

n_j	Sample surface normal (Ch. 2)
p_j	Packing Length of Polymer j (Fetters, et. al. 1999; Ch 1, 3, 4, 5 and 6)
$\boldsymbol{q}$	Scattering wave vector ($q=\|\boldsymbol{q}\| = 4\pi\times\sin(\theta)/\lambda$; $\boldsymbol{q} = 2\pi \times \boldsymbol{s}$; Ch. 1, 2)
q	Magnitude of scattering wave vector $\boldsymbol{q}$ (Ch. 1, 2)
q_x, q_y	Components of scattering wave vector (Ch. 2)
q_j^u	Position in reciprocal space prior to film compression (Ch. 2)
q_k^c	Position of same point following film compression (Ch. 2)
q_0	Magnitude of scattering wave vector before film compression (Ch. 2)
q_r	Radius of scattering ellipse at angle θ on detector (Ch. 2)
q_{ru}	Scattering ellipse radius at angle θ_u in uncompressed structure (Ch. 2)
$q_{\min}$, $q_{\max}$	Minor and Minor Radii of scattering ellipse (Ch. 2)
δq	Average radial width of Bragg scattering peak (Ch. 2)
θ	Bragg Scattering Angle (2θ is angle between incident and scattered X-ray; Ch. 1, 2, 3, 5 and 6)
θ	Angle on detector from rotation axis (Ch. 2)
θ_0	Angular position of Bragg Spot on detector (Ch. 2)
θ_{bc}	Angle between the two in-plane lattice vectors in the balls-at-lamellae structure (Ch. 3)
θ_e	Angle between the scattering ellipse major axis and the y-axis (Ch. 2)
θ_n	Altitude of film normal in the un-rotated sample (Ch. 2)
θ_u	Angle on detector from rotation axis in uncompressed structure (Ch. 2)
θ_w	Angular width of Bragg scattering peak (Ch. 2)
δθ	Average angular width of Bragg scattering peak (Ch. 2)
$\rho^c(x_k)$	Electron density at point x_k in the compressed structure (Ch. 2)
$\rho_e(\boldsymbol{x})$	Electron density at point $\boldsymbol{x}$. (Ch. 1)
$\rho_i(\boldsymbol{x})$	Fraction of segments of type X at point $\boldsymbol{x}$ (dimensionless; Ch. 1)
$\rho^u(x_k)$	Electron density at point x_k in the uncompressed structure (Ch. 2)
ρ_X	Density of homopolymer X (g/cm^3 ; Ch. 1, 2, 3, 5 and 6)
r_0	Radius of Bragg Spot on detector (Ch. 2)
r_{AB}	Radius of the inner half-toroid in the rings-at-cylinders structure (Ch. 4)
r_{BC}	Radius of the outer half-toroid in the rings-at-cylinders structure (Ch. 4)
$r_j(u)$	Function describing the path followed by the backbone of a continuous Gaussian chain (u is the fractional distance along the backbone; $0 \le u \le 1$; ends of polymer chain at $r_j(0)$ and $r_j(1)$). (Ch. 1, 4)
r_w	Radial width of Bragg scattering peak (Ch. 2)
R_j	Average root mean square path length of block j. (Ch. 4)
R_{kl}	Unitary 3×3 rotation matrix (Ch. 2)
$\boldsymbol{s}$	Scattering vector ($s=\|\mathbf{s}\| = 2\sin(\theta)/\lambda = q / (2\pi)$) (Ch. 1, 3, 5 and 6).
s	Magnitude of scattering vector $\boldsymbol{s}$ (Ch.1, 3, 5 and 6)
$s_{cen,j}$	Center of j-th scattering peak in a powder pattern (Ch. 3)
$s_{\min}$	Magnitude of minimum accessible scattering vector (Ch. 1)
s_x, s_y, s_z	Component of scattering vector (e.g. $s_x = q_x/(2\pi)$) (Ch. 3, 5 and 6)
$S_{jk}(x_l)$	Stress field at point x_l (Ch. 2)
S^m_{jk}	Fourier coefficients of stress field (Ch. 2)
$S(s_y)$	In-plane rod-rod correlation function (Ch. 3)

$S_{sph}(s_{yz})$	In-plane ball-ball correlation function (Ch. 3)
$\Delta S[\rho_i]$	Change in Entropy per copolymer relative to disordered state. (Ch. 1)
σ_0	Root Mean Square displacement amplitude of the distance between nearest neighbors (Ch. 3)
σ_g	Gaussian component of Voigt peak shape (Ch. 3)
σ_l	Lorentzian component of Voigt peak shape (Ch. 3)
t	Thickness of contracted film relative to uncontracted film (Ch. 2)
t_{ij}	Thickness of interface between polymers i and j (Ch. 3)
T	Temperature (Ch. 1, 4)
T_g	Polymer Glass Transition Temperature (Ch. 1)
T_m	Polymer Crystallization Temperature (Ch. 1)
u	Fractional distance along a polymer backbone (Ch. 1, 4)
U_e	Average elastic energy per unit volume (Ch. 2)
V	Molecular volume of the copolymer. (Ch. 1)
V_{cell}	Volume of the unit cell. (Ch. 2, 4)
V_{chain}	Volume of a polymer chain. (Ch. 1, 4)
V_{ref}	Reference volume taken to be the effective "segment" volume (Ch. 1)
V_{sample}	Volume of the sample (Ch. 1)
V_X	Molecular Volume of block X (Ch. 1)
$V(x, \sigma_l, \sigma_g)$	Voigt Function (Ch. 3)
$w_i(\boldsymbol{x})$	Mean-field Potential for segments of type i at position $\boldsymbol{x}$ (Ch. 1)
w_j	Relative width of the j-th slab in the slab model of the triple-lamellae structure. (Ch. 3)
$[x,y,z]$	Direction in real space lattice (Ch. 1)
$\langle x,y,z \rangle$	Set of symmetry-related directions in real space lattice (Ch. 1)
x_k^u	Position of a point in sample before compression (Ch. 2)
x_j^c	Position of a point in sample after compression (Ch. 2)
x_e, y_e	Coordinates of direct beam on detector (Ch. 2)
$X_j(x_k)$	Position a point x_k is mapped to following elastic distortion (Ch. 2)
x_j	Relative position of center of j-th slab in the slab model of the triple-lamellae structure (Ch. 3)
y_1	Relative offset between the first and second rods along the y-axis for the rods-at-lamellae structure (Ch. 3)
$y_1,\ z_1$	Relative offset between the balls at the two AC interfaces along the two in-plane crystal axes in balls-at-lamellae structure (Ch. 3)
z	Chain stretching distance. For each point in a domain, z is the distance chains with ends at that point must stretch to reach the domain interface (Milner et. al. 1988; Ball et. al. 1991). (Ch. 4)

Chapter One – Introduction

In a block copolymer, two or more chemically distinct polymer chains (blocks) are joined by covalent bonds to form a single macromolecule (Hamley, 1998, Ch1, p1; Figure 1.1). The covalent linkages between these individual blocks prevent macroscopic phase separation even when the polymer blocks are thermodynamically incompatible. Instead, the individual blocks can microphase separate to form domains with sizes comparable to the dimensions of the individual polymer chains (1-100nm) as is illustrated in Figure 1.2. Because individual blocks can be selected to confer distinct chemical or physical properties, block copolymers have found extensive industrial applications including use as structural plastics, blend stabilizers, emulsifiers and contact sensitive adhesives (Ruzette and Leibler, 2005).

Many applications rely primarily upon the ability of block copolymers to suppress macroscopic phase separation (Lodge, 2003). Increasingly there is interest in also harnessing the ability of block copolymers to form numerous nanometer-scale structures. For example, block copolymers can act as templates directing the assembly of inorganic precursors into periodic structures (Templin, et. al. 1997; Bockstaller, et. al. 2005). These block copolymer/inorganic composite materials may be of use for selective membranes, catalysts, porous electrodes, low dielectric insulators and optical materials (Bockstaller et. al., 2005). However, the structure directing capacity of block copolymers is only now being explored.

This thesis reports the structural characterization of block copolymer and copolymer/inorganic materials prepared in the laboratory of Professor Uli Wiesner in the Department of Material Science at Cornell University. The results contribute to the understanding of structure formation in multi-domain and multi-component

polymeric systems. In particular, the structural effects of a third, chemically distinct block was studied for a set of ABC block copolymers and a new, four-layer woodpile structure was identified in an ABC triblock copolymer/aluminosilicate material.

The remaining sections of this chapter provide an overview of block copolymer physics and the use of block copolymers as structure-directing agents. There are several good introductions to the physics of block copolymers (Hamley, 1998; Matsen, 2002; Grason, 2006) and the discussion in this chapter closely follows Bates and Fredrickson's article in "Physics Today" (Bates and Fredrickson, 1999).

Section 1.1 describes the molecular structure of block copolymers and introduces the notation used to describe their physical properties. The thermodynamic properties of polymer melts and solutions are summarized in Section 1.2. The entropy of each copolymer chain is described in terms of the continuous Gaussian chain model while the enthalpy of mixing between the thermodynamically incompatible blocks is described using the Flory-Huggins segment-segment interaction parameter (χ_{ij}). Microphase separation of individual blocks into nanometer-sized domains reduces the mixing enthalpy per copolymer but also lowers the entropy per copolymer. Section 1.3 describes the general order-disorder transition resulting from this trade-off between enthalpy and entropy. The relative strength of interactions between the blocks (χ_{ij}) then determines whether the copolymer blocks are mixed, weakly segregated (WSL) or strongly segregated (SSL). Section 1.3 also summarizes existing analytic and computational descriptions of block copolymer structures in the limits of weak, intermediate and strong segregation.

After many years of theoretical and experimental work, the phase behavior of AB diblock copolymers is relatively well understood (Matsen and Bates, 1997). Section 1.4 summarize this phase behavior and uses the preferred interfacial curvature

between domains to provide a qualitative explanation for the known AB diblock structures (Matsen, 2002; Grason, 2006). Compared to AB diblock copolymers, the phase behavior of ABC triblock copolymers is far more complicated and not nearly as well understood (Bates and Fredrickson, 1999). Progress in this area is summarized in Section 1.5 along with a discussion of current experimental challenges in this area.

The use of organic molecules to the direct the assembly of inorganic precursors has been the subject of considerable research and is reviewed in a number of publications (Kresge et. al., 1992; Soler-Illia et. al., 2002; Schuth and Schmidt, 2002; Shenhar et. al., 2005; Bockstaller et. al., 2005). Section 1.6 provides a brief introduction to the used of block copolymers as structural templates with a particular focus upon the general synthetic approach developed by the laboratory of Professor Uli Wiesner (Templin et. al., 1997; Ulrich et. al., 1999; Simon et. al. 2001).

In the work described in this thesis, block copolymer and copolymer/inorganic materials were characterized using a variety of experimental techniques such as Transmission Electron Microscopy (TEM) and Small Angle X-ray Scattering (SAXS). Although the SAXS technique is very similar to conventional X-ray scattering, an overview of SAXS is provided in Section 1.7 to complement introductory texts upon this subject (Als-Nielsen and McMorrow, 2001; Glatter and Kratky, 1982).

Finally, Section 1.8 provides an overview of the topics discussed in the remaining chapters.

1.1 Molecular Structure

As illustrated in Figure 1.1, the molecular structure of a block copolymer depends upon the number and type of blocks and the manner in which the blocks are connected together. The simplest architecture is the linear AB diblock copolymer shown in Figure 1.1a, in which a homopolymer chain of monomers of type A is

covalently linked to a homopolymer chain of monomers of type B. A linear AB diblock copolymer is usually prepared via the repeated addition of monomers of B to the end of the previously synthesized chain of poly(A). The type of monomer in a block determines many of the properties and modern polymer synthetic techniques provide access to a wide range of components (Hamley, 1998, Fig1.2, p4.). AB diblock copolymer are frequently described by listing the components in order (eg. poly(isoprene-block-ethylene oxide), PI-b-PEO).

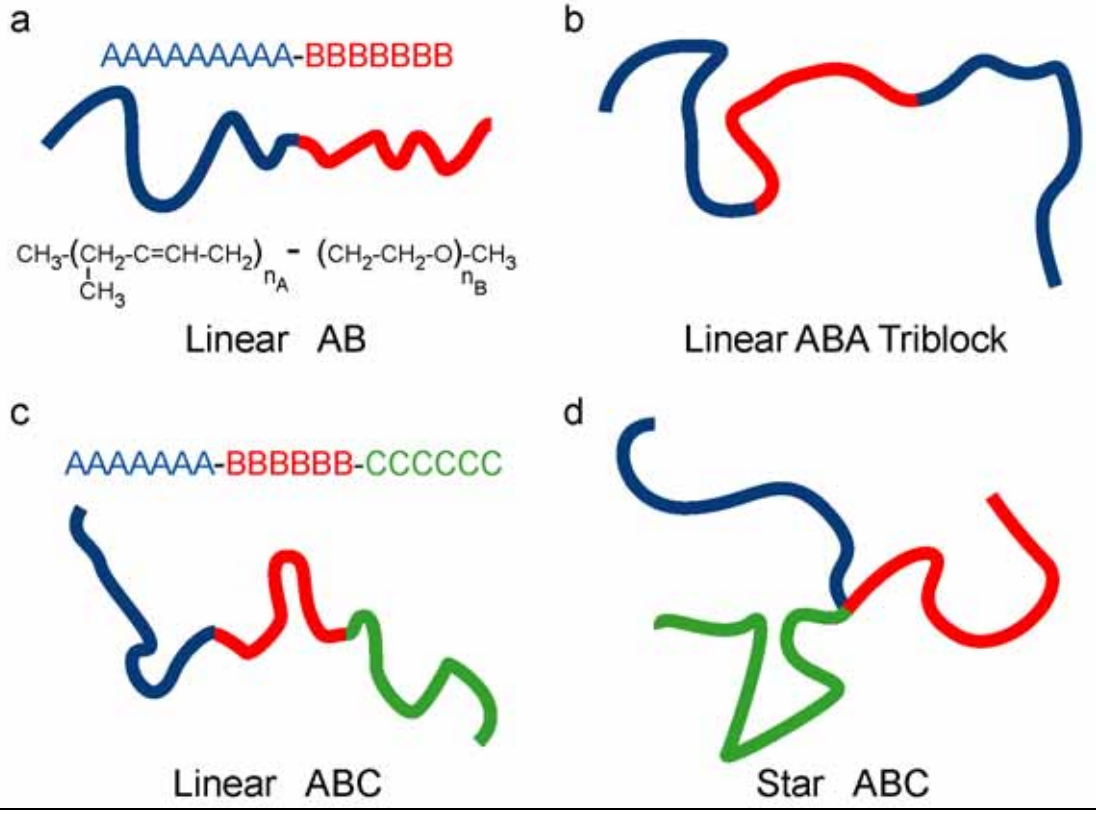

Figure 1.1- Block Copolymer Architectures. (a) Linear AB diblock copolymer. The structure can be represented as chains of monomers (top), lines tracing the backbone of the A (blue) and B (red) blocks or molecular formulae for the A (poly(isoprene), PI) and B (poly(ethylene oxide), PEO) blocks. (b) Linear ABA triblock copolymer. (c) Linear ABC triblock copolymer. (d) Star ABC triblock copolymer.

More complicated molecular structures can be achieved by the addition of extra blocks. For example, the poly(styrene-block-butadiene-block-styrene) (PS-b-PB-b-PS) copolymers widely used in the footwear industry correspond to the linear ABA triblock copolymer architecture shown in Figure 1.1b. Alternatively, the linear ABC triblock copolymer structure shown in Figure 1.1c can be formed by the addition of a third type of monomer (C). Finally, alternative synthetic techniques can be used to form branched architectures such as the star ABC triblock copolymer morphology shown in Figure 1.1d. In the work described here, only block copolymers with AB diblock or linear ABC triblock architectures are considered.

Within the field of polymer science, the average size of a block copolymer is frequently described in terms of the number average molecular weight (M_n), and weight average molecular weight (M_w) defined as,

$$M_n = \frac{\sum_i n_i M_i}{\sum_i n_i}, \qquad M_w = \frac{\sum_i (n_i M_i) \times M_i}{\sum_i n_i M_i}, \tag{1.1}$$

where n_i is the number of molecules with molecular weight M_i. The polydispersity index is defined as the ratio of M_w/M_n and is equal to 1 for a monodisperse system. Actual block copolymers can have quite low polydispersity indices ($M_w/M_n < 1.1$) thanks to synthetic approaches such as living anionic polymerization (Bates and Fredrickson, 2003). Both theory (Sides and Fredrickson, 2004; Cooke and Shi; 2006) and (Lynd and Hillmyer, 2005; Noro et. al., 2005) experiment suggest this level of polydispersity has only a small effect on the phase behavior of AB diblock copolymers.

An effective volume for the block copolymer, V, can be defined as,

$$V = \frac{M_A}{\rho_A} + \frac{M_B}{\rho_B} + \ldots, \tag{1.2}$$

where M_X is the number average molecular weight of block X and ρ_X is the density of the corresponding homopolymer. The size of individual blocks can be expressed in terms of their number average molecular weight (M_X) or molecular weight fractions. However, it is again convenient to describe their size in terms of effective block volume fractions,

$$f_X = \frac{V_X}{V} = \frac{M_X}{\rho_X V} \ , \tag{1.3}$$

where V_X is the volume a homopolymer corresponding to polymer block X.

Because the monomers in each block can differ substantially in size, it is more convenient to think of the chains in terms of segments, each of volume V_{ref} (commonly taken to be the average monomer volume). The average number of segments per copolymer, N, can then be defined as,

$$N = \frac{V}{V_{ref}} , \tag{1.4}$$

while the average number of segments in block X is given by,

$$N_X = \frac{V_X}{V_{ref}} = f_X N \ . \tag{1.5}$$

1.2 Polymer Thermodynamics

The physics of polymeric and block copolymer systems is described in a number of introductory texts and review articles (Lifshitz et. al., 1979; Young, 1983; Bates and Fredrickson, 1990; Hamley, 1998; Matsen 2002). The interactions between monomers, temperature and presence of solvent all have significant effects upon the physical state of a polymeric system. For example, at room temperature the chains in polyethylene (widely used in plastic bags) are organized into a semi-crystalline structure while the chains in polystyrene (used in drinking cups and as a packing foam) are trapped in a glassy, amorphous state. In both the crystalline and glassy

states, the monomers are frozen in place and the system behaves as a solid (Hamley, 1998).

When polyethylene is heated above its melting temperature (T_m) or polystyrene is heated above its glass transition temperature (T_g), the monomers can move past each other and develop local, liquid-type ordering. In this state, commonly referred to as a melt, each polymer backbone can explore a vast range of conformations and also move throughout the system. Because monomers cannot freely move in the glassy or crystalline states, microphase separation in block copolymers must be studied above the glass (T_g) or crystallization (T_m) temperatures of the individual polymer blocks. Solvents can also dramatically transform the state of polymeric system. For example, at room temperature a solid polystyrene cup can be rapidly dissolved in acetone (commonly used in nail polish remover) to form a goopy, fluid mess and the polystyrene does not return to the solid, glassy state until most of the solvent has evaporated. Solvents are very useful for increasing the mobility of polymer chains and can be used to mix polymers that would otherwise be solid at a particular temperature.

The thermodynamic behavior of polymer melts and polymer solutions was first described by Huggins (Huggins, 1941) and Flory (Flory, 1942). In the Flory-Huggins model, the monomers of the polymer and individual solvent molecules are described in terms of units or segments (volume V_{ref}) that are assumed to occupy space with a constant number of segments per unit volume. The local concentration of monomers (or solvent molecules) of type X, can then be described in terms of the average fraction of segments, $\rho_X(\boldsymbol{x})$, of type X residing at a point, $\boldsymbol{x}$. Interactions between segments are assumed to be short-ranged and to depend only upon the local concentration of the different types of segment. In contrast, the entropy of each

polymer is a non-local quantity because it depends upon the number of allowable conformations for the entire polymer backbone. Despite its simplicity, this mean-field approach of Huggins and Flory works remarkably well for a wide range of polymeric systems (Young, 1983; Hamley, 1998). The success of the Flory-Huggins model depends in part upon each polymer chain having an enormous number of degrees of freedom (>> 100). Because the enthalpy/entropy of each chain depends upon the sum of interactions/conformations along the chain, the significance of fluctuations at individual segments of the chain are considerably reduced.

The configurational entropy of a polymer chain depends upon the allowed paths of the polymer backbone. In a homogeneous melt, attractive and repulsive interactions between monomers average out over short distances so the path of the polymer backbone approximates a random walk (Flory, 1949). Thus, for a sufficiently long chain the unperturbed root mean squared end-to-end length, L_X, is given by,

$$L_X = \sqrt{\frac{V_X}{p_X}} \ , \tag{1.6}$$

where V_X is chain volume and p_x is defined as the monomer packing length (Fetters, et. al. 1999). Fetters and colleagues (Fetters, et. al. 1994 and 1999) have assembled extensive tables of packing lengths for easy calculation of molecular scale, L_X, for different polymers.

In a spatially inhomogeneous melt, the variations in monomer density restrict the allowed conformations of the polymer chains, decreasing their entropy. For block copolymers, this loss in entropy is often approximated using the continuous flexible Gaussian chain model (Matsen, 2002). In this model, the position of each point along the polymer backbone is described by the continuous function, $r_X(u)$, where the variable u is the fractional distance along the backbone ($0 \le u \le 1$) and the ends of the chain are located at $r_X(0)$ and $r_X(1)$. Stretching a section of the chain reduces the

number of allowed conformations, decreasing entropy and increasing the Gibbs free energy of the chain. For a given path of the backbone, $r_X(\mathbf{u})$, the stretching energy of the chain is given by (Matsen, 2002),

$$G_{\text{stretch,X}}\left[r_X(u)\right] = k_B T \times \frac{3p_X}{2V_X} \times \int_{u=0}^{u=1} \left(\frac{dr_X(u)}{du} \right)^2 du \quad , \tag{1.7}$$

where k_B is Boltzmann's constant and T is the temperature.

The mixing enthalpy per copolymer in the Flory-Huggins model is given by the sum of mixing enthalpies for the each segment along the chain. In this model, the segments surrounding each polymer segment act as a solvent for it and the interactions between these segments are described in terms of the dimensionless Flory-Huggins segment-segment interaction parameter, χ_{ij}. Theoretically, χ_{ij} is defined such that $k_B T \times \chi_{ij}$ is the increase in enthalpy when a segment of type i is inserted into a solution of segments of type j (Lodge, 2003). This idealized definition is rarely achieved in experimental measurements of χ_{ij}, but the "experimentalist's χ_{ij}" is still a useful descriptor of the interactions between different chemical species. The Flory-Huggins interaction parameter can be roughly estimated using a semi-empirical relationship first proposed by Hildebrand and Scott (Madkour, 2001),

$$\chi_{ij} = \frac{V_{ref} \times \left(\delta_i - \delta_j\right)^2}{k_B T} \quad , \tag{1.8}$$

where δ_i and δ_j are the Hildebrand solubility parameters for the two polymers. As is evident from Equation 1.8, δ_i has units of (Energy/Volume)$^{1/2}$ (e.g. $J^{1/2}m^{-3/2}$) and values of these solubility parameters are tabulated for a wide range of monomer species (Brandrup and Immergut, 1989). For most pairs of polymers the interaction parameter, χ_{ij}, is small and positive (χ_{ij} = 0.001 to 0.1 typically; Semenov, 1985).

When the interactions between segments are weak and local, the presence of a segment of type i at a point $\boldsymbol{x}$ does not have a large effect upon the local fraction of

segments of type j, $\rho_j(\boldsymbol{x})$, in the neighborhood of point, $\boldsymbol{x}$. Assuming the interactions are essentially pair-wise, the average mixing enthalpy per segment at point $\boldsymbol{x}$ is then given by,

$$\Delta H_{\text{segment}}(\boldsymbol{x}) = k_B T \times \sum_{j,j\neq i} \frac{1}{2} \chi_{ij} \rho_i(\boldsymbol{x}) \rho_j(\boldsymbol{x}). \tag{1.9}$$

Each block copolymer molecule has an average of N segments so the average mixing enthalpy per copolymer is simply the sum over these segments given by,

$$\Delta H[\rho_i] = k_B T \times \sum_{i,j;i\neq j} \frac{\chi_{ij} N}{2} \left\langle \rho_i(\boldsymbol{x}) \rho_j(\boldsymbol{x}) \right\rangle_{\boldsymbol{x}} \tag{1.10}$$

where the average is taken over the volume of the system. Because the mixing enthalpy per copolymer is proportional to the average number of segments per copolymer (N), the product, $\chi_{ij}N$, is widely used to describe the thermodynamic incompatibility of pairs of polymer blocks. Note that $\chi_{ij}N$ does not dependent upon the polymer segment volume, V_{ref}, because χ_{ij} depends linearly upon V_{ref} while N is inversely proportional to V_{ref}. Even when the mixing enthalpy per segment is small ($\chi_{ij} < 1$), the mixing enthalpy per copolymer can still be very significant ($\chi_{ij}N >> 1$) because of the large number of segments in each copolymer ($N \sim 10^2$ to 10^6 typical).

Experimentally, the thermodynamic incompatibility between blocks i and j ($\chi_{ij}N$) can be controlled in several different ways. During synthesis, chemical modification of individual blocks (χ_{ij}) and changes to average number of segments per copolymer (N) have direct and obvious effects upon $\chi_{ij}N$. Following synthesis, the value of $\chi_{ij}N$ can still be manipulated through its dependence on temperature (T) and solvent content. In general, the mixing enthalpy per monomer (ΔH_i) has a weak dependence on temperature (T) and so $\chi_{ij}N$ increases as temperature is lowered and $\chi_{ij}N$ decreases as temperature is increased ($\chi_{ij} \approx A/T+B$; Bates and Fredrickson, 1990). The effective value of $\chi_{ij}N$ can also be reduced through the addition of good solvent

(one compatible with each type of monomer in the copolymer). Because a good solvent mixes well with all blocks, the copolymer segment density is lowered along with the total number of unfavorable interactions between different segments. Thus, the relative incompatibility of blocks i and j ($\chi_{ij}N$) can be reduced by heating or the addition of solvent while $\chi_{ij}N$ is increased by cooling or the removal of solvent.

Finally, it should be noted that in addition to the chain entropy and mixing enthalpy, other interactions are present in block copolymers. For example, long-range electrostatics can be important in ionic polymers (ionomers) and long-range interactions can also arise when the individual monomers have permanent dipole moments (Sayar et. al., 2003). The effect of permanent dipole moments on phase behavior has been modeled (Petschek and Wiefling, 1987; Halperin, 1990) but has not yet been shown to play a significant role in most block copolymer systems (Sayar et. al., 2003; Goldacker et. al., 1999).

1.3 Microphase Separation

Within a block copolymer melt, micro-domains can reduce the unfavorable enthalpy of mixing but they also reduce the entropy of the polymer chains. The resulting structure depends upon the interplay between the enthalpy and entropy. Different copolymer structures (including the disordered state) can be characterized by the spatial dependence of the local volume fraction of each monomer species, $\rho_i(x)$. Taking the isotropic state ($\rho_i(\boldsymbol{x}) = f_i$) as a reference, the change in enthalpy per copolymer is simply,

$$\frac{\Delta H[\rho_i]}{k_B T} = \sum_{i,j;i\neq j} \frac{\chi_{ij}N}{2} \left\langle \rho_i(\boldsymbol{x})\rho_j(\boldsymbol{x}) \right\rangle_x - \sum_{i,j;i\neq j} \frac{\chi_{ij}N}{2} f_i f_j \qquad (1.11)$$

$$= \sum_{i,j;i\neq j} \frac{\chi_{ij}N}{2} \left\langle (\rho_i(\boldsymbol{x}) - f_i) \times (\rho_j(\boldsymbol{x}) - f_j) \right\rangle_x \quad .$$

Clearly, the mixing enthalpy per copolymer can by lowered by density fluctuations and for a diblock copolymer all density modulations lower the enthalpy relative to a homogeneous state. The change in entropy per copolymer, $\Delta S[\rho_i]$, is also a unique functional of the density distribution and is guaranteed to positive since the maximum entropy corresponds to the homogenous state ($\rho_i(x) = f_i$). Thus, the free energy of a structure relative to the homogenous state is given by,

$$\begin{aligned}\frac{\Delta G[\rho_i]}{k_B T} &= \frac{\Delta H[\rho_i] - T\Delta S[\rho_i]}{k_B T} \\ &= \sum_{i,j;i\neq j} \frac{\chi_{ij} N}{2} \left\langle (\rho_i(\boldsymbol{x}) - f_i) \times (\rho_j(\boldsymbol{x}) - f_j) \right\rangle_{\boldsymbol{x}} + \frac{\Delta S[\rho_i]}{k_B} \quad .\end{aligned} \tag{1.12}$$

Entropy favors more homogenous density distributions while the magnitude of the interaction parameters ($\chi_{ij}N$) determines the relative benefits of density modulations. As the equilibrium state corresponds to the global minimum of $\Delta G[\rho_i]$, order-disorder or order-order transitions can be driven by changes in the interaction parameters ($\chi_{ij}N$).

Figure 1.2 illustrates this process for a symmetric ($f_A = f_B$, $p_A = p_B$) AB diblock copolymer. When $\chi_{AB}N$ is small, enthalpy is less significant and the disordered state has the lowest free energy. As the value of $\chi_{AB}N$ increases, the enthalpy of the disordered state becomes prohibitive and the system undergoes a first-order phase transition into a weakly segregated lamellar structure (Figure 1.2b). For large values of $\chi_{AB}N$, the blocks become strongly segregated and the blocks only mix in a narrow region at the domain interfaces (Figure 1.2c). As noted in the previous section, lowering the temperature increases $\chi_{AB}N$ while heating or the addition of solvent reduces $\chi_{AB}N$. Thus, temperature and solvent content can be used to switch between the ordered and disordered states.

A quantitative description of phase separation requires calculations of the relative entropy per copolymer, $\Delta S[\rho_i]$. Unfortunately, $\Delta S[\rho_i]$ is not a local or simple functional and so the free energy of a morphology can only be computed via analytic approximations or computational methods. Good analytic approximations exist when the blocks are either weakly ($|\rho_i(\boldsymbol{x})-f_i| \ll 1$) or strongly ($\rho_i(\boldsymbol{x}) \approx 1$ or 0) segregated while computational methods are effective across the phase diagram (Matsen, 2002).

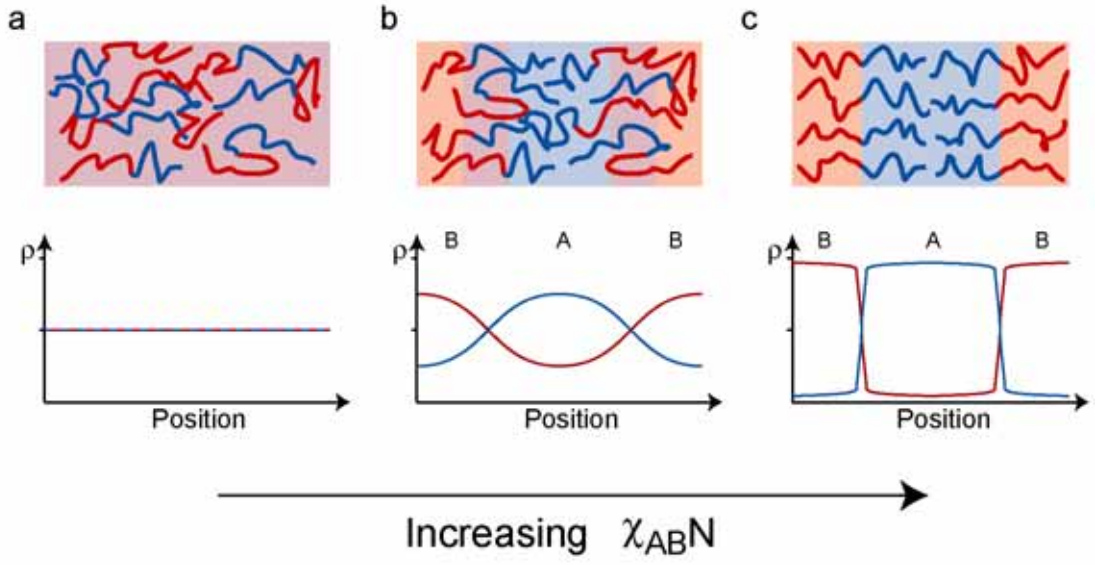

Figure 1.2- Phase segregation in a symmetric AB diblock copolymer ($f_A = f_B = 0.5$, $p_A = p_B$). (a) When $\chi_{AB}N$ is small ($\chi_{AB}N < 10.5$), the blocks mix in a disordered state. (b) A first order phase transition to a weakly segregated lamellar structure occurs when $\chi_{AB}N$ has an intermediate value ($\chi_{AB}N \sim 10.5$). The density of A and B blocks (ρ_A, ρ_B) varies smoothly as a function of position. (c) When $\chi_{AB}N$ is large ($\chi_{AB}N >> 10.5$), the blocks become strongly segregated with narrow interfaces between the domains (Bates and Fredrickson, 1990).

In the Weak Segregation Limit (WSL; $|\rho_i(\boldsymbol{x})-f_i| \ll 1$), the order-disorder transition can be described using a Landau-Ginzburg description (Callen, 1985, Ch 10, p255) as was first demonstrated for AB diblock copolymers by Leibler (Leibler,

1980). The theory uses the response of a non-interacting copolymer to an external potential to link the density-density correlations in the disordered state to the free energy of weakly segregated structures (Leibler, 1980). This approach has since been applied to other copolymer systems and also extended to include effects neglected in the original treatment (Hamley, 1998, Ch2, p80). However, despite the conceptual simplicity of the theory, the calculations are messy and laborious (Hamley, 1998, Ch2, p77) and the power series expansion of $\Delta S[\rho_i]$ is only valid for small density fluctuations ($|\rho_i(\boldsymbol{x})-f_i| \ll 1$).

In the Strong Segregation Limit (SSL; $\rho_i(\boldsymbol{x}) \approx 1$ or 0), the blocks reside within distinct domains while the connections between blocks are localized at the narrow domain interfaces (Figure 1.2c). Mixing occurs only at the domain interfaces and so the mixing enthalpy is proportional to interfacial area. Within each domain, the loss in chain entropy can be estimated using polymer brush models because the must chains stretch from the interfaces to fill space (Hamley, 1998, Ch2, p70). In the SSL, the interplay between entropy and enthalpy is effectively recast into a competition between surface area and chain extension. Semenov first applied this approach to AB diblock copolymers (Semenov, 1985) and several forms of the SSL approximation have since been applied to a wide range of block copolymer systems (Zheng and Wang, 1995; Likhtman and Semenov, 1994). Although actual block copolymer melts rarely satisfy the formal requirements for the SSL, Semenov's formulation provides a convenient way to relate the geometry of a structure to an approximate free energy.

Even though actual block copolymer melts rarely satisfy the assumptions of Leibler's and Semenov's models, these analytic approximations provide important qualitative insight into the order-disorder transition and relative stability of different morphologies. However, block copolymer behavior can be described remarkably well

by numeric Self Consistent Mean-Field Theory (SCMFT). Matsen gives an excellent review of the formulation and efficient solution of self-consistent mean field theory for block copolymers (Matsen, 2002). Briefly, in SCMFT, the interactions between a segment, *i*, and neighboring segments are approximated by the enthalpy averaged over all local conformations, $w_i(\boldsymbol{x})$. Copolymers are well suited to mean field approaches because $<\rho_i(\boldsymbol{x})>$ and $w_i(\boldsymbol{x})$ change slowly compared to the length-scale of the interactions (of the same order as segment size). Because the average energy for each species, $w_i(\boldsymbol{x})$, depends on the local density of all species, $\rho_i(x)$, which in turn is determined by the local enthalpy for each species, $w_i(\boldsymbol{x})$, the values of these two sets of fields must be solved so as to achieved self-consistency while simultaneously minimizing the free energy (Matsen, 2002).

SCMFT was first applied to lamellar, hexagonal and bcc micelle phases in AB and ABA block copolymers by Helfand (Helfand, 1975), but it was a further twenty years before Matsen and Schick determined the stability of all relevant periodic AB diblock morphologies (Matsen and Schick, 1994). This work unified the phase behavior of AB diblock copolymers was from weak to strong segregation ($10 \leq \chi_{AB}N \leq 40$) and also predicted a new 3-Dimensional bicontinuous network structure (double gyroid) at almost the same time as this structure was discovered (Hadjuk, et. al. 1994; Forster et. al., 1994). A number of refinements and alternative formulations of SCMFT have since been made including corrections for the mean-field approximation (Fredrickson, 2002) and commercial packages are available to simulate the dynamics of block copolymer materials (Mesodyne - Fraaije et. al., 1997). With current computer power and algorithms, numerical field theory permits effective simulation of many copolymer systems.

1.4 Diblock Copolymer Morphologies

As shown in Figure 1.3, AB diblock copolymers can form several different morphologies and many years of theoretical and experimental work were required to understand their phase behavior (Matsen and Bates, 1997). To a good approximation, AB diblock copolymers have a "universal" phase diagram in which the equilibrium structure is determined by the block volume fraction f_A and block-block interaction parameter $\chi_{AB}N$ while segment asymmetry ($p_A \neq p_B$), molecular weight and polydispersity shift the boundaries between phases.

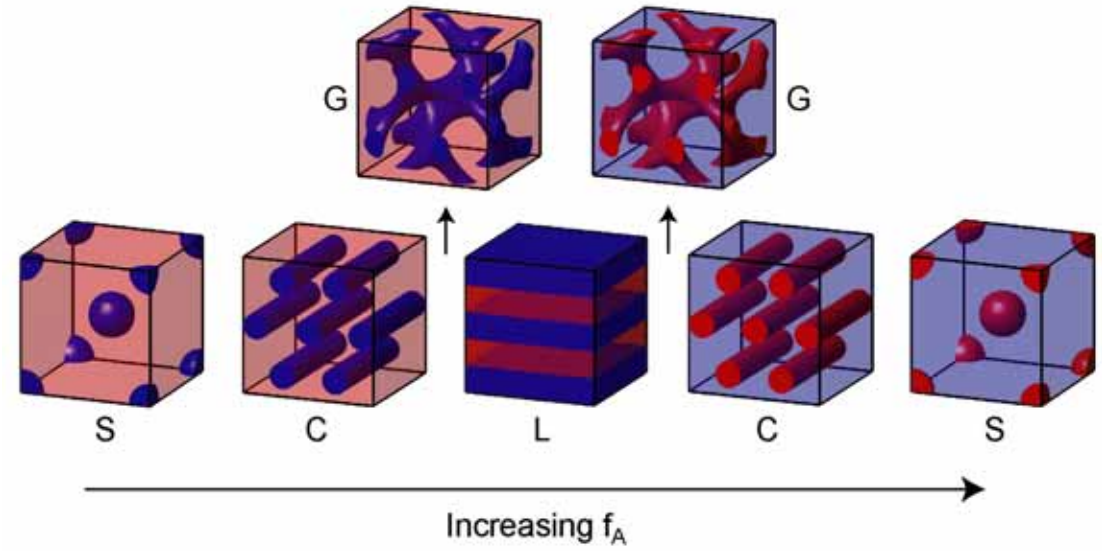

Figure 1.3- Diblock Copolymer Morphologies. Depending on the volume fraction of A (f_A) and interaction parameter ($\chi_{AB}N$), the A (blue) and B (red) blocks can form spherical (S), cylindrical (C) or lamellar (L) domains. For volume fractions between those cylinder and lamellar structures, the double gyroid (G) network structure can form for some values of the block-block interaction parameter ($\chi_{AB}N$).

The effect of block volume fraction (f_A) on the equilibrium morphology can be understood by considering the preferred curvature of domain interfaces. Figure 1.3

shows an asymmetric block copolymer ($f_A = 0.25, f_B = 0.75$) with flat and curved domain interfaces. If the interface flat (Figure 1.4a), the thickness of the two domains are proportional to their volume fractions and the thickness of the B domain (d_B) is three times that of the A domain (d_A). Curving the domain interface towards the smaller A domain (Figure 1.4b) reduces chain stretching in the B-domain but increases chain stretching in the A domain. Thus, the tradeoff between stretching in the A and B domains leads to an optimal interfacial curvature that depends on the block volume fractions and packing lengths (p_A, p_B). In the absence of segment asymmetry ($p_A = p_B$), the optimal interface curves toward the smaller block and the curvature increases as the block volume fraction decreases (Matsen, 2002; Grason, 2006).

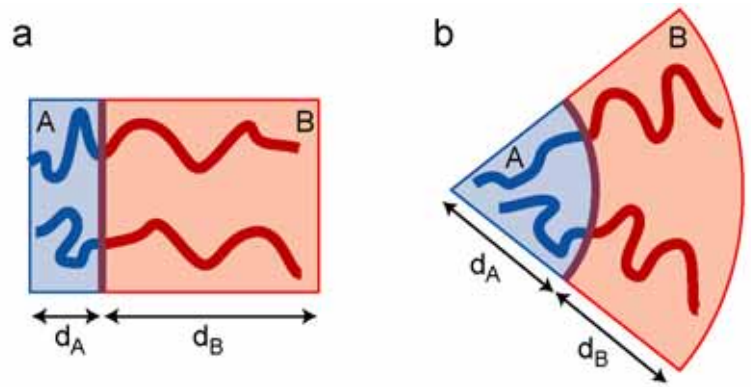

Figure 1.4- Domain Interfacial Curvature. Both panels show an AB diblock copolymer with the same interfacial area and $f_A = 0.25$. (a) At the flat interface the width of the A domain (d_A) is one third of that of the B domain (d_B). (b) At a cylindrical interface, both domains have the same width.

This trend in preferred domain curvature is reflected in the succession of "classical" diblock morphologies shown in Figure 1.3. For equal volume fractions ($p_A = p_B$), the A and B blocks form lamellar domains with flat interfaces. At lower volume fractions of the A or B block, the minor block forms curved cylindrical

domains and for the lowest volume fractions the minority block forms even more tightly curved spherical domains. The double gyroid morphology (Hadjuk, et. al. 1994) is also consistent with this trend in preferred interfacial curvature. In this three-dimensional, bicontinuous network structure, the minority block forms tube-like struts that connect together at 3-fold nodes with an average curvature less than cylindrical domains and greater than lamellar domains. Thus, the preferred curvature of domain interfaces is a very useful for a qualitative understanding the equilibrium morphologies formed in block copolymers.

The phase behavior of diblock copolymers is also well understood at a more quantitative level with excellent agreement between SCMFT calculations and experimental studies of a number of diblock copolymer systems (Matsen and Bates, 1996).

1.5 Linear ABC Triblock Copolymers

Compared to AB diblock copolymers, the presence of a third, distinct block in linear ABC triblock copolymers leads to a significant increase in the complexity and number of morphologies (Zheng and Wang, 1995; Bates and Fredrickson, 1999) with over twenty-five structures reported to date (Epps, et. al. 2004). Examples of complex ABC copolymer morphologies include several bicontinuous network structures (Mogi, et. al. 1992b; Matsushita, et. al. 1998; Bailey, et. al. 2002; Epps, et. al. 2004, Tyler and Morse, 2005), a non-centrosymmetric lamellar structure (Goldacker, et. al. 1999; Takano, et. al. 2003), chiral cylinders (Krappe, et. al. 1995), multi-compartment micelles (Li, et. al. 2004) and two-dimensional "knitting" (Breiner, et. al. 1998) and ladder (Kaneko, et. al. 2006) structures.

The larger morphological complexity of ABC triblock copolymers reflects the increased number of molecular parameters with two independent block volume

fractions ($f_A, f_B, f_C = 1 - f_A - f_B$) and three block-block interaction parameters ($\chi_{AB}N$, $\chi_{BC}N$ and $\chi_{AB}N$). Changes in interaction parameters can induce morphological transitions, even when the block volume fractions remain constant. This process is illustrated in Figure 1.5 for three ABC triblock copolymer morphologies in which the block volume fractions are all equal ($f_A = f_B = f_C = 1/3$).

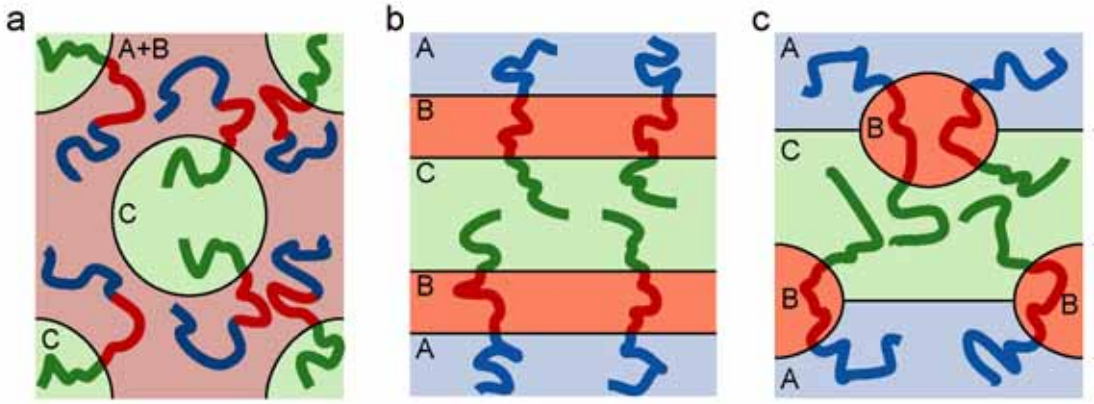

Figure 1.5- ABC Triblock Morphologies. Far more structures can form in ABC triblock copolymers, as illustrated by these three ABC morphologies, all of which have the same volume fraction of the three blocks are equal ($f_A = f_B = f_C$). (a) Two-phase cylinder morphology favored when $\chi_{AB}N << \chi_{BC}N \approx \chi_{AC}N$. (b) Triple-Lamellae morphology favored when $\chi_{AB}N \approx \chi_{BC}N << \chi_{AC}N$. (c) Cylinders-at-lamellae structure favored when $\chi_{AC}N < \chi_{AB}N \approx \chi_{BC}N$.

For example, the A and B domains can mix together if $\chi_{AB}N$ is small (< 15) leading to a two-domain structure (Abetz, et. al. 1996) such as the cylinder structure shown in Figure 1.5a. Alternatively, if contact between the A and C blocks is unfavorable ($\chi_{AC}N >> \chi_{AB}N, \chi_{BC}N$), the B domain can separate these the end-domains as in the ABCBA triple lamellae structure (Matsushita, et. al. 1980) shown in Figure 1.5b. Finally, when the middle B block in strongly incompatible with both the A and C end blocks ($\chi_{AB}N \approx \chi_{BC}N >> \chi_{AC}N$), the formation of AC interfaces is

favored as in cylinders-at-lamellae morphology (Auschra and Stadler, 1993; Figure 1.5c).

Understanding the rich phase behavior of ABC copolymers presents several theoretical and experimental challenges. Just like AB diblock copolymers, ABC triblock structures can be well described using SCMFT. However, initial conditions determine which local minimum is found by SCMFT so it can be difficult to find the global minimum of free energy (Bohbot-Raviv and Wang, 2000; Fredrickson, et. al. 2002). Experimentally, the synthesis of ABC triblock copolymers is challenging and presently there are no simple ways to produce a combinatorial library of block compositions (Bates and Fredrickson, 1999). Furthermore, a three-domain structure can form via a two-domain intermediate (Yamauchi, et. al. 2003; Maniadis, et. al. 2004) making it especially difficult to determine if an ABC copolymer structure is an equilibrium morphology (Bates and Fredrickson, 1999).

Given these difficulties, a useful approach has been to study the morphologies formed in a particular regime. Examples of this include studies on series of ABC block copolymers with a small middle block (Stadler, et. al. 1995), large middle block (Mogi, et. al. 1992; Mogi, et. al. 1994; Nakazawa and Ohta, 1993), a single large end block (Breiner, et. al. 1997) and series in which the size of the C block was varied (Bailey, et. al. 2001; Bailey, et. al. 2002; Ludwigs, et. al. 2003b). Although the progression of morphologies in each regime has provided many useful insights, much of parameter space remains to be explored.

1.6 Structural Templating

In several biological materials such as bones and shells, the properties of biological polymers are augmented through the inclusion of mineral components such as calcium carbonate or silica (Aizenberg, et. al. 2005). These inorganic materials are

integrated at the molecular level with proteins and peptides directing the assembly of nanometer sized inorganic particles into complex, hierarchical structures (Volcani, 1981; Shimizu, et. al. 1998). As the resulting organic/inorganic composites have outstanding material properties (Aizenberg, et. al. 2005), there has been considerable interest in mimicking biological self-assembly processes.

A significant step in this direction was taken at the Mobile Oil Corporation, where researchers used micro-phase separation in a surfactant solution to synthesize well-ordered mesoporous silicates (Kresge, et. al. 1992; Monnier, et. al. 1993). Because the accessible pore sizes (2 - 10nm) were much larger than the molecular-scale (< 1.3nm) pores in zeolites, surfactant-templated silicates found use as large-pore molecular sieves (Soler-Illia, et. al. 2002). Since this pioneering work, the structure-directing properties of a range of surfactants, block copolymers, peptides and other organic molecules have been extensively investigated and these self-assembled organic/inorganic materials are of interest for many applications including chemical sensors (Shenhar, et. al. 2005), catalysts (Schuth and Schmidt, 2002), low dielectric insulators (Schuth and Shmidt, 2002), solid-state electrolytes (Kosonen, et. al. 2002) and optical materials (Yoon, et. al. 2005).

This work focuses on the use of amphiphilic block copolymers to form nanometer-scale structures in silica-type materials. Amphiphilic block copolymers can be thought of as giant surfactants (~50 to 1000 times the molecular volume of simple surfactants) and their use to structure silica-type materials permits access to larger (10-100nm) mesoporous structures (Templin, et. al. 1997; Zhao, et. al. 1998). Figure 1.6 illustrates the general synthetic approach developed in the laboratory of Professor Uli Wiesner (Templin, et. al. 1997; Simon, et. al. 2001; Jain and Wiesner, 2004). In this approach, solutions of the organic (block copolymer) and inorganic

(silica-type sol particles) precursors are combined the solvent then evaporated to yield the final copolymer/inorganic film. This general process of film formation by evaporation of solvent is known as solvent casting and is used extensively throughout the field of polymer science.

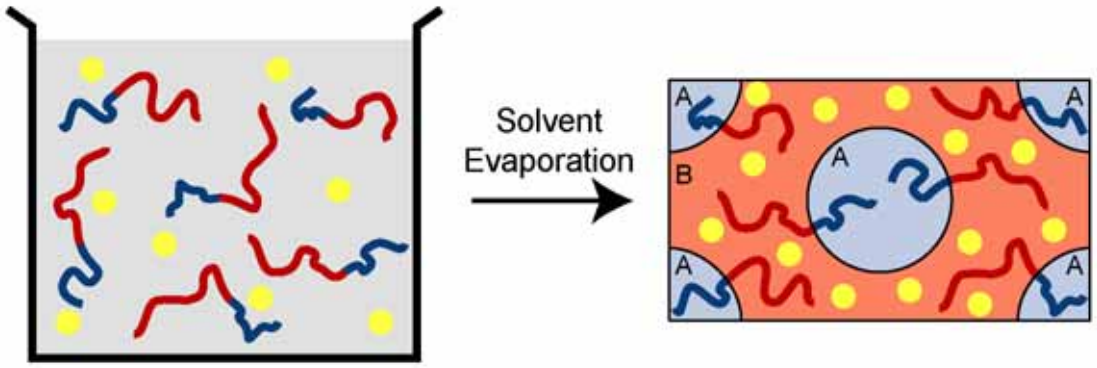

Figure 1.6 - Structural Templating of a silica-type sol (yellow balls) with an amphiphilic AB diblock copolymer. As shown on the left, the block copolymer and inorganic precursors can be combined to form an isotropic solution. As the solvent evaporates, the system undergoes microphase separation and the inorganic precursors partition into the hydrophilic (red) domains.

The silica-type precursors consist of a sol of organically modified aluminosilicate particles with a narrow, well-controlled size distribution that can be varied from 0.5 to 6nm diameter (Warren, et. al. 2007). These particles grow and link together via hydrolysis reactions (Simon, et. al. 2001) and under acidic conditions the particles would eventually cross-link into a gel. Prior to any gelation, the solution of silica-type sol particles is combined with a solution of an amphiphilic block copolymer containing a PEO block (eg. PI-b-PEO). As solvent evaporates, the blocks of the copolymer microphase separate with the hydrophilic PEO block and aluminosilicate partitioning together as shown in Figure 1.6. The resulting structure depends upon the volume fraction of the different domains (Ulrich, et. al. 1999). The

lamellar, cylindrical and spherical diblock copolymer morphologies have all been achieved in diblock copolymer/aluminosilicate materials (Simon et. al., 2001).

Throughout the solvent evaporation process, the sol particles continue to cross-link, especially at the later stages as they become densely packed (Jain and Wiesner, 2004). At the end of the solvent casting process, the aluminosilicate particles are linked together by a three-dimensional network of covalent bonds. If the composite material is re-exposed to solvent, the PEO-aluminosilicate domains can retain their structure. Because the network of covalent bonds within the PEO-aluminosilicate domain trap the PEO block, the other blocks of the copolymer remain attached even in the presence of solvent (Ulrich, et. al. 1999). The covalent bonding network within the PEO-aluminosilicate domains can also preserve its structure when the polymer component is removed by heating above the polymer above its thermal decomposition temperature (termed calcination or pyrolysis; Simon, et. al. 2001). Thus, this synthetic approach provides both block copolymer/aluminosilicate composites and mesoporous aluminosilicate structures.

Despite considerable progress in this area, many interesting research opportunities remain, such as adapting the process to other inorganic materials (e.g. titanium dioxide, silicon carbonitride) and developing methods to position catalytic particles at the domain interfaces. In addition to these synthetic advances, improvements in structural control are also important. For example, morphologies with a three-dimensional network of channels (such as the double gyroid) have outstanding transport properties but have been hard to synthesize (Hayward, et. al. 2004). Chapter 2 describes the characterization of a network structure formed in a PI-b-PEO/aluminosilicate composite.

Another interesting direction is to use structure-directing agents with more complex phase behavior than AB diblock copolymers. Linear ABC triblock copolymers form an enormous number of morphologies but have yet to be widely used to structure silica-type materials (Mahajan, 2005). Because ABC triblock copolymers can form three, chemically distinct domains they may be able to simultaneous position multiple types of inorganic material (Bockstaller, et. al. 2005; Chiu, et. al. 2005). Chapters 5 and 6 describe two new ABC block copolymer/aluminosilicate structures.

1.7 Small Angle X-ray Scattering

Block copolymers have been studied with a wide range of experimental techniques such as Atomic Force Microscopy (AFM; e.g. Ludwigs et. al., 2005), rheology (Kossuth et. al., 1999; Cho et. al., 2004), gas permeability (Kinning et. al., 1987) and dielectric spectroscopy (Ruzette et. al., 2001; Cho et. al., 2004). For structural studies, two of the most widely used techniques are Transmission Electron Microscopy (TEM; Thomas and Midgley, 2004) and Small Angle X-ray Scattering (SAXS; Chu and Hsiao, 2001). The technique of x-ray scattering (Als-Nielsen and McMorrow, 2001; Warren, 1969) and SAXS (Guinier and Fournet, 1955; Glatter and Kratky, 1982) are well described in a number of introductory texts and the reader is strongly encouraged to consult these references in preference to the following overview of SAXS from block copolymers.

X-rays are electromagnetic waves and X-ray scattering from a material provides information about the local densities of electrons and atomic nuclei within that material. In conventional X-ray scattering, the X-ray wavelength (λ), sample thickness and other relevant parameters are chosen such that the majority of scattered X-rays have the same energy as the incident beam (elastic scattering) and have not undergone multiple scattering events within the sample. When these conditions are

achieved, X-ray scattering from a material can be understood in terms of kinematic diffraction (Chapter 4, Als-Nielsen and McMorrow, 2001). In kinematic diffraction, the angle between the incident and scattered radiation (2θ; Figure 1.7) is inversely related to the length-scale being probed. SAXS is a variant of conventional X-ray scattering in which X-ray scattering close to the incident X-ray beam (typically $2\theta < 0.1$ radians) is used to study ordering at longer length-scales (typically 5 to 100nm).

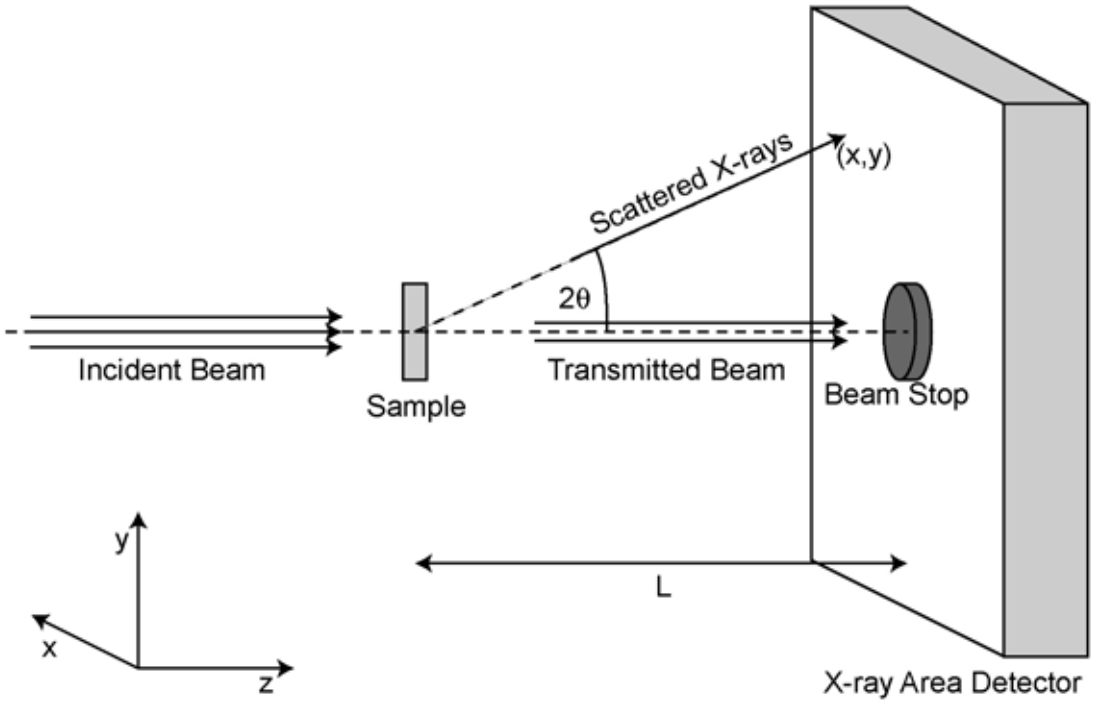

Figure 1.7 – Schematic of Small Angle X-ray Scattering (SAXS) setup. The sample is inserted into the incident beam of monochromatic X-rays and the intensity of the scattered X-rays is measured with a two-dimensional area detector. X-rays scattered by an angle 2θ are detected at a position (x, y) that depends upon the distance between the sample and detector (L). A beam stop prevents the intense, transmitted beam from reaching the detector.

Figure 1.7 shows a schematic of typical SAXS setup. The sample is inserted into a tightly collimated (typical angular divergence < 10^{-3} radians) beam of approximately monochromatic x-rays (typical wavelength $\lambda \sim 0.15$nm). A two-dimensional x-ray area detector a distance, *L*, from the sample measures the intensity of the scattered x-rays as a function of scattering direction while a small beam stop prevents the intense, transmitted beam from reaching the sensitive X-ray detector. An example of a SAXS diffraction pattern from an ABC triblock copolymer is shown in Figure 1.8a.

The direction of scattered x-rays can conveniently be described in terms of the scattering wave-vector, $\boldsymbol{q}$, defined as,

$$\boldsymbol{q} = \boldsymbol{k}_{\text{scattered}} - \boldsymbol{k}_{\text{incident}} \ , \tag{1.13}$$

where $\boldsymbol{k}_{\text{incident}}$ is the wave-vector of the incident X-ray and $\boldsymbol{k}_{\text{scattered}}$ is the wave-vector for the scattered X-ray. Frequently, scattering is described in terms of the closely related scattering vector, **s**, defined as,

$$\boldsymbol{s} = \frac{\boldsymbol{q}}{2\pi}, \tag{1.14}$$

and the use of $\boldsymbol{q}$ or $\boldsymbol{s}$ is largely a matter of taste. For elastic scattering, the incident X-ray beam and scattered X-rays have the same wavelength, λ, and the magnitude of **s** is then given by,

$$s = |\boldsymbol{s}| = \frac{2\sin\theta}{\lambda} \ , \tag{1.15}$$

where 2θ is the angle between the incident and scattered X-rays. Thus, for elastically scattered X-rays the scattering direction determines the scattering vector ($\boldsymbol{s}$). As noted above, scattering at small angles probes ordering at longer length-scales (1/s). When the scattering angle is small ($\sin(\theta) << 1$), the scattering vector can be approximated by,

$$\boldsymbol{s} \approx \frac{1}{\lambda}\left(\frac{x}{L}\hat{\boldsymbol{x}} + \frac{y}{L}\hat{\boldsymbol{y}}\right), \tag{1.16}$$

where (*x, y)* is the position of a point on the detector relative to the transmitted beam.

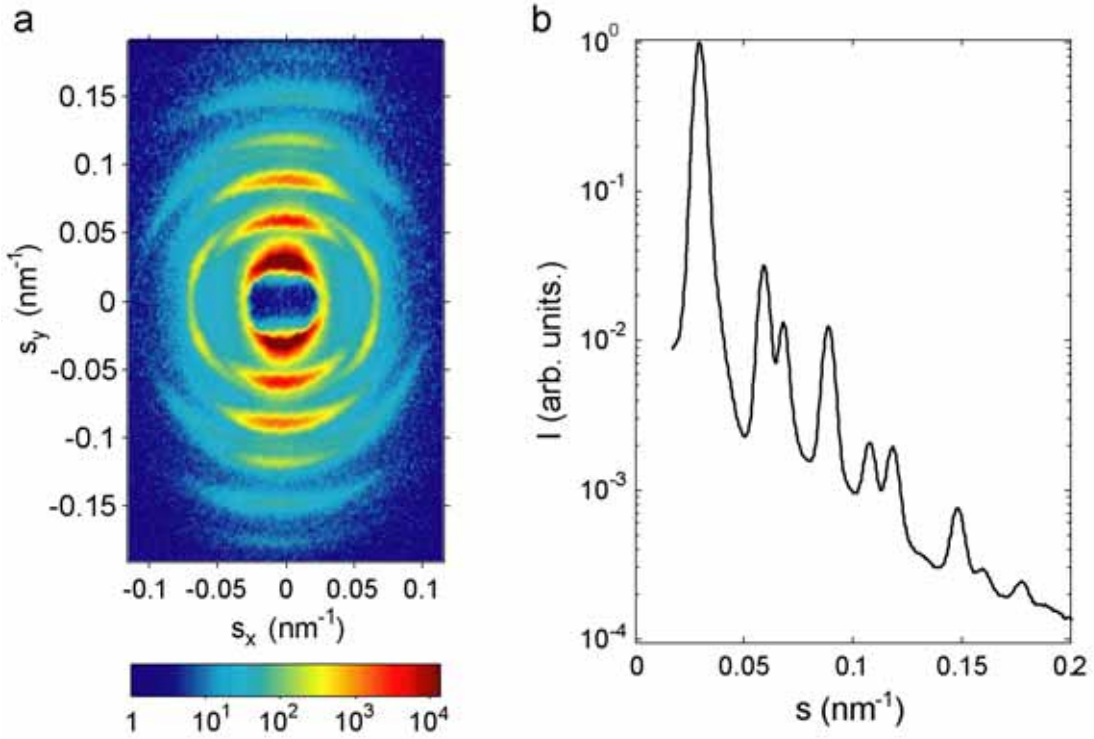

Figure 1.8 – Examples of SAXS data from block copolymers. (a) Two-dimensional diffraction pattern from an oriented ABC copolymer with the rods-at-lamellae structure (Chapter 3). The low intensity at the center of the image is caused by the shadow of the beam stop blocking the intense transmitted beam. (b) One-dimensional (powder average) scattering intensity per steradian, I(s), as a function of scattering vector magnitude, s from an unoriented sample of the same rods-at-lamellae structure. The data collection procedure is described in Section 3.2.

In general, the scattering intensity per steradian, I(**s**), can be approximated by,

$$I(\boldsymbol{s}) = \frac{C}{V_{\text{sample}}} \times \left| \int_{V_{\text{sample}}} \rho_e(\boldsymbol{x}) \exp(-i2\pi\, \boldsymbol{s} \bullet \boldsymbol{x}) d^3\boldsymbol{x} \right|^2 \tag{1.17}$$

where C is a constant, V_{sample} is the volume of the sample and $\rho_e(\boldsymbol{x})$ is the electron density at point, $\boldsymbol{x}$, within the sample. The intensity of scattering, $I(\boldsymbol{s})$, is determined by the order within the material with a spatial period of 1/s along the direction of **s**. Mathematically, $I(\boldsymbol{s})$ is proportional to the squared amplitude of the Fourier transform of the electron density of the material, $\rho_e(\boldsymbol{x})$. In a crystal, the electron density is periodic and the scattering intensity is then,

$$I(\boldsymbol{s}) = C \times \sum_{h,k,l} \left|F_{hkl}\right|^2 \times \delta^3\left(\left(h\boldsymbol{b_1} + k\boldsymbol{b_2} + l\boldsymbol{b_3} - \boldsymbol{s}\right) \times V_{\text{sample}}^{1/3}\right) \times V_{\text{sample}}\,, \tag{1.18}$$

where $\boldsymbol{a_1}$, $\boldsymbol{a_2}$ and $\boldsymbol{a_3}$ and $\boldsymbol{b_1}$, $\boldsymbol{b_2}$, and $\boldsymbol{b_3}$ are the real and reciprocal lattice vectors defined as,

$$a_i \bullet b_i = 1 \qquad \text{and} \qquad a_i \bullet b_j = 0 \quad \text{for} \quad i \neq j\,, \tag{1.19}$$

while F_{hkl} is the structure factor defined as,

$$F_{hkl} = \int_{V_{\text{cell}}} \rho_e(\boldsymbol{x}) \exp\left(-i2\pi\left(h\boldsymbol{b_1} + k\boldsymbol{b_2} + l\boldsymbol{b_3}\right) \bullet \boldsymbol{x}\right) \frac{d^3\boldsymbol{x}}{V_{\text{cell}}}\,, \tag{1.20}$$

where V_{cell} is the volume of the unit cell. Consequently, SAXS from a block copolymer "single crystal" should only show bright Bragg spots where,

$$\boldsymbol{s} = h\boldsymbol{b_1} + k\boldsymbol{b_2} + l\boldsymbol{b_3} \quad \text{and} \quad \left|F_{hkl}\right|^2 \neq 0\,. \tag{1.21}$$

Such Bragg spots are evident in the SAXS pattern shown in Figure 1.8a. Frequently, however, the microstructure within a block copolymer consists of many small, randomly oriented crystallites. For such powder samples, the scattering intensity per steradian, $I(s)$, depends only upon the magnitude of the scattering vector (s) and the two-dimensional scattering pattern consists of a series of concentric rings with the scattering intensity per steradian, $I(s)$, given by,

$$I(s) = \frac{C}{4\pi \times s^2} \times \sum_{h,k,l} \left|F_{hkl}\right|^2 \times \delta\left(\left(\left|h\boldsymbol{b_1} + k\boldsymbol{b_2} + l\boldsymbol{b_3}\right| - s\right) \times V_{\text{sample}}^{1/3}\right) \times V_{\text{sample}}^{1/3}\,. \tag{1.22}$$

In such a powder scattering pattern (e.g. Figure 1.8b), the position of the scattering peaks are given by,

$$s = \left| h\boldsymbol{b_1} + k\boldsymbol{b_2} + l\boldsymbol{b_3} \right| \quad \text{and} \quad \left| F_{hkl} \right|^2 \neq 0 . \tag{1.23}$$

Although SAXS from an un-oriented sample contains less information than SAXS from an oriented sample, the position and intensity of the scattering peaks can still be very helpful when determining the lattice and symmetries of a block copolymer structure.

Before concluding this section, it is helpful to note several features of experimental SAXS data from block copolymers. Firstly, as is clear in Figure 1.8, scattering cannot be measured at the smallest angles because of the beam stop used to block the intense transmitted beam. The size and angular divergence of the incident X-ray beam determine the minimum size of the beam stop which in turn sets the minimum scattering vector ($s_{\min}$) and maximum length-scale ($1/s_{\min}$) that can be probed. Laboratory-based SAXS beam lines rarely exceed the limit, $s_{\min} > 0.01\text{nm}^{-1}$ and $1/s_{\min} < 100\text{nm}$ owing to a trade-off between the size and brightness of the source.

Secondly, experimental scattering peaks (e.g. Figure 1.8) have a finite width rather than the delta functions in Equations 1.18 and 1.22. A substantial part of this width results from instrumental effects including the distribution of wavelengths in the incident X-ray beam, the finite size and angular divergence of the beam and the point spread function of the x-ray detector. However, disorder within the block copolymer structure also contributes to the measured peak width. The dynamics of crystal formation and growth in block copolymers is much slower than in most small molecule systems and block copolymer structures can get trapped in poorly ordered, meta-stable structures. Consequently, reducing variations in crystallite orientation and

lattice size can require extended annealing (hours to weeks) at elevated temperature or in solvent vapor.

Finally, the diffraction pattern from a given block copolymer structure (e.g. Figure 1.8b) is frequently dominated by one or two very strong scattering peaks. This effect is largely caused by the relatively broad interfaces between the polymer domains. Unlike the electron density in a ionic or metallic crystal with small unit cell, the electron density, $\rho_e(\boldsymbol{x})$, in a block copolymer structure is a fairly smooth function of position, $\boldsymbol{x}$, and so the Fourier transform is often dominated by a small number of terms.

These three general features are evident in much of the SAXS data presented in the following chapters. SAXS is a powerful tool for studying the structure of block copolymers, especially when used in combination with Electron Microscopy and Electron Tomography (Midgley and Weyland, 2003).

1.8 Summary and Overview of Thesis

This chapter has provided an overview of block copolymer physics and the use of block copolymers to form nanometer-scale structures in inorganic materials. The remainder of the thesis describes the characterization of structures formed in several block copolymer and block copolymer/aluminosilicate composite materials.

As described in Section 1.4, the bicontinuous double gyroid morphology can form in AB diblock copolymers when the volume fraction of the minority phase lies between that of the cylinder and lamellar phases. In the double gyroid structure, both the minority and majority phases form continuous, three-dimensional networks and achieving such a bicontinuous structure in block copolymer/inorganic composite materials is of interest for applications such as membranes, catalysts and electrodes (Kresge et. al., 1992; Urade et. al., 2007). Chapter 2 describes the characterization of

a bicontinuous AB diblock copolymer/ aluminosilicate morphology prepared by Dr. Ralph Ulrich (Ulrich, 2000; Finnefrock et. al., 2001). Because the morphology within the material was deformed during its synthesis, the SAXS data were not consistent with the symmetry of the double gyroid (Ia3d; Space Group Q230; Hahn, 2002). However, a distorted double gyroid structure was shown to be consistent with the observed SAXS and TEM data by estimating the effect of deformation during the solvent casting process. Models of several other network structures were compared to the SAXS and TEM data and the double gyroid structure was found to be most consistent. This result improves upon an earlier analysis of the structure of this material (Finnefrock et. al., 2001; Finnefrock et. al., 2003) and suggests that diblock copolymer/aluminosilicate materials and pure block copolymers have similar phase behavior.

Chapters 3 and 4 describe studies of the phase behavior of ABC triblock copolymers with a small ($f_B < 0.5$), strongly incompatible ($\gamma_{AC} << \gamma_{AB}, \gamma_{BC}$) B block and roughly equivalent A and C blocks ($f_A \approx f_B$; $\gamma_{AB} \approx \gamma_{BC}$; $p_A \approx p_C$). As noted in Section 1.5, such ABC copolymers can have particular rich phase behavior owing to competition between the obligatory AB and BC interfaces and the optional AC interface. Dr. Surbhi Mahajan synthesized a series of ABC triblock copolymers (Ch 4, Mahajan, 2005) with different B domain volume fractions ($f_B = 0.10$, 0.15 and 0.25) and characterization of these copolymers is described in Chapter 3. In all three copolymers, the A and C blocks formed lamellar domains while the structure of the B block depended strongly upon f_B. The experimental data were consistent with the B domains forming lamellae (Figure 1.5b) at the large B block volume fraction ($f_B = 0.25$), rod-like domains (Figure 1.5b) at intermediate B block volume fraction ($f_B = 0.15$) and ball-like domains at the lowest B block volume fraction ($f_B = 0.10$). This

sequence of phases agrees with an earlier experimental study of PS-b-PB-b-PMMA triblock copolymers (Stadler et. al., 1995).

Chapter 4 describes a study of the thermodynamic stability of these morphologies using the strong segregation limit (SSL) approach of Semenov (Semenov, 1985). Estimates of the Gibbs free energy of each structure suggest that when $\gamma_{AC} < \gamma_{AB} + \gamma_{BC}$, the B domains should form lamellae at the larger B domain volume fractions (f_B), rods at intermediate values of f_B, and balls at the smallest values of f_B. This result is consistent with the experimental results described in Chapter 3 and corrects an earlier SSL analysis performed by Stadler and colleagues (Stadeler et. al., 1995).

As noted in Section 1.6, there is considerable interest in using the rich phase behavior of ABC triblock copolymers to direct inorganic precursors into complex morphologies. Chapters 5 and 6 describe the characterization of two new structures found in ABC triblock copolymer/aluminosilicate materials synthesized by Dr. Surbhi Mahajan (Ch 5, Mahajan, 2005). Materials in which the B and C domains had roughly equivalent volume fractions ($f_B \approx f_C$) and the volume fraction of the A domain was small ($f_A \approx 0.1$) formed a hexagonally patterned lamellar morphology described in Chapter 5. This structure appears to be a variation upon a diblock double-lamellae structure. The B and C domains form lamellae, while the small A domains appear to reduce their unfavorable (but obligatory) contact with the B domain ($\gamma_{AB} >> \gamma_{AC}$) by forming micelles. These micellar A domains appear to form pillars through the lamellar B domain consistent with the "pillared-lamellae" structure proposed by Bailey and colleagues (Bailey, et. al. 2001).

Chapter 6 describes an unusual structure found in an ABC triblock copolymer/aluminosilicate material with block volume fractions ($f_A = 0.19$, $f_B = 0.32$

and $f_C = 0.49$) close to those of the "pillared-lamellae" materials. Using electron tomography, Dr Matthew Weyland determined the complex structure and arrangement of the electron-dense B domains. The individual B domains formed zig-zag shaped strands (concertinas). In the bulk material, these wiggly strands were arranged in a four-layer woodpile structure (Sozuer and Dowling, 1994) in which strands in successive layers ran in alternate directions and the third and fourth layers of strands were offset. Such a non-parallel rod stacking structure has not previously been reported in block copolymers. Unlike the cylindrical domains found in the AB diblock copolymer cylinder phase, in this material the outside of the strands is formed from two types of domain (A and C). These A and C domains may prevent efficient stacking of the strands in a parallel fashion, thereby stabilizing the observed four-layer woodpile structure. However, the interactions favoring the woodpile structure have not been unambiguously identified. The new ABC triblock copolymer/aluminosilicate structures described in Chapters 5 and 6 confirm the complicated phase behavior of ABC copolymers does indeed permit the synthesis of new copolymer/inorganic morphologies.

Finally, the results of these studies and potential for further experiments are discussed in Chapter 7.

Chapter Two : Diblock Copolymer/ Aluminosilicate Network Structure

2.1 Introduction

Porous, inorganic materials formed using organic molecules have many applications (Kresge, et. al., 1992). For membranes and catalysts, structures with continuous networks of pores are particularly useful and these have been formed using both surfactants (Monnier et. al., 1993; Gao, et. al., 2006; Bagshaw et. al., 1995) and block copolymers (Zhao et. al., 1998 ; Chan et. al., 1998). This chapter describes a network structure formed by casting a film (solvent casting) from of a solution with a diblock copolymer and organically modified ceramic precursors (Templin, et. al., 1996; Simon et. al, 2001; Finnefrock, et. al. 2001).

Small angle x-ray scattering (SAXS) and transmission electron microscopy (TEM) showed that the material consists of a powder of relatively large crystallites (~ 100 microns). After accounting for shrinkage during solvent casting (Klotz et. al., 2000; Finnefrock et. al. 2003), individual Bragg reflections could be indexed to crystallites with a body-centered cubic lattice. In the pure diblock copolymer system, network structures showed the Ia$\bar{3}$d crystallographic symmetry (Space Group Q^{230}) and double-gyroid morphology (Floudas, et. al., 2001). However, diffraction patterns from the hybrid material possessed {1,1,0} and {2,0,0} reflections which are forbidden for the Q^{230} space-group. An earlier analysis concluded that the material had the Im$\bar{3}$m crystallographic symmetry (Space Group Q^{229}) and suggested the plumber's nightmare morphology (Huse and Leibler, 1988; Figure 2.20c) was

consistent with the structure of the network of pores (Finnefrock, et. al. 2001; Finnefrock et. al., 2003).

However, as discussed in this chapter, uniaxial compression during the solvent casting process breaks the symmetries of the original cubic lattice so reflections forbidden in the original cubic lattice are permitted in the compressed lattice. Indeed, for models with the double-gyroid morphology, compression leads to significant {110} and {200} reflections. The experimental structure factors are consistent with such a distorted double-gyroid model and inconsistent with corresponding models of the plumber's nightmare morphology. Furthermore, TEM of the material closely resemble projections of the double-gyroid model while differing markedly from projections of the plumber's nightmare.

Thus, the simplest model consistent with the experimental data is a double gyroid morphology with mild distortions caused by solvent casting. This structural re-assignment suggests that the phase diagram of these copolymer/ inorganic hybrids is indeed quite similar to that of copolymer/homopolymer blends (Floudas et. al., 2001).

2.2 Experimental Methods

2.2.1 Synthesis

The synthesis of the diblock copolymer/aluminosilicate material performed by Ralph Ulrich has been described previously (Finnefrock, et. al. 2001, 2003). Briefly, a poly(isoprene-b-ethylene) oxide (PI-b-PEO) diblock copolymer was prepared by living anionic polymerization (Molecular Weight of 16.4 kg/mole, Volume/Weight fraction of PEO of 35%/38%, and polydispersity of 1.07) and is referred to as polymer V36 in Ralph Ulrich's PhD thesis (p51, Ulrich 2000). Small Angle X-ray Scattering

(SAXS) from the pure copolymer was consistent with a hexagonal morphology with a unit cell of ~23nm (page 58, Ulrich 2000).

Following the sol-gel protocol developed in the laboratory of Uli Wiesner (Templin et. al., 1997, Simon et. al., 2001, Jain and Wiesner, 2004), a solution of the polymer (5% by weight in a (1:1 by volume) chloroform/ tetrahydrofuran mixture) was combined with a pre-hydrolyzed solution of 3-glycidyloxypropyl trimethoxysilane (GLYMO) and aluminium sec-butoxide (80:20 by mole). This solution was transferred to a Petri dish and kept at an elevated temperature (~343 Kelvin) while the organic solvent evaporated over the course of 1-2 hours. After further annealing of the sample under rough vacuum at ~403K for ~45 minutes, the final film thickness was approximately 1mm. Assuming the mean density of PI and PEO-aluminosilicate to be 0.91 g/cm^3 and 1.4 g/cm^3, the final volume fraction of PI in the copolymer/aluminosilicate hybrid was 36% (Templin et. al., 1997).

To prepare mesoporous aluminosilicate from the films, the organic material was burnt out via "calcination". As described in Ralph Ulrich's thesis (p114, Ulrich 2000), the films were slowly heated (~1K/minute) in air to a maximum temperature of 823K and kept at this temperature for a period of 6 hours before slowly cooling (~1K/minute) back to room temperature. Following calcination, elemental analysis indicated the presence of 0.1% by weight carbon and 1.5% by weight hydrogen. Weight loss following calcinations was 75%, close to the theoretical prediction of 78%. The calcined material was brittle, hard and white.

2.2.2 Gas Adsorption/Desorption

To measure the porosity of the calcined material, nitrogen adsorption and desorption isotherms were measured at 77K using a Quantachrome Autosorb 6B (Quantachrome Corportation, Boynton Beach, FL). Samples were out-gassed at 423K

and 1mPa for 13h before measurements were made (Finnefrock, et. al. 2001). The nitrogen sorption isotherm was of type IV according to the BDDT classification with a specific surface area of 300 m^2/gram according to the Brunauer-Emmett-Teller method (BET; Brunauer, et. al. 1940). Using the Barret-Joyner-Halenda method, the average pore diameter was calculated to be 8.9nm and the specific pore volume was 0.47 mL/g (Finnefrock, et. al. 2001).

2.2.3 Transmission Electron Microscopy

At the Max Planck Institute for Polymer Physics (Mainz, Germany), Ralph Ulrich examined thin sections of the material via Transmission Electron Microscopy (TEM; Finnefrock et. al., 2001). The uncalcined material was used as is, while the calcined material was manually powdered before embedding the powder in UHU glue (Henkel). Thin sections of both materials (thickness ~ 100nm) were cut using a diamond knife Leica-ultramicrotome (UCT) at 218K and sections were floated off the knife blade onto an aqueous DMSO solution, transferred to EM grids, and examined without staining. TEM was performed on a Leo 912 Ω (tungsten filament) operated at 120kV with an objective aperture angle of 16.5mrad. All images were taken in the elastically filtered imaging mode. To enhance contrast, images were acquired with a defocus of about 2.5μm. Images were acquired using a slow-scan CCD camera (1000×1000 pixels, 14-bit ADC). Because of its higher electron density, the PEO-aluminosilicate phase appears darker than the PI phase in these bright-field images.

2.2.4 Small Angle X-ray Scattering

Small Angle X-ray Scattering (SAXS) data were gathered from both uncalcined and calcined materials using a laboratory source (Finnefrock et. al., 2001). Briefly, CuK_α x-rays (λ=1.54Å) were generated with a rotating anode Rigaku RU-3HR generator (Tube Voltage = 48kV, Tube Current = 58mA, 2mm×0.2mm point

focus on a Copper Anode), filtered by a nickel foil (thickness = 10 μm; Goodfellow, PA) and focused and further monochromatized with a pair of Franks mirrors (Hadjuk, 1994). The flux at the sample was ~4×10^7 X-rays per second in a beam roughly 1mm×1mm. The x-rays scattered by the sample were imaged with a home-built 2-D X-ray area detector consisting of a phosphor screen, fiber-optic coupler and 1024×1024 pixel CCD (Tate, et. al. 1995) positioned at the end of an 80cm flight tube. The much brighter transmitted x-ray beam was blocked with a small circle of lead tape (typical diameter of 3mm) just inside the end of the flight. The distance from the sample to the detector and position of the beam center were determined using a silver behenate calibrant (d_l = 5.8376nm; Blanton, et. al. 1995). The scattering measured on the detector could then be described in terms of the scattering wave vector, $\boldsymbol{q}$, where $q = |\boldsymbol{q}| = 4\pi\times\sin\theta/\lambda$ and 2θ is the total scattering angle. Scattering vectors smaller than $q < 0.1\text{nm}^{-1}$ could not be measured because of the beam-stop blocking the main beam.

Small flakes of the both the calcined and uncalcined material (~3mm × ~1mm× ~0.5mm) readily "stuck" to the walls of standard x-ray capillaries (diameter = 1.5mm, Charles Supper Co, MA.). To achieve sample rotation about a vertical axis, x-ray capillaries were suspended with modeling clay from a small AirPax Stepper Motor that was mounted with double-sided epoxy tape to the top of a motorized X-Y translation stage. Samples were centered by eye on the stepper motor rotation axis before acquiring data. For calcined samples, a 90 second exposure was generally sufficient because of the large density contrast between the aluminosilicate and pores. Longer exposures of up to 800 seconds duration were required for the uncalcined material owing to the lower density contrast between the PI and aluminosilicate-PEO domains.

2.3 Results

2.3.1 SAXS

As shown in Figure 2.2 and Figure 2.1, the material produces quite unusual diffraction patterns where the Bragg reflections lie on ellipses rather than circles. Furthermore, the eccentricity and tilt of these ellipses varied systematically as the sample was rotated.

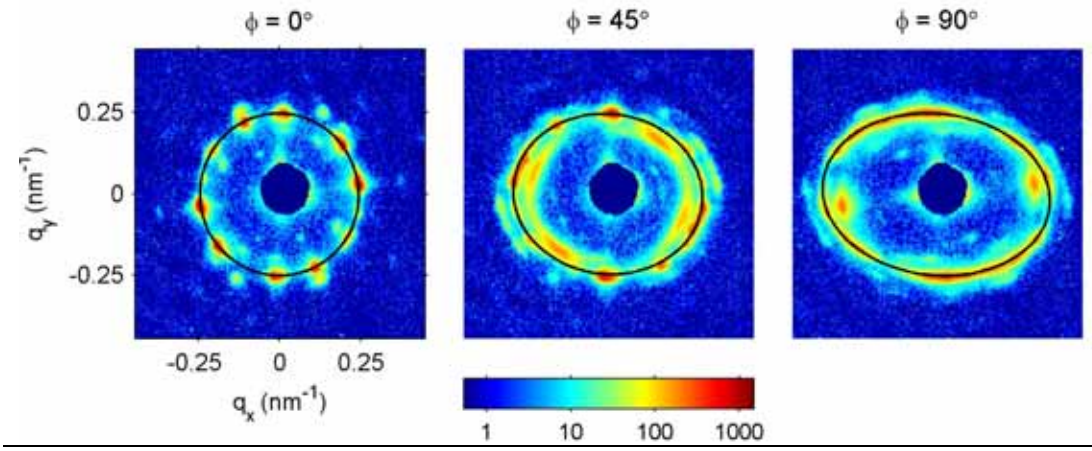

Figure 2.1 - A sequence of SAXS images (90 second exposures) taken from the uncalcined sample at different values of the rotation angle, ϕ, about the q_y (vertical) direction. The oligo-crystalline character of the sample is evident from the multitude of distinct Bragg spots seen in each image. The black ellipse marks the position of the {211} reflections as determined by least squares fitting. The eccentricity and tilt of the ellipse varies considerably as the rotation angle is altered.

In Section 2.3.1.1, this ellipticity is accounted for by the anisotropic contraction of the sample during solvent casting (Klotz et. al., 2000). The magnitude of anisotropic contraction is quantified, and individual diffraction images are "rectified" so as to evaluate the powder average of an idealized, uncompressed sample. After making this correction, the Bragg reflections can be indexed to a body-centered cubic lattice as described in Section 2.3.1.2.

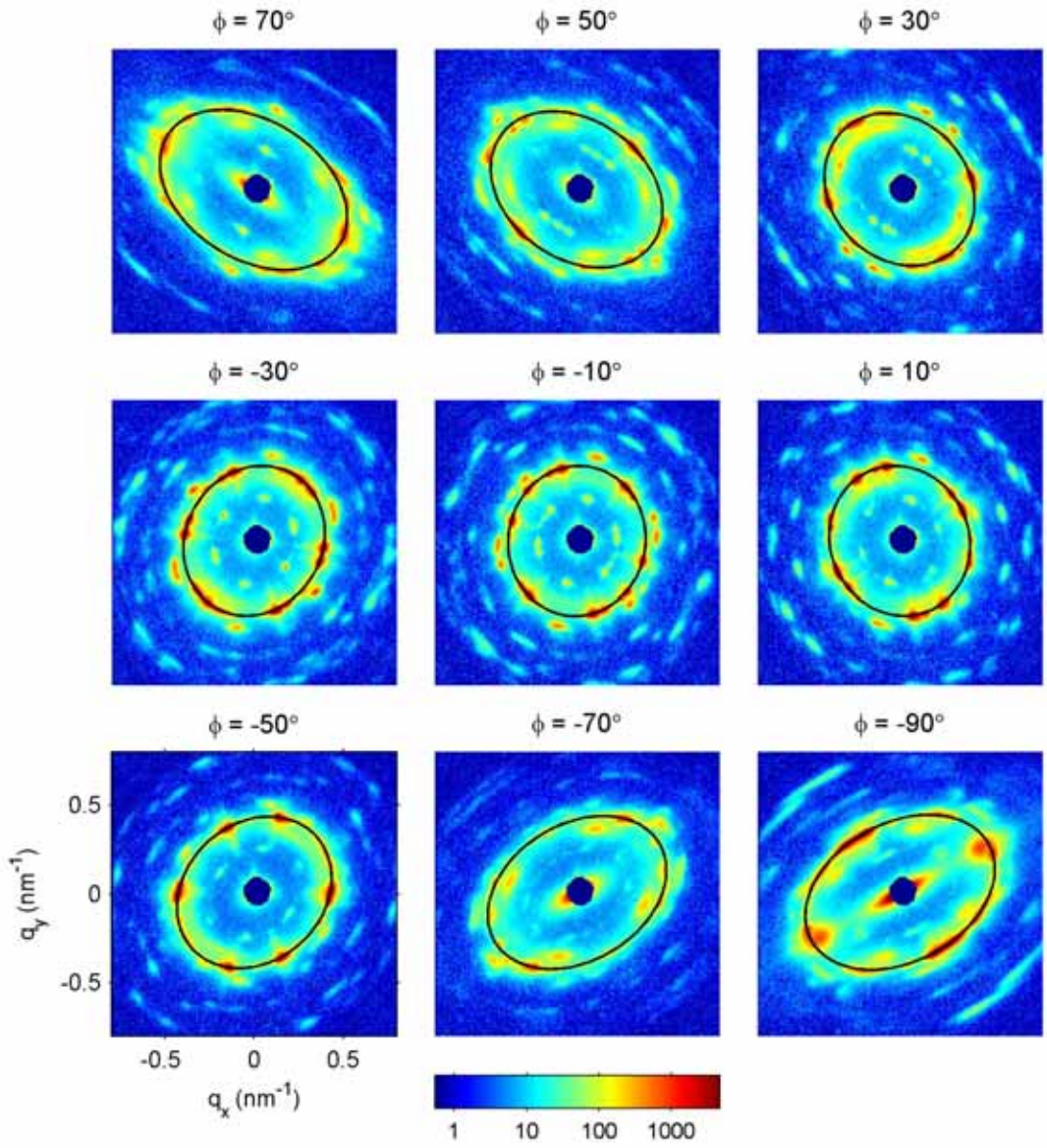

Figure 2.2- A sequence of SAXS images (90 second exposures) taken from the calcined sample at different values of the rotation angle, ϕ, about the q_y (vertical) direction. The oligo-crystalline character of the sample is evident from the multitude of distinct Bragg spots seen in each image. The black ellipse marks the position of the {211} reflections as determined by least squares fitting. The eccentricity and tilt of the ellipse varies considerably as the rotation angle is altered.

2.3.1.1 Elliptical Diffraction

The elliptical shape of the 2-D diffraction rings can be accounted for within the following model (Klotz et. al., 2000; Finnefrock et. al. 2003). Samples were prepared by the slow evaporation of solvent and although the solution is initially quite fluid, as solvent evaporates and cross-links form within the aluminosilicate, the viscosity rises so that at the later stages of casting the material is effectively a solid. Because the film is firmly pinned to the substrate, as the remaining solvent evaporates the film contracts along the direction perpendicular to the surface. In other words, the film becomes thinner without a substantial change in its area. The effect of this strain field on individual crystal domains is depicted in Figure 2.3.

Irrespective of crystallographic orientation, the lattice of each domain is compressed along the direction of the surface normal. This transformation can be described by the equation,

$$x_j^c = M_{jk} x_k^u \ , \tag{2-1}$$

where x_k^u is the position of a point before compression, x_j^c the position after compression and M_{jk} is a 3×3 matrix. For a uniaxial compression the transformation matrix, M_{jk}, can be written as,

$$M_{jk} = \left(\delta_{jk} - n_j n_k\right) + t\, n_j n_k \ , \tag{2-2}$$

where n_j is the surface normal and t is the ratio of compressed film thickness to uncompressed film thickness. Uniaxial compression in real space leads to uniaxial expansion in reciprocal space. Before compression, the Fourier transform of the structure can be defined as,

$$F^u\left(q_j\right) = \int \rho^u\left(x_k\right) \exp\left(-iq_l x_l\right) d^3 x_k \ , \tag{2-3}$$

where $F^u(q_j)$ is the Fourier amplitude for the uncompressed structure, q_j is the wave-vector and $\rho^u(x_k)$ is the electron density at point x_k.

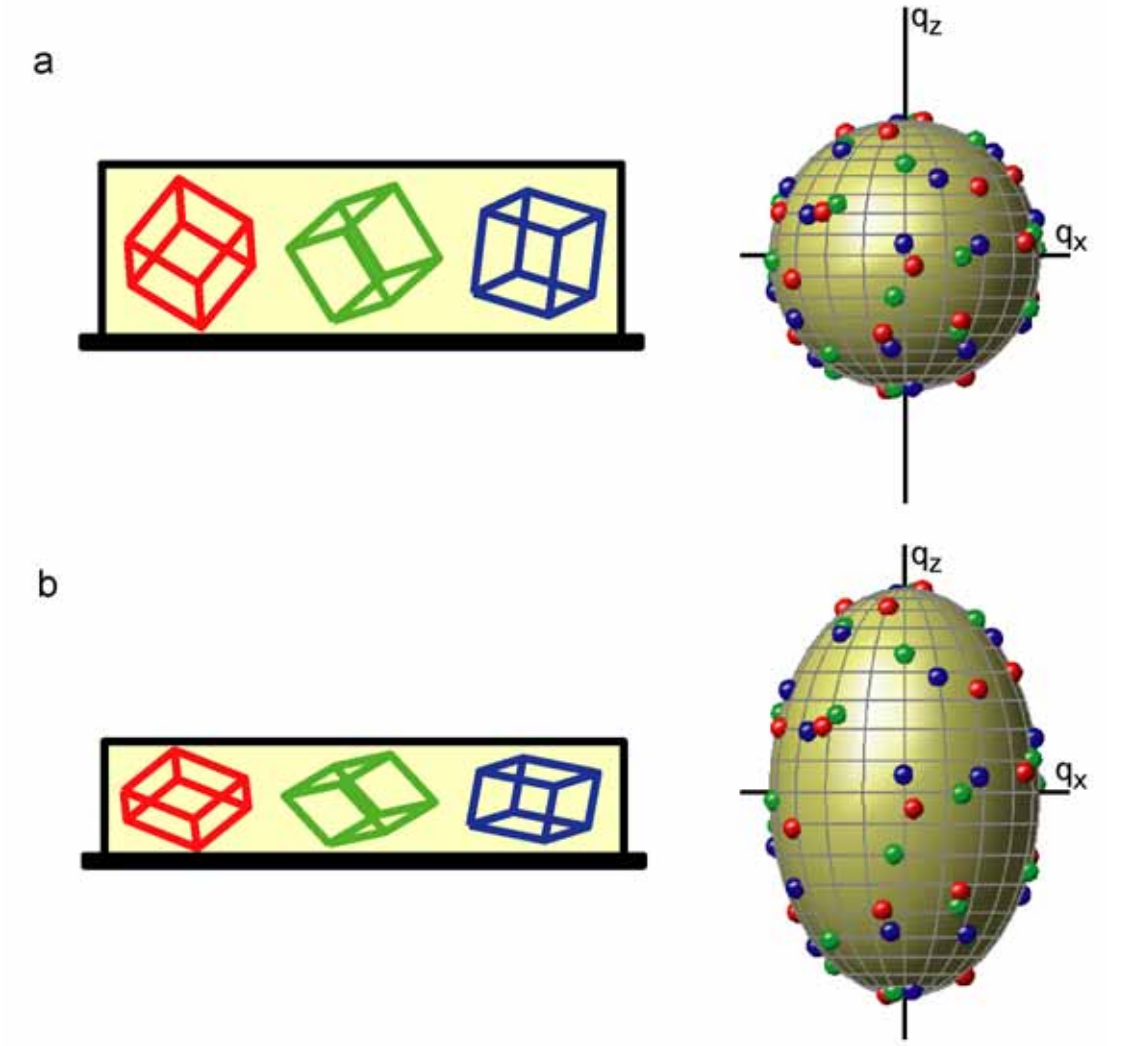

Figure 2.3 – Cartoon illustrating the effect of sample contraction on crystallites with a cubic lattice. (a) Ideal isotropic case. The orientation of three crystallites is illustrated on the left, while on the right the positions of the {211} reflections are marked in the same color. For a given value of $h^2+k^2+l^2$, all reflections lie on the surface of a sphere. (b) Following contraction of the sample perpendicular to the substrate, the unit cell of individual crystallites also contracts in this direction. As shown on the right for the {211} reflections, the reciprocal lattice becomes elongated and reflections with a given value of $h^2+k^2+l^2$ now lie on the surface of a prolate spheroid.

The Fourier transform following film compression, $F^c(q_j)$, is then,

$$\begin{aligned} F^c(q_j) &= \int \rho^u(x_k)\exp(-iq_l M_{lm} x_m) d^3 x_k \quad , \\ &= F^u(M_{lm} q_l) \quad , \end{aligned} \tag{2-4}$$

Thus, film compression transforms points in reciprocal space according to the equation,

$$q_j^u = M_{kj} q_k^c , \tag{2-5}$$

where q_j^u is a point in reciprocal space prior to film compression and q_k^c the same point following film compression. Before film compression, the Fourier transform for an ideal powder sample would consist of concentric spherical shells. Following film compression, each of these spheres would be transformed into a prolate spheroid described by the equation,

$$1 = \frac{\left|q_j^u\right|^2}{q_0^2} = \frac{\left|M_{kj} q_k^c\right|^2}{q_0^2} = \frac{\left(\left|q_j^c\right|^2 - \left|q_j^c n_j\right|^2\right) + t^2 \left|q_j^c n_j\right|^2}{q_0^2} , \tag{2-6}$$

where q_0 is the original radius of the sphere. As illustrated in Figure 2.3b, the spheroid is stretched along the film normal, n_j, by a factor of $1/t$.

The 2-D diffraction pattern measured by x-ray scattering is proportional to the square of the magnitude of the Fourier transform on the surface of the Ewald Sphere. As shown in Figure 2.4, the shape of a diffraction ring is given by the intersection of a prolate spheroid and the Ewald Sphere. For these diffraction rings, the angle through which x-rays scatter is small (< 1°) so the Ewald Sphere may be approximated by a plane. Equation 2-6 permits direct determination of the diffraction ring shape. Defining the x-ray beam to directed along the z-axis and the sample rotation axis about the y-axis (vertical), a point, q_j, on the Ewald Sphere can be conveniently parameterized as,

$$q_j = q_r [\sin\theta, \cos\theta, 0] , \tag{2-7}$$

where q_r is the radius and θ the angle from the rotation axis. In the same polar coordinate system, the surface normal of the sample is,

$$n_j = \left[\sin\theta_n \cos(\phi - \phi_n), \cos\theta_n, \sin\theta_n \sin(\phi - \phi_n)\right] , \tag{2-8}$$

where θ_n and ϕ_n are the altitude and azimuth of the un-rotated sample.

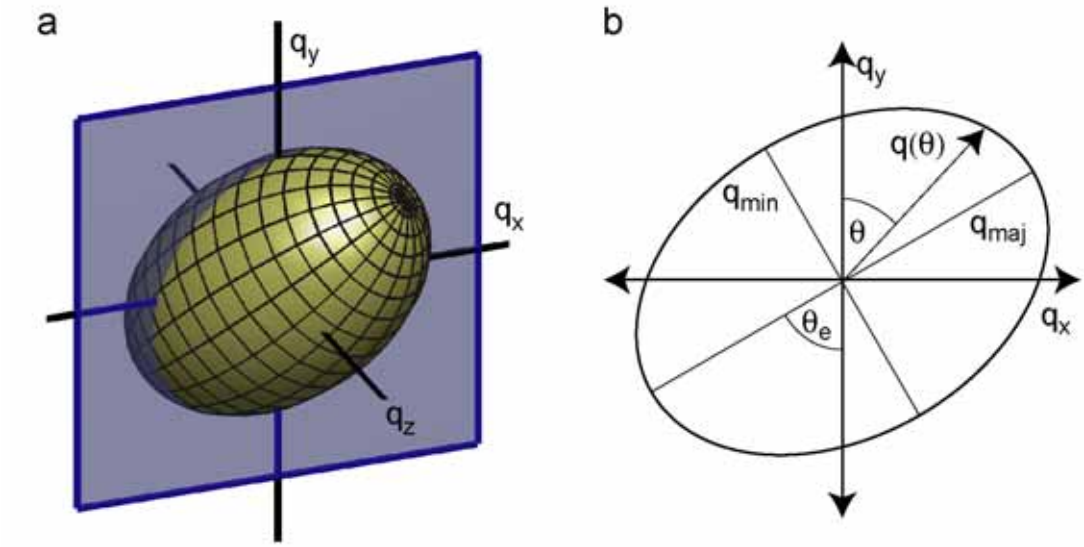

Figure 2.4 – Cartoon illustrating the intersection of the Ewald Sphere and the prolate spheroid of Bragg Reflections from Figure 2.3. The observed 2-D diffraction ring shape is simply the intersection of the spheroid with the Ewald Sphere shown in (a). For the small scattering angles considered here, the Ewald sphere is approximately a plane. (b) The shape of the scattering ring can be described by an ellipse with semi-minor axis, $q_{\min}$, and semi-major axis, q_{maj}, at an angle θ_e with respect to the y-axis.

Substituting Equations 2-7 and 2-8 into Equation 2-6 gives,

$$1 = \frac{q_r^2}{q_{\text{maj}}^2 q_{\min}^2}\left(q_{\text{maj}}^2 \sin^2(\theta - \theta_e) + q_{\min}^2 \cos^2(\theta - \theta_e)\right) , \tag{2-9}$$

$$q_{\text{maj}} = \frac{q_0}{\sqrt{1 - (1 - t^2) \times (1 - \sin^2\theta_n \sin^2\phi_n)}} ,$$

$$q_{\min} = q_0 ,$$

and $$\theta_e = \arctan(\tan\theta_n \cos(\phi - \phi_n)).$$

The shape of the diffraction ring is an ellipse with a minor radius of length $q_{\min}$, major radius of length q_{maj}, and an angle θ_e between the major axis and the y-axis. The same parameterization is also convenient for computing the diffraction image that would have been observed for the sample in the absence of compression. Substituting Equations 2-7 and 2-8 into Equation 2-5, a point (q_r, θ) at radius q_r and angle θ on the actual Ewald Sphere correspond to a point (q_{ru}, θ_u) at radius q_{ru} and angle θ_u on the Ewald Sphere of an uncompressed sample given by,

$$q_{ru} = q_r\sqrt{1-\varepsilon^2\cos^2(\theta-\theta_e)} \quad , \tag{2-10}$$

$$\cos(\theta_u) = \frac{\cos\theta - \varepsilon^2\cos(\theta-\theta_e)\cos(\theta_e)}{\sqrt{(1-\varepsilon^2\cos^2\theta_e)\times(1-\varepsilon^2\cos^2(\theta-\theta_e))}} \quad ,$$

$$\text{where} \quad \varepsilon = \sqrt{1-\frac{q_{\min}^2}{q_{\text{maj}}^2}} \quad .$$

The inverse transformation is given by,

$$q_r = q_{ru}\sqrt{1+\frac{\varepsilon^2}{1-\varepsilon^2}\cos^2(\theta_u-\theta_{ue})}\,, \tag{2-11}$$

$$\cos(\theta-\theta_e) = \frac{\cos(\theta_u-\theta_{ue})}{\sqrt{1-\varepsilon^2\sin^2(\theta_u-\theta_{ue})}} \quad ,$$

$$\text{where} \qquad \cos\theta_{ue} = \frac{\cos\theta_e}{\sqrt{1+\frac{\varepsilon^2}{1-\varepsilon^2}\sin^2\theta_e}} \quad .$$

To apply these equations, the shape of the diffraction ellipses must be estimated. To illustrate the ellipse-fitting procedure, Figure 2.5 shows the diffraction pattern from the calcined sample at ϕ = -90 degrees (lower right panel in Figure 2.2). A convenient parameterization for the ellipse displayed in Figure 2.5 is given by the equations,

$$x(\theta) = x_e + \frac{q_{\min}q_{\text{maj}}\sin\theta}{\sqrt{q_{\text{maj}}^2\sin^2(\theta-\theta_e)+q_{\min}^2\cos^2(\theta-\theta_e)}} \quad , \tag{2-12}$$

$$y(\theta) = y_e + \frac{q_{\min}q_{\text{maj}}\cos\theta}{\sqrt{q_{\text{maj}}^2\sin^2(\theta-\theta_e)+q_{\min}^2\cos^2(\theta-\theta_e)}} \quad ,$$

where (x_e,y_e) is the ellipse center, q_{maj} is the ellipse major radius, q_{min} is the ellipse minor radius, θ_e is the angle between the y-axis and the major ellipse radius and θ is the angle between y-axis and the point $(x(\theta),y(\theta))$.

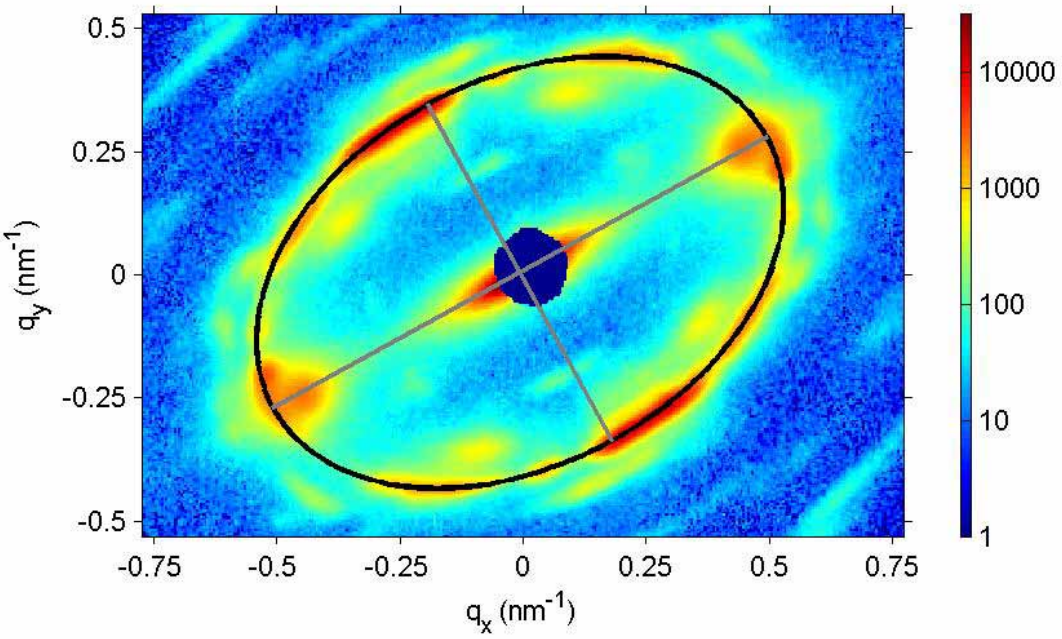

Figure 2.5 – Diffraction from the calcined material for ϕ = -90 degrees. The bright {211} Bragg reflections all lie on an ellipse marked in black. The major and minor radii of the ellipse are q_{maj}=0.572 nm^{-1} and q_{min}=0.39 nm^{-1} respectively, while the angle between the rotation axis (vertical) and the ellipse major axis is θ_e = 61.25 degrees.

The parameters of Equation 2-12 can be obtained to within a few percent simply by fitting the ellipse by eye. A more precise estimate can be obtained by measuring the ellipse radii, $q(\theta)$, as function of angle and then performing a non-linear fit of this to the elliptical radii given by,

$$q(\theta) = \sqrt{\frac{c_0}{c_2(\theta)} + \left(\frac{c_1(\theta)}{c_2(\theta)}\right)^2} + \frac{c_1(\theta)}{c_2(\theta)} \qquad (2\text{-}13)$$

where,

$$c_0 = 1 - \left(\frac{a_e^2}{q_{maj}^2} + \frac{b_e^2}{q_{\min}^2} \right), \tag{2-14}$$

$$c_1 = \frac{a_e}{q_{maj}^2}\cos(\theta_e - \theta) + \frac{b_e}{q_{\min}^2}\sin(\theta_e - \theta),$$

$$c_2 = \frac{\left(q_{maj}^2 + q_{\min}^2\right) - \left(q_{maj}^2 - q_{\min}^2\right)\cos(2(\theta_e - \theta))}{2q_{maj}^2 q_{\min}^2},$$

$$a_e = x_e \sin\theta_e + y_e \cos\theta_e ,$$

$$b_e = -x_e \cos\theta_e + y_e \sin\theta_e ,$$

and x_e and y_e describe the offset of the ellipse origin relative to the radial integration origin. The result for such a fit is shown in Figure 2.6. The black circles show the radius of the most intense scattering for bins with a width $\Delta\theta = 10$ degrees. Because of the large difference between major and minor ellipse radii, it was essential to precondition the peak finder with an initial estimate of $q(\theta)$ and this was conveniently done using the hand-fitted ellipse parameters. $q(\theta)$ cannot be accurately determined for the directions in which there are no Bragg Reflections. In all the images, less than 4 bins out of 36 had ill-defined values of $q(\theta)$ and these bins were identified and excluded on the basis of their lower peak intensity. The combination of these two strategies gave a robust fitting procedure.

The ellipse radii and tilt determination illustrated in Figures 2.5 and 2.6 can be combined with Equations 2-10 and 2-11 to compute the corresponding diffraction image from the hypothetical state prior to sample compression. As shown in Figure 2.7, following the transformation all diffraction rings assume a circular form. This transformation also permits a sensible rotational (powder) average to be constructed, as shown in Figure 2.8.

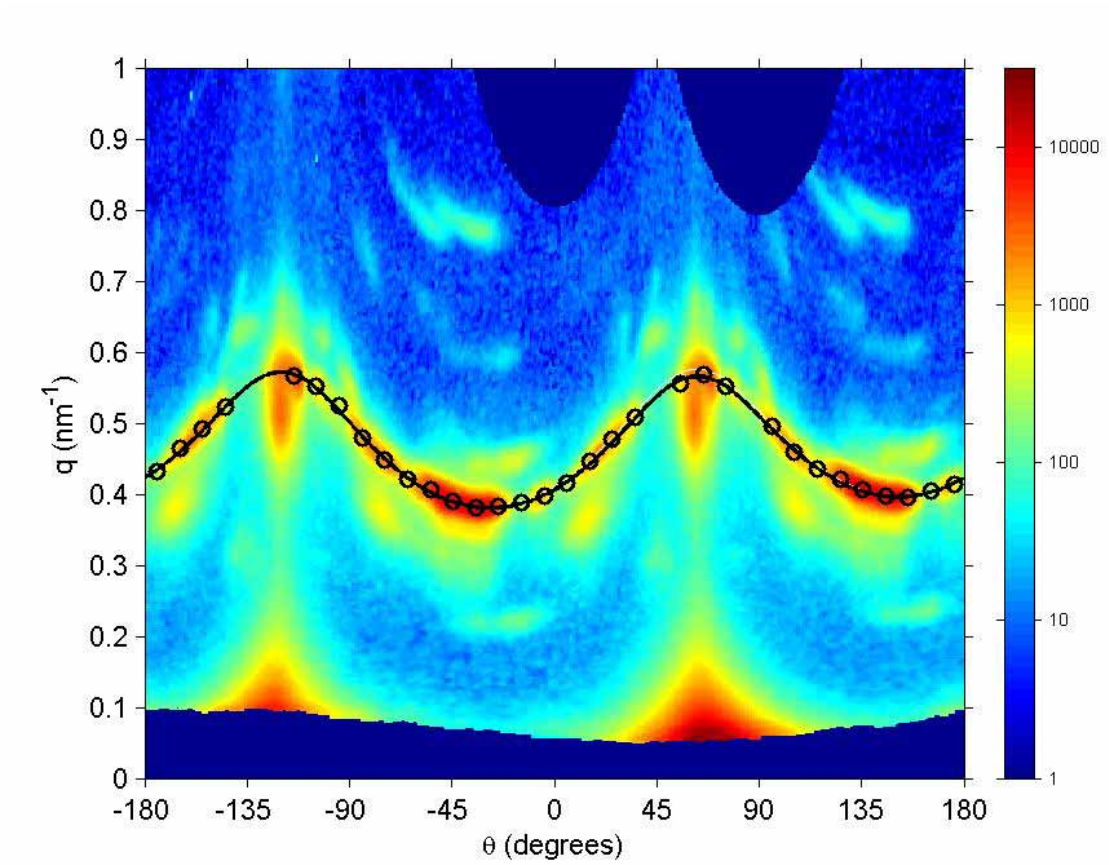

Figure 2.6 – Least Squares Fitting of Diffraction Rings. This image shows the same diffraction data as in Figure 2.5, only in polar (q,θ) coordinates. The black circles mark the peak position of the brightest diffraction ring fitted at10 degree intervals. The black line marks the non-linear least-squares best fit of Equation 2-13 to these radii. The major and minor radii of the ellipse are $q_{maj} = 0.569\ nm^{-1}$ and $q_{min} = 0.389\ nm^{-1}$ respectively, while the angle between the rotation axis (vertical) and the ellipse major axis is $\theta_e = 61.35$ degrees. While the results are similar to those obtained by hand fitting (Figure 2.5), least squares fitting is both more precise and less subjective.

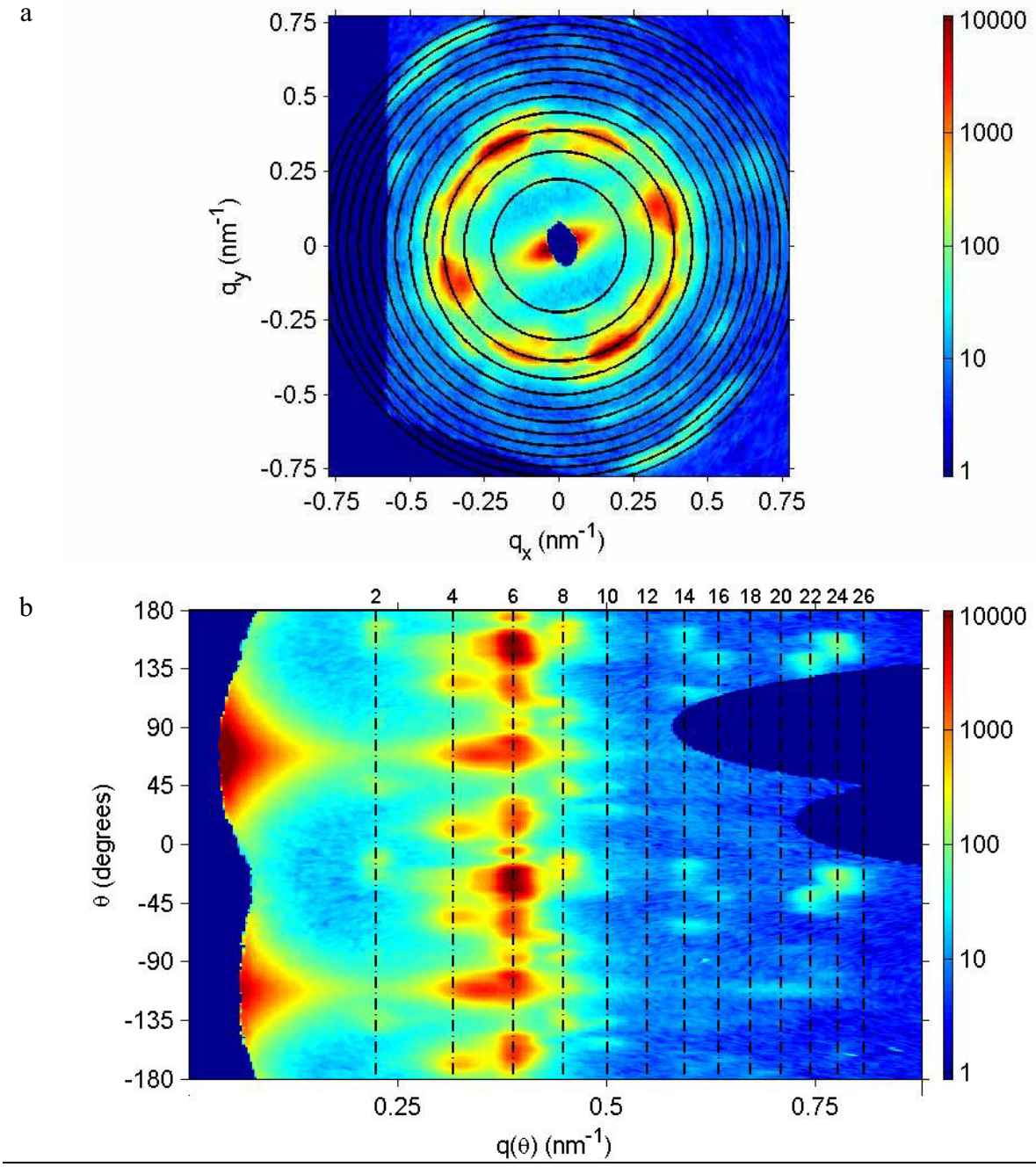

Figure 2.7 –Rectification of Diffraction Images. Using Equation 2-10, the diffraction data shown in Figures 2.5 and 2.6 was transformed into the coordinate system of the uncompressed sample. As expected, the transformed diffraction rings form circles in Cartesian coordinates (a) and straight lines in polar coordinates (b). The black lines indicate peaks for even values of $h^2+k^2+l^2$ of a cubic lattice with unit cell size of 396 Angstroms. Distinct Bragg reflections are visible for $h^2+k^2+l^2$ = 2, 4, 6, 8, 10, 14, 16, 22 and 24.

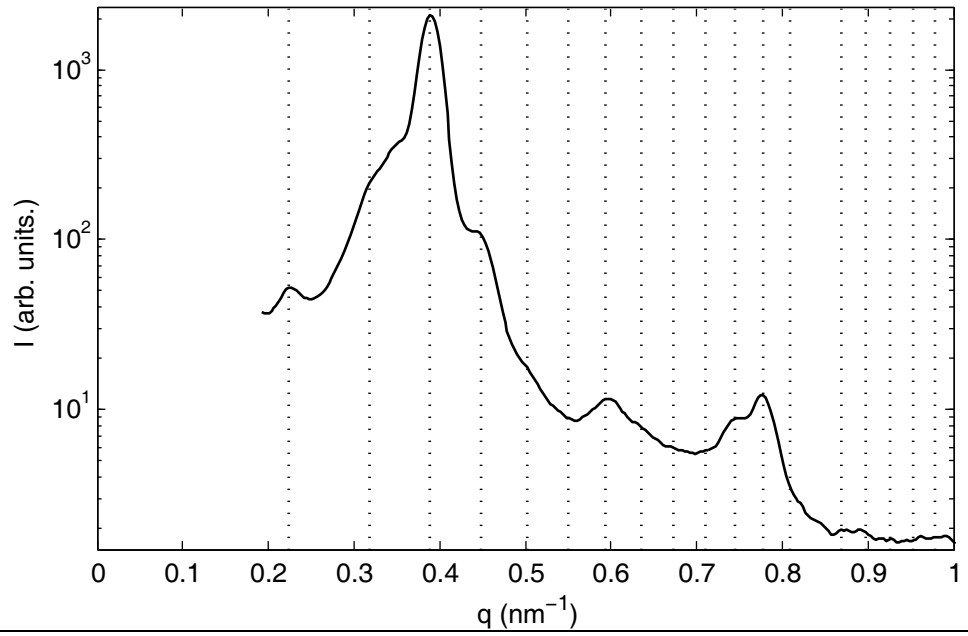

Figure 2.8 –Powder average of diffraction from calcined sample at ϕ = -90° following transformation to uncompressed coordinates. The dotted lines indicate values of $h^2+k^2+l^2$ for a body-centered cubic lattice with unit cell size of 39.6nm.

While analysis of individual diffraction patterns is informative, the compression model can be tested more rigorously by confirming the dependence of the ellipse parameters on sample rotation angle, ϕ, given by Equation 2-9. Ellipse parameters were fitted for a sequence of 23 diffraction images from the calcined sample (of which Figure 2.2 represents a subset). Figure 2.9 illustrates a non-linear least-squares fit of these data to Equation 2-9.

Data from a rotation series also permits an estimate of the powder pattern from the "uncompressed" structure. By definition, the power average is given by,

$$I(q) = \frac{1}{4\pi q^2} \int_{q'_j} \left|F^u\left(q'_j\right)\right|^2 \delta\left(\left|q'_j\right| - q\right) d^3 q'_j \ , \qquad (2\text{-}15)$$

where $I(q)$ is the average scattering factor for radius q. Using Equations 2-4 and 2-5, $F^u(q_j')$ can be replaced with $F^s(q_j')$ to give,

$$I(q) = \frac{1}{4\pi q^2} \int_{q'_j} \left| F^s\left(q'_j\right) \right|^2 \delta\left(\left| M_{jk} q'_k \right| - q \right) \det\left(M_{lm}\right) d^3 q'_j \ . \tag{2-16}$$

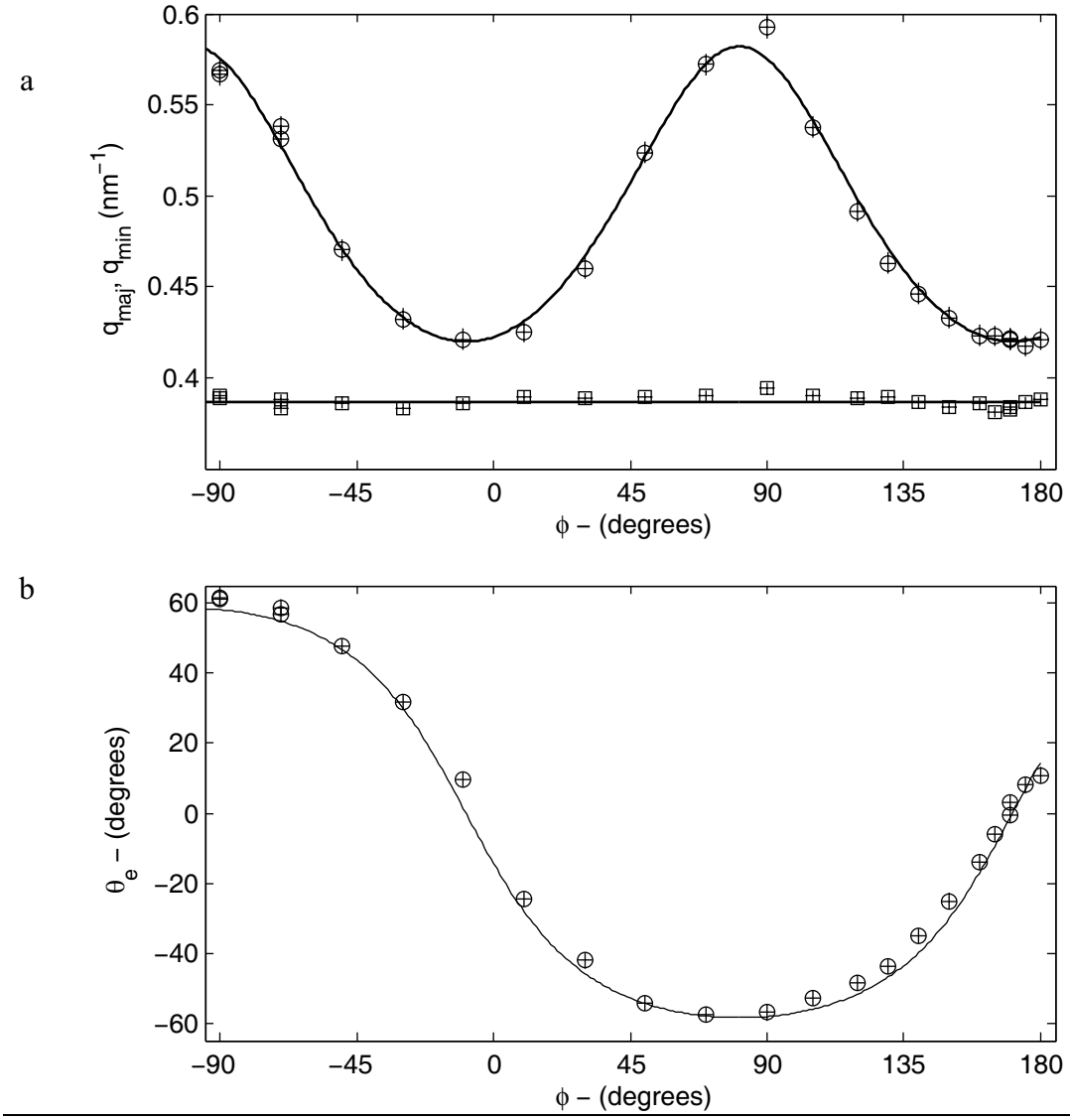

Figure 2.9 – Ellipse parameter dependence on rotation angle. a) Major (q_{maj}, circles) and minor (q_{min}, squares) ellipse radii as a function of rotation angle (ϕ). b) Angle between ellipse major axis and rotation axis (θ_e) as a function of rotation angle. The black lines indicate the fit to Equation 2-9 for a unit cell of 39.2 ± 0.8 nm, cell shrinkage to t = 0.663 ± 0.013 and initial orientation of the surface normal (θ_n=58.4±1.3°, ϕ_n = 9.1 ± 4.1°).

Substitution of M_{jk} from Equation 2-2 and conversion to polar form (Equations 2-7 and 2-8) gives the simple form,

$$I(q) = \int_{\theta,\phi} \left| F^s\left(\frac{q}{g(\theta,\phi)}, \theta, \phi\right)\right|^2 \times \frac{t \times \sin\theta \, d\theta \, d\phi}{4\pi g^3(\theta,\phi)} \quad , \tag{2-17}$$

where $g(\theta,\phi) = \sqrt{1-\varepsilon^2(\phi)\cos^2(\theta-\theta_e(\phi))}$,

and where $|F^s(q,\theta,\phi)|^2$ is directly proportional to the experimentally measured scattering intensity in polar coordinates.

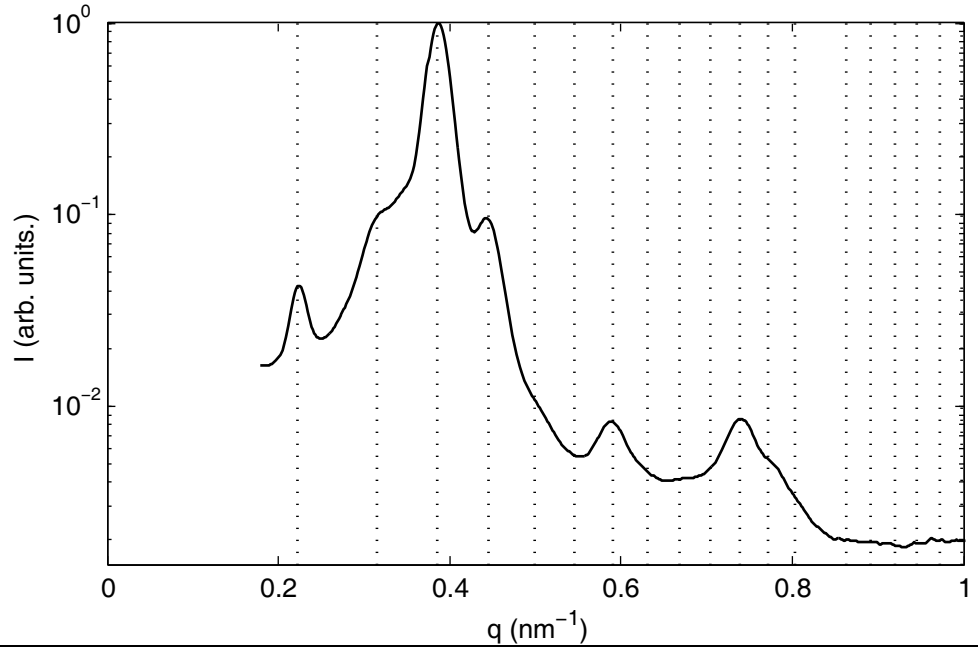

Figure 2.10 –Integrated powder average of diffraction from calcined sample. The dotted lines indicate values of $h^2+k^2+l^2$ for a body-centered cubic lattice with unit cell size of 39.8 ± 1.4 nm.

Applying Equation 2-17 to the rotation series illustrated in Figure 2.2 results in the approximate powder average shown in Figure 2.10. The dashed lines in Figure 2.10 indicate the radii for even values of $h^2+k^2+l^2$ for a cubic lattice with a unit cell of

39.8 ± 1.4 nm. Distinct peaks are evident for values of $h^2+k^2+l^2$ of 2, 6, 8, 14 and 22, while clear shoulders are apparent at 4, 24 and a much less pronounced shoulder appears to be present at 10. Table 2.1 summarizes the peak intensities determined by fitting the calcined sample powder pattern using the Voigt peak profile (David, 1986). Although the fit shows some dependence on the peak profile used, the $h^2+k^2+l^2 = 6$ reflections are at least 5 times more intense than any of the other reflections.

Table 2.1 – Integrated Peak Intensities for Calcined Sample Powder Average shown in Figure 2.10

q (nm^{-1})	**$h^2+k^2+l^2$**	**{hkl}**	**Multiplicity**	**Integrated Intensity**	**$<I_{\{hkl\}}>$**
0.223	2	{110}	12	0.77 ± 0.08	1.5 ± 0.1
0.317	4	{200}	6	7.0 ± 0.3	28 ± 1
0.387	6	{211}	24	100	100
0.447	8	{220}	12	8.6 ± 0.5	17 ± 1
0.499	10	{310}	24	0	0
0.547	12	{222}	8	0	0
0.591	14	{321}	48	1.34 ± 0.2	0.7 ± 0.1
0.631	16	{400}	6	0.45 ± 0.1	1.8 ± 0.4
0.670	18	{330}, {411}	12 + 24	0.51 ± 0.1	0.34 ± 0.06
0.706	20	{420}	24	0.72 ± 0.1	0.7 ± 0.1
0.740	22	{332}	24	2.8 ± 0.4	2.8 ± 0.4
0.773	24	{422}	24	1.3 ± 0.1	1.3 ± 0.1
0.805	26	{431}	48	0.58 ± 0.1	0.29 ± 0.04

Diffraction from the uncalcined sample was measured for a much smaller set of rotation angles. Furthermore, because of the reduced electron density contrast, the 90 second exposures used to gather the scattering images in Figure 2.1 do not show the same wealth of Bragg Reflections. However, the same ellipse fitting procedure can be applied and the results are summarized in Table 2.2. The sample shrinkage ($t \leq 0.71$) for the as-made material is comparable to the calcined material, while the unit cell length is ~57% larger than in the calcined material.

Table 2.2 – Ellipse Parameters for the Diffraction Images of the as-made material shown in Figure 2.1

ϕ	Unit Cell (nm)	q_{maj}/q_{min}	θ_e
0°	63.2	0.98	-7.6°
45°	62.5	0.85	-83.2°
90°	61.9	0.71	-83.6°

Table 2.3 – Integrated Peak Intensities for Uncalcined Sample Powder Average shown in Figure 2.11

q (nm^{-1})	**$h^2+k^2+l^2$**	**(hkl)**	**Multiplicity**	**Integrated Intensity**	**$\langle I_{\{hkl\}} \rangle$**
0.143	2	{110}	12	0.6 ± 0.5	1.4 ± 0.9
0.202	4	{200}	6	24 ± 1	95 ± 5
0.247	6	{211}	24	100	100
0.285	8	{220}	12	5.2 ± 0.3	10.5 ± 0.6
0.319	10	{310}	24	0	0

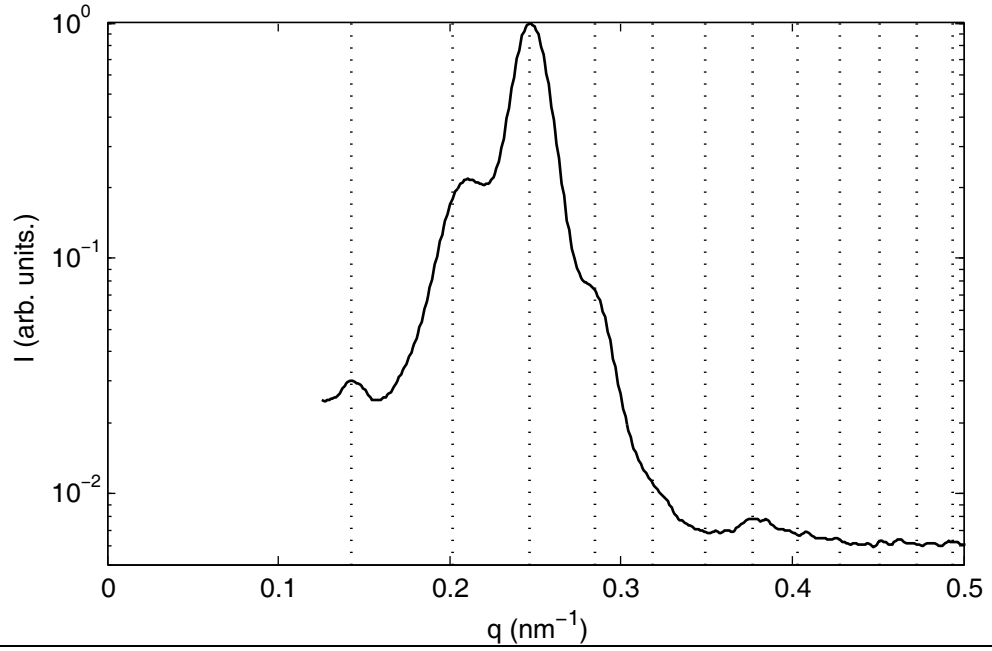

Figure 2.11 – Integrated powder average of diffraction from the un-calcined sample. The dotted lines indicate values of $h^2+k^2+l^2$ for a body-centered cubic lattice with unit cell size of 62.3 ± 2.6 nm.

As shown in Figure 2.11, the short exposure times and small number of images leads to a rather poor powder average. Furthermore, the $h^2+k^2+l^2 = 4$ peak appears to be offset towards larger q. Under these circumstances, estimates of scattering intensities are quite unreliable. However, for the purposes of completeness Table 2.3 summarizes a non-linear least squares fit of the powder scattering curve to Voigt peak profiles.

2.3.1.2 Indexing Individual Images

As shown in Figures 2.12 and 2.13, distinct Bragg reflections are evident in individual diffraction images. The angular position of these spots provided additional information to that obtained via the radial average of traditional powder analysis.

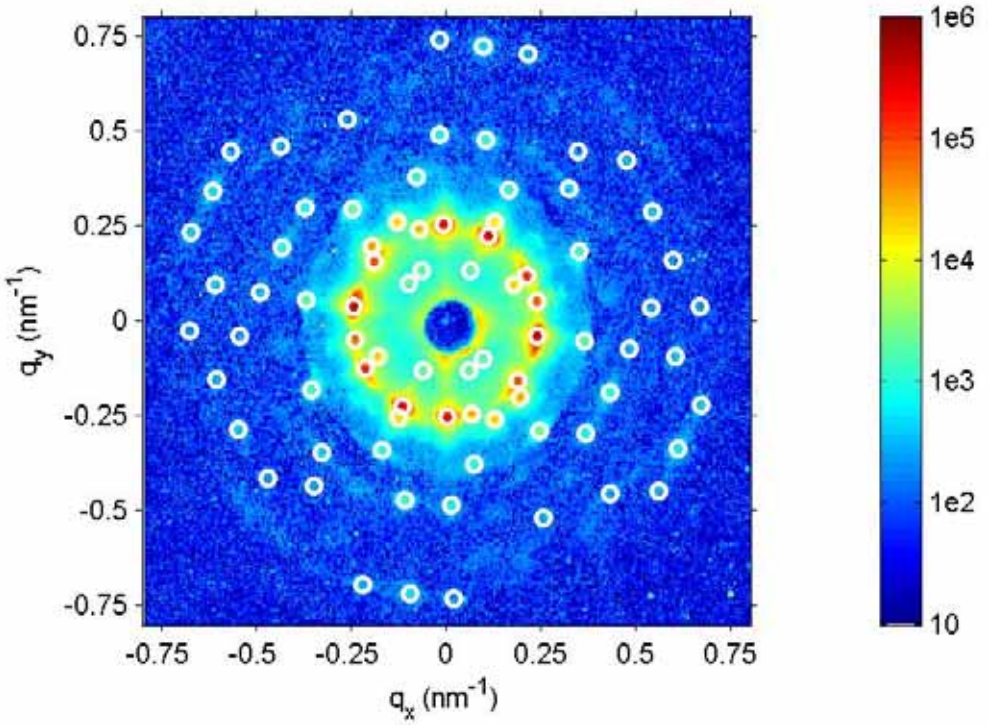

Figure 2.12- Small Angle X-ray Scattering from the uncalcined material. Forty-two individual exposures each of 800 seconds duration were summed to obtain the large dynamic range. The white circles indicate the position of 80 individual Bragg reflections determined by least squares fitting.

The position (radius, $r = r_0$, and angle, $\theta = \theta_0$) of individual diffraction spots was estimated manually. Then, in the vicinity of the diffraction spot ($|r-r_0|<\Delta r$, $|\theta-\theta_0|<\Delta\theta$), the intensity, $I(r,\theta)$ was fitted via non-linear least squares to a polar Gaussian peak sitting on a constant background given by,

$$I(r,\theta) = \frac{I_0}{(2\pi)^{3/2}\times\theta_w^2\times(r_w^2+r_m^2)r_w}\times\exp\left(\frac{-(r-r_0)^2}{2r_w^2}+\frac{-(\theta-\theta_0)^2}{2\theta_w^2}\right)+B\ , \qquad (2\text{-}18)$$

where I_0 is the integrated spot intensity, r_0 and θ_0 are the radial and angular position of the peak center, r_w and θ_w are the radial and angular width of the peak and B is a constant background level.

Values of $h^2+k^2+l^2$ could be assigned unambiguously for $h^2+k^2+l^2 \leq 16$ using the lattice sizes estimated in Section 2.3.1.1. These peaks were then used to refine the position of beam-center, lattice constant and ellipticity via a least-squares fit, and then diffraction spot positions were scaled into lattice units. Figures 2.14 and 2.15 show I_0 as a function $|\boldsymbol{q}|^2$ following this scaling of q_x and q_y. The average intensity of spots is reported in Table 2.4.

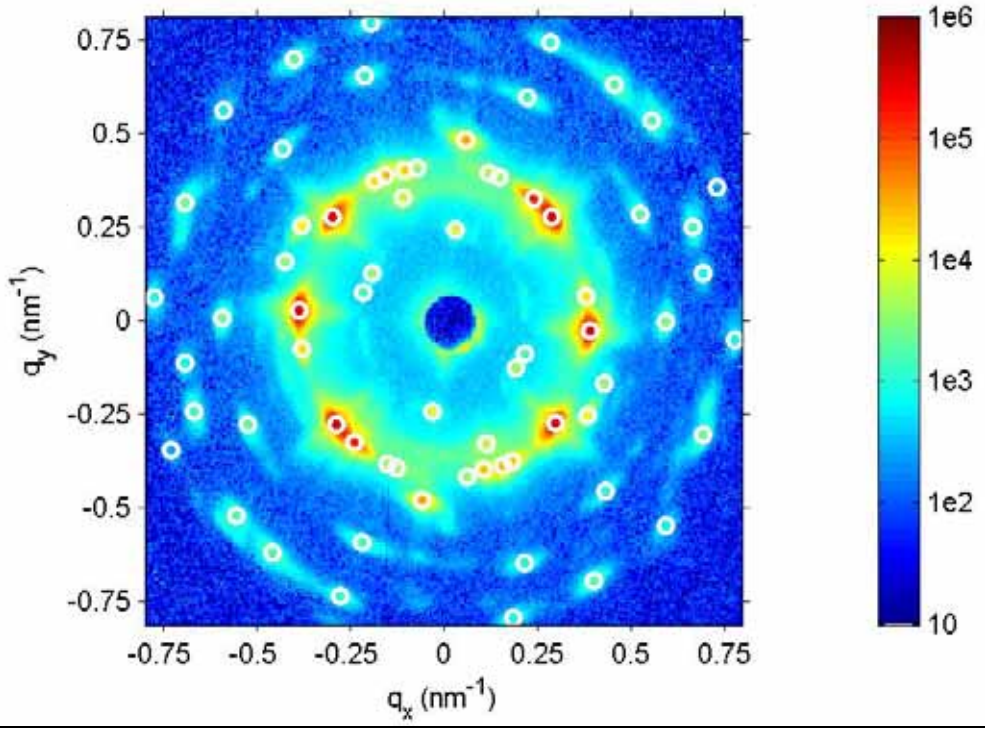

Figure 2.13 - Small Angle X-ray Scattering from the calcined material. Twelve individual exposures each of 90 seconds duration were summed to obtain the large dynamic range. The white circles indicate the position of 68 individual Bragg reflections determined by least squares fitting.

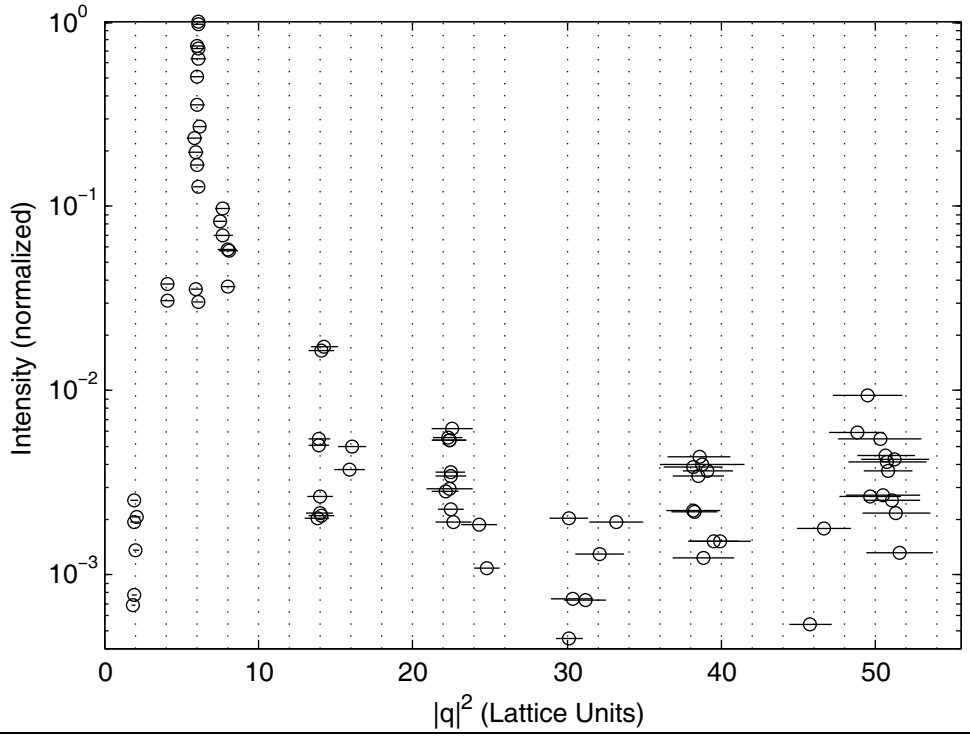

Figure 2.14 – I(q) versus $|q|^2$ for the 80 Bragg Reflections from the uncalcined material fitted in Figure 2.12. The best fit to the unit cell is 63.3nm with shrinkage of 3.9% at 6° from the vertical. The horizontal error bars indicate the peak-width of the Gaussian diffraction spots, while the vertical dotted lines denote the allowed values $h^2+k^2+l^2$. Intensities have been scaled relative to the intensity of the strongest Bragg Reflection.

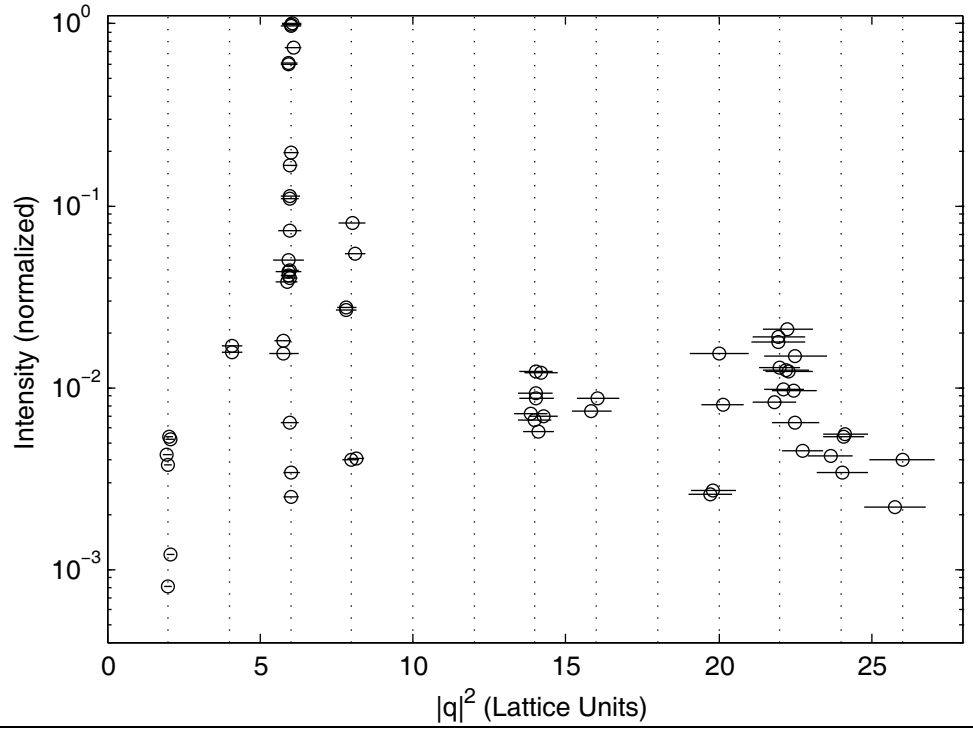

Figure2.15 - I(q) versus $|q|^2$ for the 80 Bragg Reflections from the calcined material fitted in Figure 2.13. The best fit to the unit cell is 39.8nm with shrinkage of 8.2% at 16° from the vertical. The horizontal error bars indicate the peak-width of the Gaussian diffraction spots, while the vertical dotted lines denote the allowed values $h^2+k^2+l^2$. Intensities have been scaled relative to the intensity of the strongest Bragg Reflection.

Table 2.4 - Experimental Structure Factors $|F_{hkl}|^2$

$h^2+k^2+l^2$	{h k l}	As-Made		Calcined	
		[a]Spots	[b]Powder	[a]Spots	[b]Powder
2	1 1 0	0.4 (6)	0.3 ± 0.1	1.3 (6)	1.5 ± 0.1
4	2 0 0	8.0 (2)	56 ± 2	6.1 (2)	28 ± 1
6	2 1 1	100 (14)	100	100 (22)	100
8	2 2 0	16 (6)	8.1 ± 0.7	12 (6)	17 ± 1
10	3 1 0	-	0	-	0
12	2 2 2	-	-	-	0
14	3 2 1	1.6 (8)	-	3.2 (8)	0.7 ± 0.1
16	4 0 0	1.0 (2)	-	3.0 (2)	1.8 ± 0.4
18	3 3 0/4 1 1	-	-	-	0.34 ± 0.06
20	4 2 0	-	-	2.7 (4)	0.7 ± 0.1
22	3 3 2	0.9 (10)	-	4.7 (12)	2.8 ± 0.4
24	4 2 2	0.3 (2)	-	1.7 (4)	1.3 ± 0.1
26	4 3 1	-	-	1.2 (2)	0.29 ± 0.04

[a]Average Bragg Spot intensity normalized to {211} reflections. The number of spots each {hkl} is given in parentheses.
[b]Fit to "pseudo-powder" average of scattering intensity made by summing scattering from a rotation series. The quoted errors are for the non-linear least squares fit and do not include systematic effects.

Although many of the reflections in Figure 2.12 lie along distinct lines (lunes), the diffraction spots clearly result from multiple crystallites. While a unique indexing is not possible, assigning diffraction spots to a set of possible crystal domains can strengthen the lattice assignment. For a given crystallite with reciprocal lattice vectors, $\boldsymbol{b_1}$, $\boldsymbol{b_2}$ and $\boldsymbol{b_3}$, the reciprocal lattice positions are given by,

$$\boldsymbol{q}_{hkl} = h\boldsymbol{b}_1 + k\boldsymbol{b}_2 + l\boldsymbol{b}_3 \,, \tag{2-19}$$

where (*h,k,l*) are the lattice indices. For a crystallite with angular mosaic spread of γ, the Bragg condition is approximately satisfied when,

$$\gamma > \frac{\left|\boldsymbol{q}_{hkl} \bullet \hat{\boldsymbol{z}}\right|}{\left|\boldsymbol{q}_{hkl}\right|} \,, \tag{2-20}$$

where the surface of the Ewald sphere has been approximated by the x-y plane (small-angle limit). The set of allowed reflections for a crystallite is simply the subset of (hkl) that satisfy lattice symmetry constraints and Equation 2-20.

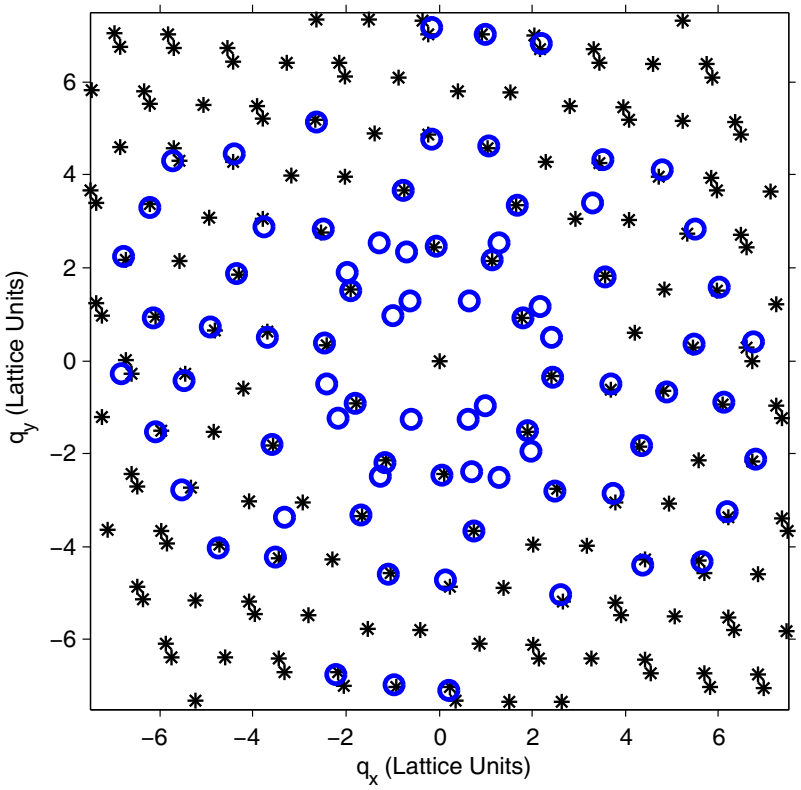

Figure 2.16 – Hand-alignment of crystallites to diffraction peaks. The blue circles indicate the diffraction peaks in Figure 2.12, while the black asterisks mark the allowed reflections for a bcc lattice with a zone-direction of [320] and a mosaic spread of 8°.

Figure 2.16 illustrates the allowed reflections for a crystallite with zone direction of approximately [320] and a large mosaic spread of 8° corresponding to roughly 3 standard deviations (average angular peak width of $\theta_w \approx 2.7°$). The allowed reflections of a crystallite may be aligned with observed diffraction spots by rotation. A convenient matrix form for the crystallite orientation and subsequent rotation is,

$$B_{jk}^{new} = \exp\left(\varphi \varepsilon_{jml} \alpha_l\right) B_{mk} \quad , \tag{2-21}$$

where α_j is the rotation axis, φ the rotation angle, ε_{jml} the anti-symmetric tensor and $B_{jk} = [\boldsymbol{b_1}, \boldsymbol{b_2}, \boldsymbol{b_3}]$ is a matrix of all three reciprocal lattice vectors. To quantify the fit, the distance of a diffraction spot ($\boldsymbol{q}_{obs}$) from a reciprocal lattice site was defined in a weighted, least-squares sense as,

$$d^2\left(\boldsymbol{q}_{obs}, \boldsymbol{q}_{hkl}\right) = \left(\frac{\left|\boldsymbol{q}_0\right| - \left|\boldsymbol{q}_{hkl}\right|}{\delta q}\right)^2 + \left(\frac{\arccos\left(\dfrac{\boldsymbol{q}_0 \bullet \boldsymbol{q}_{hkl}}{\left|\boldsymbol{q}_0\right| \times \left|\boldsymbol{q}_{hkl}\right|}\right)}{\delta\theta}\right)^2 , \tag{2-22}$$

where δq is the radial width ($\delta q \sim 0.05$ inverse lattice units) and $\delta\theta$ is the angular width ($\delta\theta \sim 3°$) of the average diffraction spot. Initial crystallite orientations were selected using a divide and conquer algorithm. A first crystallite was oriented so as to match the maximum number of diffraction spots and spots were assigned to it on the basis of a distance cut-off. Using the remaining diffraction spots, the process was repeated to orient the next crystallite. When all diffraction spots had been assigned, the orientations of individual crystallites were iteratively adjusted to achieve the best possible fit. The results of this procedure are shown in Figures 2.17 and 2.18.

These assignments are far from unique. In Figure 2.17, the reflections lying on crystallographic "lunes" were indexed to a single, main crystallite (red - [320]). Three other crystallites were then sufficient to account for the remaining reflections. However, some reflections assigned to the main (red) crystallite could also be indexed

to these other crystallites. For example, using a different divide-and-conquer algorithm (Finnefrock, et. al. 2003) Adam Finnefrock indexed the un-calcined material diffraction peaks to 5 crystallites, as shown in Figure 2.19. However this ambiguity does not affect the main conclusion that a small number of cubic crystallites can account for the observed reflections.

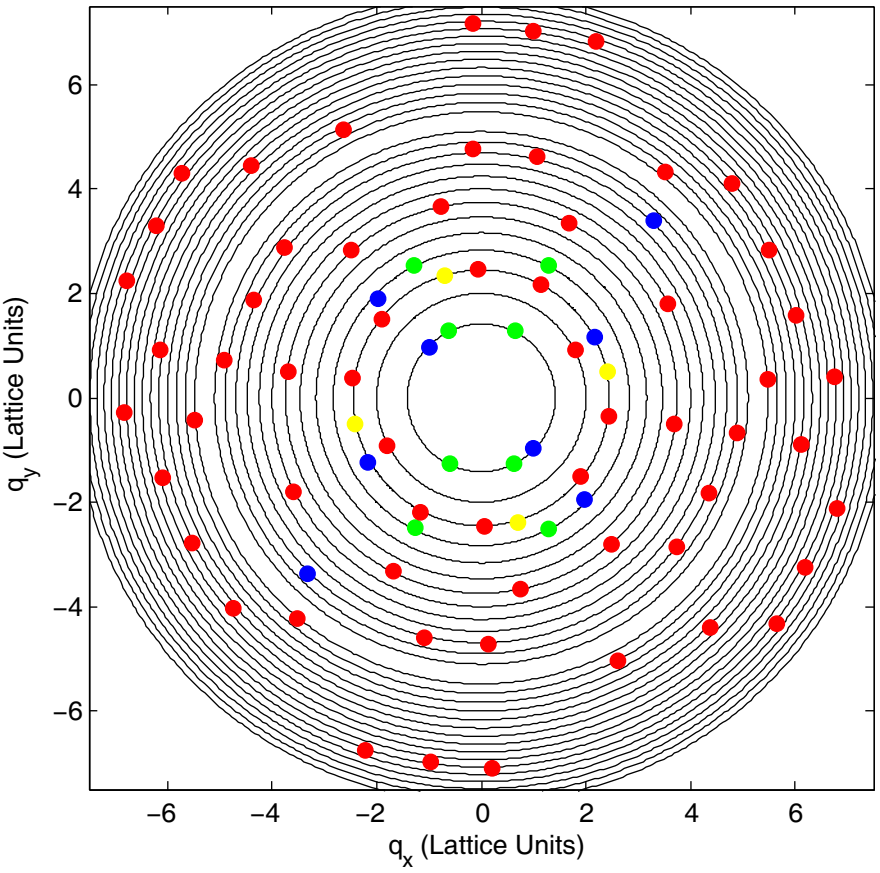

Figure 2.17 – Indexing of Diffraction Spots from Uncalcined sample SAXS data shown in Figure 2.12. The peaks can be assigned to four crystallites with zone directions red-[320], blue-[311], green-[111] and yellow-[531].

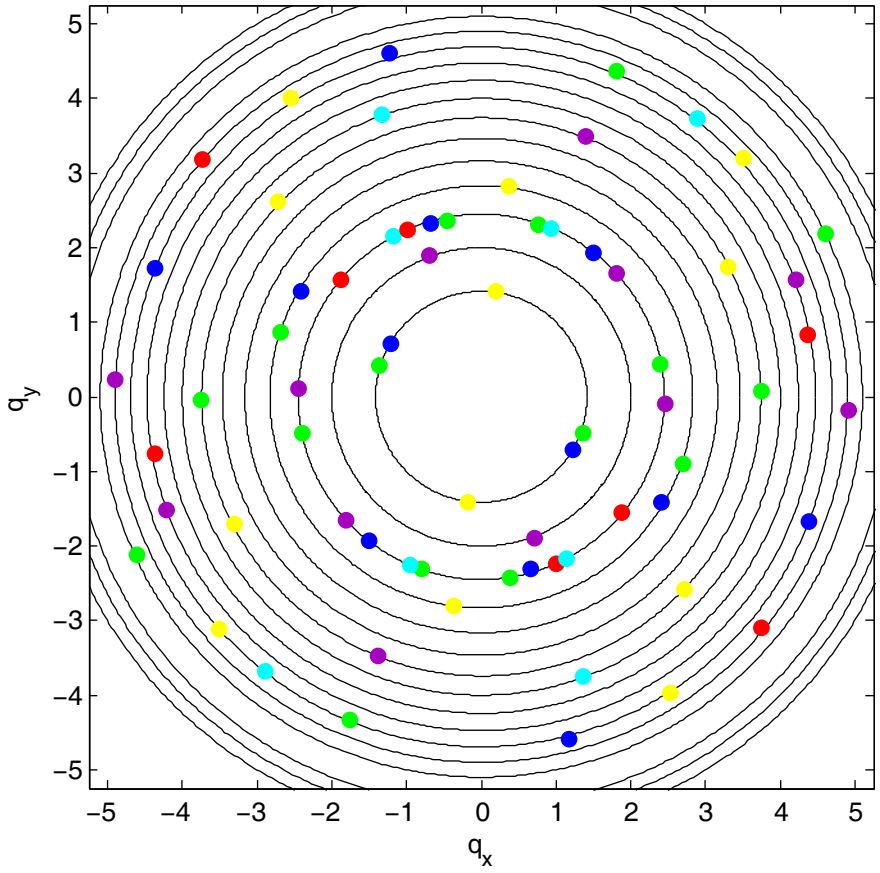

Figure 2.18 -Indexing of Diffraction Spots from calcined material SAXS shown in Figure 2.13. The peaks have been assigned to six crystallites with zone directions red-[421], blue-[433], green-[111], magenta-[210], yellow-[331] and cyan-[210].

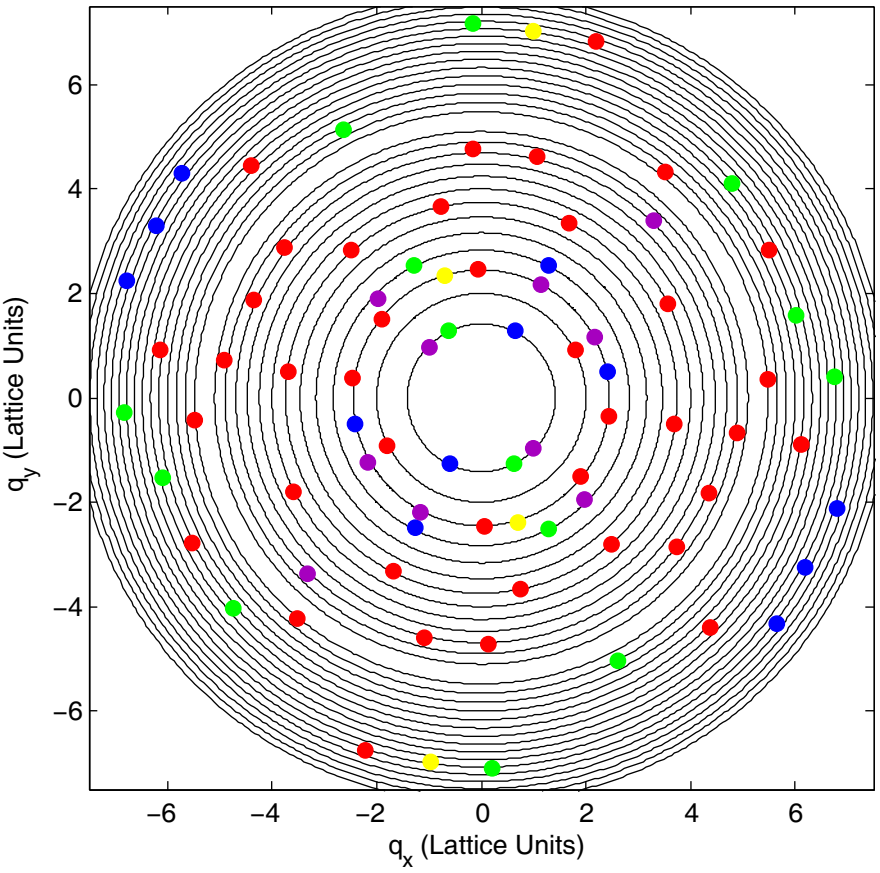

Figure 2.19 – Alternative indexing of Diffraction Spots from uncalcined material SAXS data shown in Figure 2.12. The peaks have been assigned to five crystallites with zone directions red-[320], blue-[331], green-[110], magenta-[311] and yellow-[751].

2.3.2 Modeling Structure Factors

There is a strong association between the bicontinuous network morphologies formed in soft-condensed matter systems and infinite periodic minimal surfaces (Luzzatti and Spegt, 1967; Scriven, L.E. 1976; Longley and McIntosh, 1983; Thomas, et. al. 1988; Hyde, 1996). Figure 2.20 illustrates networks related to Schoen's gyroid surface (Schoen, 1970) and Schwarz's D and P surfaces ((Schwarz, 1890).

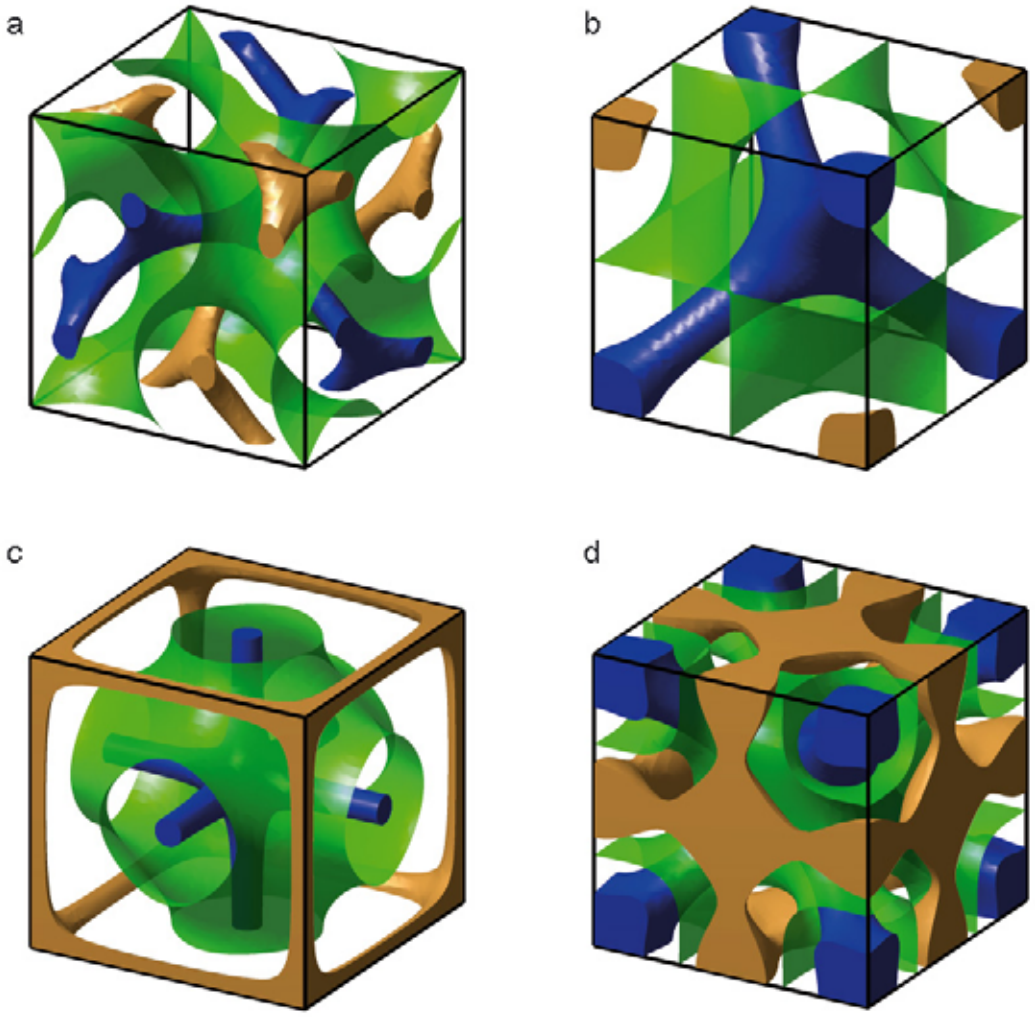

Figure 2.20 - The unit cell of cubic network structures based on Schoen's G (a, Space Group Q^{230}, Ia$\underline{3}$d, p706, IUCr), Schwartz's D (b, Space Group Q^{224}, Pn$\underline{3}$m, p683,IUCr),Schwartz's P (c, Space Group Q^{229}, Im$\underline{3}$m, p702 IUCr) and Schoen's I-WP (d, Space group Q^{229}, Im$\underline{3}$m) Infinite Periodic Minimal Surfaces. The green IPMS divides space between the gold and blue skeletal frames, each of which forms a continuous network in all three spatial directions.

These three morphologies have all been observed in soft-matter and can even occur in a single system (Maddaford and Trokcioglu, 1993). The G, D and P structures represent merely three out of a multitude of IPMS (eg. Wohlgemuth et. al., 2001). Non-cubic, bicontinuous network structures were recently observed in block

copolymers (Bailey et. al., 2002; Cochran and Bates, 2004; Takenaka et. al, cond-mat/0605268), and there some reports of other cubic networks such as Schoen's I-WP structure (Radiman et. al. 1990; Luzatti et. al., 1996) or Neovius's C(P) structure (Karcher and Polthier, 1996; Strom and Anderson, 1992) in surfactant systems. However, in studies to date the G, D and P networks appear to be most prevalent.

Comparison between sample diffraction and the structure factors of models is helpful for elucidating network morphology and Table 2.5 reports the structure factor magnitudes for models of the G, D, P and I-WP structures developed by Garstecki and Holyst (Garstecki and Holyst, 2000, 2001, 2002a, 2002b, 2003a, 2003b).

None of these models match the measured structure factors (Tables 2.1 and 2.3 and Figures 2.14 and 2.15). The double diamond structure (Schwarz's D surface, Figure 2.20b) is a poor candidate because the lattice is not body-centered and requires the presence of reflections with odd values of h+k+l, such as the intense {111} reflections. In contrast, the G, P and I-WP structures have BCC lattices. However, the P structure considered in earlier publications (Finnefrock et. al. 2001; Finnefrock et. al. 2003) requires the {110} and {200} reflections to be considerably stronger than the {211} reflections. The I-WP structure is also a poor match because the {211} reflections should be markedly weaker than the {110} and {200} reflections no matter whether the minority phase is located on the 4-fold network, the 8-fold network or both networks (Garstecki and Holyst, 2003b). Finally, while most of the observed reflections match well with the gyroid, the observed {110} and {200} reflections are forbidden in the gyroid structure because of the glide planes and screw axes of the Q^{230} space-group (p706, IUCR).

Table 2.5 : Structure Factors $|F_{\{hkl\}}|^2$ for Model Network Structures

$h^2+k^2+l^2$	[a,b]D	[a]P	[a]I-WP	[a]G	[c,d]G_{el}	[e,d]G_{CC}	[f,d]G_{CT}	[g]Expt
2	**100**	**100**	**42**	-	0.43	**28**	**23**	1.5 ± 0.1
3	**71**	-	-	-	-	-	-	0
4	6.5	**89**	**100**	-	1.0	**95**	**96**	**28 ± 1**
6	1.3	**22**	1.4	**100**	**100**	**100**	**100**	**100**
8	0	0	5.3	**38**	**41**	**26**	**77**	**17 ± 1**
9	0.31	-	-	-	-	-	-	0
10	0.47	0.05	8.6	-	0.08	1.2	7.6	0
12	3.0	0.06	2.5	-	0	0.1	0.9	0
14	0.48	1.4	0.18	0.21	0.21	0.9	3.2	0.7 ± 0.1
16	0	1.1	0.62	0.95	0.92	5.0	2.4	1.8 ± 0.4
17	2.1	-	-	-	-	-	-	0
18	0.57	1.95	0.45	-	0.08	2.0	1.5	0.34±0.06
19	1.8	-	-	-	-	-	-	0
20	0	0	1.3	0.06	0.24	2.4	0.7	0.7 ± 0.1
22	1.6	4.0	0.26	0.07	1.1	3.9	0.8	2.8 ± 0.4
24	0	3.35	0.03	0.23	0.63	1.8	0.5	1.3 ± 0.1
26	0	0	0.66	0.18	0.32	1.6	0.3	0.29±0.04

[a] $|F_{\{hkl\}}|^2$ for the double diamond (D), plumber's nightmare (P), I-WP and double gyroid (G) models calculated using the parametric functions of Garstecki and Holyst (2003a). For the D, P and G structures the volume of both networks was 18%. For the I-WP structure the volume of the four-fold network was 36%.
[b] Intensities of the {311} and {421} reflections of the D structure were below 0.1%.
[c] Elastic model of the G structure (G_{el}) following 30% uniaxial contraction.
[d] $\langle|F_{\{hkl\}}|^2\rangle$ averaged over the [100], [110], [111] and [16,9,4] directions.
[e] Constant Curvature model of G structure (G_{CC}) under 30% uniaxial compression.
[f] Constant Thickness model of G structure (G_{CT}) under 30% uniaxial compression.
[g] Experimental values for pseudo-powder average of calcined material.

Unlike the structural models in Figure 2.20, the crystallites in the material are not strictly cubic. Each triclinic crystallite is related to a cubic lattice by a uniaxial expansion, but the compressed unit cell cannot have all of the crystallographic symmetries allowed in a cubic unit cell (Sakurai et. al., 2001; Urade et. al., 2007). If the uniaxial compression is an affine transformation, the original symmetry constraints on (hkl) are preserved in the triclinic lattice, even though the triclinic lattice lacks these symmetries. In general, though, reflections in the compressed lattice are not subject to the same symmetry constraints and the preservation of lattice pseudo-symmetries depends on both the character and magnitude of the transformation. For example, Sakurai and colleagues (Sakurai et. al., 2001) reported the appearance of {110} and {200} reflections when a styrene-butadiene-styrene block copolymer in the gyroid phase was plastically deformed under tension. In contrast, for the thin films of surfactant-templated bicontinuous aluminosilicate described by Hayward and colleagues (Hayward et. al., 2004), only the {211} and {220} reflections of the Q^{230} lattice were observed despite a uniaxial compression of ~15% during solvent casting. %. In a more recent study (Urade et. al., 2007) of a double gyroid mesoporous silica film, the as-made structure did not show the forbidden {110} or {200} reflections (~7% contraction). However, calcination caused the film to contract by ~40% and weak {110} reflections were then observed.

To see if a distorted double gyroid structure is consistent with the observed structure factors, the structural deformations caused by lattice contraction were calculated for several models. The rheological properties of the block copolymer/aluminosilicate material varied during the solvent casting process (Jain and Wiesner, 2004). Initially, when the solvent content was high, the material should have been able to flow in response to applied stress. As the solvent content dropped, the PI and PEO-aluminosilicate phases separated to form 3-dimensional, interpenetrating

networks. Even though the individual polymer blocks and aluminosilicate particles could still move within their respective domains, in this liquid crystalline state the domain topology could not readily change and the bulk material should have exhibited a solid-like response to applied stress (Kossuth et. al., 1999). In the final stages of solvent evaporation, the growing, 3-dimensional network of covalent bonds within the PEO-aluminosilicate domains should have immobilized both the PEO and PI polymer blocks. If the uniaxial compression occurred after extensive cross-linking of the aluminosilicate-sol, the deformation should correspond to the response of an inhomogeneous, elastic solid, as described in Section 2.3.2.1. In contrast, if the distortion occurred while the individual polymer blocks could move within their respective domains, the response of the material can be better described using liquid crystal models (Section 2.3.2.2).

2.3.2.1 Elastic Model of Sample Distortion

This section describes the response of a material with spatially varying elastic properties to a macroscopic strain field. The material is assumed to have a periodic structure so following deformation, a point x_j, is mapped to a new position $X_j(x_k)$, given by,

$$X_j(x) = M_{jk} x_k + \sum_m A_j^m \exp\left(i q_k^m x_k\right) , \tag{2-23}$$

where M_{jk} is the transformation matrix and A_j^m is the Fourier amplitude corresponding to reciprocal lattice vector q_j^m. The strain field, $e_{jk}(x_l)$, at point $X_j(x_k)$ is defined as (Volume2, p39-3, Feynman, et. al., 1977),

$$e_{jk}(x_l) = \frac{1}{2}\left(\frac{\partial X_j}{\partial x_k} + \frac{\partial X_k}{\partial x_j}\right) - \delta_{jk} = \sum_m e_{jk}^m \exp\left(i q_l^m x_l\right) \quad , \tag{2-24}$$

where $$e_{jk}^m = \frac{i}{2}\left(A_j^m q_k^m + A_k^m q_j^m\right) + \delta\left(q_l^m\right) \times \left(\frac{M_{jk} + M_{kj}}{2} - \delta_{jk}\right) \quad .$$

If the elastic response at a given point is isotropic, the stress field, $S_{jk}(x_l)$, is

$$S_{jk}(x_l) = 2\mu(x_l)e_{jk}(x_n) + \lambda(x_l)e_{mm}(x_n)\delta_{jk} \ , \tag{2-25}$$

where $\mu(x_l)$ and $\lambda(x_l)$ are the first and second Lame elastic coefficients at point x_l (Volume2, p39-6, Feynman, et. al., 1977). Again, the elastic coefficients are most simply described by a Fourier expansion,

$$\mu(x_l) = \sum_m \mu^m \exp\left(iq_l^m x_l\right), \tag{2-26}$$

$$\lambda(x_l) = \sum_m \lambda^m \exp\left(iq_l^m x_l\right),$$

because the coefficients μ^m and λ^m are easily related to material structure factors. Substituting Equations 2-25 and 2-26 into Equation 2-27, the stress tensor is then,

$$S_{jk}(x_l) = \sum_m S_{jk}^m \exp\left(-iq_l^m x_l\right), \tag{2-27}$$

$$\text{where} \quad S_{jk}^m = \sum_{n,p}\left(2\mu^n e_{jk}^p + \lambda^n e_{ll}^p \delta_{jk}\right)\delta\left(q_r^m + q_r^n + q_r^p\right).$$

The average elastic energy density per unit volume, U_e, is then just,

$$U_e = \int_{V_{cell}} \frac{1}{2} S_{jk}(x_l) e_{jk}(x_m) \frac{d^3x}{V_{cell}}, \tag{2-28}$$

$$= \frac{1}{2}\sum_m S_{jk}^m e_{jk}^m \ ,$$

where V_{cell} is the unit cell volume. For a given macroscopic transformation, M_{jk}, and elastic properties defined by a finite set of reciprocal lattice vectors q_j^m and Lame coefficients μ^m and λ^m, the distortion amplitudes, A_j^m, can be rapidly determined numerically via conjugate-gradients minimization of Equation 2-28 (Press et. al., 1986) using the derivative form,

$$\frac{\partial U_e}{\partial A_j^m} = iS_{jk}^m q_k^m \ . \tag{2-29}$$

Finally, the structure factors following the non-affine transformation can be determined using the new electron density, $\rho^c(X_j(x_k))$ given by,

$$\rho^c\left(X_j\left(x_k\right)\right)d^3X = \rho^u\left(x_k\right)d^3x \ , \tag{2-30}$$

Equation 2-5 describes the transformation of the reciprocal lattice, while the new Fourier amplitude $F^c(q_j^m M^1_{jk})$ corresponding to the lattice vector $q_j^m M^1_{jk}$ is given by,

$$\begin{aligned} F^c\left(q_j^m M_{jk}^{-1}\right) &= \int_{V_{cell}} \rho^u\left(x_l\right)\exp\left(-iq_j^m M_{jk}^{-1} X_k\left(x_n\right)\right)\frac{d^3x}{\det\left(M\right)V_{cell}} \ , \\ &= \int_{V_{cell}} \sum_n F^u\left(q_j^n\right)\exp\left(i\left(q_j^n - q_j^m\right)x_j - iq_j^m M_{jk}^{-1}\sum_p A_k^p \exp\left(iq_l^p x_l\right)\right)\frac{d^3x}{\det\left(M\right)V_{cell}}, \\ &\approx \frac{F^u\left(q_j^m\right) - iq_j^m M_{jk}^{-1}\sum_{n,p} A_k^p F^u\left(q_j^n\right)\delta\left(q_l^n + q_l^p - q_l^m\right)}{\det\left(M\right)} \ , \end{aligned} \tag{2-31}$$

where $F^u(q_j^m)$ are the Fourier amplitudes of the original structure.

Figure 2.21 illustrates the change in structure factors predicted by Equation 2-31 for a network with the gyroid symmetry following elastic compression. The uncompressed gyroid structure was assumed to be a constant-thickness membrane (volume = 64%) separating two networks (Harper, 1996). The reciprocal space representation of the structure was restricted to wave-vectors with $h^2+k^2+l^2 \leq 64$. The elastic properties of the PEO-aluminosilicate sol and poly(isoprene) phases are unknown so to estimate an upper bound for elastic effects, the stiffness of the membrane was taken to be 10 times that of the networks. The value of Poisson's ratio does not dramatically alter the results so only calculations for $\sigma = 0$ are presented in Figure 2.21. The uniaxial compression was taken to be 70% of the original volume, and the effects of compression were examined for several directions.

Although the structure factors of a gyroid under elastic compression are qualitatively similar to the experimental results, the magnitude of the {110} and {200} reflections are about an order of magnitude lower.

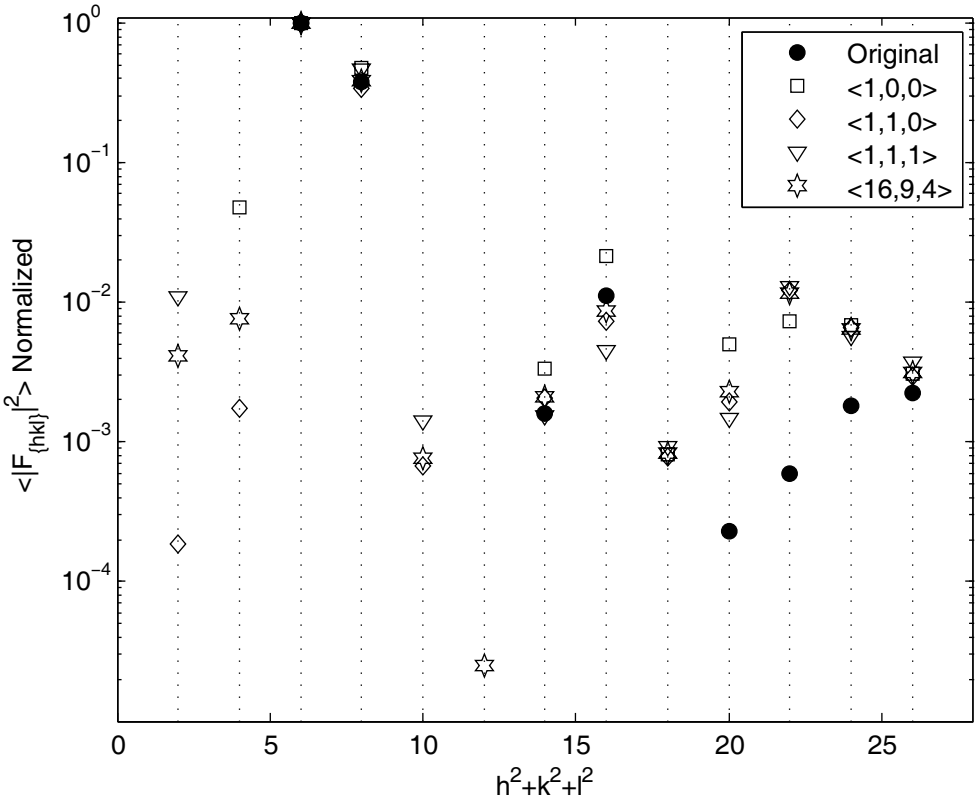

Figure 2.21 – Structure factors for a double-gyroid network compressed uniaxially to 70% of its original volume. The gyroid structure was modeled as a constant-thickness membrane separating two networks each of 18% volume. The membrane was taken to be 10 times stiffer than the networks and Poisson's ratio for both phases was 0. The structure factors following an elastic, uniaxial compression to 70% of the original volume are shown for compression along several different directions. Structure Factors have been normalized relative to the $<|F_{\{211\}}|^2>$.

2.3.2.2 Liquid Crystal Models of Sample Distortion

During hybrid formation, covalent cross-links between aluminosilicate clusters in the PEO phase transform the material from a fluid to a solid (Jain and Wiesner, 2004). However, even before covalent cross-links immobilize the individual polymer blocks, the double gyroid structure can exhibit a solid-like response to applied stress because the major and minor domains form interpenetrating 3-dimensional networks (Kossuth et. al., 1999). In this liquid crystal state, the shape (but not topology) of domains can be easily changed because the individual aluminosilicate clusters and polymer blocks can move within their respective domains. Thus, strain imposed at intermediate stages of the solvent casting process should cause larger structural changes than suggested by the elastic model in Section 2.3.2.1. The optimal domain shapes for a liquid crystal with a given unit cell and domain topology can be used to estimate the distortion of domains. As the energetic interactions of such a hybrid/copolymer system have not been quantified, simpler energetic models were employed.

One approach for describing a network structure is a membrane of uniform thickness centered on a surface of minimal area (IPMS) (Anderson et. al. 1988; Harper and Gruner, 2000), where the thickness of the membrane determines its volume fraction. These "constant-thickness" models are a good approximation for water-rich, surfactant bilayer network structures and have also been applied to the structure of block copolymers (Harper, 1996, Garstecki and Holyst 2003a,b). Figure 2.22 illustrates the effect of uniaxial compression on such a constant-thickness model of a gyroid network. For each structure, the mid-plane of the membrane was described with a discrete surface (1536 facets per unit cell) and the shape of this surface optimized numerically to achieve zero mean curvature across it (Brakke, K.A. 1992, 1996 and 2005). The thickness of the membrane was then adjusted to give a volume

fraction of 64% and the position of the inner and outer membrane surfaces computed. Finally, structure factors were evaluated by applying Abbe's transformation to the discrete representation of the inner and outer membrane surfaces (Harper, 1996).

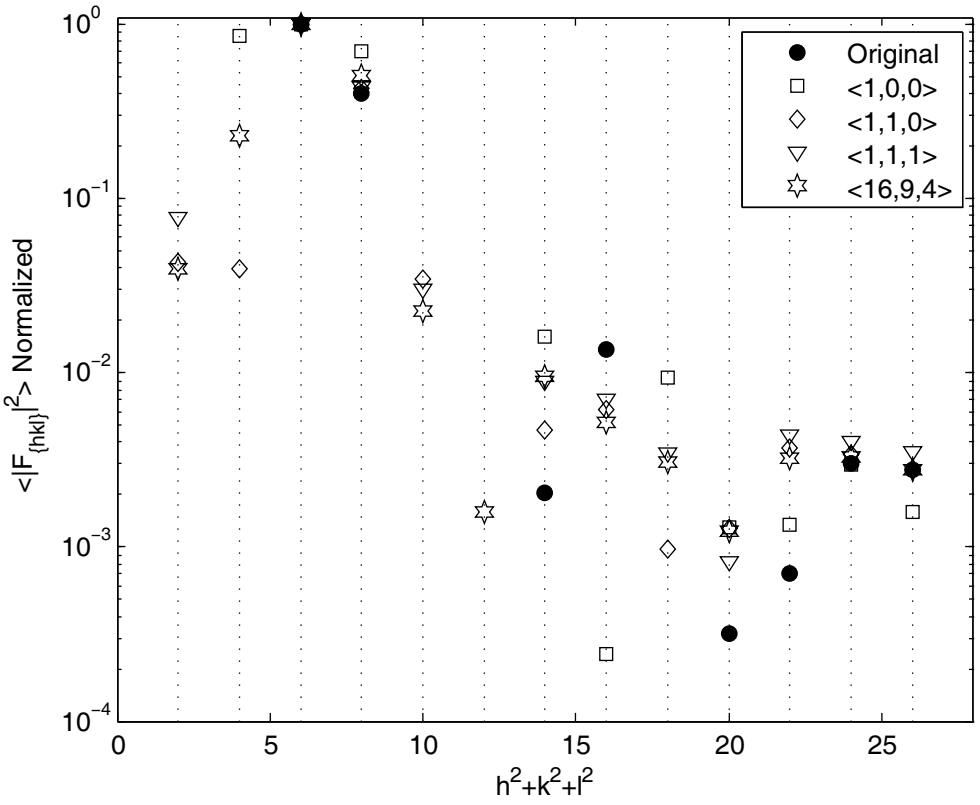

Figure 2.22 – Structure factors for a "constant thickness" IPMS model of a network the gyroid topology after uniaxial compression to 85% of its original volume. As the unit cell is compressed, the IPMS shape changes leading to different structure factors. The results for 15% uniaxial compression along several different directions are presented for a gyroid structure with a membrane volume fraction of 64%.

As expected, an imposed strain can cause larger structural re-arrangements when material can move within the continuous PI and PEO-aluminosilicate domains. Indeed, the magnitude of the {1,1,0} and {2,0,0} reflections already matches or exceeds the observed structure factors for a modest 15% compression. Interestingly,

under even larger distortions of the lattice the G surface can be continuously transformed into either the D or P (Fogden and Hyde, 1999)

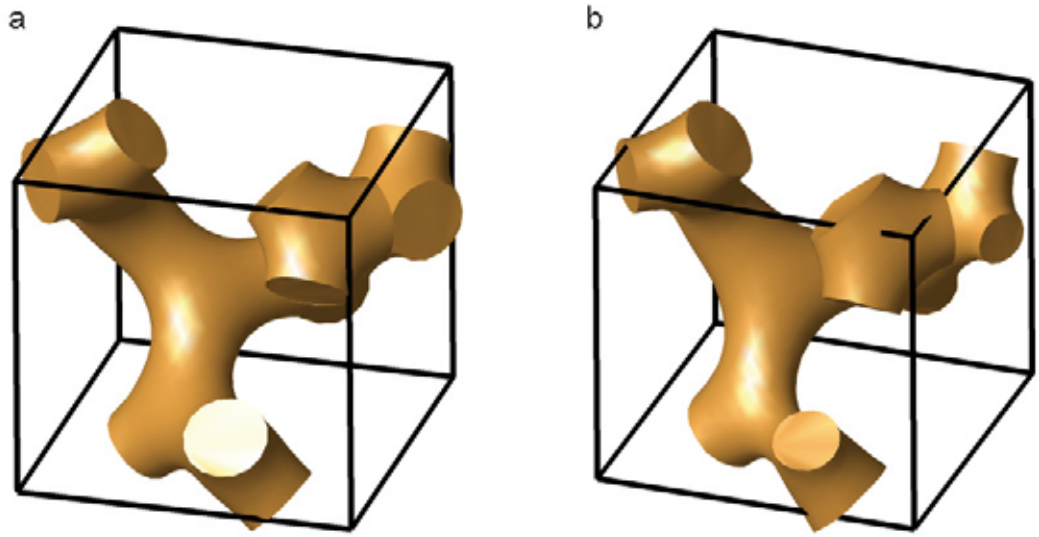

Figure 2.23 - Illustration of a single gyroid network under a 15% uniaxial compression along the [16,9,4] direction. Figure 2.23a shows the effect of an affine compression on a surface with constant curvature (enclosing 18% of the unit cell volume) in the original cubic unit cell. Figure 2.23b illustrates the shape of the surface with constant curvature following compression..

Constant curvature surfaces have also been used to describe block copolymer energetics (Thomas et. al. 1988; Lambert et. al. 1996; Harper 1996) and Figure 2.23 illustrates the effects of compressing the unit cell for such a structural model. To calculate the structure factors shown in Figure 2.24, the surface of a single gyroid network was described with a triangulated surface (2304 facets per unit cell) and the surface numerically optimized so as to achieve constant mean curvature under the constraint of a network volume of 18% (Brakke, K.A. 1992, 1996 and 2005). Once again, the Abbe transform was employed to compute structure factors for the single network. In the general triclinic lattice, the relative position of the two networks could

be ambiguous since the constraints in the cubic case are the glide planes and screw axes of the Q^{230} lattice. However, in practice several alternative criteria for positioning the two networks yield the indistinguishable structure factors.

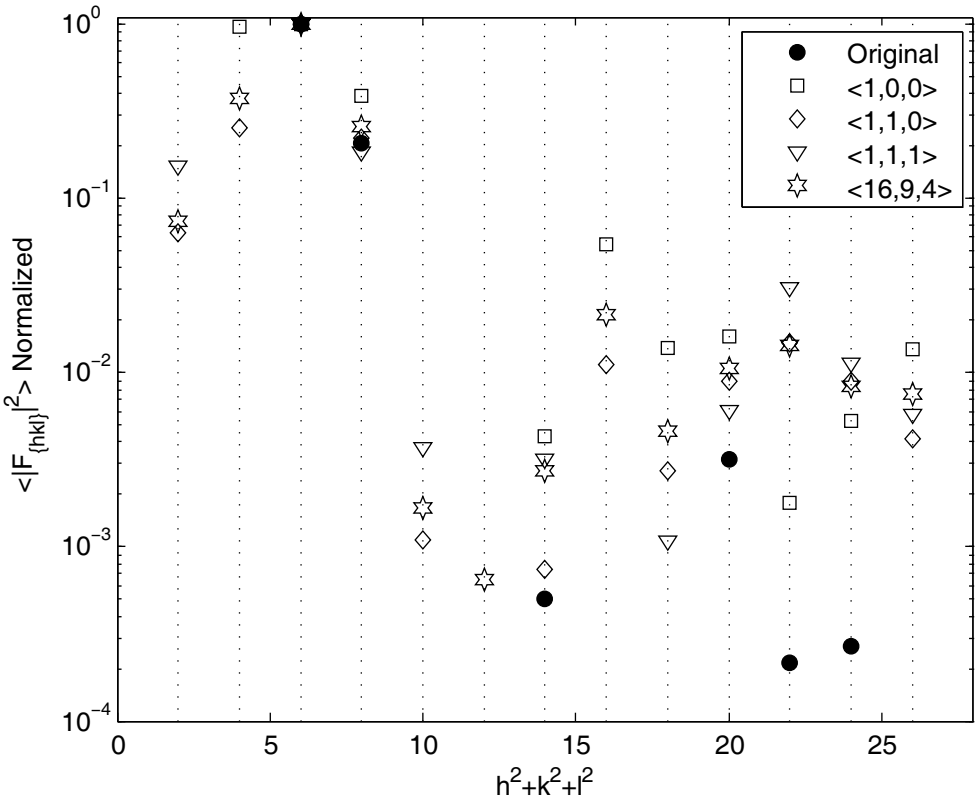

Figure 2.24 –Structure factors for a "constant curvature" model of a network the gyroid topology after 15% uniaxial compression. As the unit cell is compressed, the surface of the network changes to re-establish "constant curvature" leading to changes in the structure factors. The results for a 15% uniaxial compression along several different directions are presented for a gyroid structure with a membrane volume fraction of 64%.

Once again, the magnitude of the {110} and {200} reflections for a compression of the unit cell by 15% equals or surpasses the magnitudes observed for the hybrid material. While neither the "constant-thickness" or "constant-curvature"

surfaces capture all the details of the copolymer/aluminosilicate hybrid energetics, they confirm that large changes in structure factor magnitudes may occur without any change in topology.

2.3.3 Transmission Electron Microscopy

Bright-field transmission electron micrographs of the as-made and calcined materials are shown in Figures 2.25 and 2.26. Bright areas correspond to the minor phase (PI or voids) while dark areas correspond to the major phase (PEO and aluminosilicate). Despite some distortion of the lattice either from solvent casting or sectioning, both materials show the classic fourfold and threefold orientations of a cubic lattice. As noted in a published description of these materials (Finnefrock et. al., 2001), the threefold "wagon-wheels" evident in Figure 2.25c are a common feature of cubic, bicontinuous structures (Hadjuk, et. al. 1995). For structure determination, 2-D projections of structural models are frequently helpful (Anderson et. al., 1992; Harper, 1996; Benedicto and O'Brien, 1997). Using published structure factors (Garstecki and Holyst, 2003a, 2003b), the [100] and [111] projections of the four cubic networks considered in Section 2.3.2 were evaluated by Fourier summation (Harper, 1996) as shown in Figures 2.27 and 2.28.

To permit easy comparison of the experimental data with these models, as illustrated in Figure 2.29, an idealized unit cell was constructed for each micrograph shown in Figure 2.25. First, the projected lattice vectors were first determined via a Fourier transform (Figure 2.29b). Following a uniaxial compression along a direction, n_j, the projected lattice vectors of a cubic lattice (size d) are given by,

$$A^p = \begin{pmatrix} a_{1x} & a_{2x} & a_{3x} \\ a_{qy} & a_{2y} & a_{3y} \end{pmatrix} = d\begin{pmatrix} 1 & 0 & 0 \\ 0 & 1 & 0 \end{pmatrix} \times \left(\left(1 - n_j n_k\right) + t n_j n_k\right) \times R_{kl}, \qquad (2\text{-}32)$$

where R_{kl} is a unitary 3×3 matrix and t is the fractional length along the compression axis. Thus,

$$A^p\left(A^p\right)^T = d^2\begin{pmatrix} 1-\left(1-t^2\right)n_x^2, & -\left(1-t^2\right)n_x n_y \\ -\left(1-t^2\right)n_x n_y, & 1-\left(1-t^2\right)n_y^2 \end{pmatrix}, \tag{2-33}$$

and,

$$d = \sqrt{\lambda_{\text{big}}} \quad \text{and} \quad t \le \sqrt{\frac{\lambda_{\text{small}}}{\lambda_{\text{big}}}}, \tag{2-34}$$

where λ_{big} and λ_{small} are the larger and smaller eigenvalues of $A^p \times (A^p)^{\text{T}}$. For each micrograph in Figure 2.25, the projected lattice vectors, cubic lattice size and minimum uniaxial compression are reported in Table 2.6. The average lattice sizes (as-made 53 ± 10nm, calcined 36 ± 3nm) roughly correspond to the SAXS values although the apparent lattice size varies considerably between micrographs, especially for the as-made material. A combination of sample distortion during sectioning, foreshortened projections and calibration effects frequently lead to such effects in block copolymer TEMS (Breiner et. al., 1998).

As shown in Figure 2.29a, an array of individual unit cells were then averaged together to generate a model unit cell (Figure 2.29c). Finally, the lattice was "rectified" into a cubic lattice as shown in Figure 2.29d. These "rectified" unit cells are displayed in Figures 2.30 and 2.31 alongside the corresponding projections of the double-gyroid and plumber's nightmare networks. For the [111] projection (Figure 2.30), the double-gyroid model shows strong similarities to the as-made and calcined micrographs, while the other network models are quite different. Although the [100] projection of the G, D, P and I-WP network structures are similar in appearance (Benedicto and O'Brien, 1997), the G network can be readily distinguished if the unit cell size is known. As seen in Figure 2.31, the as-made and calcined material match the gyroid structure.

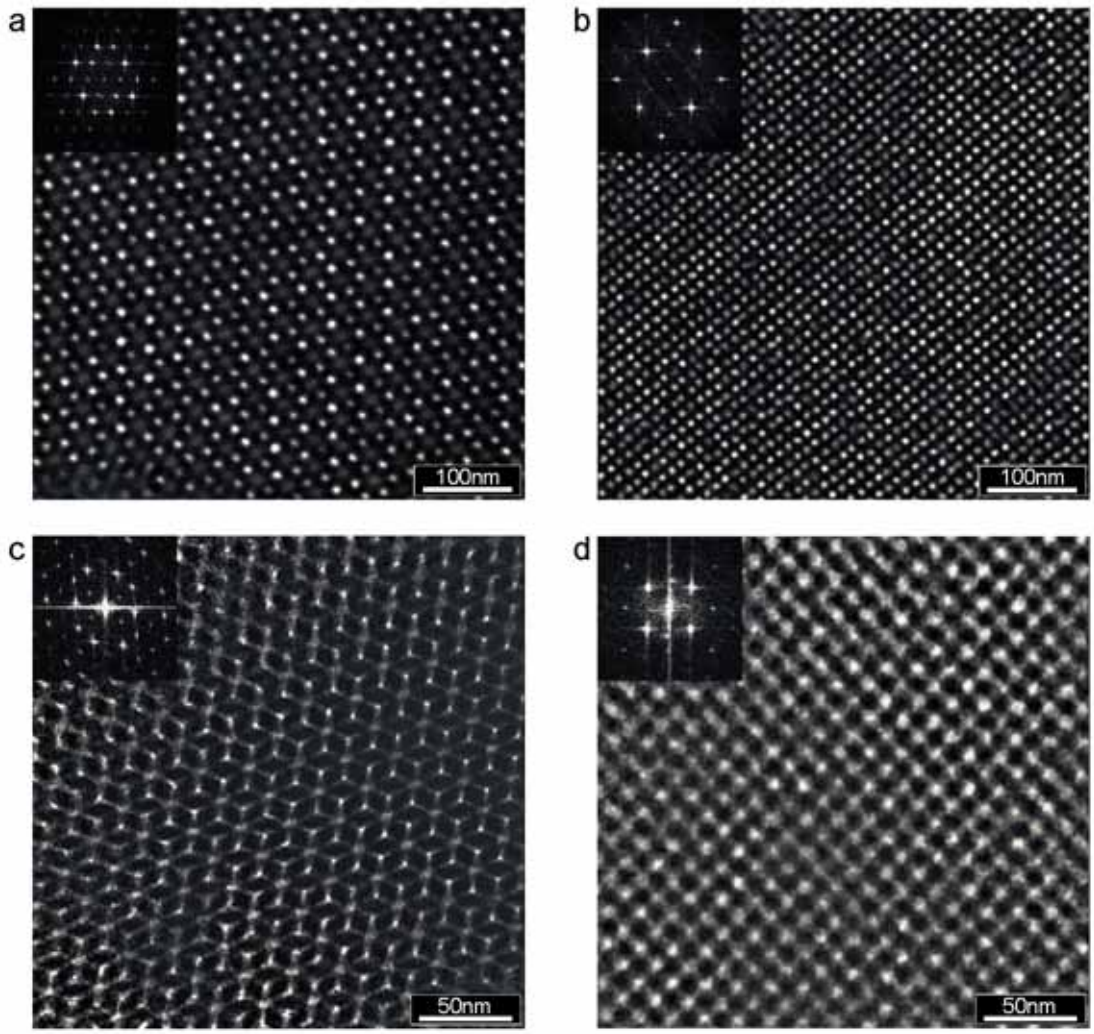

Figure 2.25 – Bright-Field Transmission Electron Micrographs of thin sections (thickness ~ 100nm) of the as-made (top) and hybrid material (bottom) highlighting the threefold (a,c) and four-fold (b,d) projections of the cubic phase. Insets in each panel show the computed Fourier Transform (logarithmic scale) and lattice parameters are given in Table 2.6.

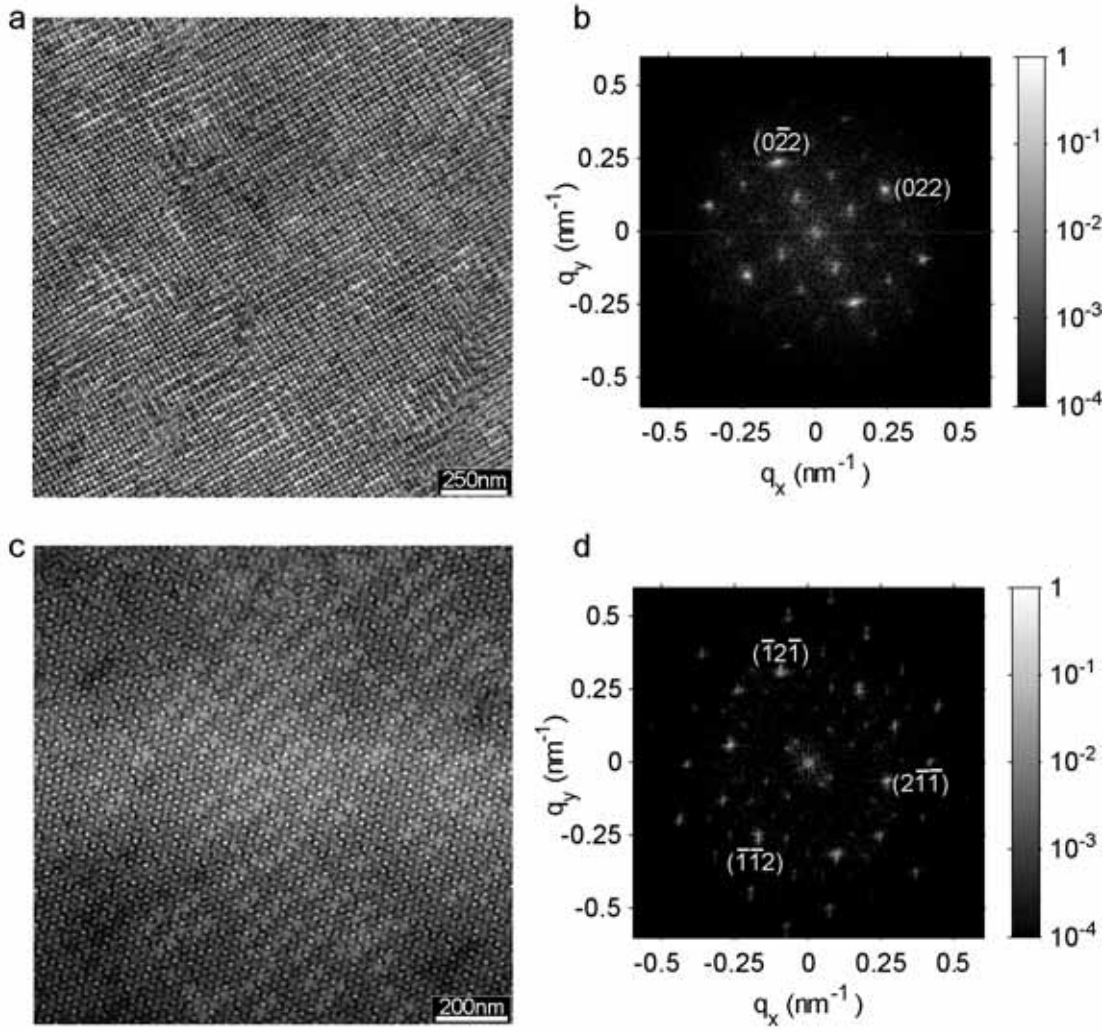

Figure 2.26 – Additional Bright-Field Transmission Electron Micrographs of as-made material showing four-fold (a) and three-fold (c) symmetry along with the corresponding Fourier transforms (b and d).

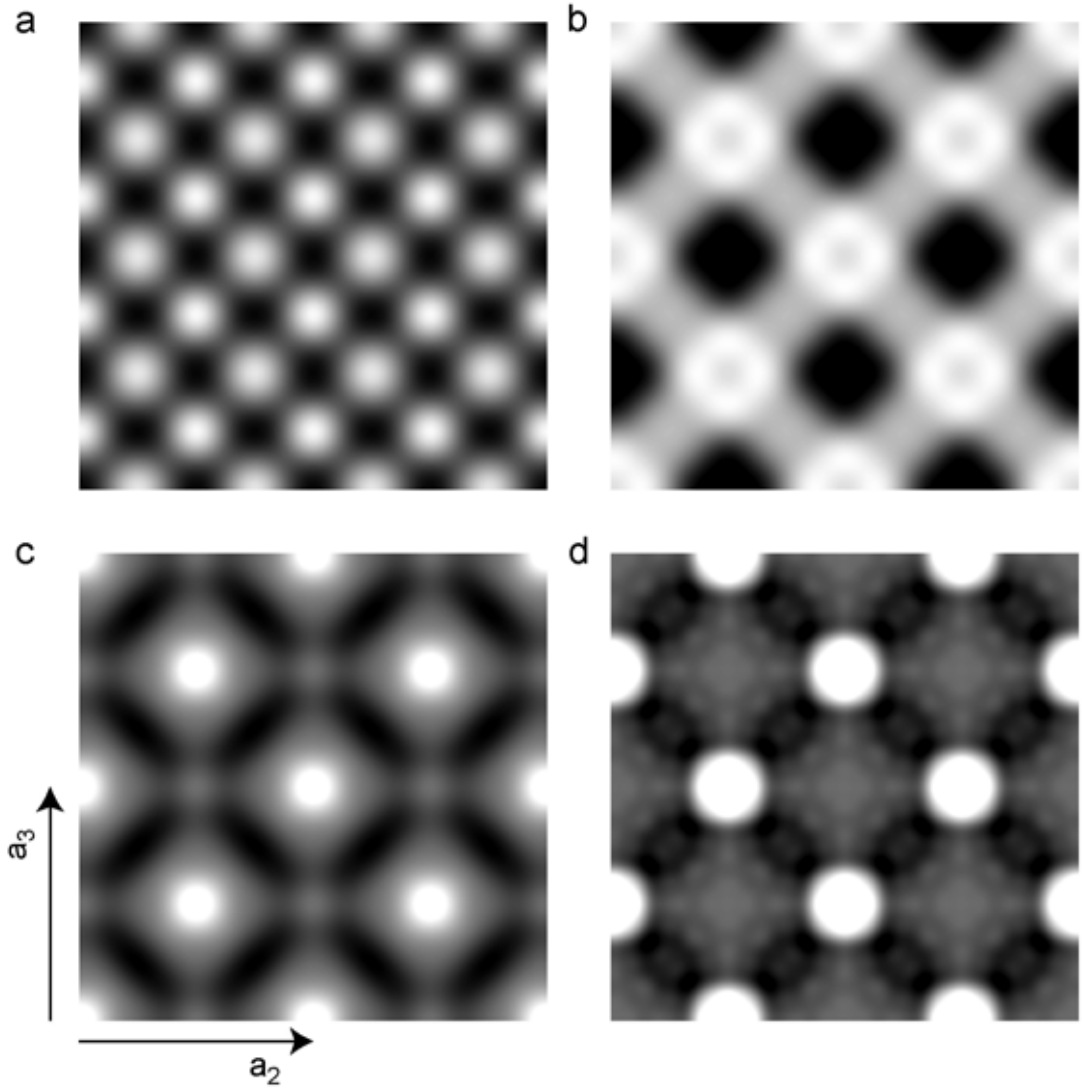

Figure 2.27 – Simulated Transmission Electron Micrographs for the [100] orientation of the double-gyroid (a), double diamond (b), plumber's nightmare (c) and I-WP networks (d). All structures have a majority volume fraction (black) of 64%. An area of 2× 2 unit cells is shown in each image and intensity is scaled so that white represents the lowest projected density (minority phase) and black the highest projected density (majority phase). This shading matches that seen for a bright-field TEM. (For the I-WP structure, the minority phase occupies the 4-fold network as shown in Figure 2.20d.)

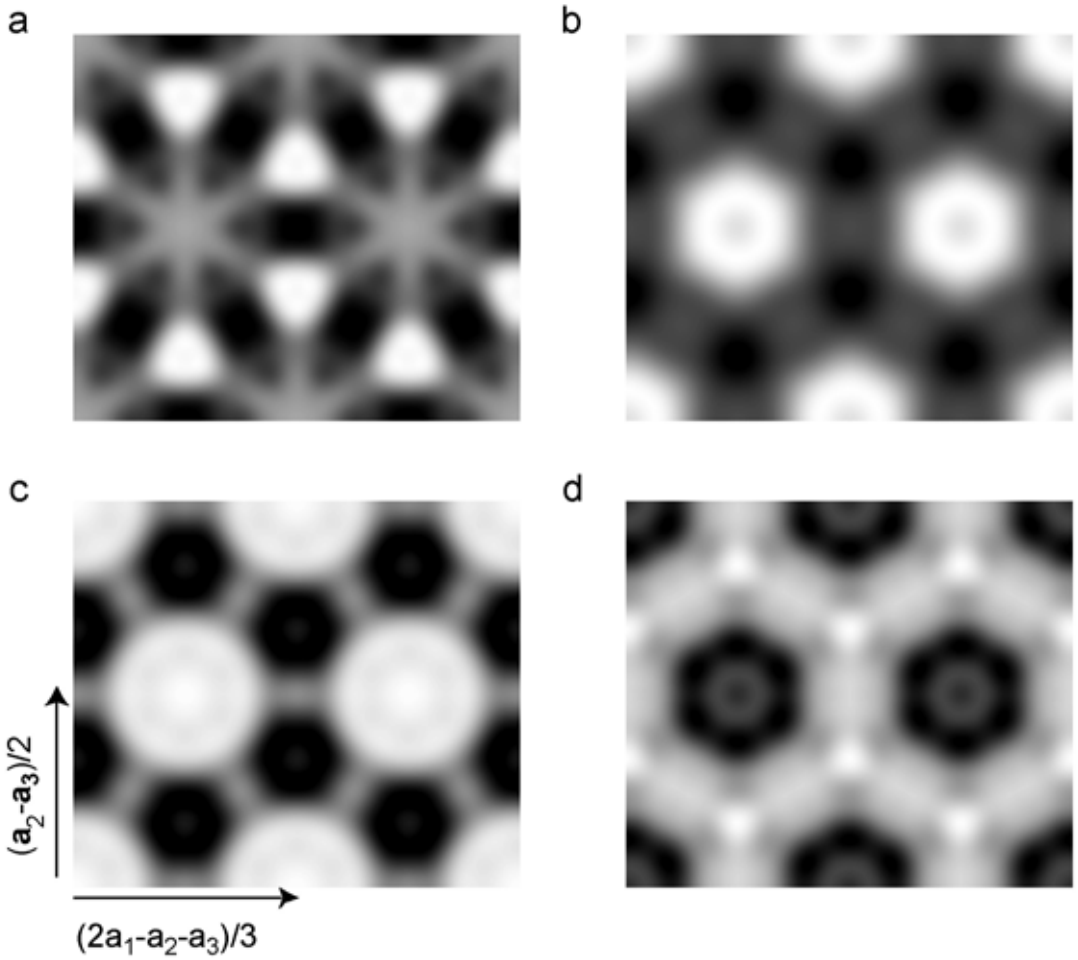

Figure 2.28 – Simulated Transmission Electron Micrographs for the [111] orientation of the double-gyroid (a), double diamond (b), plumber's nightmare (c) and I-WP networks (d). All structures have a majority volume fraction (black) of 64%. Each image has a horizontal width of $(8/3)^{1/2}$ and height of $2^{1/2}$ lattice units. The lowest projected density (minority phase) is shaded white and black indicates the maximum possible projected density (majority phase). This shading matches that seen for a bright-field TEM. (For the I-WP structure, the minority phase occupies the 4-fold network as shown in Figure 2.20d.)

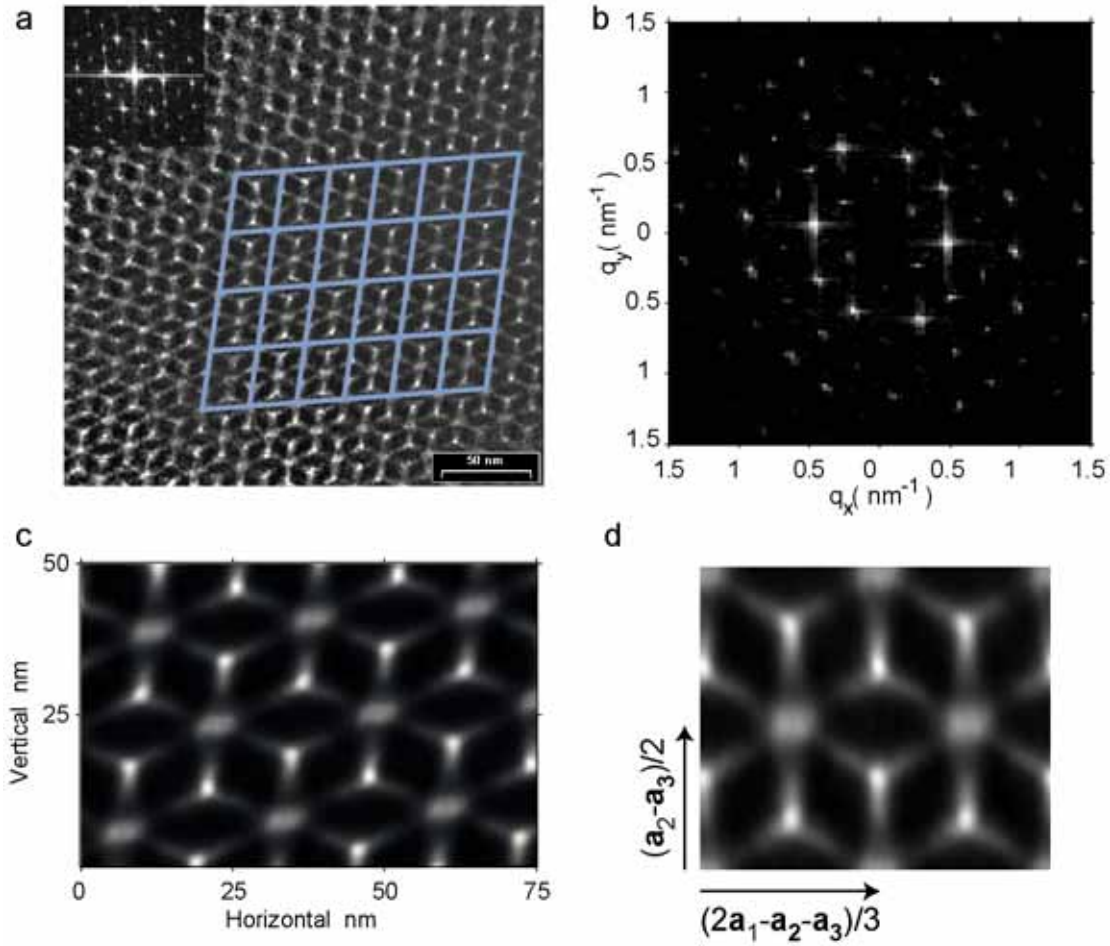

Figure 2.29 –Averaging and transformation of electron micrographs to produce an idealized unit cell. The original micrograph is shown in (a) along with the 4×6 lattice used to average the unit cell. The unit cell size is determined from the Fourier transform(b), and then the contents of the units averaged as shown in (c). Finally, the intensity can be displayed using basis vectors from a cubic lattice as shown in (d).

Table 2.6 - Projected Unit Cell Parameters determined from Micrographs in Figures 2.25 and 2.26.

Micrograph	**Projected Unit Cell Vectors (nm)**	**Apparent Unit Cell Size (nm)**	**Minimum Unit Cell Contraction**
Figure 2.25a As-made [111]	$\boldsymbol{a_1}$ = 32.3 x + 21.1 y $\boldsymbol{a_2}$ = -31.8 x + 10.5 y $\boldsymbol{a_3}$ = -0.5x -31.6 y	47.4	22%
Figure 2.26c As-made [111]	$\boldsymbol{a_1}$ = 45.2 x - 6.3 y $\boldsymbol{a_2}$ = -15.5 x + 35.3 y $\boldsymbol{a_3}$ = -29.6x -28.9 y	56.2	18%
Figure 2.25b As-made [100]	$\boldsymbol{a_2}$ = 40.3 x - 5.8 y $\boldsymbol{a_3}$ = -37.7 y	42.3	15%
Figure 2.26a As-made [100]	$\boldsymbol{a_2}$ = 63.8 x -16.5 y $\boldsymbol{a_3}$ = 15.0 x + 60.9 y	65.9	5%
Figure 2.25c Calcined [111]	$\boldsymbol{a_1}$ = 26.6 x + 2.0y $\boldsymbol{a_2}$ = -10.9 x + 15.5 y $\boldsymbol{a_3}$ = -15.7x -17.5 y	33.4	33%
Figure 2.25d Calcined [100]	$\boldsymbol{a_2}$ = 36.3 x - 1.4y $\boldsymbol{a_3}$ = 0x -37.7 y	38.1	5%

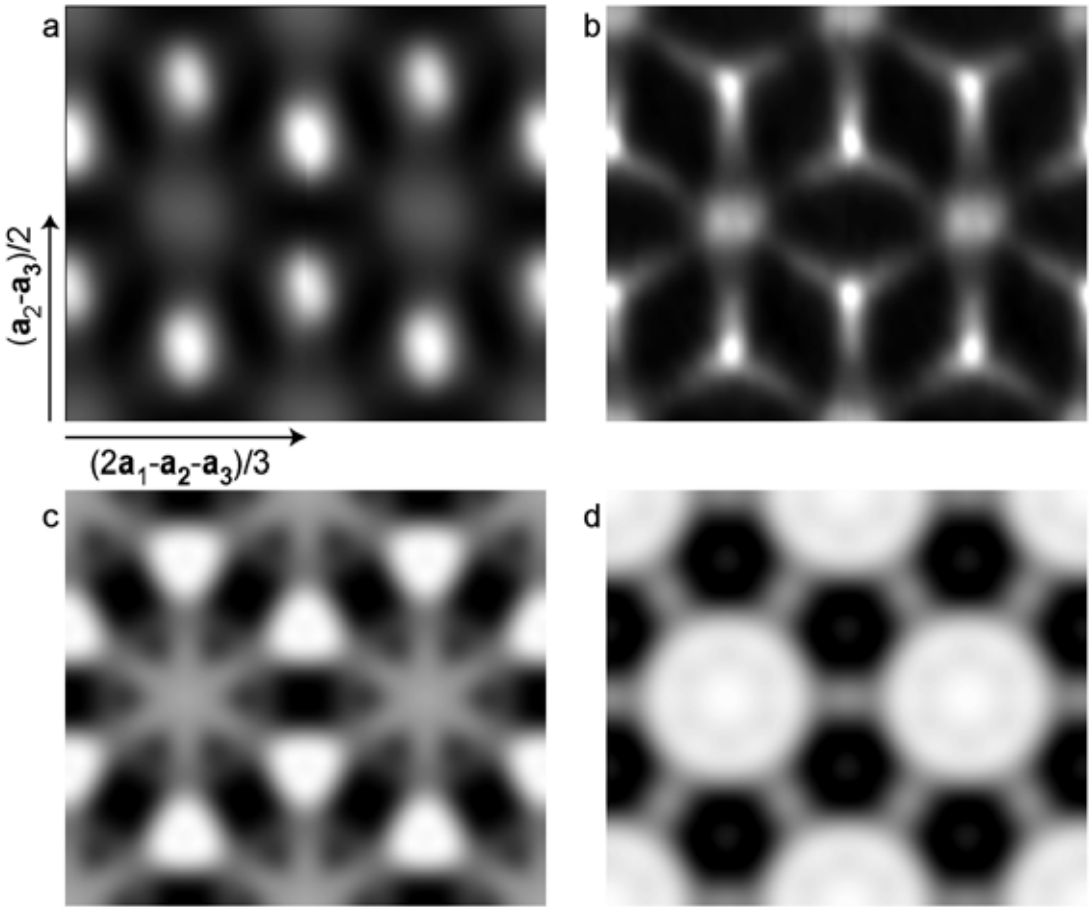

Figure 2.30 – Comparison of Transmission Electron Micrograph average unit cells (rectified [111] direction) for as-made (a) and calcined (b) with models for the double-gyroid (c) and plumber's nightmare (d).

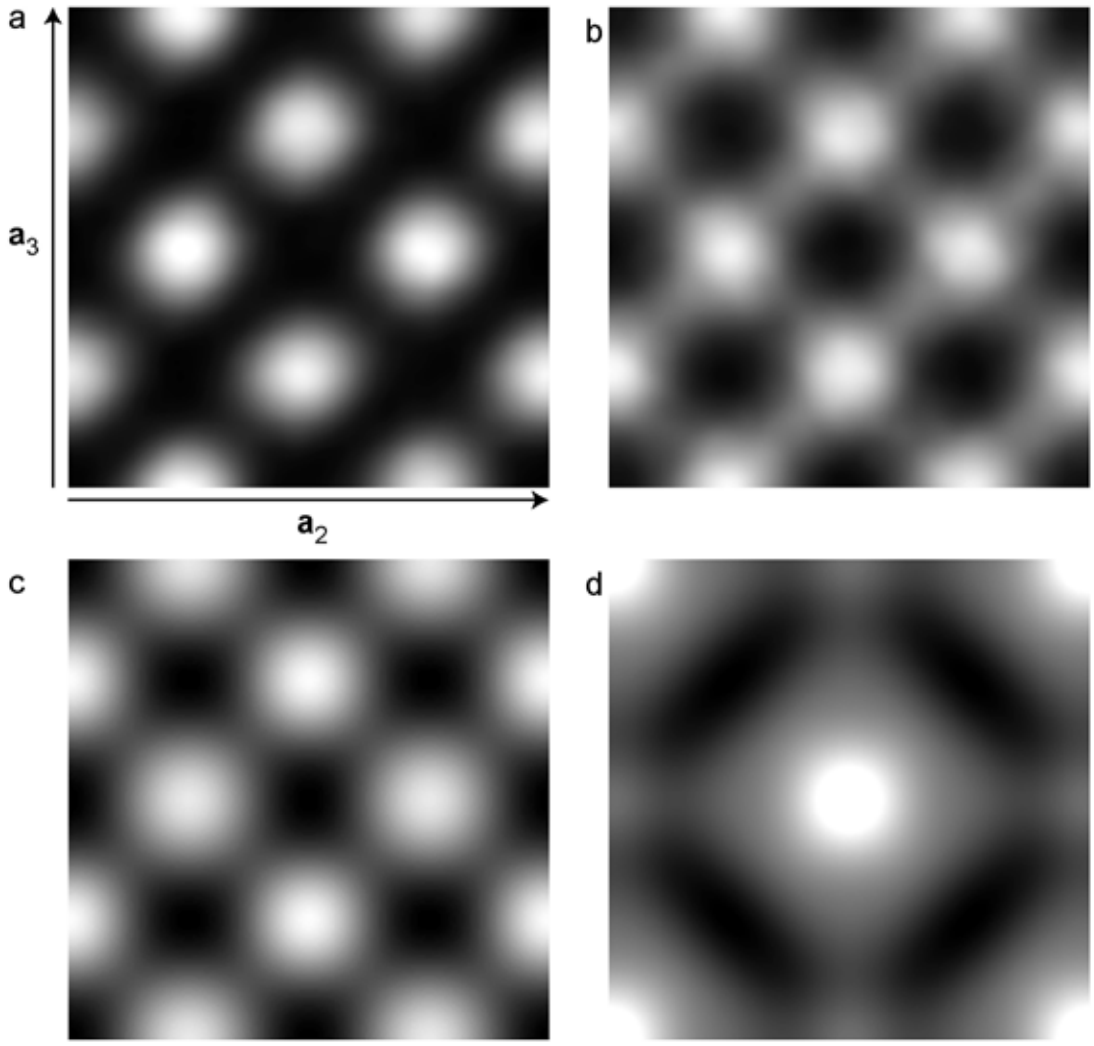

Figure 2.31 – Comparison of Transmission Electron Micrograph average unit cells (rectified [100] direction) for as-made (a) and calcined (b) with models for the double-gyroid (c) and plumber's nightmare (d).

2.4 Discussion

Although the bicontinuous character of a material can be inferred by measurements of rheology (Schulz et. al., 1994), permeability (Kinning et. al., 1987) or conductivity (Cho et. al., 2004), determining the network structure can be more challenging (Hyde, 1996). Many bicontinuous materials lack long-range periodicity and single-crystal specimens are certainly the exception (Anderson et. al, 1989; Hyde,

1996; Jinnai et. al., 2006). Frequently, dynamic and/or static disorder smears out all but a handful of diffraction peaks in powder patterns preventing unambiguous identification of space-group (Hyde, 1996; Finnefrock, 2003). Furthermore, the 2-D projections of different network structures are often quite similar (Hadjuk, 1995; Harper, 1996; Benedicto and O'Brien, 1997). Unsurprisingly, structure assignments can be contentious (Hadjuk, 1995; Hyde, 1996).

Porosity measurements (Section 2.2.2) and TEM "wagon-wheels" (eg. Figure 2.25c) strongly suggest this material has a network structure, but which one is it? Although the P network was originally proposed (Finnefrock et. al., 2001; Finnefrock et. al., 2003), several weaknesses of this model are outlined in Section 2.4.1. Section 2.4.2 describes the much better match between the experimental data and a "distorted gyroid" model. Finally, in Section 2.4.3 the presence of the gyroid structure is related to current ideas on network formation in block copolymers.

2.4.1 Match to Plumber's Nightmare Model

The analysis of Finnefrock and colleagues (Finnefrock et. al., 2001; Finnefrock et. al., 2003) assumed that reflections forbidden by the original cubic lattice symmetry were not allowed when the sample shrank. Given this assumption, Q^{229} is indeed the highest symmetry space-group consistent with the observed reflections (Hadjuk et. al., 1994; p147, Vol III, International Tables for X-ray Crystallography, C.H. MacGillvray and G.R. Rieck eds, Kynock Press, Birmingham England, 1968). Furthermore, the plumber's nightmare structure would also account for the apparent weakness/absence of {3,1,0} and {2,2,2} reflections (Table 2.5).

However, any simple structural model based on the P minimal surface should have strong {1,1,0} reflections and this is certainly not the case (Tables 2.1 and 2.3). Furthermore, the TEM projections of the material do not resemble those of the P

network structure (Figures 2.30 and 2.31). Although it may be possible to account for the differences, a simple P network is a poor match to the experimental data.

2.4.2 Match to the Distorted Gyroid Model

The experimental structure factors differ significantly from those of the D, P and I-WP network models (Table 2.5). In contrast, except for the {1,1,0} and {2,0,0} reflections, the G network is an excellent match to the SAXS data. Furthermore, transmission electron micrographs from both the as-made and calcined materials resemble [100] and [111] projections of a gyroid network. Thus, of the G, D, P and I-WP structures, the G network is the best match to the experimental data. Given the extensive contraction of the material during solvent casting, it is not unreasonable that the network lacks some of the symmetries of the gyroid. Indeed, as shown in Section 2.3.2, modest compression of a G network naturally causes {1,1,0} and {2,0,0} reflections with strengths comparable to those observed from the material. This "distorted gyroid" network is the simplest model consistent with the observed SAXS, TEMS and the apparent process of structure formation.

2.4.3 Cubic Structures in Block Copolymers

In block copolymer network structures, the minority block occupies the network "channels" its polymer chains must stretch to fill the nodes of the network (Hadjuk, 1994; Jinnai, et. al. 2000; Martinez-Veracoechea and Escebedo, 2006). Compared to the 4-fold and 6-fold nodes of the D and P networks, the G network's 3-fold nodes incur a smaller entropic penalty (Matsen, 2002). Indeed, for pure block copolymers only 3-fold networks have been observed (Hadjuk, 1994; Bailey, et. al, 2002; Cochran and Bates, 2004; Takenaka et. al, cond-mat/0605268) or predicted (Matsen and Shick, 1994; Tyler and Morse, 2005; Cochrane, et. al. 2006). This is quite different from surfactant systems where nodes can be filled with fluid and

networks with the D and P symmetries have been observed (Schwarz and Gomper, 1999 and 2001).

In this PI-PEO/aluminosilicate material the network channels are occupied by the minority PI block. Since the chains of this block must stretch to fill up the nodes of the network, the double-gyroid network (3-fold nodes) would be expected to have a lower free energy than the P-network (6-fold nodes). The present structural assignment matches this prediction, suggesting that structure formation in PI-PEO/aluminosilicate may be quite similar to that in pure PI-PEO (Templin et. al, 1997; Floudas, et. al. 2001; Simon et. al., 2001).

The calculations in Section 2.3.2 also suggest that care must be taken in attributing "forbidden" reflections to new or co-existing block copolymer structures. For example, the faint, "forbidden" {1,1,0} and {2,0,0} reflections observed during the phase transition between the hexagonal and gyroid phases have been attributed to commensurate, co-existing cubic lattices with Q^{230} and Q^{229} (Zhu et. al., 2005). This is certainly a possibility, but it is important to note that these reflections could also result from residual distortion during the phase transition.

Finally, this result does not exclude the possibility of block copolymer networks with 4, 6 or even 8-fold nodes. Calculations suggest the addition of a suitable homo-polymer to the minority phase of a copolymer can relieve chain frustration at nodes and stabilize the D network and possibly even the P network (Matsen, 1995; Likhtman and Semenov, 1997; Dotera, 2002). While these predictions for copolymer/ homopolymer blends await experimental confirmation (nb. Winey et. al. 1992 pre-dates the identification of the gyroid), Q^{229} bicontinuous networks have been reported for copolymer/aluminosilicate composites (Zhao et. al 1998; Sakamoto et. al. 2000; Jain et. al., 2005). These structures might reflect aluminosilicate acting to

relieve nodal frustration but non-equilibrium kinetics during structure formation may also be significant.

2.4.4 Role for Electron Tomography

The present analysis relies upon structural models to interpret the experimental SAXS and TEM data. Implicit assumptions about the structure of the material are introduced through the selection of these models. Furthermore, even if a given model is consistent with all the experimental data, there is no guarantee it is the only one. Methods that directly determine the structure of a material, such as 3-D electron tomography, avoid these difficulties (Sakamoto et. al., 2000; Jinnai et. al., 2006). Since this PI-b-PEO/aluminosilicate material is well suited to a 3-D electron tomography, in the future it would be very interesting to study the material with this technique.

2.5 Conclusion

This chapter described the structural analysis of a mesoporous network formed in a hybrid aluminosilicate/block copolymer material. Of the network structures considered in this study, the SAXS and TEM data from this material are most consistent with a distorted double gyroid structure. This result implies the phase diagram for these copolymer/aluminosilicate materials is more similar to the pure copolymer phase diagram than previously thought, since the double-gyroid is also found in diblock copolymers (Floudas, et. al. 2001). The study also highlighted the implicit assumptions introduced when comparing TEM and SAXS data to structural models, confirming the advantage of using direct methods such as EM tomography.

Chapter Three - Lamellar ABC Copolymers

3.1 Introduction

ABC triblock copolymers can form an enormous range of morphologies including the "knitting pattern" (Breiner, et. al., 1998; Ott, et. al. 2001), helices (Krappe, U. et. al., 1995), non-cubic networks (Mogi et. al., 1992b; Epps, et. al. 2004) and non-centrosymmetric lamellae (Goldacker, et. al. 1999; Takano, et. al. 2003). Systematic exploration of ABC copolymer morphologies remains challenging, though, because the equilibrium morphology depends upon block volume fractions ($f_A, f_B, f_C = 1-f_A-f_B$) and the strength of interactions between all three pairs of blocks ($\chi_{AB}N$, $\chi_{BC}N$, $\chi_{AC}N$) (Bates and Fredrickson, 1999; Zheng and Wang, 1995). Despite this, phase behavior has been studied for several regimes including ABC copolymers with a small end block ($f_C < f_A \approx f_B$) (Bailey, et. al. 2001 and 2002), large end block (Breiner, et. al. 1997) and large middle block ($f_B >> f_A \approx f_C$) (Mogi, et. al. 1992, 1994; Nakazawa and Ohta, 1993; Phan and Fredrickson 1998).

This chapter describes studies of three poly(ethylene-*alt*-propylene)-*b*-poly(ethylene oxide)-*b*-poly(*n*-hexyl methacrylate) (PEP-*b*-PEO-*b*-PHMA; ABC) copolymers with roughly equivalent A and C domains ($f_A \approx f_C$) and relatively large (f_B=0.25), intermediate (f_B=0.15) and small (f_B=0.1) B-block volume fractions. For these copolymers, the relatively low interfacial tension of AC interfaces favors contact between the end blocks over the obligatory AB and BC interfaces ($\gamma_{AC} < \gamma_{AB}, \gamma_{BC}$). Domain ordering within each copolymer was studied via Small Angle X-ray Scattering (SAXS) while the connectivity of the B domains was inferred from conductivity measurements of samples doped with lithium triflate. The experimental

data are consistent with transitions between triple-lamellae (Figure 3.1 ; Matushita, et. al. 1980), rods-at-lamellae (Auschra and Stadler, 1993; Liu et. al., 2003) and balls-at-lamellae (Beckmann et. al. 1994; Erhardt, et. al. 2001) structures as B-domain volume fraction decreased. This sequence of morphological transitions was previously observed in poly(styrene)-b-poly(butadiene)-b-poly(methyl methacrylate) (PS-b-PB-b-PMMA) copolymers (Stadler et. al., 1995).

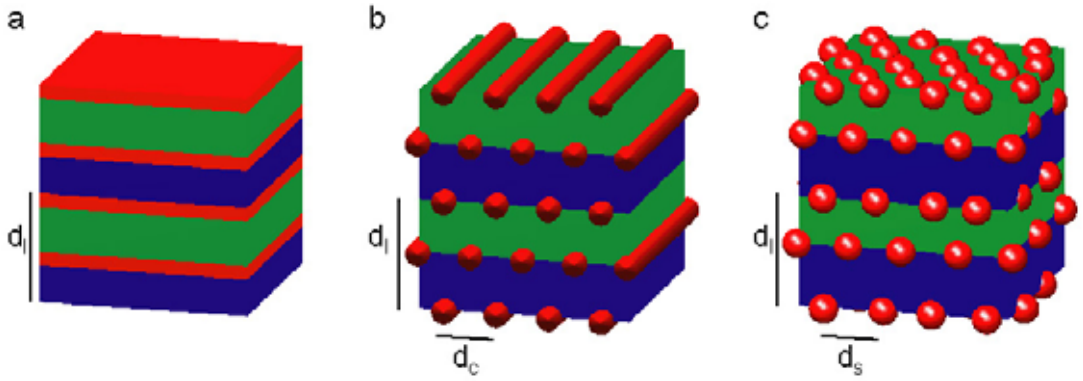

Figure 3.1 – Cartoons depicting the triple-lamellae (a), rods-at-lamellae (b) and balls-at-lamellae (c) morphologies (A - blue, B - red, C - green).

3.2 Experimental Methods

3.2.1 Synthesis of Copolymers

Figure 3.2 shows the molecular structure of the poly(ethylene-*alt*-propylene-block-ethylene oxide-block- *n*-hexyl methacrylate) (PEP-*b*-PEO-*b*-PHMA) copolymers studied in this chapter. The properties of the three blocks are summarized in Table 3.1.

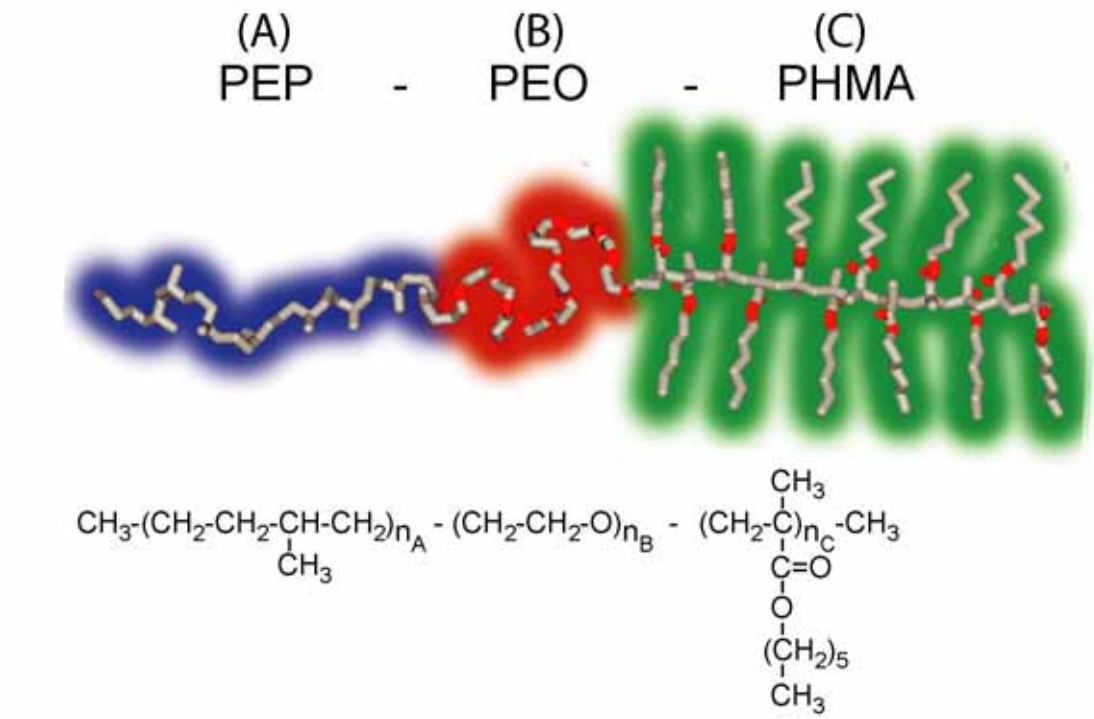

*Figure 3.2 – Molecular architecture of poly(ethylene-*alt*-propylene)-*b*-poly(ethylene oxide)-*b*-poly(*n*-alkyl methacrylate) (PEP-b-PEO-b-Pn-alkyl-MA) ABC triblock copolymers (blue, PEP block; red, PEO block; green, Pn-alkyl-MA block). (original image prepared by Andrew Burns)*

Table 3.1 - Molecular Properties of PEP, PEO and PHMA

Polymer	**Monomer Weight (g/mol)**	**Density (g/cm^3)**	**Packing Length (nm)**	**Hildebrand Solubility (δ) $(MPa)^{½}$**
PEP	70.01	0.857[a]	0.210[a]	16.0[e]
PEO	44.05	1.13[b]	0.195[a]	20.2[f]
PHMA	170.31	1.007[c]	0.473[d]	17.6[f]

[a](Fetters, et. al. 1994), [b](Zhu, et. al. 2001), [c](Rodgers and Mandelkern, 1957), [d](Fetters, et. al. 1999 at T=100 °C), [e](Schmidt and Hillmyer, 2002), [f](page VII-554 to VII-555, Brandrup and Immergut, 1989).

The Flory-Huggins Interaction parameter between blocks, χ_{ij}, were estimated using the relationship (Madkour, 2001),

$$\chi_{ij} = \frac{V_{ref}\left(\delta_i - \delta_j\right)^2}{k_B T} \tag{3-1}$$

where V_{ref} is the monomer segment volume, δ_i and δ_j are the Hildebrand solubility parameters for blocks i and j, k_B is Boltzmann's constant and T is the temperature. For an interface between the corresponding homopolymers, the interfacial tension, γ_{ij}, is given by (Helfrand and Sapse, 1975),

$$\gamma_{ij} = k_B T \times \sqrt{\frac{\chi_{ij}}{6V_{ref}}} \times \frac{2}{\sqrt{p_i} + \sqrt{p_j}} \times \frac{\sqrt{p_i / p_j} + \sqrt{p_j / p_i} + 1}{3} \tag{3-2}$$

and the interfacial width, t_{ij}, given by,

$$t_{ij} = \sqrt{\frac{V_{ref}}{\chi_{ij}} \times \frac{p_i + p_j}{3 p_i p_j}} \tag{3-3}$$

where p_i and p_j are the packing length of the two polymers (Fetters, et. al. 1994).

Table 3.2 - Domain Interfacial Properties at Room Temperature (T=25°C)

Polymer Pair	**AB**	**BC**	**AC**
[a]χ_{ij}	0.605	0.232	0.088
[b]γ_{ij} (kT/nm^2)	1.880	0.989	0.594
[c]t_{ij} (nm)	0.88	1.21	1.92

[a]Calculated with Equation 3-1 and a segment volume V_{ref}=85cm^3/mol=0.141nm^3.
[b]Interfacial Tension calculated with Equation 3-2.
[c]Interfacial Thickness calculated with Equation 3-3.

The PEP-b-PEO-b-PHMA copolymers were synthesized by Dr Surbhi Mahajan using a novel synthetic procedure (Mahajan et. al., 2004; Chapter 3, Mahajan, 2005; Grubbs,

2005). Briefly, the first block (PEP) was formed by the anionic polymerization of isoprene followed by catalytic hydrogenation. The second block (PEO) was grown onto this chain via living anionic polymerization. Finally, the third block (PHMA) was grown via atom transfer radical polymerization. Copolymer molecular weight, polydispersity, and block mass fractions were determined via gel permeation chromatography and ^{1}H NMR (Mahajan et. al., 2004). The molecular characteristics for Copolymers **1**, **2** and **3** are summarized in Table 3.3.

Table 3.3 - Characterization of PEP-PEO-PHMA block copolymers

	[a]**Copolymer 1**	**Copolymer 2**	**Copolymer 3**
[b]f_A	0.34	0.44	0.52
f_B	0.25	0.15	0.10
f_C	0.41	0.41	0.38
V (cm^3/mol)	35267	28548	23910
M_n (g/mol)	34800	27390	22730
M_w/M_n	1.09	1.06	1.07
[c]$\chi_{AB}N$	251	203	170
$\chi_{BC}N$	96	78	65
$\chi_{AC}N$	37	30	25
[d]L_A (nm)	9.74	9.97	9.91
L_B (nm)	8.66	6.03	4.51
L_C (nm)	7.12	6.41	5.65

*[a]Copolymers **1**, **2** and **3** correspond to copolymers EPOM29, EPOM37 and EPOM38 in Surbhi Mahajan's thesis (Table 5.1, page 85; Mahajan, 2005).*
[b]Block volume fractions for room temperature homopolymer densities (Table 3.1).
[c]Flory-Huggins Interaction Parameters given in Table 3.1.
[d]RMS end-to-end block lengths computed with packing lengths in Table 3.1.

Additional copolymers were synthesized with poly(n-butyl methacrylate) and poly(n-octyl methacrylate) in the C block position. The block volume fractions of these poly(ethylene-*alt*-propylene)-*b*-poly(ethylene oxide)-*b*-poly(*n*-butyl methacrylate) (PEP-*b*-PEO-*b*-PBMA) and poly(ethylene-*alt*-propylene)-*b*-poly(ethylene oxide)-*b*-poly(*n*-octyl methacrylate) (PEP-*b*-PEO-*b*-POMA) compounds are reported in Table 3.4.

*Table 3.4- Composition of Copolymers **5**-butyl and **6**-octyl*

Copolymer	**M_w (g/mol)**	**M_w/M_n**	**[a]f_A**	**f_B**	**f_C**
5-butyl	36250	1.13	0.20	0.16	0.64
6-octyl	38600	1.16	0.27	0.08	0.65

[a]Block volume fractions assumed room temperature homopolymer density values of ρ_{PBMA} = 1.06g/cm^3 and ρ_{POMA} = 0.965 g/cm^3 (Rodgers and Mandelkern, 1957).

3.2.2 X-ray Scattering

X-ray scattering data were gathered from samples using a laboratory source. Briefly, CuK$_\alpha$ x-rays (λ=0.154nm) were generated with a rotating anode Rigaku RU-3HR generator (Tube Voltage = 42kV, Tube Current = 56mA, 2mm×0.2mm point focus on a Copper Anode viewed at ~6° take-off angle to yield an effective source size of 0.2mm × 0.2mm square), filtered by a nickel foil (thickness = 10 μm; Goodfellow, PA) and focused and further monochromatized with a pair of Franks mirrors (Hajduk, 1994). The flux at the sample was ~4×10^7 X-rays per second in a beam roughly 1mm×1mm. Small Angle X-ray Scattering (SAXS) data was gathered using a 50cm or 80cm flight tube while Wide Angle X-ray Scattering (WAXS) was measured using a 1.5cm flight tube. At the end of the flight tube, the transmitted x-ray beam was blocked with a small (typical diameter of 2-3mm) circle of lead tape while the

scattered x-rays were imaged with a home-built 2-D X-ray area detector consisting of a phosphor screen, fiber-optic coupler and 1024×1024 pixel CCD similar to that described in Tate et. al., 1995. The distance from the sample to detector and position of the beam center were determined using silver beheanate (d_l = 5.8376nm; Blanton, et. al. 1995) and silver stearate (d_l = 4.868nm; Vand, et. al. 1949) calibrants. Scattering lengths in text are given as $s = 2\ sin\ (\theta)/\lambda$, where 2θ is the total scattering angle.

Powder samples were prepared by transferring 3mg of copolymer in a stock solution (1mg copolymer: 10 μL chloroform) into standard glass x-ray capillaries (diameter = 1.0mm or 1.5mm; Charles Supper Co, MA). The solution was concentrated into the bottom ~3mm of the capillary by repeated centrifugation and solvent extraction under a rough vacuum (~100 Pascals). This more concentrated copolymer solution was then dried in a vacuum oven (Hereaus Vacutherm Oven, Thermo Scientific, MA) at a temperature of 60°C for ~12 hours. This temperature was comfortably above the glass temperature of all three polymer blocks (T_g(PEP) ≈-62°C, T_g(PEO) ≈ -60°C, T_g(PHMA) ≈ -5°C; Chapter 4, Mahajan 1995) and the melting temperature of PEO (T_m(PEO)~ 50°C). Exposure to oxygen at elevated temperatures caused the copolymers to degrade, so samples were cooled to room temperature before transferring them to the x-ray sample stage.

Aligned samples were prepared by casting copolymer solutions in both X-ray capillaries and Teflon (Dupont, Inc.; polytetrafluoroethylene (PTFE)) wells. For X-ray capillary samples, a 1mg copolymer/ 6μL chloroform solution was transferred to a 1.5mm glass X-ray capillary. The capillary was then placed in a small borosilicate tube and the tube sealed with parafilm (SPI Supplies, PA). Although chloroform can slowly permeate through parafilm, a small pinhole was added to ensure the chloroform

could escape as samples were dried at 50°C for ~12 hours. This casting procedure formed a thin film of copolymer along the inner wall of the X-ray capillary. Additional samples were prepared by casting 1mg copolymer/6 μL chloroform solution into small wells (diameter 7-10mm, depth 3-6mm) milled in a block of PTFE (McMaster-Carr, GA). The block of PTFE was placed at the bottom of a glass beaker that was then sealed with parafilm. Once again, slow removal of solvent overnight (at 50°C) yielded a transparent film (thickness ~1mm). Small pieces of the films were cut to size with a razor blade and placed in glass x-ray capillaries.

3.2.3 Ionic Conductivity Measurements

Differences in ionic conductivity can be used to identify morphological transitions (Ruokolainen, et. al. 1998; Cho, et. al. 2004). Samples for ionic conductivity measurements were prepared by Dr Surbhi Mahajan and conductivity measurements made by Dr Byoung-Ki Cho. Briefly, solutions of copolymers **1**, **2** and **3** (15mg copolymer : 1ml tetrahydrofuran (THF, C_4H_8O)) were mixed with a solution of lithium triflate (56mg $LiCF_3SO_3$: 1ml THF) to give a final triflate concentration of 1 Li^+: 50 ethylene-oxide units. After filtering solutions through a 0.45μm PTFE filter, films were prepared by evaporating THF in a rotary evaporator followed by heating to 100°C in a vacuum oven. Using a glove-box, the films of copolymer **1-Li**, **2-Li** and **3-Li** were then transferred from the roto-vap round-bottomed flask into a Teflon sample holder (diameter 5.07mm and thickness 1.68mm). Finally, this Teflon sample holder was sandwiched between two gold plated electrodes and loaded into a NOVOCONTROL Turnkey Concept 80 Broadband Dielectric Spectrometer (Novocontrol, NC). Ionic conductivity was measured in the range of 10^1 to 10^6 Hertz and direct conductivity obtained by extrapolation to zero frequency (Kosonen, et. al. 2002).

3.2.4 AFM

AFM measurements were performed by Dr Phong Du. A thin film of copolymer **2** was prepared by spin-coating a solution (~10mg copolymer : 1ml of toluene) onto a silicon substrate and the film was then annealed for 1 hour at 130°C degrees in the vacuum oven. Phase images were taken using a Veeco Nanoscope III Multimode scanning probe microscope (Veeco, CA) employing tapping mode etched silicon tips.

3.3 Results

3.3.1 SAXS

The domain morphologies of copolymers **1**, **2** and **3** were studied via Small Angle X-ray Scattering (SAXS).

3.3.1.1 Copolymer 1

A powder pattern from copolymer **1** is shown in Figure 3.3. The scattering profile was fitted via non-linear least squares to the form,

$$I(s) = I_{back}(s) + \sum_{j=1}^{N_{peak}} \frac{I_j}{4\pi s_{cen,j}^2} \times V\left(s - s_{cen,j}, \sigma_l\left(s_{cen,j}\right), \sigma_j\left(s_{cen,j}\right)\right) \qquad (3\text{-}4)$$

where $I_{back}(s)$ describes the background scattering, I_j is the integrated scattering intensity of the j-th scattering peak centered at $s_{cen,j}$ with peak shape given by the function $V(x, \sigma_l, \sigma_g)$. Scattering peak shape results from the convolution of many factors including the finite domain size of crystallites, variations in lattice spacing through the sample, x-ray beam size and divergence and the point-spread function of x-ray detector and was approximated by a Voigt function,

$$V(x, \sigma_l, \sigma_g) = \int_{-\infty}^{\infty} \frac{1}{\sqrt{2\pi}\sigma_g} \times \exp\left(\frac{-\left(x - x'\right)^2}{2\sigma_g^2}\right) \times \frac{\sigma_l}{x'^2 + \sigma_l^2} \frac{dx'}{\pi} \qquad (3\text{-}5)$$

where σ_l and σ_g describe the peak width and shape in term of Lorentzian and Gaussian components (Young and Wiles, 1982; Humlicek, 1982; David, 1986).

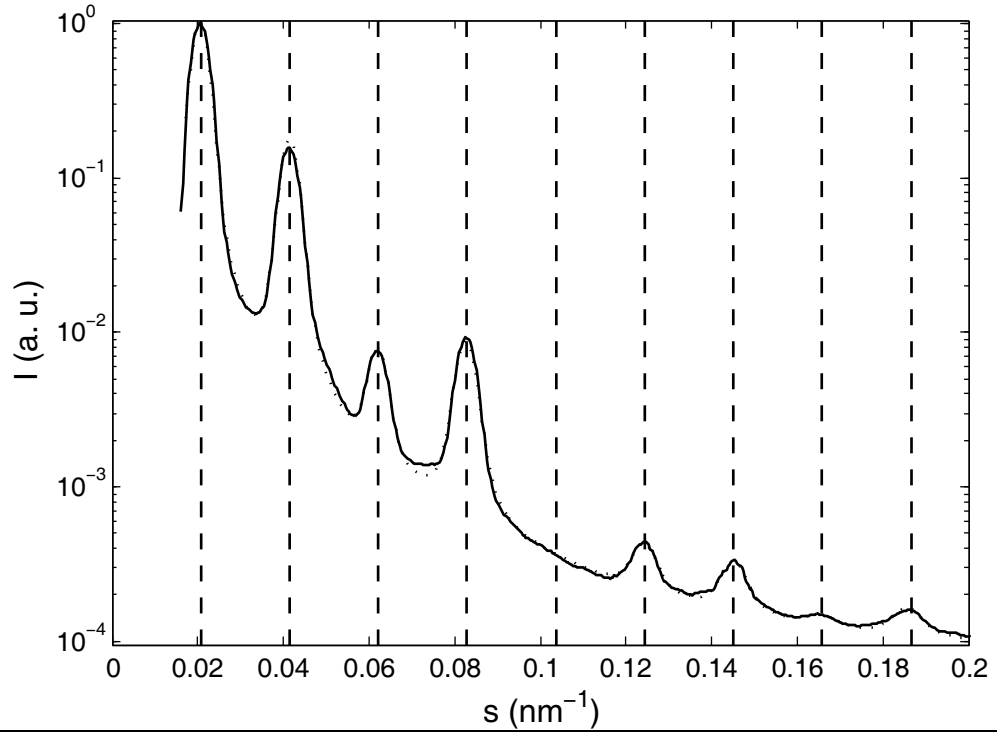

Figure 3.3 – Scattering intensity per steradian (I) versus scattering vector(s) for Copolymer **1** *at 75 °C following integration of six exposures (900 seconds). The fit to the scattering profile (Equation 3-4) is marked by the dotted line and can only be distinguished from the experimental data in a few places. The dashed vertical lines mark the allowed peak positions for a lamellar structure with repeat spacing of d_l = 48.35 ± 0.24 nm. The scattering intensity per steradian (I) is normalized so the strongest scattering corresponds to a value of I = 1 (a. u. stands for arbitrary units).*

The dependence of peak width was assumed to take the form,

$$\sigma_l(s_{cen}) = \sqrt{\sigma_{l0}^2 + \sigma_{g1}^2 s_{cen}^2}$$
$$\sigma_g(s_{cen}) = \sqrt{\sigma_{g0}^2 + \sigma_{g1}^2 s_{cen}^2} \qquad (3\text{-}6)$$

where σ_{l0}/σ_{g0} and σ_{l1}/σ_{g1} describe the dependence of peak width on scattering angle. Background scattering was fitted to an inverse polynomial,

$$I_{back}(s) = \sum_{k=0}^{3} \frac{B_k}{s^k} \tag{3-7}$$

where B_k are constant coefficients. Results of the fit are summarized in Table 3.5.

*Table 3.5 - Peak Parameters of Scattering from copolymer **1** shown in Figure 3.3.*

h - Peak Index	[a] s_{cen} ($\times 10^{-2}$ nm^{-1})	[b] $s_{cen} \times d_l$	[a] I (percent)
1	2.0581 ± 0.0026	0.995 ± 0.010	100
2	4.1427 ± 0.0021	2.003 ± 0.010	73.9 ± 1.3
3	6.2035 ± 0.0040	2.999 ± 0.010	6.48 ± 0.16
4	8.2596 ± 0.0028	3.994 ± 0.010	16.32 ± 0.36
5	-	-	-
6	12.426 ± 0.010	6.008 ± 0.010	1.163 ± 0.047
7	14.5172 ± 0.0097	7.019 ± 0.010	1.414 ± 0.051
8	16.541 ± 0.047	7.997 ± 0.010	0.247 ± 0.032
9	18.584 ± 0.019	8.986 ± 0.010	0.856 ± 0.043

[a] Uncertainties for s_{cen} and I are from non-linear least squares fit of peak positions. Peak width parameters were $\sigma_{L0} = (5.81 \pm 0.44) \times 10^{-4}$ nm^{-1}, $\sigma_{L1} = (1.006 \pm 0.084) \times 10^{-2}$, $\sigma_{G0} = (1.562 \pm 0.031) \times 10^{-3}$ nm^{-1} and $\sigma_{G1} = (9.9 \pm 1.3) \times 10^{-3}$.
[b] Uncertainties for $s_{cen} \times d_l$ are for a least-squares fit of plot of s_{cen} versus h. The lamellar repeat spacing is $d_l = 48.35 \pm 0.24$nm.

As is clear from the dotted lines in Figure 3.3, all peak positions can be described by a single index,

$$s_h = \frac{h}{d_l} \tag{3-8}$$

where d_l is the unit cell "height". SAXS for copolymer **1** showed only a modest dependence on temperature in the range of 50ºC to 200ºC. Below the crystallization temperature of the PEO block, the lattice size increased discontinuously and the scattering peaks broadened although the orientation of domains was unchanged.

Previous studies have shown that copolymer morphology can be quite sensitive to doping with inorganic compounds (Bronstein, L. et. al., 1997; Epps, et. al., 2003). However, SAXS data from **1-Li** (Figure 3.4, Table 3.6) indicate that the morphology was largely unchanged by the addition of a small concentration of lithium triflate.

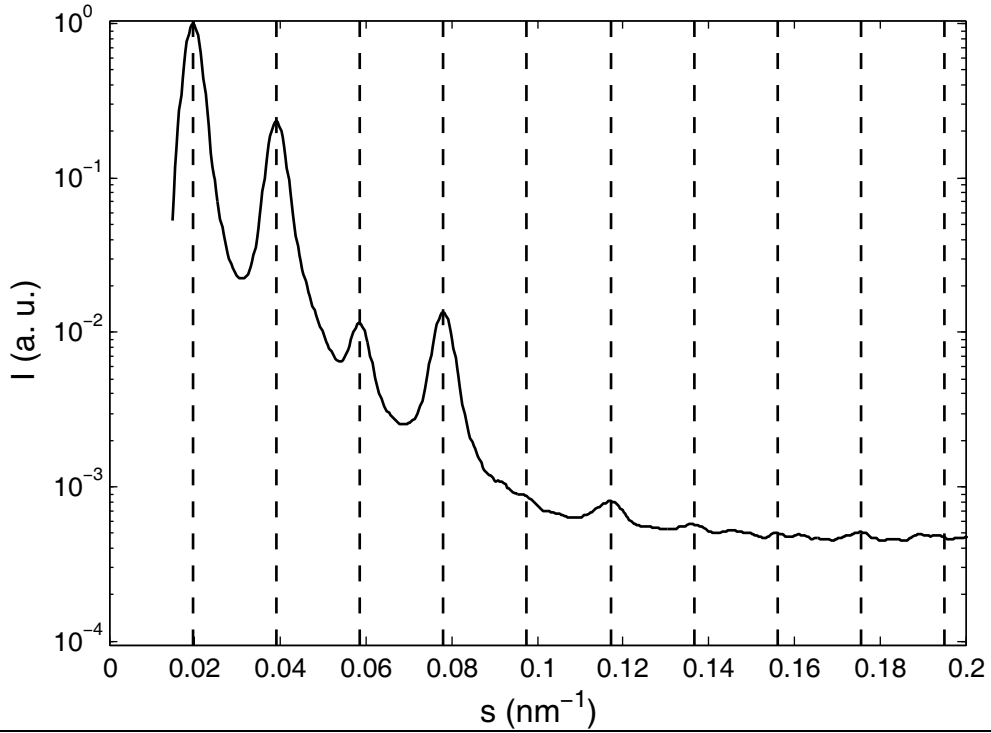

*Figure 3.4 - Plot of I versus s for copolymer **1-Li** at 60ºC following integration of two exposures (900 seconds). Dashed lines mark peak positions for a lamellar structure with a repeat spacing of d_l = 51.25 ± 0.26nm.*

*Table 3.6 - Peak Parameters of Scattering from copolymer **1-Li** shown in Figure3.4.*

h	s (nm^{-1})	[a]s × d_l	I (rel. percent)
1	1.9492 ± 0.0023	0.999 ± 0.007	95.6 ± 1.3
2	3.9260 ± 0.0021	2.012 ± 0.007	100
3	4.8538 ± 0.0045	3.000 ± 0.007	8.72 ± 0.20
4	7.7936 ± 0.0031	3.994 ± 0.007	22.42 ± 0.34
6	11.707 ± 0.019	6.000 ± 0.007	1.15 ± 0.07

[a]*d_l = 51.25 ± 0.26 nm as determined from linear regression of s versus h.*

3.3.1.2 Copolymer 2

In contrast to copolymer **1**, scattering from copolymer **2** (Figure 3.5, Table 3.7) could not be indexed to a single repeat spacing. However, all peaks could be indexed to a rectangular lattice with peak positions of,

$$s_{hk} = \sqrt{\frac{h^2}{d_l^2} + \frac{k^2}{d_c^2}} \tag{3-9}$$

where d_l and d_c and the height and width of the unit cell. The "non-lamellar" {1,1}, {3,1} and {5,1} peaks in Figure 3.5 are quite clear and their positions match the rectangular lattice. However, the peak intensities in Table 3.7 are not a true powder average because the intensity of diffraction rings varied around each ring.

Further information about the structure of copolymer **2** was obtained by preparing oriented specimens. Block copolymer structures can be aligned via electric fields (Morkved et. al., 1996; Boker, et. al. 2002), shearing (Keller, et. al. 1970; Kannan and Kornfield, 1994; Stangler and Abetz, 2003) and solvent-casting (Coulon, et. al. 1989; Fukunaga, K. et. al. 2000). Following solvent casting, copolymer **2** exhibited considerable fiber-type alignment (Finkenstadt and Millane, 1998). 2-D SAXS from a film cast in a Teflon well is shown in Figure 3.6.

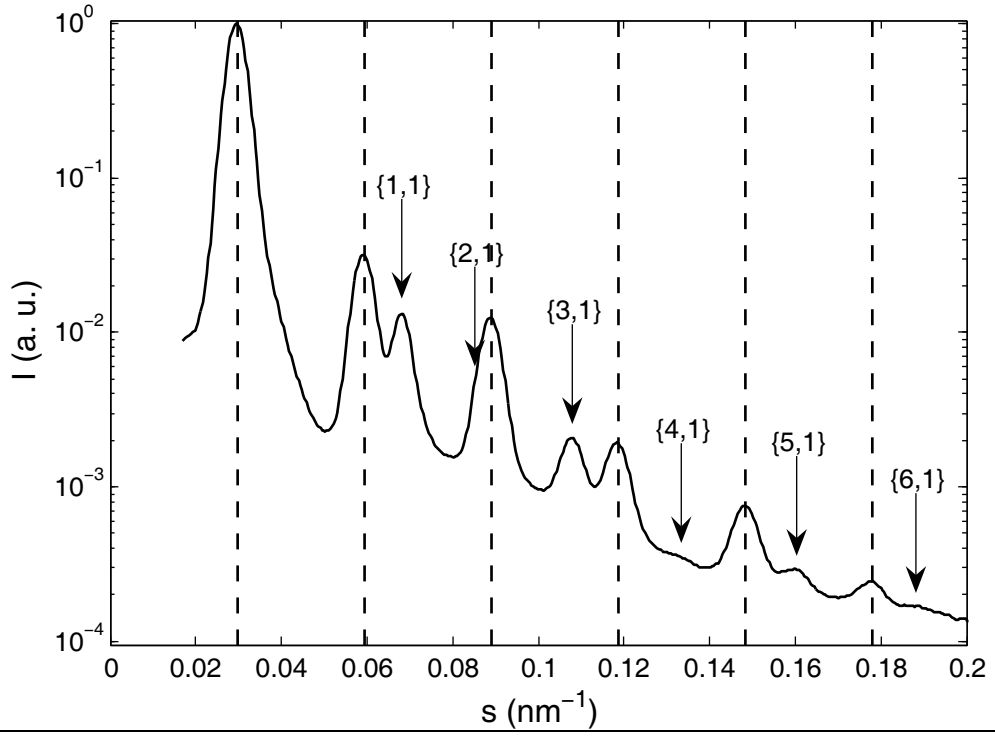

Figure 3.5 – Plot of I versus s for Copolymer **2** *at 75 °C following integration of forty exposures (900 seconds). The observed Bragg peaks can be indexed to a rectangular unit cell (d_l = 33.76 ± 0.17 nm, d_c=16.393 ± 0.082 nm). The predicted positions for {h,0} reflections are indicated by black, dashed vertical lines while the {h,1} (h≠0) reflections are marked with vertical arrows.*

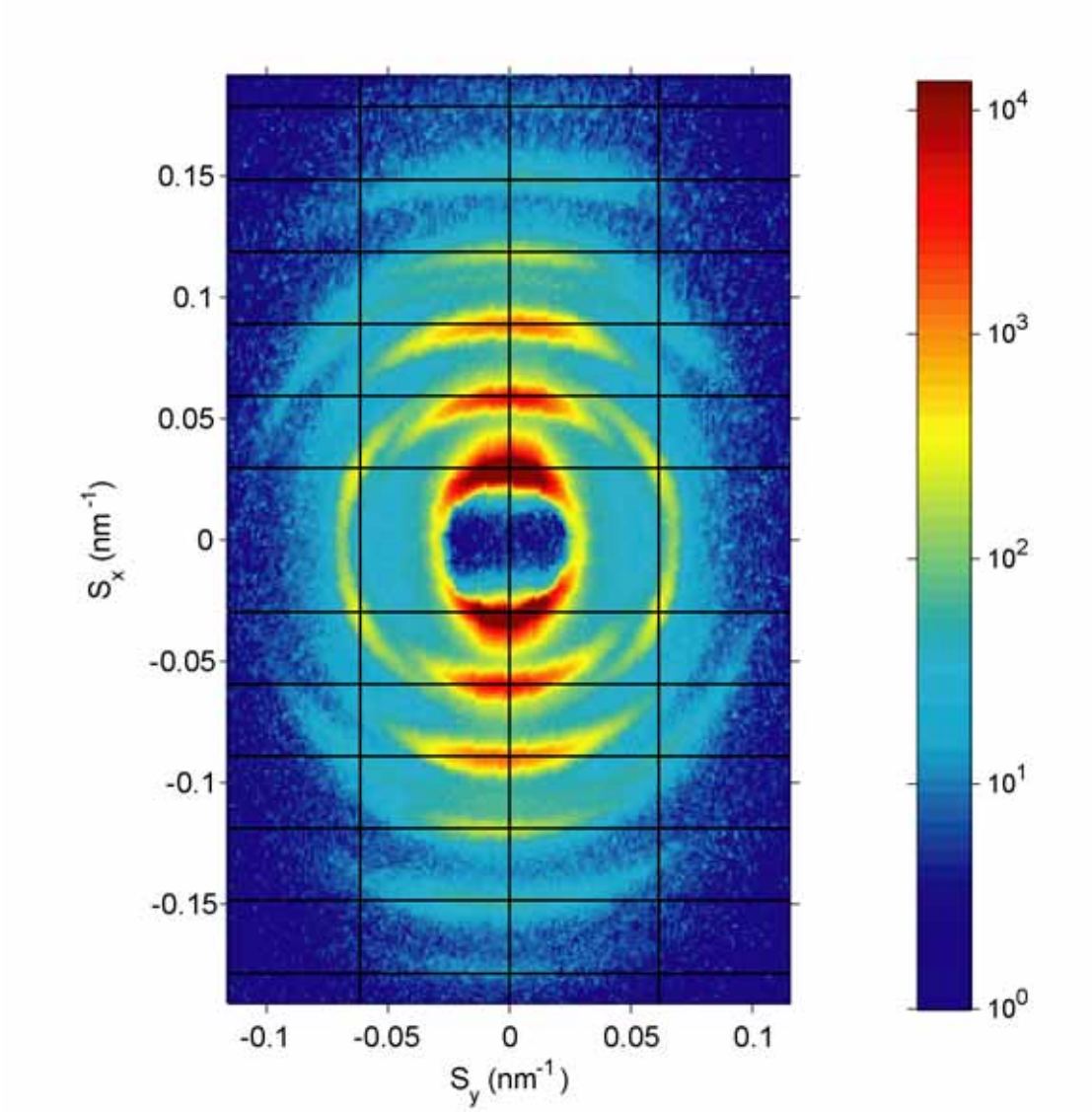

*Figure 3.6 – 2-D SAXS from an aligned sample of copolymer **2** at 75°C (logarithmic scale; 36 exposures each of 100 seconds duration). The surface normal was directed along the vertical axis. The (h,0) reflections are located on the vertical axis ($s_x = h/d_l$, $s_y = 0$ nm^{-1}) as indicated by the black horizontal layer lines. The (h,±1) reflections also sit on the layer lines but are shifted out onto the vertical row lines ($s_x = h/d_l$, $s_y = \pm 1/d_c$) for a rectangular unit cell of $d_l = 33.76 \pm 0.17$nm $\times d_c = 16.393 \pm 0.082$nm..*

*Table 3.7 - Peak Parameters of Scattering from copolymer **2** shown in Figure 3.5.*

{h,k}	[a] s_{cen} ($\times 10^{-2}$ nm^{-1})	[a] I (relative)	[b] $s_{cen} \times d_l$	$\sqrt{h^2 + k^2\left(\frac{d_l}{d_c}\right)^2}$
{1,0}	2.942 ± 0.003	100	0.993 ± 0.010	1
{2,0}	5.949 ± 0.004	13.04 ± 0.32	2.001 ± 0.010	2
{1,1}	6.833 ± 0.005	7.07 ± 0.19	2.307 ± 0.010	2.289
{3,0}	8.875 ± 0.004	13.87 ± 0.30	2.996 ± 0.010	3
{3,1}	10.768 ± 0.007	2.81 ± 0.09	3.635 ± 0.010	3.639
{4,0}	11.829 ± 0.007	3.20 ± 0.10	3.993 ± 0.010	4
{5,0}	14.835 ± 0.009	1.62 ± 0.07	5.008 ± 0.010	5
{5,1}	15.977 ± 0.054	0.18 ± 0.03	5.394 ± 0.010	5.408
{6,0}	17.797 ± 0.035	0.27 ± 0.03	6.008 ± 0.010	6
{6,1}	19.01 ± 0.22	0.040 ± 0.024	6.420 ± 0.010	6.344

[a] Uncertainties for s_{cen} and I from non-linear least squares fit of peak positions. Peak width parameters were $\sigma_{L0} = (8.40 \pm 0.37) \times 10^{-4}$ nm^{-1}, $\sigma_{L1} = (6.2 \pm 1.3) \times 10^{-3}$, $\sigma_{G0} = (1.887 \pm 0.033) \times 10^{-3}$ nm^{-1} and $\sigma_{G1} = (1.8 \pm 6.3) \times 10^{-3}$.
[b] Rectangular unit cell size is $d_l = 33.76 \pm 0.17$ nm by $d_c = 16.393 \pm 0.082$ nm from a weighted least-squares fit of s_{cen}^2 versus $(h/d_l)^2 + (k/d_c)^2$.

The {*h*,0} reflections were aligned with the surface normal of the sample and rotation of the sample about this axis left the diffraction pattern unchanged. This fibre-type alignment was fairly strong with a width of FWHM=15°. The four sharp peaks off the vertical axis ($s_x \approx \pm 0.06$ nm^{-1}, $s_y \approx \pm 0.03$ nm^{-1}) are at the expected positions for the {1,1} reflections of a rectangular lattice, while the arcs extending from ($s_x \approx$ -0.06 nm^{-1}, $s_y \approx \pm 0.09$ nm^{-1}) to ($s_x \approx 0.06$ nm^{-1}, $s_y \approx \pm 0.09$ nm^{-1}) are consistent with the {3,1} reflections. To improve the estimates of Bragg reflection intensities, the 2-D SAXS pattern shown in Figure 3.6 was fiber averaged using the form,

$$I(s) = \int_{\phi=0}^{\phi=2\pi} I(s,\phi) \times \frac{|\sin\phi| d\phi}{4} \qquad (3\text{-}10)$$

where $I(s,\phi)$ is the intensity of scattering at a radius s and angle ϕ from the vertical (y-axis). The average scattering intensity, $I(s)$, was then fitted to Equation 3-4 and the results are summarized in Table 3.8. No scattering was apparent for either the {0, 1} or the {h,±2} reflections.

*Table 3.8 - Integrated Intensity of Bragg Peaks from Copolymer **2** from Oriented SAXS data shown in Figure 3.6.*

{h,k}	**Intensity (relative)**
{1,0}	100
{2,0}	16.80 ± 0.35
{1,1}	15.04 ± 0.31
{3,0}	15.64 ± 0.29
{3,1}	4.56 ± 0.13
{4,0}	3.74 ± 0.11
{5,0}	1.10 ± 0.08
{5,1}	0.18 ± 0.06

SAXS from copolymer **2** showed an interesting dependence on temperature as illustrated in Figures 3.7 and 3.8. When the copolymer was heated, the {h,1} reflections abruptly disappeared between T=120°C and T=121°C but the {h,0} reflections remained right up to T = 200°C. Upon cooling of the copolymer, the {h,1} reflections reappeared at a similar temperature of $T \approx 120.3 \pm 0.4$°C.

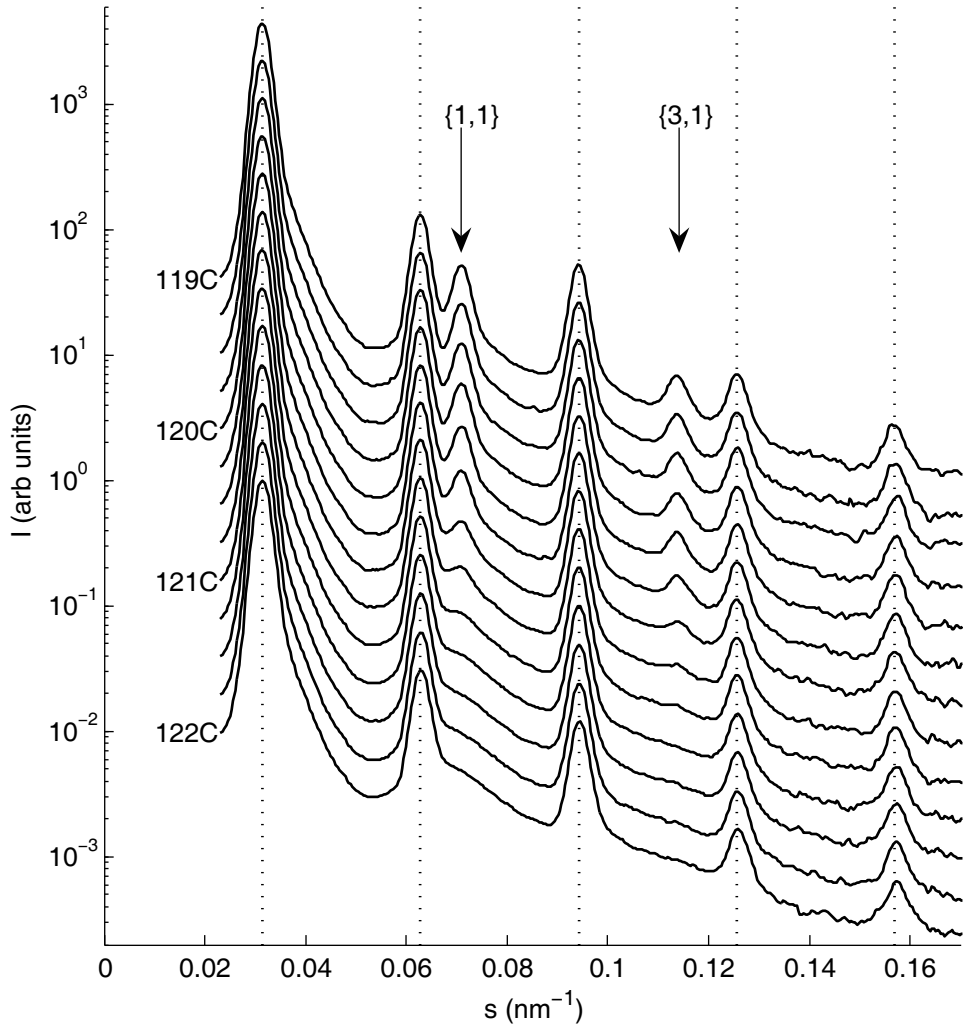

*Figure 3.7 – Temperature dependence of SAXS from Copolymer **2**. SAXS data was gathered as the sample was slowly cooled from 122°C to 119°C (0.25°C steps each lasting 30 minutes). For clarity, successive plots of I versus s are offset by factors of 2. {h,0} reflections are indicated by vertical dotted lines (d_1 = 31.86 ± 0.16nm) while arrows mark the {1,1} and {3,1} reflections (d_c = 15.73 ± 0.10 nm) that appear below T=120.3 ± 0.4°C.*

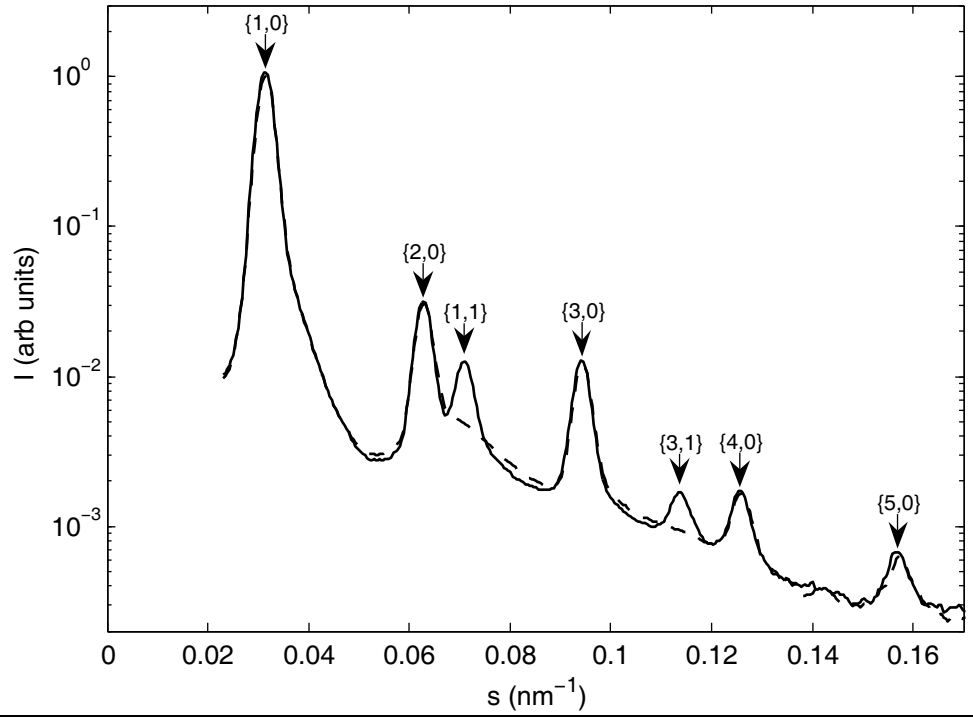

*Figure 3.8 – Scattering from Copolymer **2** above (dashed; T=122ºC) and below (solid; T=119ºC) the order-order transition. Black dotted vertical lines denote lamellar repeats (d_l = 31.86 ± 0.16nm) while {1,1} and {3,1} reflections are marked with arrows (d_c = 15.73 ± 0.10 nm).*

Closer examination of SAXS from copolymer **2** above and below the transition (Figure 3.8) reveals two striking features. Firstly, the {*h*,0} reflections are essentially unchanged by the phase transition. This implies that the transition does not effect structure along the [1,0] direction despite a significant change in order along the [0,1] direction. Secondly, the sharp {1,1} reflections below the transition are replaced by a broad scattering feature above the transition ($s \approx 0.07\text{nm}^{-1}$), suggesting the presence of non-crystalline order above the transition temperature.

Below the crystallization temperature of the PEO block, copolymer **2** showed considerable meta-stability in comparison to copolymer **1**. The eventual crystallization of PEO domains caused a discontinuous increase in lattice size and

broadened both the angular and radial width of the scattering to the extent that only the{1,0} and {2,0} reflections could be resolved.

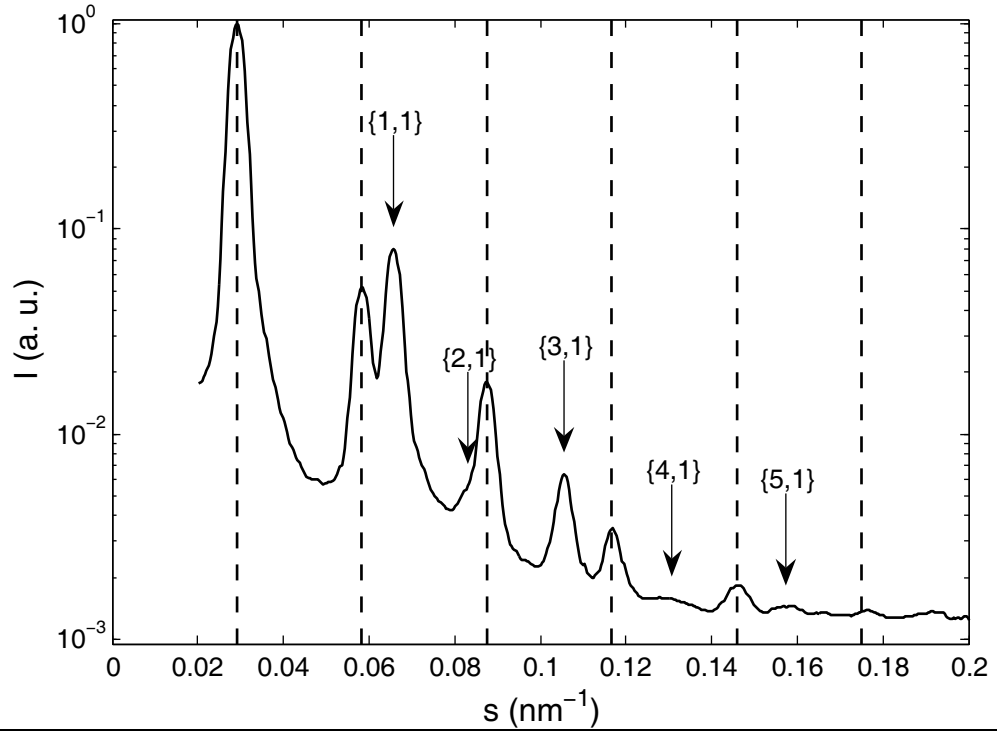

Figure 3.9 – Plot of I versus s for Copolymer **2-Li** *at 70 °C following integration of two exposures (600 seconds). Bragg peaks index to a rectangular unit cell (d_l = 34.27 ± 0.26 nm, d_c=16.951 ± 0.085 nm). {h,0} reflections are indicated by black, dotted vertical lines while arrows mark the {h,1} (h≠0) reflections.*

SAXS from compound **2-Li** (Figure 3.9 and Table 3.9) was quite similar to that from copolymer **2**, and the observed diffraction peaks could again be indexed to a rectangular lattice. The {1,1} and {3,1} reflections appear to be stronger for the compound **2-Li** structure, although this might be biased by grain orientation within the sample. Another interesting feature is the shoulder (s = 0.083 nm^{-1}) on the side of the {3,0} peak which corresponds to the expected location of the {2,1} reflections.

*Table 3.9 - Scattering Peak Parameters from copolymer **2-Li** (Figure 3.9).*

{h,k}	[a] s_{cen} ($\times 10^{-2}$ nm^{-1})	[a] I (relative)	[b] $s_{cen} \times d_l$	$\sqrt{h^2 + k^2\left(\frac{d_l}{d_c}\right)^2}$
{1,0}	2.932 ± 0.002	100	1.005 ± 0.008	1
{2,0}	5.841 ± 0.004	20.32 ± 0.62	2.002 ± 0.008	2
{1,1}	6.584 ± 0.003	47.2 ± 1.2	2.256 ± 0.008	2.2554
{3,0}	8.730 ± 0.004	17.85 ± 0.52	2.992 ± 0.008	3
{3,1}	10.549 ± 0.008	6.91 ± 0.28	3.615 ± 0.008	3.6176
{4,0}	11.694 ± 0.013	3.33 ± 0.21	4.007 ± 0.008	4
{5,0}	14.627 ± 0.039	1.40 ± 0.19	5.012 ± 0.008	5

[a] *Uncertainties for s_{cen} and I from non-linear least squares fit of peak positions.*
[b] *Rectangular unit cell size of $d_l = 34.27 \pm 0.26$nm by $d_c = 16.951 \pm 0.085$nm.*

The temperature dependence of SAXS from compound **2-Li** is shown in Figure 3.10. Previous studies have shown that the addition of lithium triflate to PEO domains can increase block-block mixing enthalpies (Ruzette, et. al. 2001), and unlike copolymer **2**, in SAXS from compound **2-Li** the {1,1} and {3,1} reflections remained quite strong up to a temperature of 150°C. However, a change in scattering was observed between 150°C and 170°C that showed similarities to the transition in copolymer **2**. Although the {h,0} peaks did not change significantly, at 170°C the {3,1} and {1,1} reflections both disappeared, additional scattering was present on both sides of the {2,0} reflection and the hint of a shoulder appeared on right of the {1,0} reflection. These changes reversed when the sample was cooled, suggesting they were not caused by thermal decomposition of the copolymer.

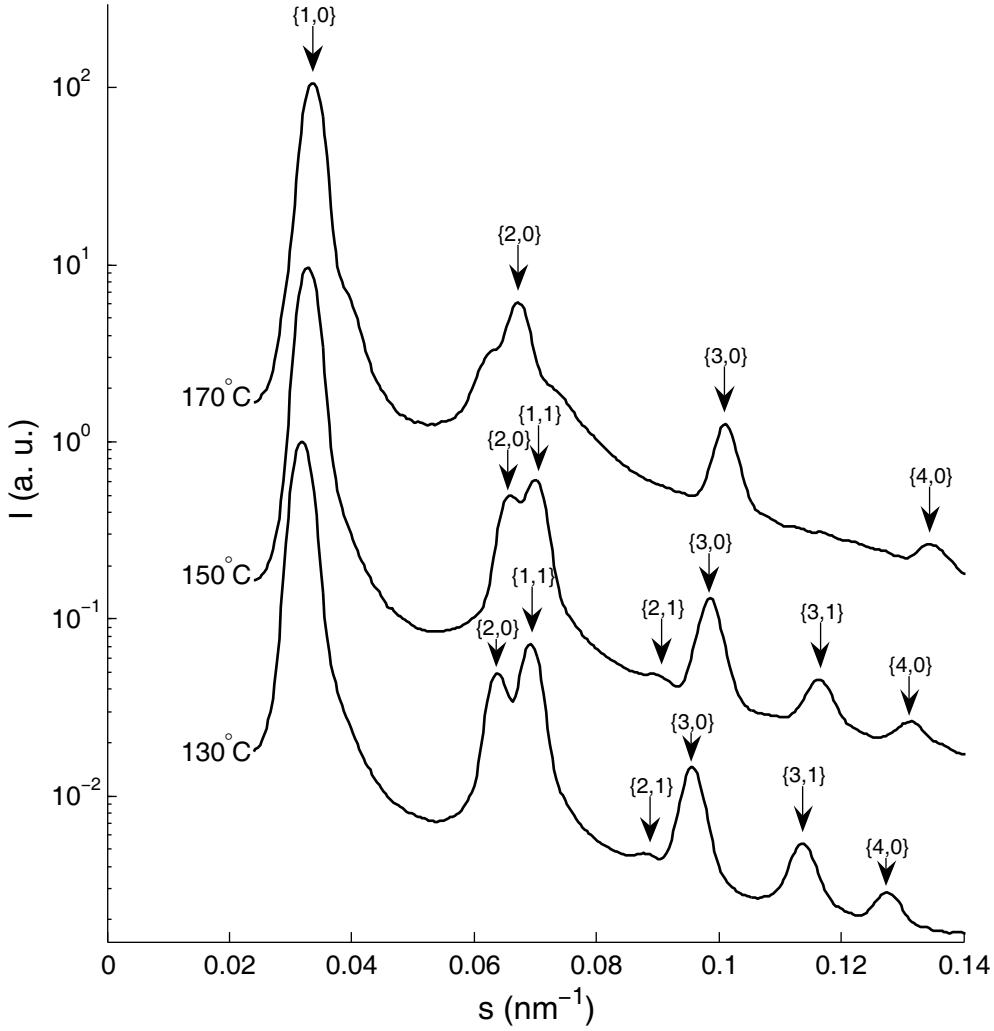

*Figure 3.10 – Temperature Dependence of SAXS from compound **2-Li**. Plots of I versus s are shown for 130ºC, 150ºC and 170ºC (offset by factors of 10). The {h, 0} reflections are largely unchanged on heating, but at 170ºC the {3,1} and {1,1} reflections cannot be resolved.*

3.3.1.3 Copolymer 3

SAXS from copolymer **3** at 75ºC is summarized in Figure 3.11 and Table 3.10.

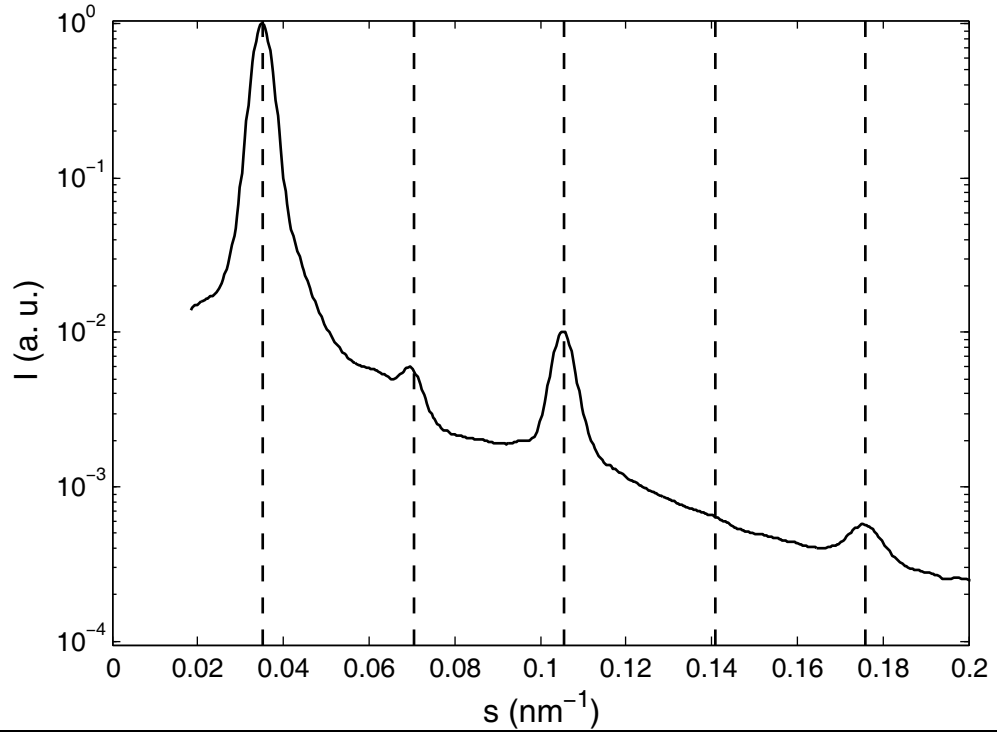

Figure 3.11 – Plot of I versus s for Copolymer 3 at 75 ℃ following integration of four exposures (300 seconds). Dashed vertical lines mark peak positions for a lamellar structure with repeat spacing of dl = 28.44 ± 0.14 nm.

The observed Bragg peaks could be described using a single index, although the fit to the scattering profile was poor in the vicinity of the *h*=2 peak (s = 0.07nm^{-1}). Scattering from an oriented sample of copolymer 3 shown in Figure 3.12 revealed the un-oriented scattering around s = 0.06nm^{-1} that gave rise to the strange shape of the *h*=2 peak shown in Figure 3.11. As shown in Figure 3.12 annealing the copolymer sharpened the Bragg peaks sufficiently so as to separate them from this scattering feature. A similar broad scattering feature was present in SAXS from compound **3-Li**

(Figure 3.13, Table 3.11), although the center of the scattering bump was closer to s=0.08nm^{-1}. The position and shape of this scattering varied both as a function of temperature and lithium triflate concentration. Although this scattering definitely originates from within the copolymer, it is difficult to attribute it to a single source owing to its broad and rather non-descript character. For instance, an impurity such as an un-polymerized AB diblock intermediate might form give rise to such scattering, although no impurities were evident in Gel Permeation Chromatography. As will be shown in the following section, though, this broad scattering feature could also result from correlations between disordered domains within the copolymer structure.

*Table 3.10 - Peak Parameters of Scattering from copolymer **3** shown in Figure 3.11.*

h	s_{cen} ($\times 10^{-2}$ nm^{-1}) [a]	$s_{cen} \times d_l$ [b]	I (percent)[b]
1	3.5089 ± 0.0020	0.9979 ± 0.0029	100
2	6.9170 ± 0.010	1.967 ± 0.003	1.21 ± 0.05
3	10.5393 ± 0.0036	2.997 ± 0.003	10.22 ± 0.18
5	17.589 ± 0.015	5.002 ± 0.003	1.10 ± 0.04

[a] *Uncertainties for s_{cen} and I are from non-linear least squares fit of peak positions. Peak width parameters were σ_{L0} =(8.19 ± 0.98)×10^{-4} nm^{-1}, σ_{L1} = (1.14 ± 0.35)×10^{-2}, σ_{G0} =(1.22 ± 0.10)×10^{-3} nm^{-1} and σ_{G1} = (6.9 ± 5.9)×10^{-3}.*

[b] *Uncertainties for $s_{cen} \times d_l$ are for a least-squares fit of plot of s_{cen} versus h. The lamellar repeat spacing is d_l =28.44 ± 0.14 nm.*

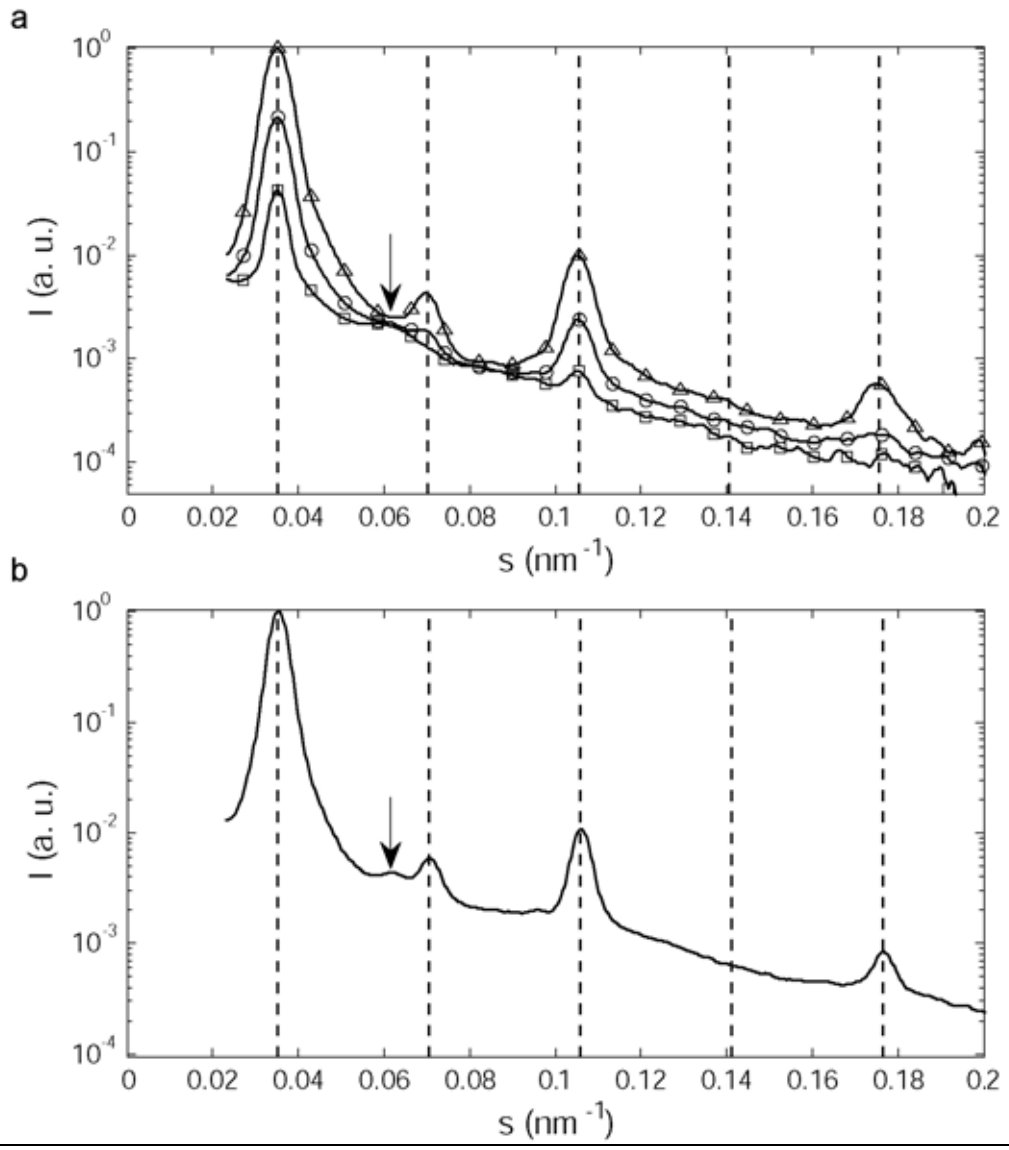

*Figure 3.12 – Scattering between Bragg Peaks from copolymer **3** (T=75°C). The non-unoriented scattering between the first and second peaks is marked in both plots with an arrow. The upper plot (a) shows scattering from an oriented sample at 0 ± 7.5° (Δ), 45 ± 7.5° (o), and 90 ± 7.5° ( ) relative to the lamellar director. The lower plot (b) shows scattering from a powder sample after annealing has sharpened the lamellar peaks.*

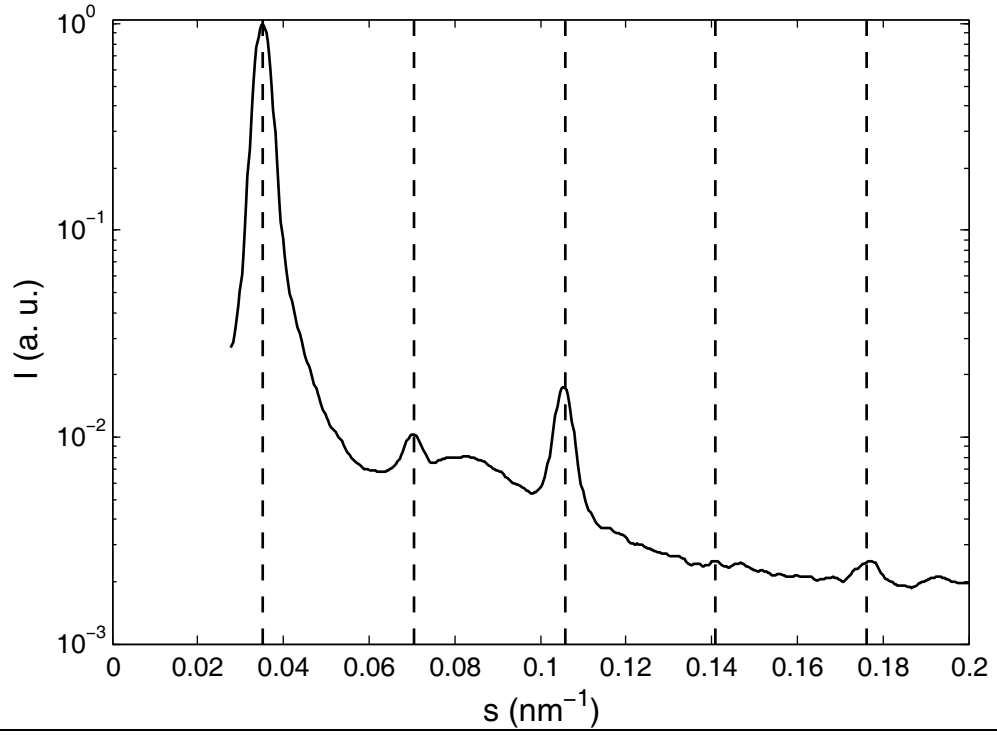

*Figure 3.13 – Plot of I versus s for copolymer **3-Li** at 60ºC following integration of two exposures (600 seconds). Dashed lines mark peak positions for a lamellar structure with a repeat spacing of d_l = 28.38 ± 0.18nm. Note the broad hump around s = 0.08 ± 0.01 nm^{-1}.*

*Table 3.11 - Peak Parameters for copolymer **3-Li** SAXS shown in Figure 3.13.*

h	s_{cen} (× 10^{-2} nm^{-1}) [a]	$s_{cen} \times d_l$ [b]	I (relative percent) [b]
1	3.5188 ± 0.0044	0.999 ± 0.016	100
2	7.113 ± 0.025	2.019 ± 0.016	2.00 ± 0.21
3	10.527 ± 0.010	2.988 ± 0.016	15.07 ± 0.87
5	17.692 ± 0.070	5.021 ± 0.016	2.24 ± 0.44

[a] *Uncertainties for s_{cen} and I are from non-linear least squares fit of peak positions.*
[b] *Uncertainties for $s_{cen} \times d_l$ are for a least-squares fit of plot of s_{cen} versus h. The lamellar repeat spacing is d_l =28.38 ± 0.18nm.*

3.3.2 Structure Factor Models

SAXS from copolymers **1**, **2** and **3** were compared to simplified structural models of the triple-lamellae, rods-at-lamellae and balls-at-lamellae structures.

3.3.2.1 Triple-Lamellae

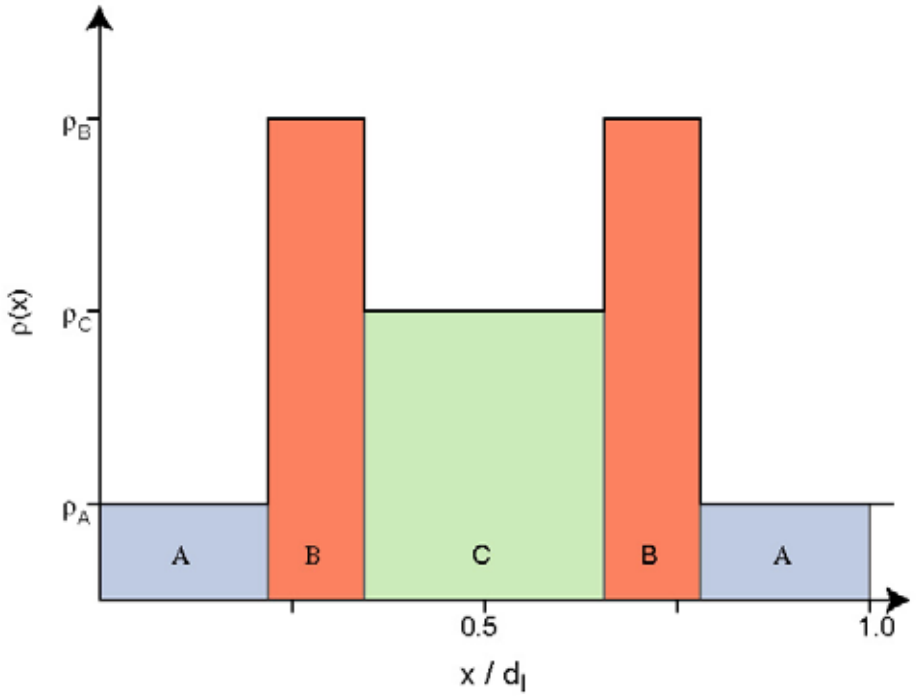

Figure 3.14 - Density profile of the slab model of ABCBA Triple-Lamellae.

The ABCBA triple-lamellae structure can be approximated by a series of slabs of constant density, as illustrated in Figure3.14 (Epps et. al., 2004). For a unit cell of period d_l, these slabs can be parameterized as indicated in Table 3.12, where $\rho_{A/B/C}$ is the density of block A/B/C, f_A the volume fraction of block A, $w_j \times d_l$ the width of the j-th slab and $x_j \times d_l$ the position of the center of the slab.

Table 3.12 – Parameters for slab model of the ABCBA Triple-Lamellae Structure

Slab Number - j	Density - ρ_j	Relative Width - w_j	Mid-Point - x_j
1	ρ_A	$f_A/2$	$f_A / 4$
2	ρ_B	$f_B/2$	$f_A/2 + f_B/4$
3	ρ_C	f_C	1/ 2
4	ρ_B	$f_B/2$	$1 - f_A/2 - f_B/4$
5	ρ_A	$f_A/2$	$1-f_A/4$

*For Copolymer **1** the block volume fractions were $f_A = 0.34$, $f_B = 0.25$ and $f_C = 0.41$ while block densities were approximated with the homopolymer densities $\rho_A = 0.86$ g/cm^3, $\rho_B = 1.13$ g/cm^3 and $\rho_C = 1.01$ g/cm^3 (Table 3.1).*

The Fourier coefficients of the structure are then,

$$F_h^{TL} = \int_{x=0}^{x=d_l} \rho(x)\exp\left(\frac{-i2\pi hx}{d_l}\right)\frac{dx}{d_l} \tag{3-11}$$

$$= \sum_{j=1}^{N} \rho_j w_j \mathrm{sinc}(\pi h w_j)\exp(-i2\pi h x_j)$$

$$= (\rho_A - \rho_B)\times f_A \times \mathrm{sinc}(\pi h f_A) + (-1)^h \times (\rho_C - \rho_B)\times f_C \times \mathrm{sinc}(\pi h f_C)$$

Alternatively, the middle and an end block may mix to form a single lamellar domain in a "double-lamellae" structure. The Fourier coefficients for this "double-lamellae" structure are simply,

$$F_h^{DL} = (\rho_1 - \rho_2)\times f_1 \times \mathrm{sinc}(\pi h f_1) \tag{3-12}$$

Using equations 3-11 and 3-12, structure factors were calculated for triple-lamellae and double-lamellae structures for the block volume fractions of copolymer **1**. Results for room temperature densities and volume fractions are presented in Table 3.13 as these were similar to those at 75ºC. Broadly speaking, the peak intensities from

copolymers **1** and **1-Li** are a better match to the triple-lamellae structure than the double-lamellae structure.

*Table 3.13 - Experimental Structure Factors for compounds **1** and **1-Li** and corresponding Triple-Lamellae and Double-Lamellae structures.*

h	[a]$I_{Copolymer\ 1}$	[b]$I_{Compound\ 1\text{-}Li}$	[c]I_{TL}	[d]I_{DL}
1	100	95.6 ± 1.3	68.0 (-)	100 (-)
2	73.9 ± 1.3	100	100 (-)	23.2 (-)
3	6.48 ± 0.16	8.72 ± 0.20	2.1 (-)	0.06 (+)
4	16.32 ± 0.36	22.42 ± 0.34	36.5 (+)	6.7 (+)
5	-	-	10.5 (+)	3.4 (+)
6	1.163 ± 0.047	1.15 ± 0.07	3.1 (-)	0.06 (-)
7	1.414 ± 0.051	-	3.9 (-)	2.30 (-)
8	0.247 ± 0.032	-	0.96 (-)	1.21 (-)
9	0.856 ± 0.043	-	0.14 (-)	0.06 (+)
10	-	-	2.25 (-)	1.2 (+)

[a]*Experimental Intensities for Copolymer **1** from Table 3.5.*
[b]*Experimental Intensities for Copolymer **1-Li** from Table 3.6.*
[c]*Triple-Lamellae Intensities for block densities at 25 ℃ (Table 3.1) and block volume fractions of copolymer **1** (Table 3.3). Fourier coefficient sign given in parentheses.*
[d]*Double-Lamellae Intensities assuming B+C blocks of copolymer **1** mix ideally to form a single domain with uniform density.*

Further support for this conclusion can be obtained by computing density profiles that combine the experimental scattering amplitudes with phases from the structural models. In general, the calculated electron density profile depends strongly on the phases that are used. However, the phases of the triple-lamellae and double-lamellae models only differ for the $h = 3$ and $h = 9$ Fourier coefficients. Furthermore,

for both models the $h = 3$ and $h = 9$ Fourier coefficients are small. Consequently, the choice of phases has a much smaller effect for this case. Figure 3.15 illustrates the density profiles for copolymers **1** and **1-Li** calculated with the phases from the double-lamellae model. The use of these phases should bias the reconstructed density profiles towards the double-lamellae model, yet both profiles show the three distinct density levels of the triple-lamellae model. Similar results are obtained using the phases for the triple-lamellae model. Thus, SAXS from copolymers **1** and **1-Li** is consistent with a triple-lamellae structure.

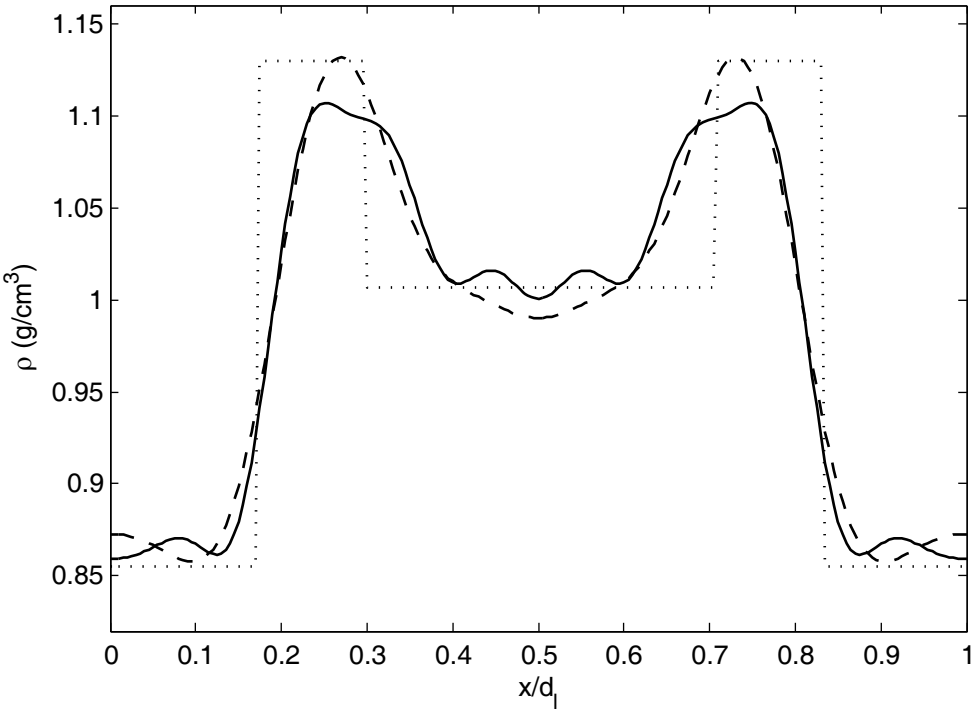

*Figure 3.15 - Density Profiles for copolymer **1** (solid), compound **1-Li** (dashed) and the slab-model of ABCBA triple-lamellae (dotted). Densities constructed using phases from double-lamellae structure and experimental structure factors scaled to the density profile of the triple-lamellae slab model (Table 3.13).*

3.3.2.2 Rods-at-Lamellae

The cylinder-at-lamellae structure has two AC interfaces per unit cell with a row of rods at each of these interfaces. As shown in Figure 3.16, the rods in these two rows can be "aligned" or "staggered". In both structures polymer chains stretch out from each cylinder of B to fill the surrounding A and C lamellae. The Voronoi cell of each cylinder bounds the region of space closest to it and the shape of the cell depends upon the position of rods in the adjacent layers. Consequently, the position of rods in adjacent layers has a small but significant effect on the energy of the copolymer structure, and the more rounded hexagonal Voronoi cell of the "staggered" packing should be favored over the rectangular Voronoi cell of the "opposed" packing.

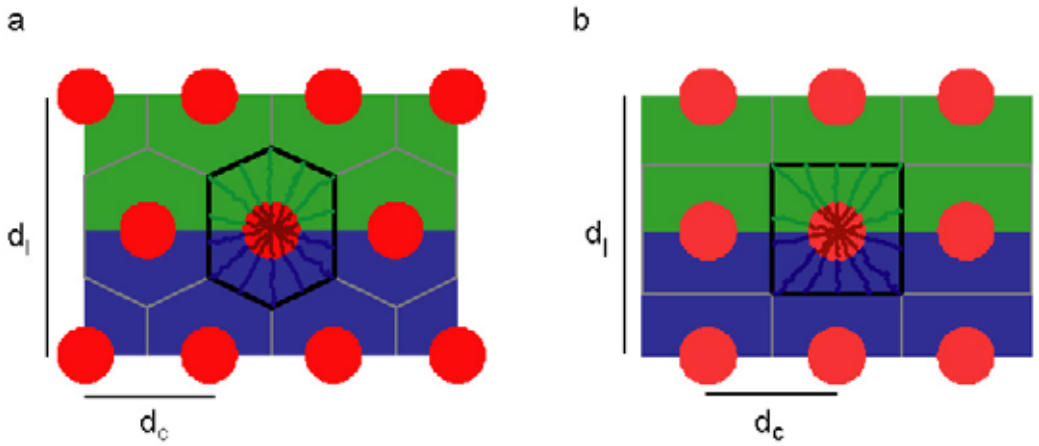

*Figure 3.16 - End-on view of rods-at-lamellae structures with "staggered" (**a**) and "opposed" (**b**) rod stacking. Polymer chains stretch out from each rod to fill the bounding Voronoi polyhedron (gray and black lines). The "opposed" stacking (P2mm, Space Group No. 6 IUCr) has a rectangular Voronoi cell while the "staggered" packing (P2mg, Space Group No. 7 IUCr) has a more rounded Voronoi hexagon.*

Experimentally, the position of rods within the unit cell is directly linked to the intensity of the {0,1} reflections. In the "opposed" stacking, the two rods have the same horizontal position, scattering from the two is in phase and the {0,1} reflections

are permitted and likely to be strong. For the "staggered" stacking the two rods are displaced horizontally by half a unit cell ($d_c/2$) and so scattering from them destructively interferes and the {0,1} reflections are forbidden. Assuming copolymer **2** has a rods-at-lamellae structure, the absence of {0,1} reflections strongly suggests the rods have adopted the "staggered" stacking. Quantitative predictions of the relative intensity of other structure factors require a model for the electron density.

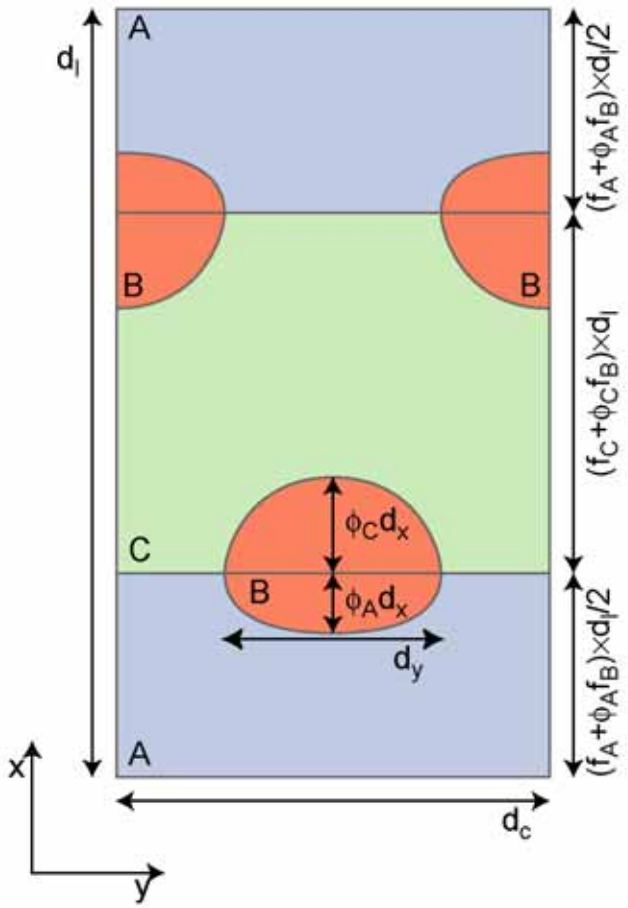

Figure 3.17 - Model of the unit cell of the rods-at-lamellae structure with "staggered" packing. The B domains are treated as two half-ellipses with semi-minor axes of $\phi_A d_x$ and $\phi_C d_x$ respectively.

Figure 3.17 shows a simple model in which the density within each of the three domains is a constant and the AB and BC interfacial profiles are approximated by half-ellipses for ease of calculation. The width and height of the ellipses are related to the volume fraction of B by,

$$\frac{\pi}{4}\times d_x \times d_y = f_B \times \frac{d_l}{2}\times d_c \tag{3-13}$$

For convenience, the density can be divided into two parts -

a) Lamellar slabs with the width and density of the A and C domains

b) Four half-ellipses with densities of ρ_B-ρ_A or ρ_B-ρ_C depending on the slab lying under the half-ellipse.

The Fourier coefficients for the structure are then,

$$\begin{aligned} F_{hk}^{rods} &= \delta_{k0}\times(\rho_A-\rho_C)\times(f_A+\phi_A f_B)\times \mathrm{sinc}(\pi(f_A+\phi_A f_B)h) \\ &+ \exp(-i\pi(h(f_A+\phi_A f_B)+2ky_1))A_{cyl}\left(\frac{h}{d_l},\frac{k}{d_c}\right) \\ &+ \exp(i\pi h(f_A+\phi_A f_B))A_{cyl}\left(\frac{-h}{d_l},\frac{k}{d_c}\right) \end{aligned} \tag{3-14}$$

where y_1 is the relative offset between the first and second rods along the y-axis (y_1=0 for "opposed" and y_1=1/2 for "staggered") and $A_{\mathrm{cyl}}(s_x, s_y)$ is the Fourier transform of the lower cylinder given by,

$$\begin{aligned} A_{cyl}(s_x,s_y) &= \frac{\phi_A f_B}{2}\times(\rho_B-\rho_A)\times\phi_{cyl}(-\phi_A s_x d_x, s_y d_y) \\ &+ \frac{\phi_C f_B}{2}\times(\rho_B-\rho_C)\times\phi_{cyl}(\phi_C s_x d_x, s_y d_y) \end{aligned} \tag{3-15}$$

where $\phi_{\mathrm{cyl}}(x,y)$ is the Fourier transform for a half-cylinder defined as,

$$\phi_{cyl}(x,y) = \int_{\theta=0}^{\theta=\frac{\pi}{2}} \exp(-i2\pi x\cos\theta)\mathrm{sinc}(\pi y\sin\theta)\frac{4\sin^2\theta d\theta}{\pi} \tag{3-16}$$

Using Equation 3-14, structure factors for the cylinder-at-lamellae model were calculated for block volume fractions of copolymer **2** and the results are reported in Table 3.14.

Table 3.14 - Structure factors for Copolymer 2 and "staggered" and "opposed" models of the rods-at-lamellae structure.

{h,k}	[a] I_{exp}	[b,c] $I_{opposed}$	[b,c] $I_{staggered}$	[b,d] $I_{staggered\ II}$
{1,0}	100	100	100	100
{2,0}	16.8 ± 0.35	21.8	21.8	22.44
{0,1}	-	24.8	0	0
{1,1}	7.52 ± 0.16	0.11	22.1	11.2
{2,1}	-	15.3	0.42	0.09
{3,0}	15.64 ± 0.29	5.6	5.6	12.4
{3,1}	2.28 ± 0.07	0.8	7.8	4.9
{4,0}	3.74 ± 0.11	3.5	3.5	8.5
{0,2}	-	3.6	3.6	0.4
{4,1}	-	2.5	1.1	0.0
{2,2}	-	1.7	1.7	0.13
{5,0}	1.10 ± 0.08	0.44	0.44	2.1
{5,1}	0.09 ± 0.03	1.2	0.27	0.7

[a] *Experimental values taken from aligned SAXS pattern of copolymer **2** described in Figure 3.6 / Table 3.8. Note the intensity of {h,1} reflections has been divided by 2 to account for their multiplicity.*
[b] *Calculations used homopolymer densities at 25°C (Table 3.1), block volume fractions for copolymer **2** (Table 3.3) and unit cell dimensions from Table 3.7.*
[c] *B-domains assumed to have a circular profile centered on AC interface ($d_x=d_y=7.25$nm, $\phi_A=\phi_C=0.5$).*
[d] *Calculation for B-domains displaced into C domain ($\phi_A=0.3$, $\phi_C=0.7$) with flattened aspect ratio ($d_x= 6.1$nm, $d_y=8.7$nm, $d_x/d_y = 0.7$).*

As expected, there is a considerable difference in structure factors for "opposed" and "staggered" packings. For the "opposed" stacking the {0,1}, {2,1} and {0,2} reflections are all be strong while the {1,1} and {3,1} reflections are quite weak. In contrast, the "staggered" stacking has strong {1,1} and {3,1} reflections which agrees well with the data for copolymer **2**. Furthermore, the B domains are expected to be flattened ($d_x<d_y$) and also displaced into the C-lamellae ($\phi_C>\phi_A$). These modifications further improve the correspondence with the experimental results. Thus, SAXS from copolymer **2** is consistent with a rods-at-lamellae model.

In addition to periodic arrangements, rods in the rods-at-lamellae morphology can have liquid-like order. Because the B-domains are confined to the AC interfaces, the in-plane position of B-domains does not affect the density profile along the lamellar axis a disordered "cylinder-at-lamellae" structure could still possess sharp Bragg reflections corresponding to the lamellar periodicity. In contrast, liquid-like ordering of the rods would destroy the {h,1} reflections. The SAXS from such a disordered "cylinder-at-lamellae" structure can be predicted with the following model. To compare scattering from periodic and disordered structures, it is helpful to define a normalized scattering intensity per unit volume,

$$I(\boldsymbol{s}) = \frac{1}{V_{\text{sample}}}\left|\int_{V_{\text{sample}}} \rho_e(\boldsymbol{x})\exp(-i2\pi \boldsymbol{s}\bullet\boldsymbol{x})d^3\boldsymbol{x}\right|^2 \tag{3-17}$$

where $\rho(\boldsymbol{x})$ the density and point $\boldsymbol{x}$ in a sample of volume, V_{sample}. For a periodic structure this is related to the lattice Fourier coefficients by,

$$I(\mathbf{s}) = \sum_{h,k}\left|F_{h,k}^{cell}\right|^2 \delta\left(V_{sample}^{1/3}\left(s_x - h/d_l\right)\right)\delta\left(V_{sample}^{1/3}\left(s_y - k/d_c\right)\right)\delta\left(V_{sample}^{1/3}s_z\right)V_{sample}^{1/3} \tag{3-18}$$

so the powder average is,

$$I(s) = \sum_{h,k} \left| F_{h,k}^{cell} \right|^2 \times \delta\left(V_{sample}^{1/3} (s - s_{hk}) \right) \times \frac{V_{sample}^{1/3}}{4\pi s_{hk}^2} \tag{3-19}$$

where $$s_{hk} = \sqrt{\left(\frac{h}{d_l}\right)^2 + \left(\frac{k}{d_c}\right)^2}$$

The observed scattering pattern is then the convolution of Equation 3-19 with the instrumental resolution as shown in Figure 3.18.

For structures in which the rods lack periodic order, the scattering can again be divided into contributions from density variations along the lamellar axis, and scattering from the B-domains at the AC interfaces. Since the structure along the lamellar axis is periodic its contribution can be determined via Equation 3-19. Scattering from the rods depends upon both the cylinder form factor (Equation 3-15) and the cylinder-cylinder structure factor. Rods at a given interface will be more strongly correlated with neighbors within the layer than with rods in adjacent layers. If the rods are entirely uncorrelated between layers, the scattering from the rods is given by,

$$I(\mathbf{s}) = 2S(s_y) \times \left| A_{cyl}(s_x, s_y) \right|^2 d_c d_l \delta\left(s_z V_{sample}^{1/3} \right) V_{sample}^{1/3} \tag{3-20}$$

where $S(s_y)$ is the in-plane cylinder-cylinder correlation function and the rods are assumed to be straight and long. If neighboring rods at an AC interface interact via a parabolic potential, the correlation function is given by,

$$S(s_y) \approx \frac{\cosh\left(\left(\pi s_y \sigma_0\right)^2\right) \sinh\left(\left(\pi s_y \sigma_0\right)^2\right)}{\sinh^2\left(\left(\pi s_y \sigma_o\right)^2\right) + \sin^2\left(\pi s_y d_c\right)} \tag{3-21}$$

where σ_0 is the Root Mean Square displacement amplitude of the distance between nearest neighbors. For a sample with fiber-type alignment along the lamellar axis (x-axis), the scattering from the rods is given by,

$$I(s_x, s_y) = S(s_y) \left| A_{cyl}(s_x, s_y) \right|^2 \frac{2 d_c d_l}{\pi s_y} \tag{3-22}$$

while for a complete powder average the intensity is,

$$I(s) = \frac{d_c d_l}{s} \int_{\theta=0}^{\pi} S(s\sin\theta)\left|A_{cyl}(s\cos\theta, s\sin\theta)\right|^2 \frac{d\theta}{\pi} \tag{3-23}$$

Using Equations 3-23 and 3-19, the scattering from a disordered cylinder-at-lamellae structure was calculated and the results are plotted in Figure 3.18.

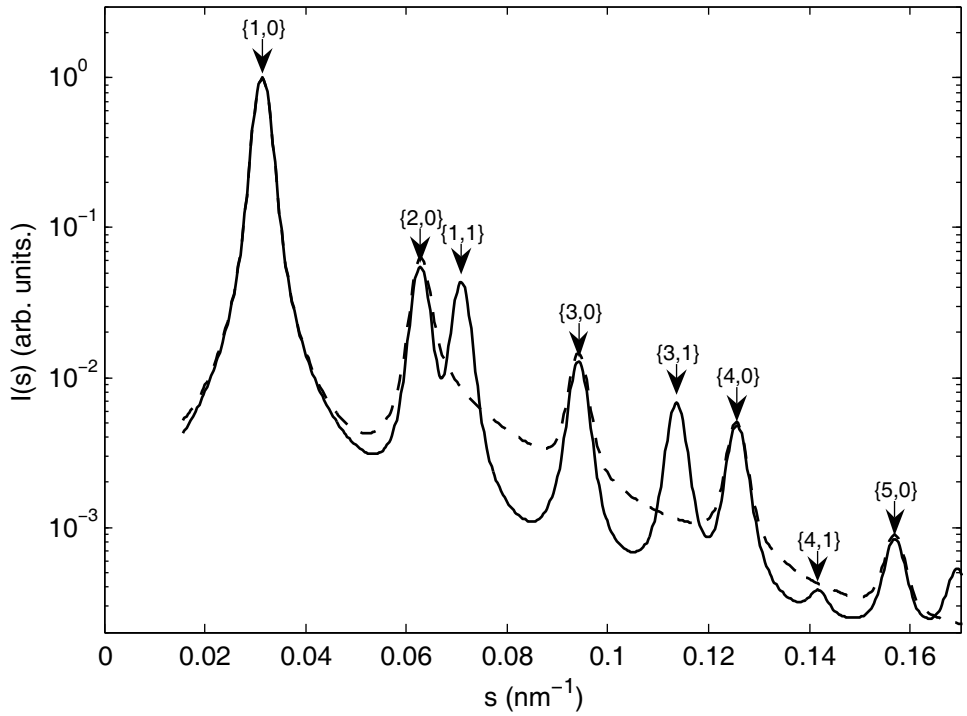

Figure 3.18 - Comparison of Scattering from rods-at-lamellae structures with ordered (solid) and disordered (dashed) rods. Lattice size and experimental peak shapes correspond to the phase transition of copolymer 2 (Figure 3.8). The cylinder shape was chosen to be a little flat (d_x/d_y = 0.7) and offset into the C-domain (ϕ_A=0.3) while σ_0=0.125d_c was chosen to be comparable to the Lindemann criterion for melting (σ_0 ~ 10% of nearest neighbor distance; Dash, 2002).

The model SAXS patterns are fairly similar to those observed for temperatures close to the phase transition in copolymer **2**. Thus the temperature dependence of SAXS

from copolymer **2** is consistent with an order-disorder transition in which the rods of a rods-at-lamellae structure switch between a "staggered' and liquid-like ordering.

3.3.2.3 Balls-at-Lamellae

The balls-at-lamellae structure can be treated in a similar manner to the rods-at-lamellae structure. The B-domains at each AC interface can be approximated by two half-ellipsoids both of diameter, d_y. and heights of $\phi_A d_x$ and $\phi_C d_x$ respectively. These dimensions are related to the lattice size and B-block volume fraction by the relationship,

$$\frac{\pi}{6} d_y^2 d_x = f_B \times \frac{d_l}{2} \times d_s^2 \times \sin\theta_{bc} \tag{3-24}$$

where d_s is the distance between adjacent balls at the AC interface and θ_{bc} is the angle between the two in-plane lattice vectors. Hexagonal ordering ($\theta_{bc} = 60^o$) should be favored when balls interact most strongly with in-plane neighbors, while square packing ($\theta_{bc} = 90^o$) is plausible if interactions with balls in adjacent layers are significant. While there are many stackings of these 2-D arrays of balls, in the simplest case the unit cell has the same period as the AC lamellar structure. For this case the Fourier coefficients are,

$$\begin{aligned} F_{hkl}^{balls} &= \delta_{k0} \times \delta_{l0} \times (\rho_A - \rho_C) \times (f_A + \phi_A f_B) \times \mathrm{sinc}(\pi(f_A + \phi_A f_B)h) \\ &+ \exp(-i\pi(h(f_A + \phi_A f_B) + 2ky_1 + 2lz_1)) A_{sph}\left(\frac{h}{d_l}, \frac{\sqrt{k^2 + l^2 - 2kl\cos\theta_{bc}}}{d_s \sin\theta_{bc}}\right) \\ &+ \exp(i\pi h(f_A + \phi_A f_B)) A_{sph}\left(-\frac{h}{d_l}, \frac{\sqrt{k^2 + l^2 - 2kl\cos\theta_{bc}}}{d_s \sin\theta_{bc}}\right) \end{aligned} \tag{3-25}$$

where y_1 and z_1 are the relative offset between the balls at the two AC interfaces along the two in-plane crystal axes, and $A_{sph}(s_x, s_{yz})$ is the B-domain domain form factor given by,

$$A_{sph}(s_x, s_{yz}) = \frac{\phi_A f_B}{2} \times (\rho_B - \rho_A) \times \phi_{sph}(-\phi_A d_x s_x, d_s s_{yz}) + \frac{\phi_C f_B}{2} \times (\rho_B - \rho_C) \times \phi_{sph}(\phi_C s_x d_x, d_s s_{yz}) \quad (3\text{-}26)$$

where $\phi_{sph}(x, y)$ is the Fourier transform of a half-ellipsoid defined as,

$$\phi_{sph}(x, y) = \int_{\theta=0}^{\theta=\frac{\pi}{2}} \exp(-i2\pi x \cos\theta) \frac{2J_1(\pi y \sin\theta)}{\pi y \sin\theta} \frac{3\sin^3\theta d\theta}{2} \quad (3\text{-}27)$$

The morphology of copolymer **3** could result from a balls-at-lamellae structure in which the disordered packing of balls suppressed the non-lamellar reflections. Alternatively, because of the low B-block volume fraction, the B and C domains might have mixed to form a "double-lamellae" structure.

*Table 3.15 - Structure Factors for Copolymer **3** and corresponding Balls-at-Lamellae and Double-Lamellae models.*

h	[a]I_{exp}	[b,c]I_{balls} I	[b,d]I_{balls} II	[b,e]I_{DL}
1	100	100	100	100
2	1.21 ± 0.05	0.53	0.83	0.39
3	10.22 ± 0.18	7.2	12.6	10.8
4	-	0.88	0.13	0.39
5	1.11 ± 0.04	0.16	1.33	3.63

[a] *Experimental values for Copolymer **3** given in Table 3.10.*
[b] *Block densities and volume fractions at 25°C (Table 3.1 , Table 3.3).*
[c] *B-domains spherical ($d_x/d_y=1$, $\phi_A=\phi_C=0.5$, $d_s = (3/8)^{1/2} d_l$).*
[d] *B domains flattened ($d_x/d_y=0.8$), asymmetric ($\phi_A=0.4$) and closer ($d_s = 0.55 * d_l$).*
[e] *For double-lamellae model B and C blocks mix ideally to form a single domain.*

Using Equations 3-12 and 3-25, scattering intensities for the double-lamellae structure and {*h*,0,0} reflections of the balls-at-lamellae model were calculated for the block volume fractions of copolymer **3**. The results in Table 3.15 indicate that both models are equally consistent with the observed Bragg Peak intensities.

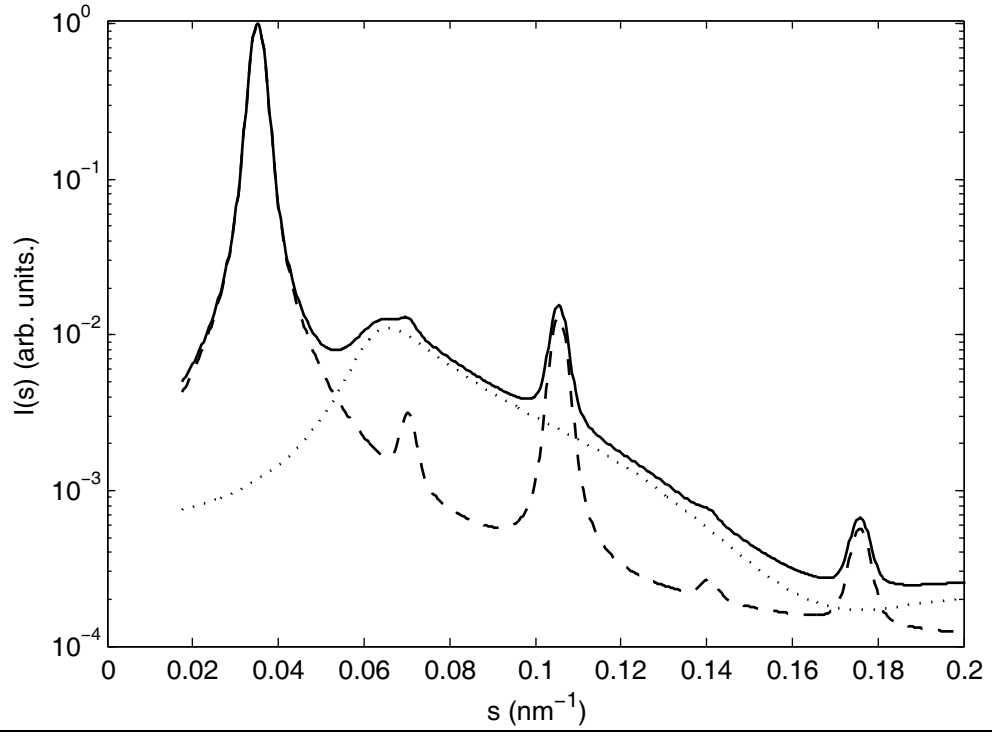

*Figure 3.19 - Scattering from the lamellar order (dashed), diffuse scattering from spherical B-domains (dotted) and total scattering (solid) from a balls-at-lamellae structure. Balls were slightly flattened and asymmetric (d_x/d_y = 0.8, ϕ_A = 0.4, d_s = 0.55×d_l) while in-plane correlations were approximated by Equation 3-21 with σ_0=0.2d_c. For comparison to scattering from copolymer **3**, the fitted peak shape parameters in Table 3.10 were used to describe the width of the lamellar scattering peaks.*

Although the "double-lamellae" and disordered balls-at-lamellae structures have very similar Bragg peak intensities, an ideal "double-lamellae" structure would have no diffuse scatter while the balls-at-lamellae structure should have a broad ring due to sphere-sphere correlations. If balls are uncorrelated between adjacent layers, the normalized scattering intensity from a single "crystal" is,

$$I(\mathbf{s}) = 2d_l d_s^2 \sin\theta_{bc} \times S_{sph}\left(\sqrt{s_y^2 + s_z^2}\right) \times \left| A_{sph}\left(s_x, \sqrt{s_y^2 + s_z^2}\right)\right|^2 \qquad (3\text{-}28)$$

while the powder average is given by,

$$I(s) = 2d_l d_s^2 \sin\theta_p \times \int_{\theta=0}^{\pi} S(s\sin\theta)\left|A_{sph}(s\cos\theta, s\sin\theta)\right|^2 \frac{\sin\theta d\theta}{2} \qquad (3\text{-}29)$$

where S_{sph} is the in-plane ball-ball structure factor. The contribution of diffuse scatter on SAXS profile is shown in Figure 3.19 and establishes that the diffuse scatter observed for copolymer **3** and compound **3-Li** could have resulted from ball-ball correlations in a balls-at-lamellae structure.

3.3.3 Ionic Conductivity

Above its crystallization temperature, lithium doped PEO has a comparatively high conductivity ($>10^{-4}$ S/cm at 70°C ; Soo et. al. 1999) and copolymers containing PEO are of interest for use in lithium rechargeable batteries (Soo, et. al. 1999). As expected, in micro-phase separated polymers the conductivity shows a strong dependence on the connectivity of the PEO domains (Wright, et. al. 1998; Ruzette, et. al. 2001; Yoshizawa, et. al. 2002) and these differences in conductivity have been used to identify morphological transitions (Ruokolainen, et. al., 1998; Cho, et. al. 2004). For example, micellar PEO domains trap lithium ions and have low conductivities, while lamellar PEO domains have good conductivities because ions can travel easily in two dimensions.

Figure 3.20 shows the conductivity of **1-Li**, **2-Li** and **3-Li**. At all temperatures the conductivity of **1-Li** was an order of magnitude greater than that of **2-Li** which in turn was an order of magnitude greater than the conductivity of **3-Li**. If the B-domains are micellar in **3-Li**, cylindrical in **2-Li** and lamellar in **1-Li**, this relative sequence is reasonable.

The conductivity of **1-Li** is comparable measurements of bulk PEO doped to the same concentration of lithium triflate (Caruso, et. al. 2002). The rapid increase in conductivity around the PEO crystallization temperature (T_m(PEO) ≈ 50°C) reflects

the chains in the B-domains undergoing a transition from semi-crystalline to liquid-like motion and ordering.

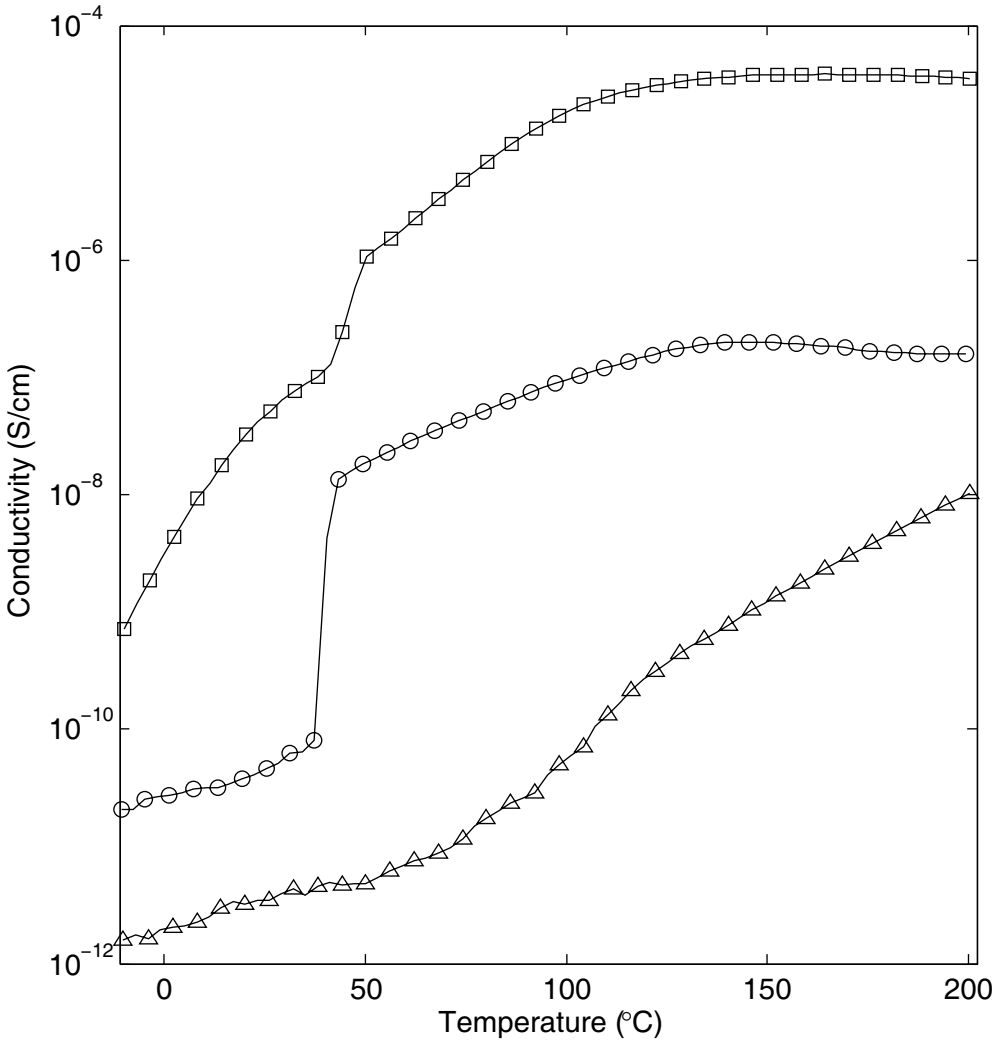

Figure 3.20 - Ionic conductivity of ***1-Li***$^+$ *( ),* ***2-Li***$^+$ *(o) and* ***3-Li***$^+$ *(Δ).*

The substantially lower conductivity of **2-Li** is consistent with the current flow along and between 1-dimensional, cylindrical B domains. Interestingly, **2-Li** showed

an even sharper increase in conductivity around the PEO crystallization temperature. This sharp increase may reflect not only the expected increase in mobility of lithium ions within the PEO domains, but also a change in PEO domain structure. For example, conductivity at temperatures below T_m(PEO) would be greatly diminished if crystallization of PEO chains caused cylindrical B-domains to break into short, worm-like micelles. Indeed, SAXS did show the domain structure within copolymer **2** was disrupted by PEO crystallization and once the PEO domains crystallized, only the first and second order lamellar reflections were observed. Thus, SAXS from copolymer **2** is consistent with melting/crystallization of the PEO domains causing a change in the structure of the PEO domains. Such a structural change would readily account for the large jump in conductivity at T_m(PEO). Although the structure of the PEO domains is not known at low temperature, above the melting temperature of PEO the conductivity of copolymer **2-Li** is consistent with the B block forming 1-dimensional domains.

Finally, the low conductivity of **3-Li** is comparable to that measured for AB diblock copolymers with a micellar conducting block (Soo, et. al. 1999). Because transport within micellar domains does not determine conductivity, no jump in conductance at T_m(PEO) is expected. The steady increase in conductance of **3-Li** with temperature is consistent with the effect of temperature on the rate at which ions can transfer between micelles. If the PEO block in **3-Li** mixed with the PHMA block to form B/C lamellar domains, the mobility of lithium ions in the PEO/PHMA blend would be reduced but the 2-D character of the domains would aid transport. In other lithium-containing polymer systems, mixing of the conducting and non-conducting domains reduced the conductivity by less than order of magnitude (Ruzette, et. al. 2001, Yoshizawa, et. al. 2002). Thus, the low conductivity of **3-Li** is more likely to reflect the trapping of lithium within micellar domains.

3.3.4 AFM

At the suggestion of Dr Peter Busch, the surface of copolymer **2** was examined via Atomic Force Microscopy (AFM).

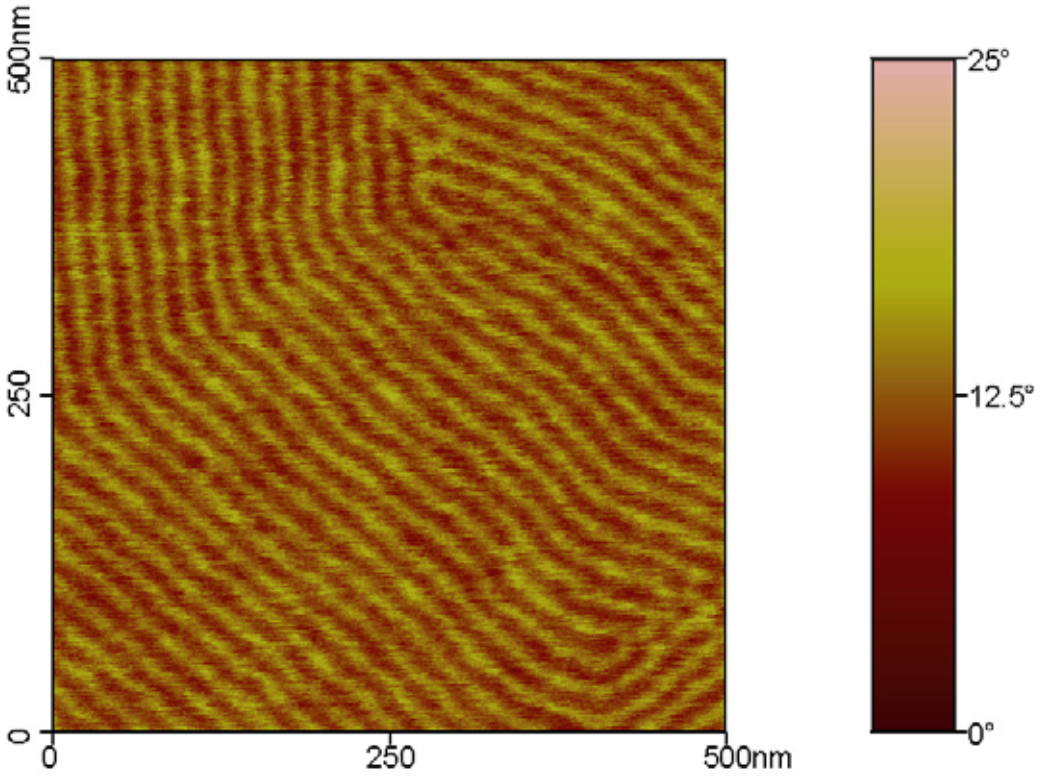

*Figure 3.21 - Atomic Force Microscopy phase image of a thin film of copolymer **2** supported on a silicon substrate. The average spacing between lines is 19 ± 2 nm. The color bar indicates the phase angle of the oscillating AFM cantilever.*

As the lamellae in solvent-cast films of copolymer **2** were oriented parallel to the surface, in the absence of surface reconstruction AFM should have probed the in-plane domain structure. For a cylinder-at-lamellae structure, cylindrical B-domains would be located approximately 9nm beneath the top of the film with a mean spacing between rods of approximately 16nm. Although the surface of a rods-at-lamellae

structure would be essentially flat, phase-contrast imaging could detect the effect of the underlying B-domains on materials properties. Figure 3.21 shows a representative phase-contrast AFM image of a film of copolymer **2**. The average spacing between lines in the image (19 ± 2nm) is consistent with the apparent cylinder-cylinder spacing measured via SAXS. The lines were also present in phase-contrast AFM images of thicker films of copolymer **2**, but were not observed in for films of copolymer **1**.

3.3.5 WAXS

A promising route to self-assembled, hierarchical materials is through the inclusion of polymer blocks with internal structure (Muthukumar et. al., 1997, Ikkala and ten Brinke, 2001).

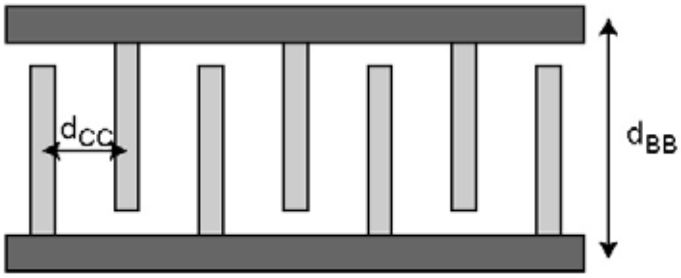

Figure 3.22 - Cartoon of structure within the Pn-alkylMA. Parallel backbones (dark, horizontal) are spaced apart by their side-chains (light, vertical). The average distance between backbones is d_{BB} while the side-chains are separated by d_{CC}.

In Pn-alkylMA homopolymers, the difference in polarizability and flexibility between the methacrylate backbone and alkyl side chains leads to a structure where rows of aligned polymer backbones are spaced apart by their alkyl side chains, as illustrated in Figure 3.22 (Beiner et. al., 2002; Beiner and Huth, 2003; Wind, et. al.

2005). This ordering has a considerable impact upon polymer dynamics as shown by dynamic mechanical, dielectric, and NMR spectroscopy (Wind, et. al., 2003). The molecular-scale ordering in copolymers **1**, **2**, **3**, **5-butyl** and **6-octyl** was studied via Wide Angle X-ray Scattering.

Figure 3.23 shows that WAXS from copolymers **1**, **2** and **3** is quite similar to WAXS from a PHMA homopolymer (Beiner, et. al. 2002). The broad peak on the right corresponds to the side-chain correlations (d_{CC} = 0.49 ± 0.01 nm) while the peak on the left results from backbone-backbone correlations (d_{BB} = 1.34 ± 0.03nm). Scattering from chain-chain correlations in the A and B blocks overlaps with the side-chain scattering from the PHMA block so the right peak is more intense and the top of the backbone-backbone peak is shifted slightly with respect to the PHMA homopolymer (d_{BB} = 14.0nm, Beiner, et. al. 2002).

Table 3.16 - WAXS Scattering Peaks for Copolymers 1, 2, 3, 6-butyl and 7-octyl.

Copolymer	**d_{bb} (nm)**	**d_{cc} (nm)**
1 (T = 75°C)	1.35 ± 0.03	0.48 ± 0.01
2 (T = 75°C)	1.34 ± 0.03	0.49 ± 0.01
3 (T = 75°C)	1.33 ± 0.03	0.49 ± 0.01
5-butyl (T = 50°C)	1.19±0.04	0.48±0.01
2-hexyl (T = 50°C)	1.35±0.03	0.48±0.01
6-octyl (T = 50°C)	1.53±0.04	0.48±0.01

WAXS from copolymers **5-butyl** and **6-octyl** shown in Figure 3.24 demonstrates the dependence of the backbone-backbone spacing on the length of the alkyl side-chains. As the length of the side-chains is increased from 4 to 6 to 8

carbons, the "mean" distance between backbones increases almost linearly (Table 3.16) while the position of the side-chain correlation peak is unchanged. The variation of peak position with side-chain length for the copolymers is practically identical that reported for P-nalkylMA homopolymers (Beiner, et. al. 2002).

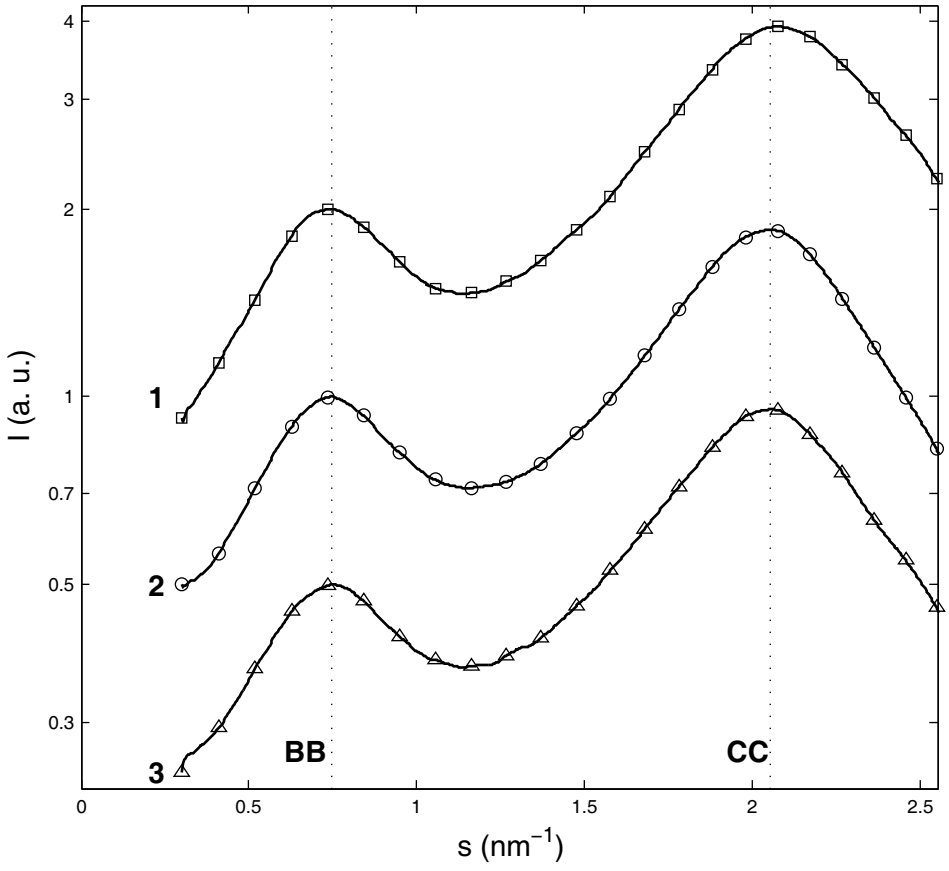

*Figure 3.23 - WAXS spectra for Copolymers **1** ( ), **2** (o) and **3** (Δ) at T=75°C illustrating correlations from both carbon chains (CC, right peak, d_{CC} = 0.49 ± 0.1nm) and Pn-hexyl-MA backbones (BB, left peak, d_{BB} = 1.34 ± 0.03nm). Curves are offset by factors of 2.*

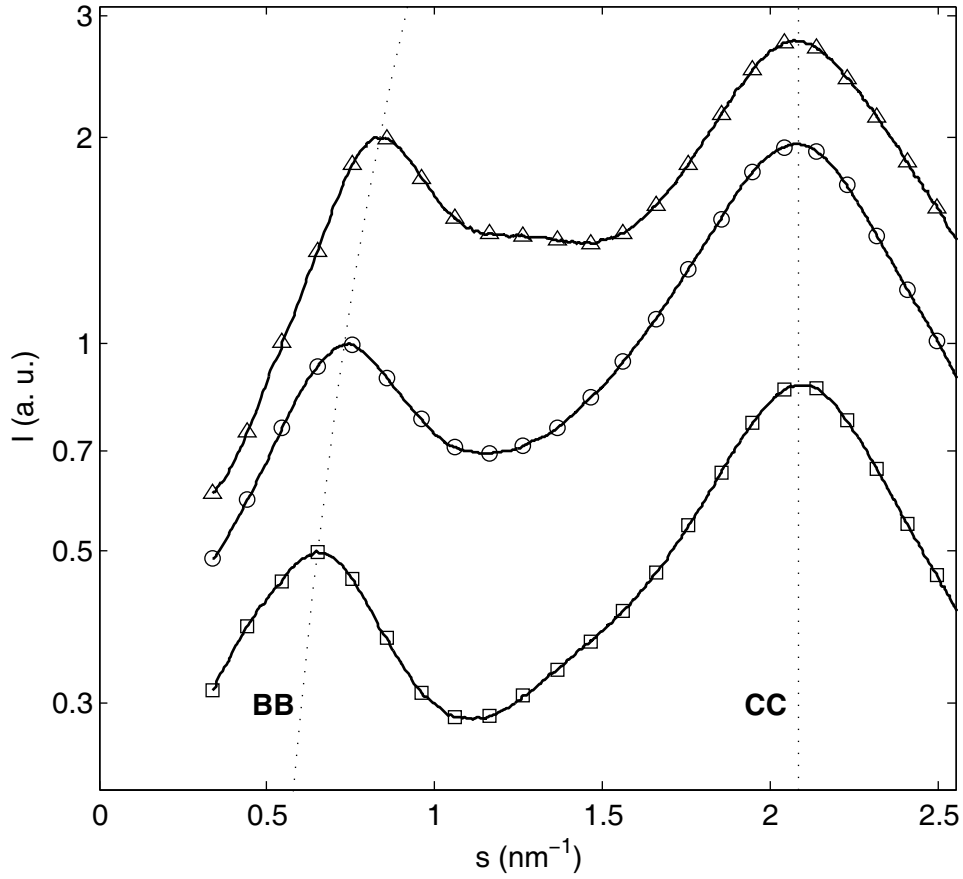

*Figure 3.24 - WAXS spectra for **5-butyl** (Δ), 2-hexyl (o), and **6-octyl** ( ) at T=50°C illustrating the dependence of Pn-alkyl-MA backbone structure on alkyl side chain length. The mean Pn-alkyl-MA backbone (BB, left peak) spacing increases as the alkyl side-chain length grows while correlations between carbon chains (CC, right peak) are largely unaffected.*

3.4 Discussion

Although block copolymer morphology is frequently determined using a combination of electron microscopy and SAXS, electron microscopy was challenging for these block copolymers. Firstly, because the glass temperature of all three blocks is below room temperature, the structure of thin sections is only preserved at cryogenic temperatures and a cryo-EM stage was not available. Secondly, PEP-*b*-

PEO-*b*-PHMA copolymers cannot readily be stained with RuO_4 or OsO_4 and contrast between the unstained blocks is poor. Despite this restriction, SAXS, ionic conductivity data and AFM provided strong constraints on the morphology of copolymers **1**, **2** and **3**. SAXS gave strong support for lamellar ordering in all three materials while distinct differences in B-domain structure were indicated by the dramatic differences in the ionic conductivity of each material.

For copolymer **1** the experimental data provides good support for a triple-lamellae structure. SAXS showed only lamellar peaks and the intensity of the peaks were comparable to those from the electron density profile of a triple-lamellae model. Furthermore, the relatively high conductivity of compound **1-Li** was consistent with charge transport in two-dimensional lamellar domains.

SAXS data from copolymer **2** could be indexed to the rectangular lattice of the rods-at-lamellae morphology (Aushra and Stadler, 1993; Liu et. al., 2003) and the intensity of the Bragg reflections matched with model structure factors. Confinement of charge transport to the one-dimensional cylindrical domains of the rods-at-lamellae structure should reduce conductivity as was observed for compound **2-Li**. Finally, the one-dimensional periodic structure at the surface of copolymer **2** matches that expected for cylindrical B-domains at the AC interface. Thus, the rods-at-lamellae morphology is in accord with the experimental data from copolymer **2**.

The morphology of copolymer **3** is not as tightly constrained by the experimental observations. Although SAXS clearly indicates lamellar ordering, the intensity of the lamellar peaks is consistent with both the balls-at-lamellae (Beckmann et. al., 1994; Erhadt, et. al. 2001) and double-lamellae structures. However, several points favor the balls-at-lamellae structure. Firstly, scattering from disordered balls in a balls-at-lamellae structure should produce a diffuse ring similar to the one observed

from both **2** and **2-Li**. If copolymer **3** had the double-lamellae morphology this scattering would imply the presence of an impurity that was not detected via Gel Permeation Chromatography. Secondly, the very low conductivity of compound **3-Li** favors the balls-at-lamellae morphology in which lithium ions are trapped inside micellar domains. A double-lamellae structure would have a much higher conductivity unless lithium ion mobility in the mixed PEO/PHMA phase was tremendously lower than has typically been observed for other mixed copolymer phases.

Finally, the large enthalpy of mixing for the B and C blocks favors the balls-at-lamellae structure. From Hildebrand Solubility parameters the estimated Flory-Huggins interaction for the B and C blocks was $\chi_{BC}N \approx 65$. While this number is approximate, the observation of an ordered BCC micelle phase in a PEO-PHMA diblock copolymer (Mahajan et. al., 2003) provides a firm lower bound of $\chi_{BC}N \geq 43$. This large enthalpy of mixing would make micelle formation likely even if the B-domain were an end-block in a diblock copolymer (Matsen and Bates, 1996) and micelle formation should be more favorable for the B domains in an ABC copolymer. Firstly, in a double-lamellae structure the AB junction is already constrained at the A-domain interface so micelle formation incurs a smaller loss of positional entropy. Secondly, A and B domains must mix at the lamellar interfaces of the double-lamellae structure. Micelles reduce this very unfavorable interaction between A and B ($\chi_{AB}N \approx 170$) as well as less costly mixing B and C domains so the reduction in enthalpy is greater than would be estimated from $\chi_{BC}N$ alone. Both of these effects favor de-mixing of B and C domains to form a balls-at-lamellae structure. Although other structures are possible, the most likely morphology for copolymer **3** is the balls-at-lamellae structure.

Thus, the most likely morphologies for copolymers **1**, **2** and **3** are respectively the triple-lamellae, rods-at-lamellae and balls-at-lamellae structures. This same sequence of structures was previously observed in PS-PB-PMMA copolymers (Stadler et. al., 1995).

In addition to the morphological transitions, the ordering of rod-shaped B-domains in copolymer **2** has not reported in previous studies of the rods-at-lamellae structure (Auschra and Stadler, 1993; Stadler et. al. 1995; Liu et. al. 2003). A staggered stacking of rods should minimize chain stretching in the A and C domains and SAXS confirms this is the arrangement within copolymer **2** at 75°C. The disappearance of order at higher temperatures is also quite interesting. Transitions between two and three domain morphologies have been the subject of both theoretical (Abetz, et. al. 1996; Manniadis, et. al. 2004) and experimental study (Neumann, et. al. 1996; Yamauchi, et. al. 2003). However, mixing of cylindrical B domains with lamellar C domains to form B/C lamellae may not be the best explanation for the transition in copolymer **2**. In general, a transition from a rods-at-lamellae structure to a double-lamellae structure would alter the unit cell size and the density profile along the lamellar axis. Such changes are not observed and the diffuse scatter seen above the transition temperature (eg. Figure 3.8) is also not expected for a double-lamellae structure.

For micellar structures in AB diblock copolymers, melting the BCC crystalline stacking of micelles leads to a disordered liquid of micelles rather than an isotropic mixture (Domindontova and Lodge, 2001; Wang et. al. 2002). By analogy, above the transition temperature of copolymer **2**, cylindrical B-domains could remain at the AC interfaces with the position of rods at successive interfaces uncorrelated. In good agreement with the experimental data, such a transition would leave the density profile

along the lamellar axis largely unchanged while diffuse scattering would result from the liquid-like ordering of cylindrical B-domains. Finally, this transition in the rods-at-lamellae structure may be particularly interesting because the one-dimensional cylindrical domains are confined at the AC interfaces along the lamellar axis, but free to move in the other direction. Dimensionality has important effects on melting (Dash, 2002; Angelescu, et. al. 2005), and this transition would be an intermediate between two and one-dimensional melting.

3.5 Conclusion

This chapter has examined the effect of reducing the volume fraction of the middle PEO block (f_B) in a series of three PEP-b-PEO-b-PHMA copolymers with roughly equivalent A and C blocks ($f_A \approx f_C$). For all three copolymers, SAXS supported a lamellar arrangement of the A and C domains while ionic conductivity measurements indicated pronounced differences in the state of the B-blocks. The experimental data were consistent with the B-block forming lamellar domains at the largest middle block volume fraction (f_B=0.25), rod-like domains at intermediate B block volume fractions (f_B=0.15) and ball-like domains at the lowest B block volume fraction (f_B=0.1). This sequence of phase transitions was previously observed in PS-b-PB-b-PMMA copolymers (Stadler, et. al. 1995).

Chapter Four - Thermodynamics of Lamellar ABC Structures

4.1 Introduction

This chapter examines the thermodynamic properties of ABC block copolymer structures in which the A and C blocks form lamellar domains. The stability of the triple-lamellae, rods-at-lamellae and balls-at-lamellae structures (Figure 3.1) has previously been studied using the Strong Segregation Limit (SSL) approach of Semenov (Stadler et. al., 1995) and the SSL density functional approximation of Ohta and Kawasaki (Zheng and Wang, 1995). However, several results of the analysis by Stadler and colleagues (Stadler et. al., 1995) conflict both with physical intuition and the conclusions of Zheng and Wang (Zheng and Wang, 1995). Subsequent computational studies using density functional theory (Bohbot-Raviv and Wang, 2000) and self-consistent mean-field theory (Tang et. al., 2004) did not resolve these differences as only two-dimensional morphologies were studied. Reexamining the SSL behavior of the triple-lamellae, rods-at-lamellae and balls-at-lamellae structures can resolve these differences and also provide a better understanding of the transitions between the three morphologies.

In this chapter, the Gibbs free energies per copolymer of these morphologies are estimated using Semenov's SSL formulation of block copolymer free energy (Semenov, 1985). The SSL formalism is developed in Section 4.2 and is applied to the triple-lamellae morphology in Section 4.2.1. When the interfacial tension between the end blocks is smaller than the combined interfacial tension of the AB and BC interfaces ($\gamma_{AC}<\gamma_{AB}+\gamma_{BC}$), decreasing the B block volume fraction (f_B) destabilizes the

lamellar B domain of the triple-lamellae structure. This instability of the lamellar B domain is described in Section 4.3. More detailed descriptions of the rods-at-lamellae (Section 4.3.1), balls-at-lamellae (Section 4.3.2) and perforated-lamellae (Section 4.3.3) structures are developed to determine the onset of this transition. In addition to these lamellar morphologies, Stadler and colleagues also considered a rings-at-cylinders morphology and this is modeled in Section 4.3.4. In Section 4.4, the approximate Gibbs free energy per copolymer of each morphology is studied and used to construct a SSL phase diagram. When $\gamma_{AC} < \gamma_{AB}+\gamma_{BC}$, the triple-lamellae structure is optimal for the larger values of B volume fraction (f_B), the rods-at-lamellae structure at intermediate values and the balls-at-lamellae structure is stable for the lowest values of f_B. The predictions of these SSL models are also compared to the three PEP-b-PEO-b-PHMA copolymers examined in Chapter 3.

4.2 Strong Segregation Limit Formulation

In the SSL ($\chi_{ij}N \rightarrow \infty$), each block of the copolymer chain resides within a distinct domain while junctions between blocks are localized at domain interfaces, as shown for the triple-lamellae structure in Figure 4.1. In this limit, the Gibbs free energy per copolymer may be approximated by (Semenov, 1985),

$$G = G_{\text{int}} + G_{\text{stretch}}, \tag{4-1}$$

where G_{int} describes the enthalpy of mixing at domain interfaces and G_{stretch} the loss of entropy from chain stretching within each domain. When the domain size is much greater than the interfacial thickness, the interfacial energy is given by,

$$G_{\text{int}} = k_B T \times \sum_{i,j,i\neq j} \gamma_{ij} A_{ij} \times \frac{V}{V_{\text{cell}}}, \tag{4-2}$$

where k_B is Boltzmann's constant, T is the temperature, $k_BT\times\gamma_{ij}$ is the interfacial free energy per unit area between blocks i and j, A_{ij} is the area of domain interfaces

between blocks i and j per unit cell, V_{cell} is the volume of the unit cell, and V the molecular volume of the copolymer. In addition to the unit cell volume (V_{cell}), it is convenient to describe the size of the block copolymer structure in terms of a linear dimension, d, commonly taken to be one of the lattice dimensions (eg. $d = d_l$ for a lamellar structure and $d = d_{cyl}$ for a cylindrical structure). Defining the coefficient,

$$C_{int} = \sum_{i,j,i\neq j} \frac{\gamma_{ij} A_{ij} d}{2V_{cell}}, \tag{4-3}$$

the interfacial free energy may then be written as,

$$G_{int} = k_B T \times C_{int} \times \frac{2V}{d}. \tag{4-4}$$

Increasing the size of the structure (d) reduces the interfacial energy per copolymer.

Turning to the second term in Equation 4-1, the value of $G_{stretch}$ depends upon the average stretching of the individual blocks. For a strongly stretched, continuous Gaussian chain, the stretching energy is given by (Matsen, 2002),

$$G_{stretch} = \frac{3k_B T}{2} \times \sum_j \frac{p_j R_j^2}{f_j V}, \tag{4-5}$$

where p_j is the packing length (Fetters, et. al. 1994), f_j the volume fraction and R_j is the average root mean square path length of the j-th block. The packing length, p_X, characterizes the persistence length of a given type of polymer and is defined by the relationship (Fetters, et. al. 1994),

$$p = \frac{V_X}{L_X^2}, \tag{4-6}$$

where V_X is the chain volume and L_X is the root mean squared end-to-end length of the chain in a homopolymer melt. For a continuous Gaussian chain, the path of a given polymer backbone can be described by the function, $r_j(u)$, in which u is the fractional distance along the backbone ($0 \leq u \leq 1$; ends of polymer chain at $r_j(0)$ and $r_j(1)$). The average root mean square path length, R_j, is then defined as,

$$R_j^2 = \left\langle \int_{u=0}^{u=1} \left(\frac{dr_j(u)}{du} \right)^2 du \right\rangle_{r_j(u)}, \tag{4-7}$$

where the average is taken over all polymer paths within the domain. The set of the polymer paths within a domain depends upon how each end of the chain is constrained (free / tethered at a domain interface) and the spatial distribution of chain ends at the domain interfaces (Matsen, 2002). Defining the coefficient,

$$C_{\text{stretch}} = \sum_j \frac{3 p_j R_j^2}{2 f_j d^2}, \tag{4-8}$$

the energy for the chain stretching may be written as,

$$G_{\text{stretch}} = k_B T \times C_{\text{stretch}} \times \frac{d^2}{V}. \tag{4-9}$$

The chain stretching energy increases with the square of the unit cell size (d).

Substituting Equations 4-4 and 4-9 into Equation 4-1, the Gibbs free energy per copolymer can be expressed as,

$$\frac{G}{k_B T} = C_{\text{int}} \times \frac{2V}{d} + C_{\text{stretch}} \times \frac{d^2}{V}. \tag{4-10}$$

When the unit cell size (d) is small, the interfacial energy is large and the stretching energy is small. Conversely, when the unit cell size is large, the interfacial energy per copolymer is small and the stretching energy is large. The optimum unit cell size may be determined by setting the derivative (with respect to d) of Equation 4-10 to zero yielding,

$$d = \sqrt[3]{\frac{C_{\text{int}}}{C_{\text{stretch}}}} \times V^{2/3}, \tag{4-11}$$

while the corresponding minimum in the Gibbs free energy per copolymer is,

$$G = 3 k_B T \times C_{\text{int}}^{2/3} \times C_{\text{stretch}}^{1/3} \times V^{1/3}. \tag{4-12}$$

In the SSL, the values of C_{int} (Equation 4-3) and C_{stretch} (Equation 4-8) determine the optimum size and minimal free energy for a given structure as is illustrated below for the triple-lamellar structure.

4.2.1 Triple-Lamellae

The arrangement of chains in the triple-lamellae morphology is illustrated in Figure 4.1. Kane and Spontak have described the thermodynamics of this structure in the SSL (Kane and Spontak, 1994).

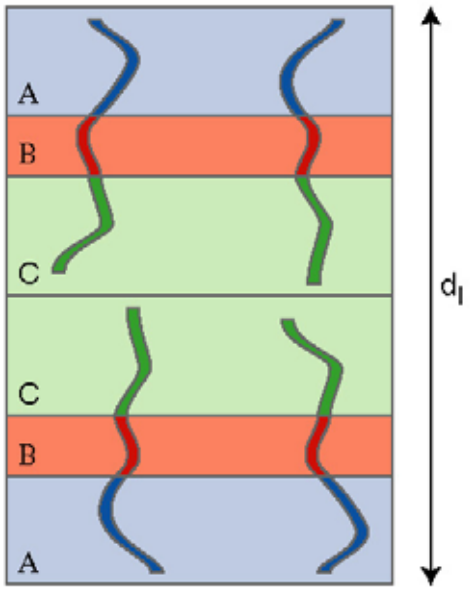

Figure 4.1 – Schematic of copolymer chain conformations in the triple-lamellae unit cell. The unit cell is of length d_l.

The AB and BC interfacial area per unit cell is,

$$A_{AB} = A_{BC} = \frac{V_{\text{cell}}}{d_l/2} = \frac{2V_{\text{cell}}}{d_l}, \tag{4-13}$$

so the interfacial energy coefficient (Equation 4-3) is,

$$C_{\text{int}}^{TL} = \sum_{i,j,i\neq j} \frac{\gamma_{ij} A_{ij} d_l}{2V_{cell}} = \gamma_{AB} + \gamma_{BC}. \tag{4-14}$$

For the triple-lamellae structure, the area of the AB and BC interfaces depends only upon the unit cell size (d_l) and so the interfacial energy is independent of the block volume fractions.

In the triple-lamellae structure, each chain starts in an A-domain, stretching across the B-domain and finishes in the C-domain (Figure 4.1). For the A and C blocks, one end of the block is free while the other is tethered at the AB or BC interface. In contrast, both ends of the B block are tethered at interfaces. This difference in chain boundary conditions leads to a different expressions for root mean square path length. Because the B block stretches between the AB and BC interfaces, the ends of the B block are separated by a distance $f_B \times d_l/2$ and

$$R_B^2 = \left(\frac{f_B d_l}{2} \right)^2 . \tag{4-15}$$

In contrast, one end of the A/C block is located at the AB/BC interface while the free end of the A/C block can be positioned anywhere within the A/C domain. The arrangement of chains in the A/C domain is equivalent to chains grafted to an interface that stretch out to fill a region of space with constant density. For a concave or flat interface, the average chain extension is then given by,

$$R_j^2 = \frac{\pi^2}{4} \left\langle z^2 \right\rangle , \tag{4-16}$$

where at each point in the domain, z is the distance chains with ends at that point stretch to reach the domain interface (Milner et. al. 1988; Ball et. al. 1991; Matsen, 2002). In the triple-lamellae structure, the spatial distribution of AB/BC junctions at the AB/BC interface is uniform so the A/C chains can stretch directly to the nearest point on the AB/BC interface. Thus, for the A-domain,

$$R_A^2 = \frac{\pi^2}{4} \left\langle z^2 \right\rangle = \frac{\pi^2}{4} \int_{z=0}^{z=\frac{f_A d_l}{2}} z^2 \frac{dz}{f_A d_l / 2} = \frac{\pi^2 f_A^2 d_l^2}{48} . \tag{4-17}$$

Similarly, for the C-domain,

$$R_C^2 = \frac{\pi^2 f_C^2 d_l^2}{48}. \tag{4-18}$$

Substituting Equations 4-15, 4-17 and 4-18 into the elastic energy coefficient defined by Equation 4-8 yields,

$$C_{\text{stretch}}^{TL} = \sum_j \frac{3p_j R_j^2}{2f_j d_l^2} = \frac{\pi^2}{32}\left(f_A p_A + \frac{12}{\pi^2} f_B p_B + f_C p_C \right), \tag{4-19}$$

$C^{\text{TL}}_{\text{stretch}}$ is roughly proportional to the average packing length of the three blocks.

Substituting Equations 4-14 and 4-19 into Equations 4-12 and 4-11, the free energy per copolymer of the triple-lamellae structure is,

$$\frac{G^{TL}}{k_B T} = \frac{3\pi^{2/3}}{2^{5/3}} \times \left(\gamma_{AB} + \gamma_{BC}\right)^{2/3} \times \left(f_A p_A + \frac{12}{\pi^2} f_B p_B + f_C p_C \right)^{1/3} \times V^{1/3}, \tag{4-20}$$

while the lamellae repeat spacing is given by,

$$d_l^{TL} = \frac{2^{5/3}}{\pi^{2/3}} \times \sqrt[3]{\frac{\gamma_{AB} + \gamma_{BC}}{f_A p_A + \frac{12 f_B p_B}{\pi^2} + f_C p_C}} \times V^{2/3}. \tag{4-21}$$

Provided the packing lengths of the three blocks are similar, the free energy and repeat spacing of the triple lamellae structure are essentially independent of block composition. It is interesting to compare the ABC triblock copolymer to the corresponding AC diblock copolymer in which the B block has been omitted (volume of A block = $f_A \times V$; no B block; volume of C block = $f_C \times V$). For an AC double-lamellae structure, the Gibbs free energy is given by,

$$\frac{G^{DL}}{k_B T} = \frac{3\pi^{2/3}}{2^{5/3}} \times \gamma_{AC}^{2/3} \times \left(f_A p_A + f_C p_C \right)^{1/3} \times V^{1/3}, \tag{4-22}$$

while the lamellae repeat spacing is,

$$d_l^{DL} = \frac{2^{5/3} \times \left(f_A + f_C\right)}{\pi^{2/3}} \times \sqrt[3]{\frac{\gamma_{AC}}{f_A p_A + f_C p_C}} \times V^{2/3}. \tag{4-23}$$

Clearly, when the interfacial tension between the A and C blocks is large ($\gamma_{AC} > \gamma_{AB}+\gamma_{BC}$) the middle B block can reduce the free energy with the lamellae B domain acting as a buffer between the highly incompatible A and C end blocks. However, if $\gamma_{AC} < (\gamma_{AB} + \gamma_{BC})$, the AC interface in the AC double-lamellae structure has a lower interfacial energy than the corresponding AB and BC interfaces in the ABCBA triple-lamellae structure. Under these circumstances, it may be possible to reduce the free energy per copolymer by changing the shape of the lamellar B domain. This instability of the triple lamellae structure is described in the following section.

4.3 Interfacial Instability

In the ABC triple-lamellae structure, the AB and BC interfacial area is independent of the width of the B-lamellae, $f_B \times d_l/2$. Figure 4.2b illustrates how parts of these AB and BC interfaces can be converted into an AC interface by forming perforations (contact between A and C domains) in the lamellar B domain. This conversion can reduce the interfacial energy when the interfacial tensions satisfy the inequality, $\gamma_{BC} + \gamma_{BC} > \gamma_{AC}$. However, the chain stretching energy of the B domain in the perforated structure is greater because the increased average thickness of the B domain (d_B). Furthermore, some chains in the A and C domains must stretch laterally to reach the AB and BC interfaces. The perforated B domain is only stable when the reduction in AB and BC interfacial energy outweighs the new AC interfacial energy, increased chain stretching energy of the B domains and change in chain stretching energy of the A and C domains. As the relative cost of chain stretching of the B is proportional to its volume fraction, f_B, the triple-lamellae structure (Figure 4.2a) is stable when the volume fraction of the B domains is large and perforated structures (Figure 4.2b) become stable when f_B is small.

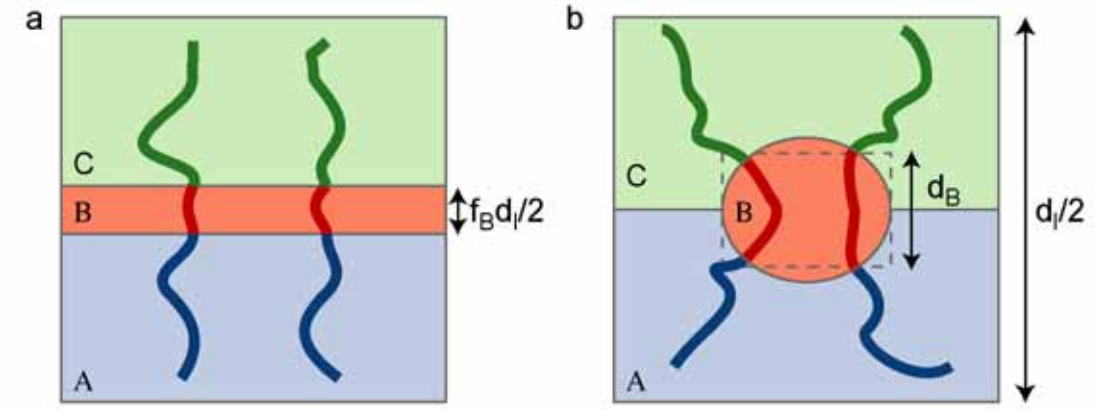

Figure 4.2 – Schematic of two ABC copolymer morphologies with lamellar A and C domains. In the triple-lamellae structure (a), the lamellar B domain has a width $f_B d_l/2$, where the lamellar repeat spacing is d_l. The structure on the right (b) has a smaller AB and BC interfacial area. However, this requires the formation of an AC interface, an increase of the B-domain average thickness (d_B) and lateral stretching of some chains in the A and C domains.

The transition between the triple-lamellae and perforated structures (e.g. rods-at-lamellae, balls-at-lamellae, perforated-B-lamellae) is analogous to the behavior of a layer of water on a hydrophobic surface. Spreading the water out across the surface increases the surface area and interfacial energy but decreases the thickness and gravitational energy of the layer. When the average thickness of the water layer is large (e.g. average thickness > 5 mm), the water layer spreads across the surface. In contrast, if the average thickness of the water layer is small (e.g. average thickness < 1 mm), a lower total energy by the layer breaking up into droplets which have a smaller total area (but are thicker).

In these ABC copolymer structures, the stretching of the chains in the B domain favors a thin, lamellar B domain structure while the AB and BC interfacial tension favors the smaller area of the thicker perforated B domain structure. To determine value of f_B at which the triple-lamellar structure becomes unstable, the free

energy per copolymer of each perforated structure must be estimated. For a given structure, the free energy depends upon the change in interfacial areas and chain stretching relative to the triple-lamellae structure. The area of the AB, BC and AC interfaces may be expressed as,

$$A_{AB} = 2 \times \frac{V_{cell}}{d_k} \times \phi_a \times \varphi_{BC} \,, \tag{4.24}$$

$$A_{BC} = 2 \times \frac{V_{cell}}{d_l} \times \phi_a \times \varphi_{BC} \,,$$

$$A_{AC} = 2 \times \frac{V_{cell}}{d_l} \times (1 - \phi_a) \times \varphi_{AC} \,,$$

where ϕ_a is the fraction of the y-z plane (plane of the AC interface) occupied by B-domains and φ_{AB}, φ_{BC} and φ_{AC} are coefficients to account for the curvature of each interface. The values of φ_{AB}, φ_{BC} and φ_{AC} depend only upon the shape of the AB, BC and AC interfaces. When the A and C domains are lamellar, φ_{AB}, φ_{BC} and φ_{AC} must be greater than or equal to one. For example, in the structure shown in Figure 4.2b, $\varphi_{AC} = 1$ because the AC interface is flat while the value of φ_{AB} and φ_{BC} would be $\pi/2$ for a cylindrical AB/BC interface and 2 for spherical interface. The interfacial energy coefficient defined in Equation 4-3 is then,

$$C_{\text{int}} = \sum_{i,j,i \neq j} \frac{\gamma_{ij} A_{ij} d_l}{2 V_{cell}} = \gamma_{AB} \varphi_{AB} \phi_a + \gamma_{BC} \varphi_{BC} \phi_a + \gamma_{AC} \varphi_{AC} \times (1 - \phi_a) . \tag{4-25}$$

Provided $\gamma_{AB}+\gamma_{BC} > \gamma_{AC}\varphi_{AC}$, reducing the in-plane area of B-domains (ϕ_a) can decrease the interfacial area coefficient.

However, reducing the in-plane area of the B-domains increases the average thickness of the B block (d_B). By volume conservation, the in-plane area and average thickness of the B-domains, d_B, are related by the expression,

$$1 \times \frac{f_B d_l}{2} = \phi_a \times d_B \,. \tag{4-26}$$

When the in-plane area of the B-domains is reduced by a factor of ϕ_a, the average thickness of the B domains increases by a factor of $1/\phi_a$. The effect of this increase in thickness on chain stretching may be described by the relationship,

$$R_B^2 = \eta_B d_B^2 = \left(\frac{f_B d_l}{2} \right)^2 \times \frac{\eta_B}{\phi_a^2} \ , \tag{4.27}$$

where η_B is the mean squared path length of chains in the block B relative to a lamellar B domain of the same average thickness ($\eta_B \geq 1$). The effect of a perforation on stretching in the A and C domains is more complicated as chains directly above or below the B domain may stretch less while chains at the side must stretch sideways (Figure 4.2b). Changes to the chain extension in the A and C domains can be parameterized as,

$$R_A^2 = \left(\frac{f_A d_l}{2} \right)^2 \times \eta_A \ , \quad R_C^2 = \left(\frac{f_C d_l}{2} \right)^2 \times \eta_C \ , \tag{4.28}$$

where η_A and η_C are the mean squared path length of A and C blocks relative to mean squared end-to-end length of the corresponding block in a triple-lamellae structure with same lattice size. η_A and η_C depend upon both (ϕ_a) and the geometry of the B-domains (e.g. rods, balls or perforated lamellae). However, in the limit of small ($f_B \rightarrow 0$), the B-domains become closely spaced and η_A and η_C approach a value of 1. Using Equations 4.27 and 4.28, the elastic energy coefficient defined by Equation 4-8 can be expressed as,

$$C_{\text{stretch}} = \sum_j \frac{3 p_j R_j^2}{2 f_j d_l^2} = \frac{\pi^2}{32} \times \left(f_A p_A \eta_A + f_C p_C \eta_C \right) + \frac{3 f_B p_B}{8} \times \frac{\eta_B}{\phi_a^2} \ . \tag{4-29}$$

In general, decreasing the relative in-plane area of the B domains (ϕ_a) increases the chain stretching energy. For a given structure, evaluating φ_{AB}, φ_{BC} and φ_{AC} and η_A, η_B and η_C permits calculation of the free energy per copolymer using Equations 4-25, 4-29 and 4-12. In the following sections, these coefficients are estimated for the rods-

at-lamellae (Section 4.3.1), balls-at-lamellae (Section 4.3.2), perforated-lamellae (Section 4.3.3) and rings-at-cylinders (Section 4.3.4) morphologies.

Before performing this more detailed analysis, it is useful to consider the general features of free energy per copolymer for a perforated structure. Substituting Equations 4-25, 4-29 into 4-10, the free energy per copolymer is given by,

$$\frac{G}{k_B T} = \gamma_{AC}\varphi_{AC} \times \frac{2V_{cell}}{d_l} + \frac{\pi^2}{32} \times \left(p_A f_A \eta_A + p_C f_C \eta_C\right) \times \frac{d_l^2}{V_{cell}} + \left(\gamma_{AB}\varphi_{AB} + \gamma_{BC}\varphi_{BC} - \gamma_{AC}\varphi_{AC}\right) \times \frac{2V_{cell}}{d_l} \times \phi_a + \frac{3 f_B p_B \eta_B}{8} \times \frac{d_l^2}{V_{cell}} \times \frac{1}{\phi_a^2}. \quad (4\text{-}30)$$

The two terms in the first row are very similar to those for an AC diblock lamellar morphology (Equation 4-22) while the terms in the second row describe the trade-off between interfacial energy and chain stretching. When the value of ϕ_a is larger the interfacial energy becomes significant while at small values of ϕ_a the chain stretching energy is large. Since the chain stretching energy of the B domain is roughly proportional to f_B, smaller values of f_B favor smaller values of ϕ_a.

If the dependence of φ_{AB}, φ_{BC} and φ_{AC} and η_A, η_B and η_C on ϕ_a is relatively weak, the optimal values of ϕ_a and d_l can be estimated by setting the derivatives of Equation 4-30 with respect to ϕ_a and d_l to zero. The free energy of the perforated structure is then given by,

$$\frac{G}{k_B T} \approx \frac{3\pi^{2/3} V^{1/3}}{2^{5/3}} \times \left(\gamma_{AC}\varphi_{AC}\right)^{2/3} \times \left(f_A p_A \eta_A + f_C p_C \eta_C\right)^{1/3} + \frac{3\pi^{2/3} V^{1/3}}{2^{5/3}} \times \left(\gamma_{AB}\varphi_{AB} + \gamma_{BC}\varphi_{BC} - \gamma_{AC}\varphi_{AC}\right)^{2/3} \times \left(\frac{12 p_B \eta_B}{\pi^2}\right)^{1/3} \times f_B^{1/3}, \quad (4\text{-}31)$$

the optimal lamellar repeat spacing (d_l) is,

$$d_l \approx \frac{2^{5/3}}{\pi^{2/3}} \sqrt[3]{\frac{\gamma_{AC}\varphi_{AC}}{\left(f_A p_A \eta_A + f_C p_C \eta_C\right)}} \times V^{2/3}, \quad (4\text{-}32)$$

and the optimal value of ϕ_a is,

$$\phi_a \approx \left(\frac{\gamma_{AC}\varphi_{AC}}{\gamma_{AB}\varphi_{AB} + \gamma_{BC}\varphi_{BC} - \gamma_{AC}\varphi_{AC}} \times \frac{12 p_B \eta_B}{\pi^2 \left(f_A p_A \eta_A + f_C p_C \eta_C \right)} \right)^{1/3} \times f_B^{1/3}. \quad (4\text{-}33)$$

As the B domain volume fraction decreases towards zero ($f_B \to 0$), the in-plane area fraction of B domains (ϕ_a) also decreases towards zero ($\phi_a \propto f_B^{1/3}$) and the free energy per copolymer (G) and lamellar repeat spacing (d_l) approach the corresponding values for an AC diblock copolymer (Equations 4-22 and 4-23). Thus, provided $\gamma_{AB}+\gamma_{BC} > \gamma_{AC}$, the triple-lamellae structure will always become unstable as f_B is reduced. Equation 4-33 also permits a rough estimate of when the perforated structure has a higher energy than the triple-lamellar structure. The optimal value of ϕ_a increases as the value of f_B increases but the area fraction of B domains in the AC interface cannot physically exceed 1. This is only true when,

$$f_B \le \frac{\gamma_{AB}\varphi_{AB} + \gamma_{BC}\varphi_{BC} - \gamma_{AC}\varphi_{AC}}{\gamma_{AC}\varphi_{AC}} \times \frac{\pi^2 \left(f_A p_A \eta_A + f_C p_C \eta_C \right)}{12 p_B \eta_B}. \quad (4\text{-}34)$$

If Equation 4-34 is not satisfied, forming perforations in the B domain require more chain stretching energy than can be saved by reducing the AB and BC interfacial energy and the lamellar B domains in the triple-lamellae structure are stable.

To a first approximation, the transition between the triple-lamellae structure and structures with perforations in the B domain (e.g. rods-at-lamellae, balls-at-lamellae) is determined by a trade-off between reducing the AB/BC interfacial area and increasing stretching of the chains in the B domain. In contrast, the relative stability of different perforated structures (e.g. rods-at-lamellae and balls-at-lamellae) depends upon the chain stretching energy of the A and C domains.

4.3.1 Rods-at-Lamellae

Figure 4.3 shows a simplified model for the rods-at-lamellae morphology. The structure has an overall lamellar repeat spacing of d_l while the rods of B at each AC interface have a spacing of d_i.

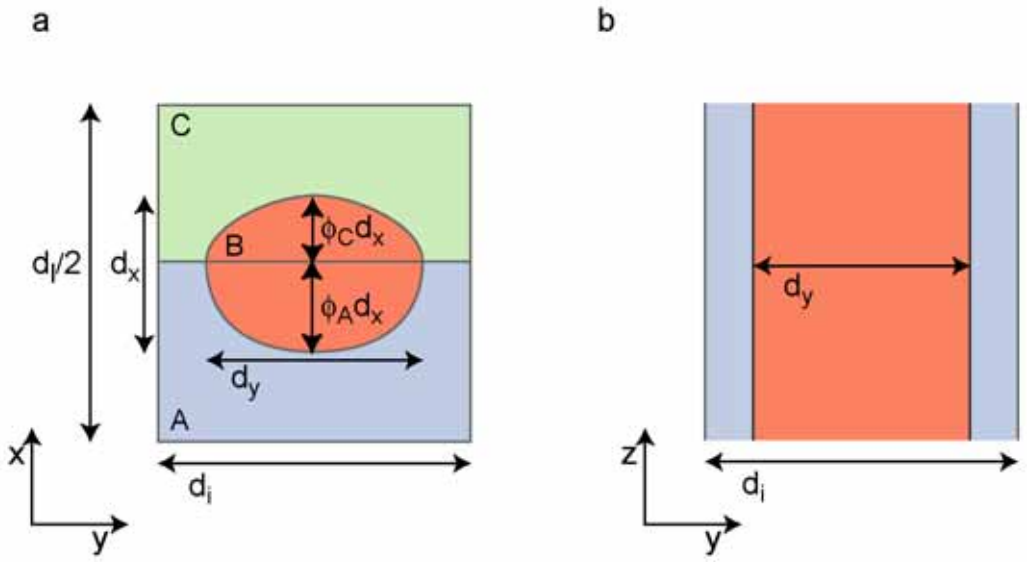

Figure 4.3 - Schematic of a half-cell of the rods-at-lamellae structure viewed from the side (a) and in the AC plane (b). Arrows indicate the lamellar repeat spacing (d_l), in-plane spacing between rods (d_i), width of each rod in the AC interface (d_y) and height of each rod along the lamellar repeat direction (d_x). The B domain projects a distance $\phi_A \times d_x$ into the A lamellae and a distance $\phi_C \times d_x$ into the C lamellae

For ease of calculation, the shape of the AB and BC interfaces can be described by scaling an archetypal profile described by the function,

$$x = h(y), \tag{4-35}$$

defined such that $h(0) = 1$ and $h(1) = 0$. Examples of rectangular, elliptical and parabolic profiles are given in Table 4.1. Using this profile function, the position of the AB interface can be defined as,

$$x_{AB} = -\phi_A d_x h\left(\frac{|y|}{d_y/2}\right) \qquad |y| \le \frac{d_y}{2}, \tag{4-36}$$

and the position of the BC interface is given by,

$$x_{BC} = \phi_C d_x h\left(\frac{|y|}{d_y/2}\right) \qquad |y| \le \frac{d_y}{2}, \tag{4-37}$$

where d_y is the width of the domain along the AC interface (y-axis), d_x is the size of the domain across the AC interface (x-axis) and ϕ_A and ϕ_C the fraction of the B-domain on the A and C sides of the AC interface. The B domain offset (ϕ_A), aspect ratio (d_x/d_y) and in-plane spacing (d_i) can all be optimized so as to minimize the free energy per copolymer. Although this parameterization requires that the B domain is widest at the AC interface, it does allow for the B domain to bulge away from the domain with the larger surface tension. Furthermore, even though the profile of the AB and BC interfaces are not independently optimized, different profiles can be examined to determine the importance of this approximation. Thus, this simple approach provides a fair amount of flexibility in describing the structure of the B domain.

Unit cell dimensions can be conveniently described in terms of the relative to the lamellar repeat spacing using the ratios,

$$\phi_i = \frac{d_i}{d_l/2}, \qquad \phi_a = \frac{d_y}{d_i}, \qquad \phi_A = 1 - \phi_C, \tag{4-38}$$

where ϕ_i is the relative width of the unit cell, ϕ_a the in-plane area occupied by the B domain and ϕ_A the fraction of B-domain volume on the A-side of the AC interface. All quantities within the structure can be described in terms of d_l, ϕ_i, ϕ_a and ϕ_A. For example, volume conservation relates the height (d_x) and area fraction (ϕ_a) of the B-domain by the expression,

$$f_B \times \frac{d_l}{2} = \int_{y=-d_y/2}^{y=d_y/2} d_x h\left(\frac{|y|}{d_y/2}\right)\frac{dy}{d_i} = d_x \phi_a H_{1,\text{rod}} \tag{4-39}$$

where the integrated moments of the profile function are defined as,

$$H_{n,rod} = \int_{y=0}^{y=1} h^n(y)dy\,. \tag{4-40}$$

Table 4.1 summarizes these moments for rectangular, elliptical and parabolic domain profiles.

Table 4.1 - Parameterizations of the AB and BC interface profiles in the rods-at-lamellae structure.

Domain Shape	**h(y)**	**$A_{rod}(\varepsilon)$**	**$H_{1,rod}$**	**$H_{2,rod}$**	**$H_{3,rod}$**
Rectangular	1	$1+\varepsilon$	1	1	1
Elliptical	$(1-y^2)^{1/2}$	[a] $E\left(\sqrt{1-\varepsilon^2}\right)$	$\pi/4$	2/3	$3\pi/16$
Parabolic	$1-y^2$	$\frac{\sqrt{1+4\varepsilon^2}}{2}+\frac{\log\left(\sqrt{1+4\varepsilon^2}+2\varepsilon\right)}{4\varepsilon}$	2/3	8/15	16/35

[a] *Complete elliptic integral of the second kind.*

The aspect ratio of the B-domain can be defined as,

$$\varepsilon = \frac{d_x}{d_y} = \frac{f_B}{\phi_a^2 \phi_i H_{1,rod}}, \tag{4-41}$$

and the area of the AB and BC interfaces are then given by the expressions,

$$A_{AB} = \frac{2V_{\text{cell}}}{d_l} \times \phi_a \times A_{\text{rod}}\left(\frac{2\phi_A f_B}{\phi_a^2 \phi_i H_{1,\text{rod}}}\right), \tag{4-42}$$

$$A_{BC} = \frac{2V_{\text{cell}}}{d_l} \times \phi_a \times A_{\text{rod}}\left(\frac{2\phi_C f_B}{\phi_a^2 \phi_i H_{1,\text{rod}}}\right),$$

where the relative area function, $A_{rod}(\varepsilon)$ is defined as,

$$A_{rod}(\varepsilon) = \int_0^1 \sqrt{1 + \left(\varepsilon \frac{dh}{dy}\right)^2}\, dy \,. \tag{4-43}$$

The relative area functions for rectangular, elliptical and parabolic domain profiles are given in Table 4.1. Using these expressions, the interfacial area coefficients for the AB, BC and AC interfaces are,

$$\varphi_{AB}^{\text{rod}} = A_{\text{rod}}\left(\frac{2\phi_A f_B}{\phi_a^2 \phi_i H_{1,\text{rod}}}\right), \quad \varphi_{AB}^{\text{rod}} = A_{\text{rod}}\left(\frac{2\phi_C f_B}{\phi_a^2 \phi_i H_{1,\text{rod}}}\right), \quad \varphi_{AC}^{\text{rod}} = 1 \,. \tag{4-44}$$

Determining the average root mean square chain lengths in the rods-at-lamellae structure is challenging because spatial distribution of chain ends at the AB and BC interfaces is non-uniform (Matsen, 2002). As shown in Figure 4.4, chains in A domain stretch both down (x-axis) and across (y-axis) to enter the B domain. Stretching of the A chains would be minimized if each chain extended to the closest point on the AB interface. This arrangement (e.g. Figure 4.4d) leads to a low density of chain junctions at the middle of the AB interface ($y = 0$) and a higher density of chain-junctions at the edges ($|y| \approx d_y$). In contrast, the stretching energy of the B-domains is low when the B chains stretch along the lamellae normal (x-axis). This arrangement results in a higher chain junction density where the B-domain is thickest ($y = 0$) and a lower chain junction density where the B domain thinnest ($|y| \approx d_y$). Because the spatial distribution of A and B block ends must match at each point on the AB interface, the actual arrangement is a compromise between these two extremes (Matsen, 2002). Failure to consider this constraint can lead to non-physical predictions (Matsen, 2003).

In this work, a simple description of each structure is obtained by estimating the lateral (y-axis) stretching. However, it should be noted that schemes do exist to match the distribution of A and B block ends (Likhtman and Semenov, 1997; Olmsted and Milner, 1998) at the AB interface.

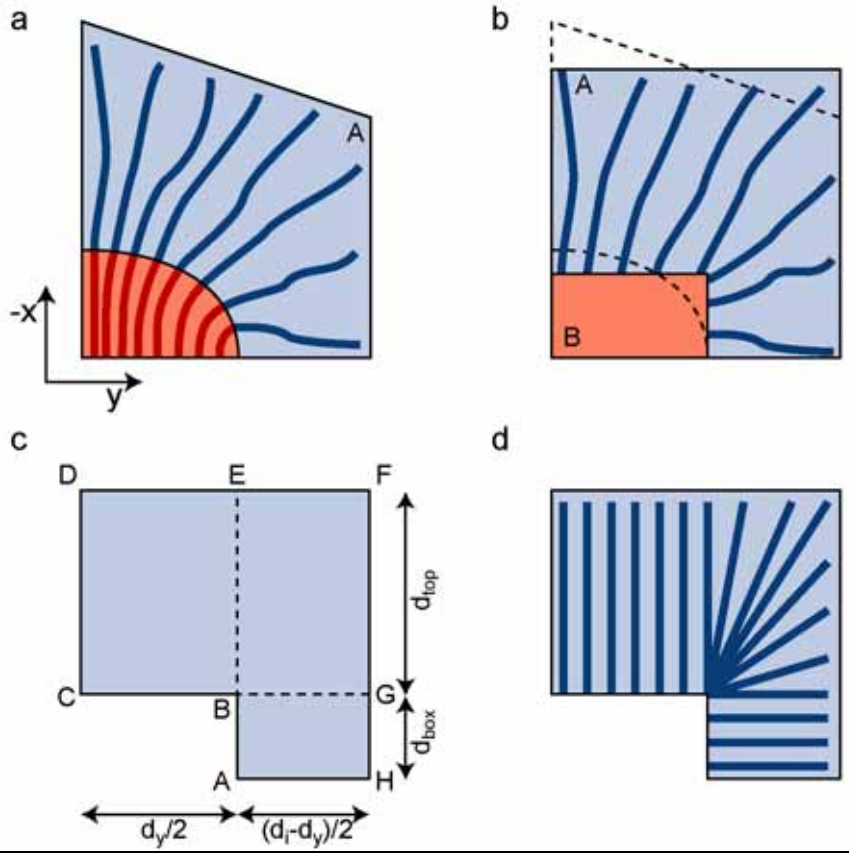

Figure 4.4 – Approximation of A domain in the rods-at-lamellae structure. (a) In the actual structure, the AB interface is curved and the outer boundary of the A domain is approximately hexagonal. (b,c) Rectangular approximation in which the inner AB interface is treated as a rectangle (width d_y and height d_{box}) with the same volume as the curved B domain. The outer A domain boundary can also be approximated by a rectangle (width d_i and height $d_{top}+d_{box}$). (d) Stretching of A chains to the closest point on the AB interface concentrates the A chain ends at the corner (point B) of the AB domain.

For the B domain, stretching can be approximated by assuming that the chains extend parallel to the x-axis. In this case,

$$R_B^2 = \int_{y=0}^{y=1} \left(d_x h(y)\right)^2 \frac{h(y)dy}{H_{1,\text{rod}}}, \qquad (4\text{-}45)$$

$$= \frac{f_B^2 H_{3,\text{rod}}}{\phi_a^2 H_{1,\text{rod}}^3} \times \left(\frac{d_l}{2}\right)^2,$$

and so,

$$\eta_B^{\text{rod}} = \frac{H_{3,\text{rod}}}{H_{1,\text{rod}}^3} \,. \tag{4-46}$$

This arrangement of chains is physically achievable but the resulting concentration of chain junctions at the middle ($y = 0$) of the B domain requires increased lateral (y-axis) stretching of the A and C chains.

For the outer A and C domains, the shape of both the inner and outer surfaces of the A domain can be approximated by rectangles, as shown in Figure 4.4a. This approximation makes it much easier to calculate distance from any point to the AB interface. Because the AB and BC interfaces are convex, using Equation 4-16 may cause a slight under-estimate of stretching in the A and C domains (Matsen, 2002). The size of this error has previously been studied for cylindrical domains (Ball et. al. 1991) and was shown to be small in comparison to the errors induced by approximating the shape of domain boundaries (Likhtman and Semenov, 1994). Finally, the average stretching of the A chains depends upon where they are connected to the AB interface.

As shown in Figure 4.4d, the least stretching occurs when each chain extends to the nearest point on the AB interface. For this arrangement of chains, the average squared distance to the interface is given by,

$$\left\langle z_A^2 \right\rangle = \frac{f_A^2 d_I^2}{12}\left(\left(1 - \frac{f_B\phi_A}{f_A}\left(\frac{1}{\phi_a} - 1\right)\right)^3 + \left(\frac{\phi_i}{2f_A}\right)^2 \times \left(1 + \frac{f_B\phi_A}{f_A}\right) \times \left(1 - \phi_a\right)^3\right), \tag{4-47}$$

resulting in a value for η_A of,

$$\eta_A^{\text{rod,low}} = \left(1 - \frac{f_B\phi_A}{f_A}\left(\frac{1}{\phi_a} - 1\right)\right)^3 + \left(\frac{\phi_i}{2f_A}\right)^2 \times \left(1 + \frac{f_B\phi_A}{f_A}\right) \times \left(1 - \phi_a\right)^3 . \tag{4-48}$$

However, this organization of the chains concentrates the AB chain junctions at the "corners" of each domain (point B in Figure 4.4c). Since the chains in the A domain

must stretch across to achieve a more even distribution at the AB interface, Equation 4-48 provides a lower estimate for stretching in the A domain.

To reach the B domain, chains starting from the edge of the unit cell (line FGH in Figure 4.4c) must stretch sideways by a distance of at least $(d_i\text{-}d_y)/2$. Assuming that every chain stretches sideways by this distance (and that stretching along the x-axis is unchanged from the triple-lamellae structure),

$$\eta_A^{\text{rod,high}} = 1 + \frac{12}{\pi^2} \times \left(\frac{\phi_i}{2 f_A} \right)^2 \times (1 - \phi_a)^2 . \tag{4-49}$$

Equation 4-49 should represent a high estimate of the chain stretching in the A domain since the many chains can stretch sideways by less than $d_i/2\text{-}d_y/2$,.

The actual stretching in the A domain should lie between these two extremes. Chains in the outer (Rectangle CDFG in Figure 4.4c) portion of the A domain must at least stretch down to the top of the B domain (line CB). Assuming the amount of lateral (y-axis) stretching is proportional to the lateral distance from the B-domain center, the distance from a point (x, y) to the AB interface is then given by,

$$z_A(x, y) = \sqrt{(x + d_{box})^2 + \left(\frac{2y}{d_i} \right)^2 \times \left(\frac{d_i - d_y}{2} \right)^2} . \tag{4-50}$$

For the inner portion of the A domain (Rectangle ABGH in Figure 4.4c), chains must stretch across to the side of the B domain (line AB). As indicated in Figure 4.4a, these chains also stretch along the x-axis. This extension can be roughly estimated by attaching all chains to point A, where the AB and AC interfaces meet. With this assumption the stretching in the inner region is given by,

$$z_A(x, y) = \sqrt{x^2 + \left(y - \frac{d_y}{2} \right)^2} . \tag{4-51}$$

Using these approximate distance functions, an intermediate estimate of chain stretching can be obtained,

$$\eta_A^{\text{rod,imd}}{}_A = \left(1 - \frac{f_B \phi_A}{f_A}\left(\frac{1}{\phi_a} - 1\right)\right)^3 + \left(\frac{f_B \phi_A}{f_A \phi_a}\right)^3 \times (1 - \phi_a) + \left(\frac{\phi_i}{2 f_A}\right)^2 \times (1 - \phi_a)^2 . \tag{4-52}$$

Since the A and C domains share the same geometry, expressions for η_C have the same form as those for η_A. For example, for the intermediate chain stretching approximation,

$$\eta_C^{\text{rod,imd}} = \left(1 - \frac{f_B \phi_C}{f_C}\left(\frac{1}{\phi_a} - 1\right)\right)^3 + \left(\frac{f_B \phi_C}{f_C \phi_a}\right)^3 \times (1 - \phi_a) + \left(\frac{\phi_i}{2 f_C}\right)^2 \times (1 - \phi_a)^2 . \tag{4-53}$$

Figure 4.5 illustrates the effect of the low, intermediate and high estimates of chain stretching on the free energy per copolymer for a rods-at-lamellae structure when the A and C blocks are symmetric ($f_A = f_C$; $p = p_A = p_C$; $\gamma = \gamma_{AB} = \gamma_{BC}$) and $\gamma_{AC} = 0$ ($p_B = p$). When $\gamma_{AC} = 0$, the Gibbs free energy of the rods-at-lamellae structure should be similar to that for an ABA triblock copolymer cylinder structure in which the B block forms cylindrical domains embedded in a matrix formed by the A block. For the ABA cylinder structure, the A domain can be approximated by a coaxial cylinder surrounding the inner B domain and the free energy per copolymer is then,

$$\frac{G^{\text{ABA cylinders}}}{k_B T} = 3 \times \left(\frac{\pi}{2}\right)^{2/3} \times \gamma_{AB}^{2/3} \times \left(p_B + \frac{p_A\left(1 - f_B^{1/2}\right)^3 \times \left(3 + f_B^{1/2}\right)}{\left(1 - f_B\right)^2}\right)^{1/3} \times f_B^{1/3} \times V^{1/3} , \tag{4-54}$$

while the diameter of the cylinders is,

$$d^{\text{ABA cylinders}} = \frac{2^{5/3}}{\pi^{2/3}} \times \gamma_{AB}^{1/3} \times \left(p_B + \frac{p_A\left(1 - f_B^{1/2}\right)^3 \times \left(3 + f_B^{1/2}\right)}{\left(1 - f_B\right)^2}\right)^{-1/3} \times f_B^{1/6} \times V^{2/3} . \tag{4-55}$$

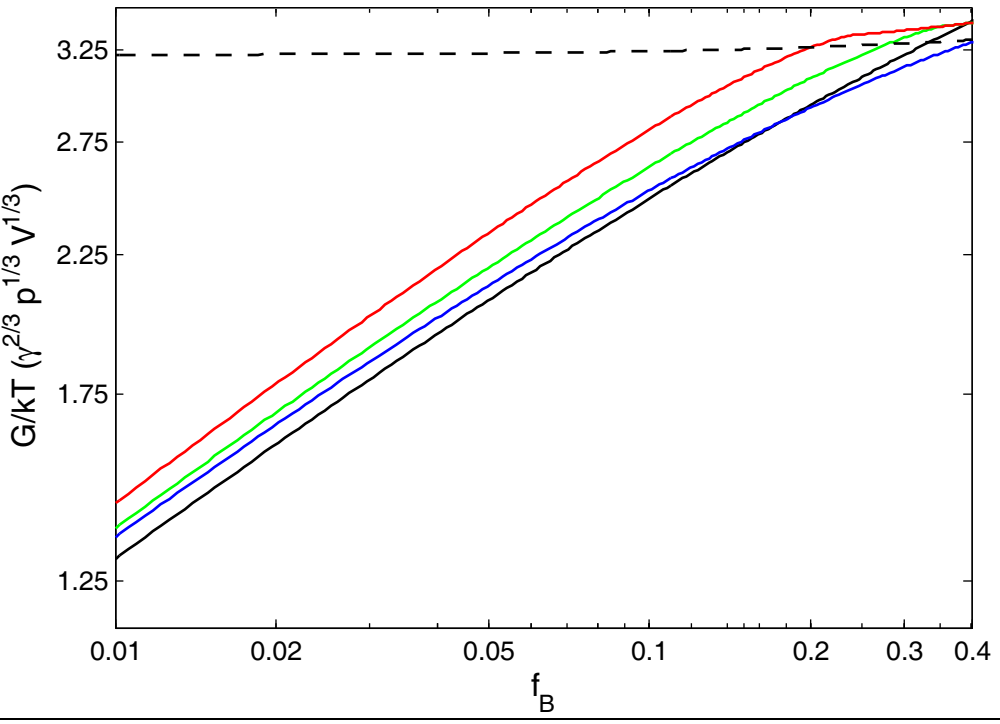

Figure 4.5 – Effects of approximations on Gibbs free energy per Copolymer (G) for the Rods-at-Lamellae structure in ABC copolymers with symmetric A and C blocks ($f_A = f_C$; $p = p_A = p_C$; $\gamma = \gamma_{AB} = \gamma_{BC}$) in which $\gamma_{AC} = 0$ and $p_B = p$. Low estimate of A/C chain stretching (blue; Equation 4-48). Intermediate Estimate of A/C chain stretching (green; Equations 4-52 and 4-53). High estimate of A/C chain stretching (red; Equation 4-49). ABA diblock cylinder Free Energy (black; Equation 4-54). ABCBA Triple-Lamellae Free Energy (black dashed; Equation 4-20). The shape of the AB and BC interfaces are assumed to be elliptical.

$G^{\text{ABA cylinders}}$ scales roughly as $f_B^{1/3}$, and when $\gamma_{AC} = 0$, the free energy of the rods-at-lamellae structure shares this approximate $f_B^{1/3}$ scaling. For all three estimates of chain stretching, reducing the B domain volume fraction (f_B) induces a transition from the triple-lamellae structure. However, a discrepancy is evident for the low stretching estimate (Equation 4-48). In an ABC copolymer in the SSL, chains in the B domain of the rods-at-lamellae structure must still stretch between the AB and BC interfaces, even when $\gamma_{AC} = 0$. This constraint is not present in the ABA cylinder

structure and so for volume fractions where the ABA cylinder structure is the equilibrium diblock morphology ($0.1 < f_B < 0.3$), the ABA cylinder structure should have a lower free energy per copolymer than the rods-at-lamellae structure. Both the intermediate (Equations 4-52 and 4-53) and high (Equation 4-49) estimates of chain stretching satisfy this requirement but the free energy calculated using the low estimate (Equation 4-48) does not. Thus, the lower estimate of chain stretching is demonstrably too low and should not be used to calculate phase boundaries. In the remainder of this chapter, the free energy of the rods-at-lamellae structure is calculated using the intermediate estimate of chain stretching.

The effect of the profile of the AB and BC interfaces can be gauged from the difference in free energy for rods-at-lamellae structures with elliptical, rectangular and parabolic domain boundaries (Figure 4.6). Unsurprisingly, the elliptical profile yields the lowest free energy and is used throughout the remainder of this chapter. At intermediate values of f_B (~ 0.1), the choice of chain stretching estimate or interfacial profile changes the free energy per copolymer by roughly 2% to 4% of the free energy of the triple-lamellae structure (G_{TL}). Such shifts have a significant effect on the B domain volume fraction (f_B) at which the triple-lamellae $\rightarrow$ rods-at-lamellae transition occurs. However, in the limit as $f_B \rightarrow 0$, the free energy per copolymer of the rods-at-lamellae approaches that of an AC double-lamellae structure (Equation 4-22) no matter which chain stretching estimate or interfacial profile is used.

Finally, it is interesting to explore the effect of internal unit cell dimensions on the calculated free energy. In the work of Zheng and Wang (Zheng and Wang, 1995), the in-plane rod-spacing (d_i) was optimized but the rods were assumed to have a circular profile ($d_x = d_y$). As shown in Figure 4.6, the free energy per copolymer is higher when the domain profile is held constant. However, in the limit as $f_B \rightarrow 0$, the

free energy per copolymer of the rods-at-lamellae still approaches that of an AC double-lamellae structure (Equation 4-22). In contrast, in the work of Stadler and colleagues (Stadler et. al. 1995) the in-plane rod spacing was assumed to be constant ($d_i = d_l/2$) and the rods had a circular profile ($d_x = d_y$). These assumptions can lead to a substantial over-estimate of the free energy, even as $f_B \rightarrow 0$.

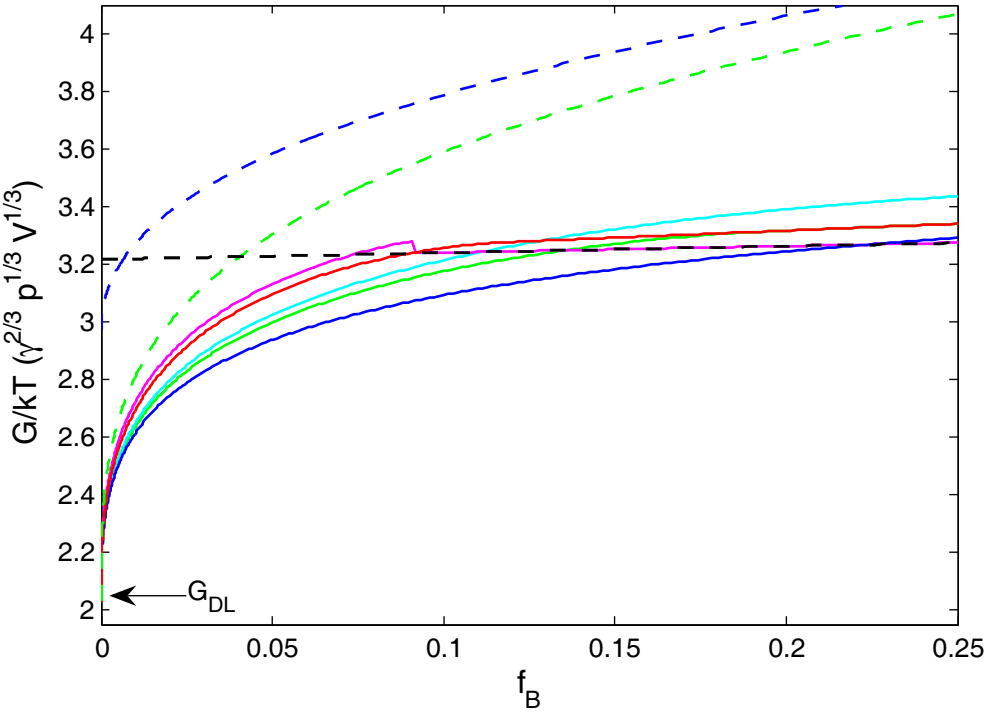

Figure 4.6 – Effect of approximations on Gibbs Free Energy per Copolymer (G) for the Rods-at-Lamellae structure in ABC copolymers with symmetric A and C blocks ($f_A = f_C$; $p = p_A = p_C$; $\gamma = \gamma_{AB} = \gamma_{BC}$) in which $\gamma_{AC} = \gamma_{AB}$ and $p_B = p$. Low estimate of A/C chain stretching (blue; Equation 4-48). Intermediate Estimate of A/C chain stretching (green; Equations 4-52 and 4-53). High estimate of A/C chain stretching (red; Equation 4-49). Parabolic B domain profile (cyan; Table 4.1). Rectangular B domain profile (magenta, Table 4.1). Circular B domain profile ($d_x = d_y$) as in the calculations of Zheng and Wang, 1995 (green dotted). Circular B domain profile ($d_x = d_y$) and fixed in-plane rod spacing of $d_{cyl}=d_l/2$ as in Stadler et. al. 1995 (blue dotted). Triple-Lamellae Free Energy (black dotted; Equation 4-20). The arrow marks the Free Energy for an AC Double-Lamellae structure (Equation 4-22).

4.3.2 Balls-at-Lamellae

The balls-at-lamellae structure may be treated in an analogous fashion to the rods-at-lamellae structure. Figure 4.7 shows a simplified model of the balls-at-lamellae domain in which the Wigner-Seitz cell is approximated by a cylinder of diameter d_i and length $d_l/2$.

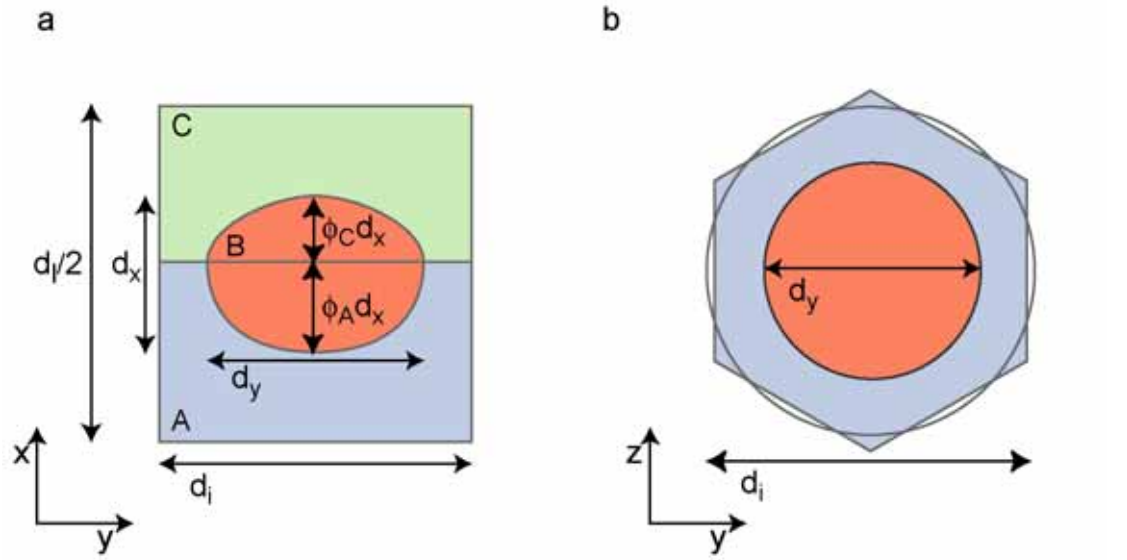

Figure 4.7 – Schematics of a half-cell of the balls-at-lamellae viewed from the side (a) and in the AC plane (b). Arrows indicate the lamellar repeat spacing (d_l), average in-plane distance between the B domains (d_i), diameter of the B-domain in the AC interface (d_y) and height of the ball along the lamellar repeat direction (d_x). The B domain projects a distance $\phi_A \times d_x$ into the A lamellae and a distance $\phi_C \times d_x$ into the C lamellae. The over-head view (b) indicates how the hexagonal perimeter of the unit cell can be approximated by a circular perimeter that encloses the same total area.

The internal unit cell dimensions may be described in terms of dimensionless ratios,

$$\phi_i = \frac{d_i}{d_l/2}, \qquad \phi_a = \frac{d_y^2}{d_i^2}, \qquad 1 = \phi_A + \phi_C, \tag{4-56}$$

where d_y is the diameter of the B-domain and ϕ_A and ϕ_C are the volume fractions of the B domain on the A and C sides of the AC interface (y-z plane). As for the rods-at-

lamellae structure, the AB and BC domain interfaces can be defined by an archetypal profile function of the form,

$$x = h(r) \tag{4-57}$$

where *h(0)* = 1 and *h(1)* = 0. The AB domain boundary is then given by,

$$x_{AB} = -\phi_A d_x h\left(\frac{\sqrt{y^2+z^2}}{d_y/2}\right) \qquad \sqrt{y^2+z^2} \le \frac{d_y}{2}, \tag{4-58}$$

and the BC domain boundary by,

$$x_{BC} = \phi_C d_x h\left(\frac{\sqrt{y^2+z^2}}{d_y/2}\right) \qquad \sqrt{y^2+z^2} \le \frac{d_y}{2}, \tag{4-59}$$

where d_x is the height of the domain across the AC interface (x-axis). By volume conservation, the height (d_x) and area fraction are related by,

$$d_x = \frac{1}{\phi_a H_{1,\text{ball}}} \times \frac{f_B d_l}{2}, \tag{4-60}$$

where the integral moments of the ball are defined as,

$$H_{\text{n,ball}} = \int_{r=0}^{r=1} h^n(r) \times 2r dr. \tag{4-61}$$

Table 4.2 summarizes these moments for spheroidal, parabolic and disk profiles. The interfacial area coefficients depend upon the aspect ratio of the B-domain,

$$\varepsilon = \frac{d_x}{d_y} = \frac{f_B}{\phi_a^{3/2}\phi_i H_{1,\text{ball}}}, \tag{4-62}$$

and the relative area function,

$$A_{\text{ball}}(\varepsilon) = \int_{r=0}^{r=1} \sqrt{1+\left(\varepsilon\frac{dh}{dr}\right)^2} \times 2r dr. \tag{4-63}$$

Relative area functions for spheroidal, parabolic and disk profiles are given in Table 4.2. The interfacial area coefficients for the AB, BC and AC interfaces are,

$$\varphi_{AB}^{\text{ball}} = A_{\text{ball}}\left(\frac{2\phi_A f_B}{\phi_a^{3/2}\phi_i H_{1,\text{ball}}}\right), \quad \varphi_{BC}^{\text{ball}} = A_{\text{ball}}\left(\frac{2\phi_C f_B}{\phi_a^{3/2}\phi_i H_{1,\text{ball}}}\right), \quad \varphi_{AC}^{\text{ball}} = 1. \tag{4-64}$$

Table 4.2 - Parameters for the B-domain shape in the balls-at-lamellae structure.

Domain Shape	**h(y)**	**$A_{ball}(\varepsilon)$**	**$H_{1,ball}$**	**$H_{2,ball}$**	**$H_{3,ball}$**
Disk	1	$1+2\varepsilon$	1	1	1
Spheroidal	$(1-y^2)^{1/2}$	$1+\frac{\varepsilon^2}{\sqrt{1-\varepsilon^2}}\log\left(\frac{1+\sqrt{1-\varepsilon^2}}{\varepsilon}\right)$	2/3	1/2	2/5
Parabolic	$1-y^2$	$\frac{2}{3}\times\left(\sqrt{1+4\varepsilon^2}+\frac{1}{\sqrt{1+4\varepsilon^2}+1}\right)$	1/2	1/3	1/4

Turning to chain stretching, the RMS length of the B block can again be estimated by assuming the chains run parallel to the lamellar axis. Thus,

$$\eta_B^{\text{ball}} = \frac{H_{3,\text{rod}}}{H_{1,\text{rod}}^3} \tag{4-65}$$

For the A domains, the outer and inner surfaces can be approximated by rectangular shapes analogous to those shown in Figure 4.4. Again, estimates of η_A depend on the distribution of chain ends at the AB interface. If the chains stretch to the nearest point on the AB interface (low estimate) then,

$$\eta_A^{\text{ball,low}} = \left(1-\frac{f_B\phi_A}{f_A}\left(\frac{1}{\phi_a}-1\right)\right)^3 + \left(\frac{\phi_i}{2f_A}\right)^2 \times \left(1-\phi_a^{1/2}\right)^3 \times \frac{3+\phi_a^{1/2}}{2} \times \left(1+\frac{f_B\phi_A}{f_A}\right). \tag{4-66}$$

If the lateral chain stretching is proportional to the distance from the center of the B-domain (intermediate estimate), then,

$$\eta_A^{\text{ball,imd}} = \left(1-\frac{f_B\phi_A}{f_A}\left(\frac{1}{\phi_a}-1\right)\right)^3+\left(\frac{f_B\phi_A}{f_A\phi_a}\right)^3\times(1-\phi_a) \qquad (4\text{-}67)$$
$$+\left(\frac{\phi_i}{2f_A}\right)^2\times\left(1-\phi_a^{1/2}\right)^2\times\left(\frac{3}{2}-\frac{f_B\phi_A}{f_A}\times\left(\frac{1}{\phi_a}-1\right)\times\frac{\phi_a^{1/2}}{1+\phi_a^{1/2}}\right).$$

Finally, if all A chains stretch laterally by an amount (d_i/2-d_y/2) (high estimate), then,

$$\eta_A^{\text{ball,high}} = 1+\frac{12}{\pi^2}\times\left(\frac{\phi_i}{2f_A}\right)^2\times\left(1-\phi_a^{1/2}\right)^2. \qquad (4\text{-}68)$$

The expressions for η_C have the same form as those for η_A. For example, using the intermediate chain stretching approximation,

$$\eta_C^{\text{ball,imd}} = \left(1-\frac{f_B\phi_C}{f_C}\left(\frac{1}{\phi_a}-1\right)\right)^3+\left(\frac{f_B\phi_C}{f_C\phi_a}\right)^3\times(1-\phi_a) \qquad (4\text{-}69)$$
$$+\left(\frac{\phi_i}{2f_C}\right)^2\times\left(1-\phi_a^{1/2}\right)^2\times\left(\frac{3}{2}-\frac{f_B\phi_C}{f_C}\times\left(\frac{1}{\phi_a}-1\right)\times\frac{\phi_a^{1/2}}{1+\phi_a^{1/2}}\right).$$

Figure 4.8 illustrates the effect of low, intermediate and high estimates of chain stretching on the free energy of the balls-at-lamellae structure for ABC copolymers in which the A and C domains are symmetric ($f_A = f_C$; $p = p_A = p_C$; $\gamma = \gamma_{AB} = \gamma_{BC}$) and $\gamma_{AC} = 0$ ($p_B = p$). In this case the free energy per copolymer for the balls-at-lamellae structure should be similar to that for an ABA triblock sphere phase in which spherical B domains are embedded in a matrix formed by the A block. For the ABA sphere structure, the shape of the A domain can be approximated by a spherical shell surrounding the inner B sphere. With this simplification, the free energy per copolymer of the ABA sphere phase is,

$$\frac{G^{\text{ABA sphere}}}{k_BT} = \frac{9\pi^{2/3}\times\gamma_{AB}^{2/3}}{2\times10^{1/3}}\times f_B^{1/3}\times V^{1/3} \qquad (4\text{-}70)$$
$$\times\left(p_B+\frac{p_A f_B^{1/3}\left(1-f_B^{1/3}\right)^3\times\left(6+3f_B^{1/3}+f_B^{2/3}\right)}{\left(1-f_B\right)^2}\right)^{1/3},$$

while the diameter of the ABA sphere is,

$$d^{\text{ABA sphere}} = \frac{2\times 10^{1/3}}{\pi^{2/3}} \times \gamma_{AB}^{1/3} \times f_B^{1/3} \times V^{2/3} \times \left(p_B + \frac{p_A f_B^{1/3}\left(1-f_B^{1/3}\right)^3 \times \left(6+3f_B^{1/3}+f_B^{2/3}\right)}{\left(1-f_B\right)^2} \right)^{-1/3} . \tag{4-71}$$

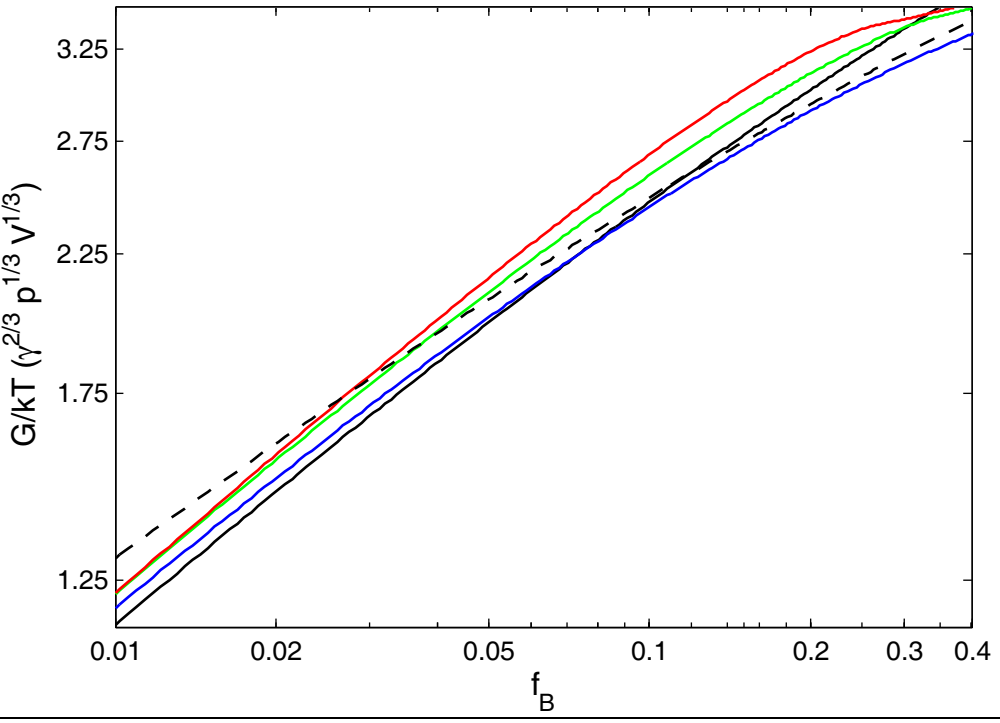

Figure 4.8 – Effects of approximations on Gibbs free energy per copolymer (G) for the Balls-at-Lamellae morphology in ABC copolymers with symmetric A and C blocks ($f_A = f_C$; $p = p_A = p_C$; $\gamma = \gamma_{AB} = \gamma_{BC}$) where $\gamma_{AC} = 0$ and $p_B = p$. Low estimate of A/C chain stretching (blue; Equation 4-66). Intermediate Estimate of A/C chain stretching (green; Equations 4-67 and 4-69). High estimate of A/C chain stretching (red; Equation 4-68). ABA diblock sphere Free Energy (black solid; Equation 4-70). ABA lamellae Free Energy (black dashed; Equation4-54). The shape of the AB and BC interfaces are assumed to be spheroidal.

$G^{\text{ABA, sphere}}$ scales roughly as $f_B^{1/3}$ and for the B domain volume fractions where the ABA sphere structure is the equilibrium morphology (f_B<0.1), $G^{\text{ABA,sphere}}$ should be smaller than the free energy per copolymer of the balls-at-lamellae structure. As is evident in Figure 4.8, when $\gamma_{AC} = 0$, the free energy of the balls-at-lamellae structure also scales roughly as $f_B^{1/3}$. However, the free energy calculated using the low estimate (Equation 4-66) is clearly too small as it both intersects with $G^{\text{ABA, sphere}}$ and never exceeds the free energy of the ABA cylinder phase. Thus, the lower estimate of chain stretching should not be used to calculate phase boundaries. In contrast, the free energy calculated using the intermediate estimate of chain stretching is greater than $G^{\text{ABA, sphere}}$ and also greater than $G^{\text{ABA,cylinder}}$ for $f_B > 0.04$. Consequently, the intermediate estimate of chain stretching (Equations 4-67 and 4-69) is employed in the remainder of the chapter.

4.3.3 Perforated-Lamellae

The perforated B-lamellae structure shown in Figure 4.9 represents a third way in which a structure with A and C lamellae can reduce the area of the mandatory AB and BC interfaces. As for the perforated lamellar structure in AB diblock copolymers (Fredrickson, 1991), analysis of this structure is greatly simplified by approximating the Wigner-Seitz cell with a cylinder of diameter d_i and length $d_l/2$. The internal cell dimensions can again be expressed as dimensionless ratios,

$$\phi_i = \frac{d_i}{d_l/2}, \qquad \phi_a = \frac{2d_y d_i - d_y^2}{d_i^2}, \qquad 1 = \phi_A + \phi_C, \tag{4-72}$$

where d_i-d_y is the diameter of the perforation and ϕ_A and ϕ_C are the volume fractions of the B domain on the A and C sides of the AC interface (y-z plane). The AB and BC domain interfaces can again be described by an archetypal profile function of the form,

$$x = h(r) \tag{4-73}$$

where *h(0)* = 1 and *h(1)* = 0. The AB domain boundary is then,

$$x_{AB} = -\phi_A d_x h\left(\frac{d_i/2 - \sqrt{y^2+z^2}}{d_y/2}\right) \qquad \frac{d_i - d_y}{2} \le \sqrt{y^2+z^2} \le \frac{d_i}{2}, \tag{4-74}$$

and the BC domain boundary by,

$$x_{BC} = \phi_C d_x h\left(\frac{d_i/2 - \sqrt{y^2+z^2}}{d_y/2}\right) \qquad \frac{d_i - d_y}{2} \le \sqrt{y^2+z^2} \le \frac{d_i}{2}, \tag{4-75}$$

where d_x is the height of the domain across the AC interface (x-axis).

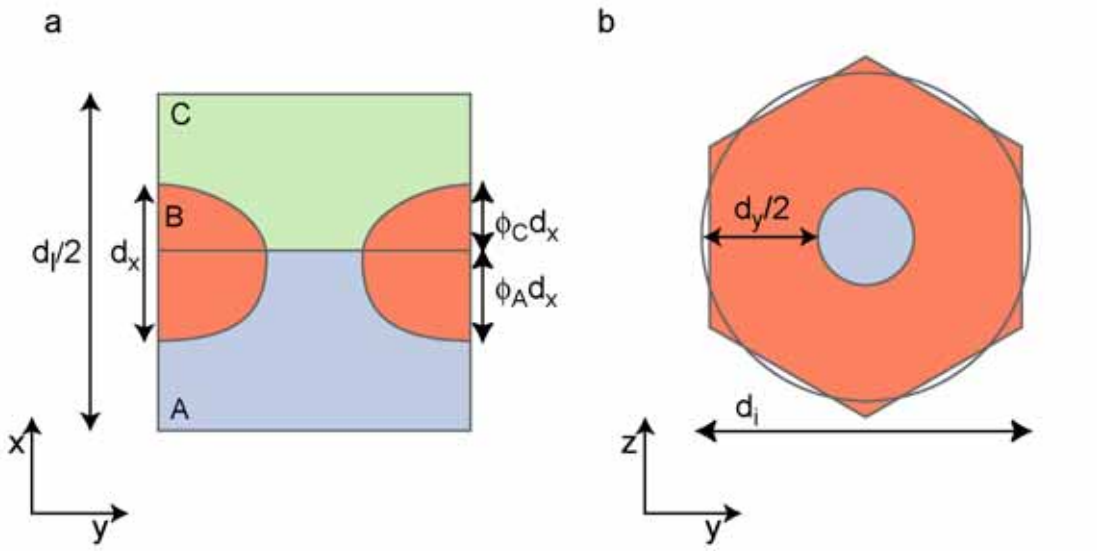

Figure 4.9 –Views of a half-cell of the perforated B-lamellae viewed from the side (a) and in the AC plane (b). Arrows indicate the lamellar repeat spacing (d_l), average in-plane distance between each perforation (d_i), average width of the B-domain in the AC interface (d_y) and height of the B-domain along the lamellar repeat direction (d_x). The B domain projects a distance $\phi_A \times d_x$ into the A lamellae and a distance $\phi_C \times d_x$ into the C lamellae. The over-head view (b) indicates how the hexagonal cell perimeter can be approximated by a circular perimeter that encloses the same total area.

By volume conservation, the height (d_x) and area fraction are related by,

$$d_x = \frac{1}{\phi_a H_{1,\mathrm{perf}}(\phi_a)} \times \frac{f_B d_l}{2}, \tag{4-76}$$

where the integral moments of can be defined as,

$$\begin{aligned} H_{\mathrm{n,perf}}(\phi_a) &= \int_{r'=0}^{r'=1} h^n(r') \times \frac{2(d_i - d_y r')dr'}{2d_i - d_y} \\ &= \frac{2H_{n,rod} - \left(1-\sqrt{1-\phi_a}\right)H_{n,ball}}{1+\sqrt{1-\phi_a}}. \end{aligned} \tag{4-77}$$

The interfacial area coefficients depend upon the aspect ratio of the B-domain,

$$\varepsilon = \frac{d_x}{d_y} = \frac{f_B\left(1+\sqrt{1-\phi_a}\right)}{\phi_h \phi_a^2 H_{1,\mathrm{perf}}(\phi_a)}, \tag{4-78}$$

and the relative area function,

$$\begin{aligned} A_{\mathrm{perf}}(\varepsilon,\phi_a) &= \int_{r'=0}^{r'=1} \sqrt{1+\left(\varepsilon\frac{dh}{dr}\right)^2} \times \frac{2d_i - 2d_r r'}{2d_i - d_y} \times dr' \\ &= \frac{2A_{\mathrm{rod}}(\varepsilon) - \left(1-\sqrt{1-\phi_a}\right)A_{\mathrm{ball}}(\varepsilon)}{1+\sqrt{1-\phi_a}}. \end{aligned} \tag{4-79}$$

The interfacial area coefficients for the AB, BC and AC interfaces are then,

$$\varphi_{AB}^{\mathrm{perf}} = A_{\mathrm{perf}}\left(\frac{2\phi_A f_B\left(1+\sqrt{1-\phi_a}\right)}{\phi_a^2 \phi_i H_{1,\mathrm{perf}}(\phi_a)}\right), \quad \varphi_{BC}^{\mathrm{perf}} = A_{\mathrm{ball}}\left(\frac{2\phi_C f_B\left(1+\sqrt{1-\phi_a}\right)}{\phi_a^2 \phi_i H_{1,\mathrm{perf}}(\phi_a)}\right), \quad \varphi_{AC}^{\mathrm{perf}} = 1. \tag{4-80}$$

Turning to chain stretching, the RMS length of the B block can again be approximated by assuming the chains run parallel to the lamellar axis to give,

$$\eta_B^{\mathrm{perf}} = \frac{H_{3,\mathrm{perf}}(\phi_a)}{H_{1,\mathrm{perf}}^3(\phi_a)} \tag{4-81}$$

For the A/C domains, the AB/BC interface can be approximated by a rectangular profile. If the chains stretch to the nearest point on the AB interface (lower estimate) then,

$$\eta_A^{\mathrm{perf,low}} = \left(1 - \frac{f_B\phi_A}{f_A}\left(\frac{1}{\phi_a} - 1\right)\right)^3 + \frac{1}{2} \times \left(\frac{\phi_i}{2f_A}\right)^2 \times \left(1 + \frac{f_B\phi_A}{f_A}\right) \times \left(1-\phi_a\right)^2. \tag{4-82}$$

If the lateral chain stretching is proportional to the distance from the edge of the Wigner-Seitz cell (intermediate estimate),

$$\eta_A^{\text{perf,imd}} = \left(1 - \frac{f_B\phi_A}{f_A}\left(\frac{1}{\phi_a} - 1\right)\right)^3 + \left(\frac{f_B\phi_A}{f_A\phi_a}\right)^3 \times (1-\phi_a) + \frac{1}{2} \times \left(\frac{\phi_i}{2f_A}\right)^2 \times (1-\phi_a). \quad (4\text{-}83)$$

Finally, if all A chains stretch laterally by an amount $(d_i\text{-}d_y)/2$ (overestimate),

$$\eta_A^{\text{perf,high}} = 1 + \frac{12}{\pi^2} \times \left(\frac{\phi_i}{2f_A}\right)^2 \times (1-\phi_a). \quad (4\text{-}84)$$

Expressions for η_C have the same form as those for η_A. For example, for the intermediate chain stretching approximation,

$$\eta_C^{\text{perf,imd}} = \left(1 - \frac{f_B\phi_C}{f_C}\left(\frac{1}{\phi_a} - 1\right)\right)^3 + \left(\frac{f_B\phi_C}{f_C\phi_a}\right)^3 \times (1-\phi_a) + \frac{1}{2} \times \left(\frac{\phi_i}{2f_C}\right)^2 \times (1-\phi_a). \quad (4\text{-}85)$$

4.3.4 Rings-at-Cylinders

In the rings-at-cylinders structure, the A and C domains form concentric cylinders as shown in Figure 4.10. Because the shape of the A and C domains are not equivalent, the rings-at-cylinders structure would not be expected when the A and C blocks are symmetric ($f_A = f_C$, $p_A = p_C$, $\gamma_{AB} = \gamma_{BC}$). However, Stadler and colleagues calculated the free energy for a model of the rings-at-cylinder structure and reported that for some parameters, the rings-at-cylinder structure had a lower free energy than any of the lamellar structures (Stadler, et. al. 1995). In contrast, Zheng and Wang (Zheng and Wang, 1995) reported the rings-at-cylinders structure only formed when the molecular properties of the A and C blocks were not equivalent (eg. $f_A \neq f_C$, $p_A \neq p_C$ or $\gamma_{AB} \neq \gamma_{BC}$). In this section a SSL treatment of the rings-at-cylinder structure is developed to resolve these differences.

For simplicity, the Wigner-Seitz cell was approximated by as a cylinder of diameter, d_{cyl}, and length d_i. The B-domain was approximated as toroid with inner and

outer halves given by an archetypal profile function, *h(y)*. The surface of the AB domain is then given by,

$$\sqrt{x^2+z^2} = \frac{d_{AC}}{2} - r_{AB}h\left(\frac{2|y|}{d_y}\right) \qquad |y| < \frac{d_y}{2}, \tag{4-86}$$

and the BC domain surface by,

$$\sqrt{x^2+z^2} = \frac{d_{AC}}{2} + r_{BC}h\left(\frac{2|y|}{d_y}\right) \qquad |y| < \frac{d_y}{2}, \tag{4-87}$$

where d_{AC} is the diameter of the cylindrical AC interface, r_{AB} is the radius of the inner half-toroid and r_{BC} the radius of the outer half-toroid.

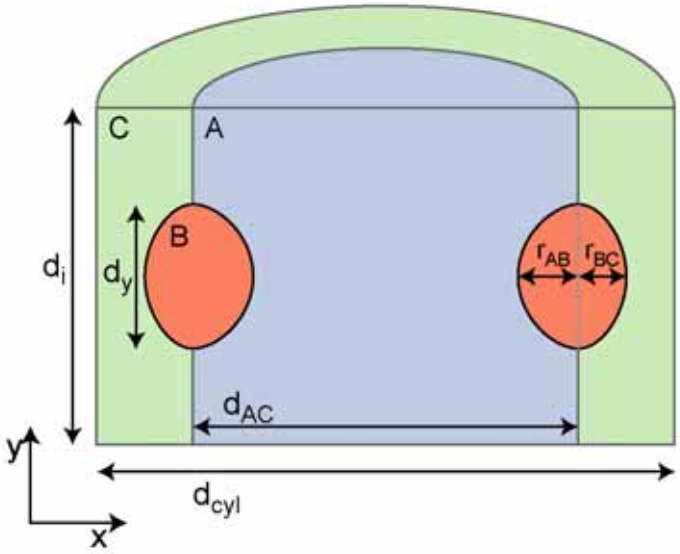

Figure 4.10 - Cross-section of the rings-at-cylinder structure viewed through the center of the cylinder. The B-domains form rings around the central cylindrical A-domain. The shape of the Wigner-Seitz cell is approximated by the outer cylinder (diameter d_{cyl}). Arrows indicate the diameter of the AC interface (d_{AC}), spacing of rings along the cylinder (d_i), width of the B-domain along the cylinder axis (d_y), and thickness of the ring-shaped B-domain on the A (r_{AB}) and C (r_{BC}) sides of the AC interface.

As for the lamellar structures, independent dimensionless ratios are a convenient way to define internal unit cell dimensions,

$$\phi_i = \frac{d_i}{d_{cyl}/2}, \qquad \phi_a = \frac{d_y}{d_i}, \qquad 1 = \phi_A + \phi_C, \tag{4-88}$$

where ϕ_A and ϕ_C are the volume fractions of the B domain residing on A/C side of the AC interface. The following dependent internal ratios are also of considerable use,

$$\phi_{AC} = \frac{r_{AC}}{d_{cyl}/2} = \sqrt{f_A + \phi_A f_B}, \tag{4-89}$$

$$\phi_{AB} = \frac{r_{AB}}{d_{cyl}/2} = \frac{\phi_{AC} H_{1,\text{rod}}}{H_{2,\text{rod}}} \times \left(1 - \sqrt{1 - \frac{\phi_A f_B H_{2,\text{rod}}}{\phi_a \phi_{AC}^2 H_{1,\text{rod}}^2}} \right),$$

$$\phi_{BC} = \frac{r_{BC}}{d_{cyl}/2} = \frac{\phi_{AC} H_{1,\text{rod}}}{H_{2,\text{rod}}} \times \left(\sqrt{1 + \frac{\phi_C f_B H_{2,\text{rod}}}{\phi_a \phi_{AC}^2 H_{1,\text{rod}}^2}} - 1 \right),$$

$$\phi_{\text{inner}} = \sqrt{f_A + \phi_A f_B - \frac{\phi_A f_B}{\phi_a}},$$

$$\phi_{\text{outer}} = \sqrt{f_A + \phi_A f_B + \frac{\phi_C f_B}{\phi_a}}.$$

The area of the three interfaces is then,

$$A_{AC} = \frac{2V_{cell}}{d_{cyl}} \times 2\phi_{AC} \times (1 - \phi_a), \tag{4-90}$$

$$A_{AB} = \frac{2V_{cell}}{d_{cyl}} \times 2\phi_{AC} \times \phi_a \times A_{\text{ring}} \left(\frac{2\phi_{AB}}{\phi_r \phi_z}, \frac{-\phi_{AB}}{\phi_{AC}} \right),$$

$$A_{BC} = \frac{2V_{cell}}{d_{cyl}} \times 2\phi_{AC} \times \phi_a \times A_{\text{ring}} \left(\frac{2\phi_{BC}}{\phi_r \phi_r}, \frac{\phi_{BC}}{\phi_{AC}} \right),$$

where,

$$A_{\text{ring}}(\varepsilon_1, \varepsilon_2) = \int_{y'=0}^{y'=1} (1 + \varepsilon_2 h(y')) \times \sqrt{1 + \left(\varepsilon_1 \frac{dh}{dy'} \right)^2} \times dy'. \tag{4-91}$$

For a rectangular toroid,

$$A_{\text{ring}}(\varepsilon_1, \varepsilon_2) = 1 + \varepsilon_1 + \varepsilon_2 + \frac{\varepsilon_1 \varepsilon_2}{2}, \tag{4-92}$$

and for a half-elliptical toroid,

$$A_{\text{ring}}(\varepsilon_1,\varepsilon_2)=E\left(\sqrt{1-\varepsilon_1^2}\right)+\frac{\varepsilon_2}{2}\left(\frac{\arcsin\left(\sqrt{1-\varepsilon_1^2}\right)}{\sqrt{1-\varepsilon_1^2}}+\varepsilon_1\right). \tag{4-93}$$

Thus, the interfacial area coefficients for the AB, BC and AC interfaces are,

$$\varphi_{AB}^{\text{ring}}=2\phi_{AC}A_{\text{ring}}\left(\frac{2\phi_{AB}}{\phi_r\phi_z},\frac{-\phi_{AB}}{\phi_{AC}}\right),\quad \varphi_{BC}^{\text{ring}}=2\phi_{AC}A_{\text{ring}}\left(\frac{2\phi_{BC}}{\phi_r\phi_z},\frac{\phi_{BC}}{\phi_{AC}}\right),\quad \varphi_{AC}^{\text{ring}}=2\phi_{AC}. \tag{4-94}$$

Turning to chain stretching, stretching of the B chains in the toroidal B domain is similar to the stretching of B chains in the rods in the rods-at-lamellae structure. To a first approximation,

$$\begin{aligned} R_B^2 &\approx \int_{z=0}^{z=1}\left((r_{AB}+r_{BC})h(z)\right)^2\frac{h(z)dz}{H_{1,\text{rod}}} \\ &\approx \frac{H_{3,\text{rod}}}{H_{1,\text{rod}}}\times\frac{d_{cyl}^2}{4}\times(\phi_{AB}+\phi_{BC})^2, \end{aligned} \tag{4-95}$$

where the errors caused by the toroidal shape go as $(r_{AB}/r_{AC})^2$. Thus η_B is,

$$\eta_B^{\text{ring}}=\frac{H_{3,\text{rod}}}{H_{1,\text{rod}}}\times\left(\frac{\phi_a(\phi_{AB}+\phi_{BC})}{f_B}\right)^2. \tag{4-96}$$

Chain stretching in the A and C domains can be approximated by assuming the B-domain is a rectangular toroid. Again, the result depends upon the distribution of AB/BC junctions at the AB/BC interface. If the chains stretch to the nearest point on the AB interface (low estimate) then,

$$\eta_A^{\text{ring,low}}=\frac{\phi_{\text{innner}}^4}{2f_A^3}+\left(\frac{\phi_i}{2f_A}\right)^2\times(1-\phi_a)^3\times\left(1+\frac{f_B\phi_A}{f_A}\right), \tag{4-97}$$

and,

$$\eta_C^{\text{ring,low}}=\left(\frac{1-\phi_{\text{outer}}}{f_C}\right)^3\times\left(\frac{3+\phi_{\text{outer}}}{2}\right)+\left(\frac{\phi_i}{2f_C}\right)^2\times(1-\phi_a)^3\times\left(1+\frac{f_B\phi_C}{f_C}\right). \tag{4-98}$$

If the chain stretching along the cylinder axis is proportional to the axial distance from the center of the B-domain (intermediate estimate), then,

$$\eta_A^{\text{ring,imd}} = \frac{\phi_{\text{innner}}^4}{2f_A^3} + \left(\frac{\phi_{AC} - \phi_{\text{inner}}}{f_A}\right)^3 \times \frac{3\phi_{\text{inner}} + \phi_{AC}}{2} \times (1-\phi_a) + \left(\frac{\phi_i}{2f_A}\right)^2 \times (1-\phi_a)^2, \quad (4\text{-}99)$$

and,

$$\eta_C^{\text{ring,imd}} = \left(\frac{1-\phi_{\text{outer}}}{f_C}\right)^3 \times \left(\frac{3+\phi_{\text{outer}}}{2}\right) + \left(\frac{\phi_{outer} - \phi_{AC}}{f_C}\right)^3 \times \frac{3\phi_{\text{outer}} + \phi_{AC}}{2} \times (1-\phi_a) \quad (4\text{-}100)$$
$$+ \left(\frac{\phi_i}{2f_C}\right)^2 \times (1-\phi_a)^2 .$$

Finally, if all A and C chains stretch along the cylinder axis by an amount $(d_i\text{-}d_y)/2$ (high estimate),

$$\eta_A^{\text{ring,high}} = \frac{1}{2f_A} + \frac{12}{\pi^2} \times \left(\frac{\phi_i}{2f_A}\right)^2 \times (1-\phi_a)^2, \quad (4\text{-}101)$$

and

$$\eta_C^{\text{ring,high}} = \frac{3+\sqrt{1-f_C}}{2\times\left(1+\sqrt{1-f_C}\right)^3} + \frac{12}{\pi^2} \times \left(\frac{\phi_i}{2f_C}\right)^2 \times (1-\phi_a)^2. \quad (4\text{-}102)$$

Stadler and colleagues (Stadler et. al. 1995) compared the free energy of the rings-at-cylinders structure to that of the triple-lamellae, rods-at-lamellae and balls-at-lamellae structures. They concluded that even when the A and C domains were equivalent ($f_A = f_C$, $\gamma_{AB} = \gamma_{BC}$, $p_A = p_C$), at intermediate B domain volume fractions ($0.01 < f_B < 0.15$) the rings-at-cylinders structure had the lowest free energy when $\gamma_{AC} << \gamma_{AB} + \gamma_{BC}$. Figure 4.11 shows the free energy per copolymer (G) as a function of B-block volume fraction (f_B) for the rings-at-rods (red), triple-lamellae (black), rods-at-lamellae (blue) and balls-at-lamellae (green) structures when $\gamma_{AC} = 0$ and the A and C blocks are equivalent volume ($f_A = f_C$; $p = p_A = p_B = p_C$; $\gamma = \gamma_{AB} = \gamma_{BC}$). Unsurprisingly, for all values of f_B , the free energy for the rings-at-cylinders structure is higher than that for the rods-at-lamellae structure.

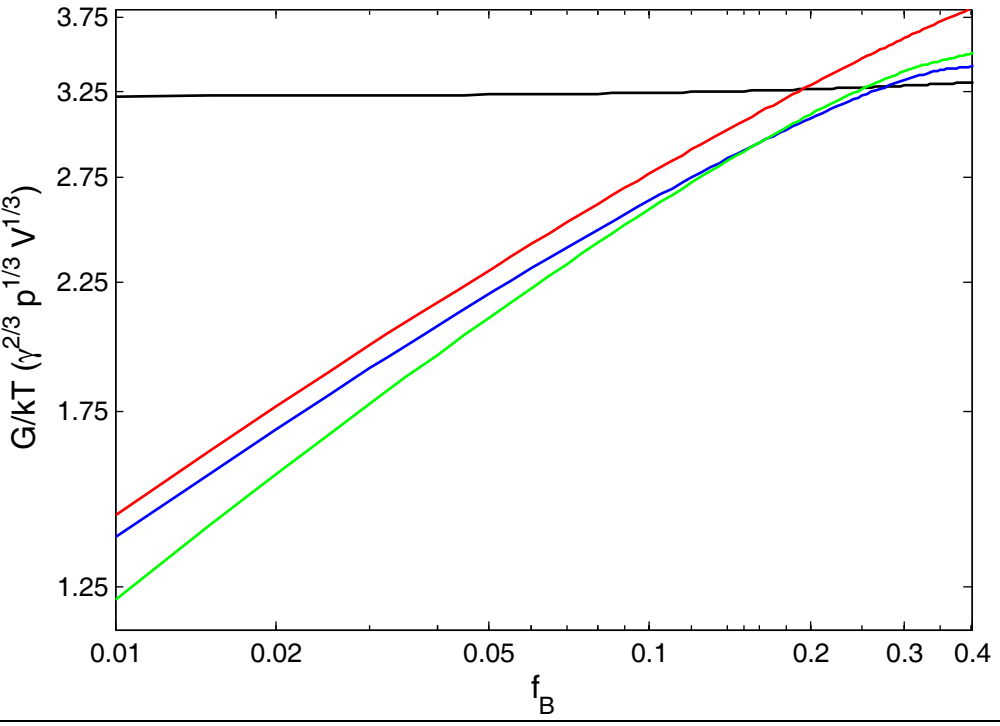

Figure 4.11 - Gibbs free energy per copolymer (G) as a function of B-block volume fraction (f_B) for the triple-lamellae (black), rods-at-lamellae (blue), balls-at-lamellae (green) and rings-at-rods (red) structures when $\gamma_{AC}=0$ and the A and C blocks are equivalent volume ($f_A=f_C$; $p=p_A=p_B=p_C$; $\gamma=\gamma_{AB}=\gamma_{BC}$). AB and BC domain interfaces assumed to be elliptical/spheroidal and chain stretching in A and C domains approximated using the intermediate estimates. At all values of f_B the free energy per copolymer of the rods-at-lamellae structure is lower than that for the rings-at-lamellae structure.

This difference between the present analysis and that of Stadler and colleagues (Stadler et. al. 1995) results from different approximations of the A and C domain chain stretching energy. Relative to a rods-at-lamellae structure with approximately the same AC/AB and BC interfacial area per copolymer), the rings-at-lamellae structure has a thinner outer C domain and thicker inner A domain. Unless the volume (or packing length) of the A domain is substantially smaller than that of the C domain, the increase in stretching energy in the inner, thicker A domain is substantially larger

than the decrease in stretching energy in the outer, thinner C domain. Consequently, when the A and C blocks are equivalent, the rods-at-lamellae structure has a lower free energy than the rings-at-lamellae structure. In their analysis, Stadler and colleagues approximated the chain stretching energy of the inner, thicker A domain with an expression for an exterior, cylindrical domain. This approximation underestimates the chain stretching in the A domain and accounts for their surprising prediction that an asymmetric cylindrical structure would be favored in ABC copolymers with equivalent A and C domains ($f_A = f_C$, $\gamma_{AB} = \gamma_{BC}$, $p_A = p_C$). The observation of the cylinders-at-ring structures (Auschra and Stadler, 1993; Balsamo et. al. 2003) may instead reflect asymmetry between the two end blocks (e.g. $p_A \neq p_C$ or $f_A \neq f_C$) or a kinetically trapped metastable morphology (Ott, et. al. 2001).

4.4 Phase Behavior

Morphologies with lamellar A and C domains are expected when the A and C domains are equivalent ($f_A \approx f_C$, $p_A \approx p_C$, $\gamma_{AB} \approx \gamma_{BC}$) and the B-domain volume fraction is not dominant ($f_B < 0.5$) (Nakazawa and Ohta, 1993; Zheng and Wang, 1995). In the SSL, the Gibbs free energy of these lamellar morphologies depends upon both the block volume fractions and the block-block interfacial tensions. This dependence is illustrated in Figure 4.12 for the case when all three blocks have identical interactions ($\gamma = \gamma_{AB} = \gamma_{BC} = \gamma_{AC}$; $p = p_A = p_B = p_C$).

In the triple-lamellae structure, the area of the AB and BC interfaces does not depend upon the B domain volume fraction (f_B) and there is no AC interface. Consequently, the free energy of the triple-lamellae morphology is independent of γ_{AC} and has only a slight dependence on f_B. When $\gamma_{AC} > \gamma_{AB} + \gamma_{BC}$, the middle lamellar B domain acts as a buffer between the A and C domains and the formation of an AC

interface is unfavorable. However, when $\gamma_{AC} < \gamma_{AB} + \gamma_{BC}$ the conversion of AB and/or BC interfaces to AC interfaces can reduce interfacial energy.

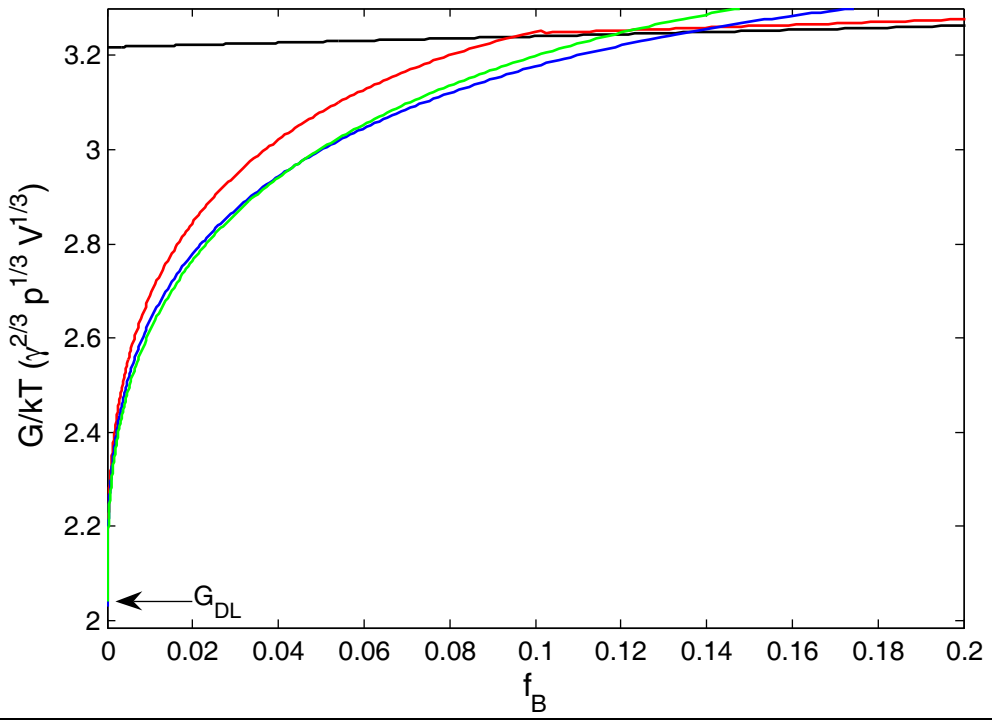

Figure 4.12 – Gibbs free energy per copolymer (G) as a function of B-block volume fraction (f_B) for the triple-lamellae (black), perforated lamellae (red), rods-at-lamellae (blue) and balls-at-lamellae (green) structures when the A and C blocks have equal volume ($f_A=f_C$) and block packing lengths ($p=p_A=p_B=p_C$) and interfacial tensions are equal ($\gamma=\gamma_{AB}=\gamma_{BC}=\gamma_{AC}$). The triple-lamellae and rods-at-lamellae structure energies are equal at $f_B=0.135$ while the free energy of rods-at-lamellae and balls-at-lamellae structures are equal at $f_B = 0.045$. AB and BC domain interfaces were assumed to be elliptical and the intermediate estimate of chain stretching was employed.

In the balls-at-lamellae, rods-at-lamellae and perforated-lamellae structures, the area of the AB and BC interfaces can be reduced at the expense of increasing the thickness of the B domain. This trade-off between reducing the interfacial energy and increasing the stretching energy of the B domain determines the optimal fraction of

AC interface occupied by B domains (ϕ_a) and to a first approximation ϕ_a is proportional to $f_B^{1/3}$, as is illustrated in Figure 4.13.

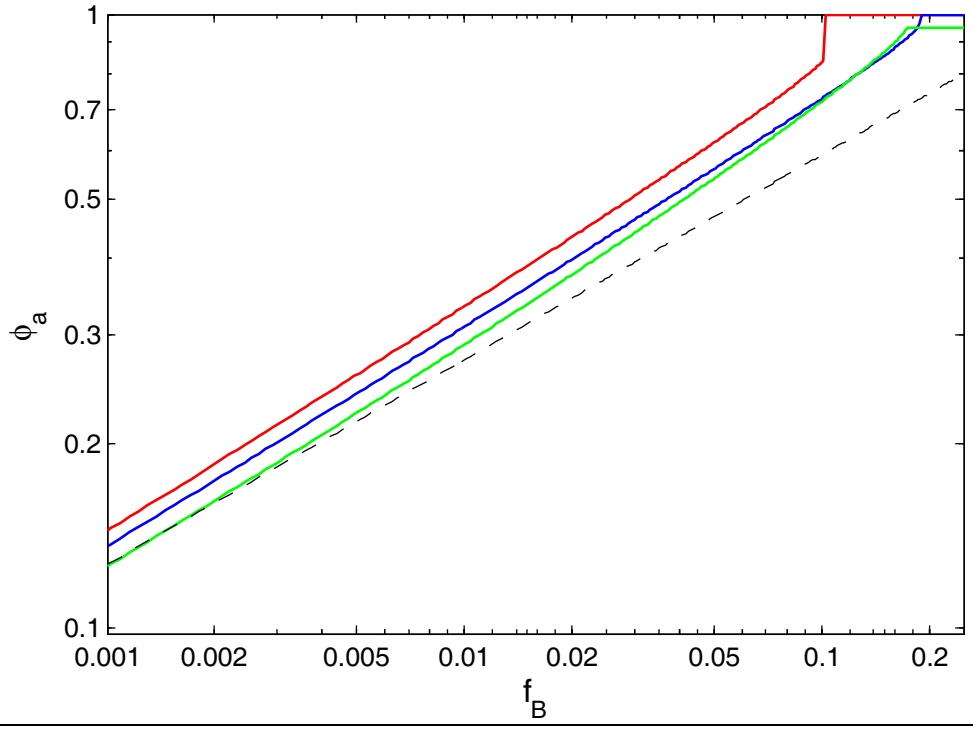

Figure 4.13 – Optimal Fraction of the AC interface (ϕ_a) occupied by B domains as function of B block volume fraction (f_B) for the perforated lamellae (red), rods-at-lamellae (blue), balls-at-lamellae(green) structures when $f_A=f_C$, $p=p_A=p_B=p_C$ and $\gamma = \gamma_{AB} = \gamma_{BC} = \gamma_{AC}$. The black dotted line indicates the approximate scaling, $\phi_a \propto f_B^{1/3}$.

When f_B is relatively large, the B domains occupy most of the AC interface ($\phi_a \approx 1$) and the triple-lamellae structure has the lowest free energy. When the B domain volume fraction (f_B) is smaller, the relative area of the AB and BC interfaces and the free energy per copolymer both decrease. In the limit as $f_B \to 0$, the relative area of the AB and BC interfaces also approaches zero ($\phi_a \to 0$) and the free energy of the balls-at-lamellae, rods-at-lamellae and perforated-lamellae structures approaches the

free energy of an AC diblock double-lamellae structure (Equation 4-22). Thus, provided $\gamma_{AC} < \gamma_{AB} + \gamma_{BC}$, the triple-lamellae structure becomes unstable below a critical B block volume fraction (f_B). For the case shown in Figure 4.12, the free energy per copolymer of the rods-at-lamellae structure drops below that of the triple-lamellae structure at $f_B \approx 0.135$. This transition between the lamellar B domain in the ABCBA triple-lamellae structure and the thicker B domains or the balls-at-lamellae, rods-at-lamellae and perforated lamellae structures results from the tradeoff between the surface area and thickness of the B domain.

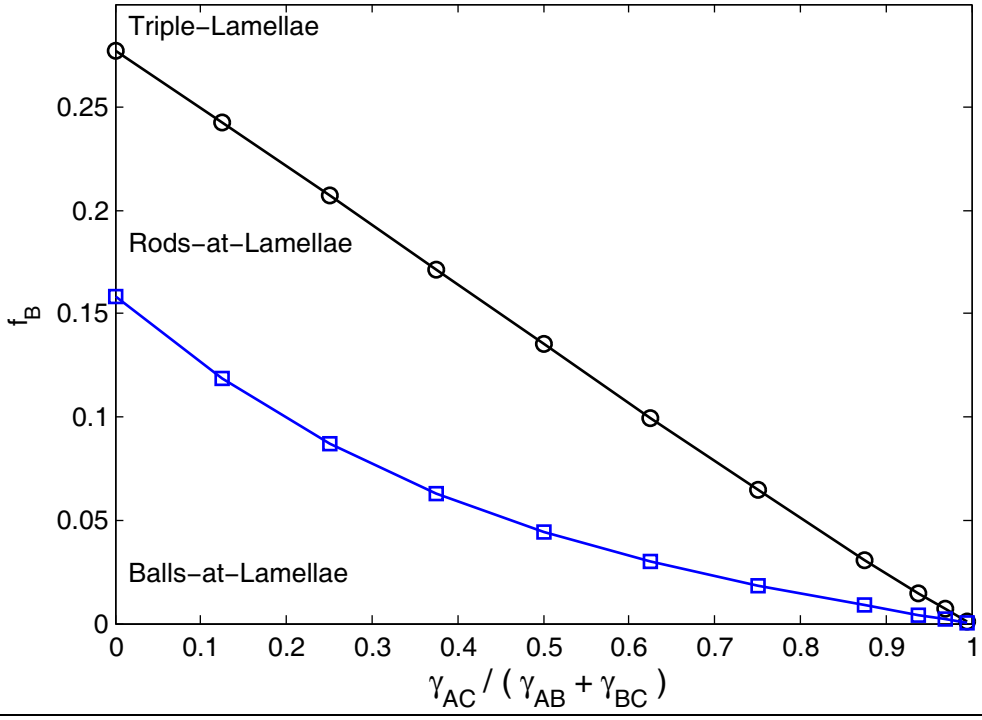

Figure 4.14 – Structural Transitions between triple-lamellae, rods-at-lamellae and balls-at-lamellae ABC copolymer structures when A and C blocks are equivalent ($f_A = f_C$; $\gamma_{AB} = \gamma_{BC}$; $p_A = p_B = p_C$). The AB and BC domain interfaces were assumed to be elliptical in shape and the intermediate estimate of chain stretching was employed (Equations 4-52 and 4-67).

Figure 4.14 illustrates the effect of γ_{AC} on this transition for ABC block copolymers in which the A and C blocks are equivalent ($f_A=f_C$, $\gamma_{AB}=\gamma_{BC}$, $p_A=p_C=p_B$). As $\gamma_{AC}/(\gamma_{AB}+\gamma_{BC})$ increases, the transition shifts to smaller values of f_B and as γ_{AC} approaches $\gamma_{AB}+\gamma_{BC}$ the transition approaches $f_B = 0$. For a given value of $\gamma_{AC}/(\gamma_{AB}+\gamma_{BC})$, the estimate of chain stretching does effect the value of f_B at which the phase transition occurs. However, the qualitative features of the transition do not depend upon which estimate of chain stretching is used. This phase behavior determined using the SSL approach of Semenov (Semenov, 1985) matches well to the predictions of Zheng and Wang using the Ohta-Kawasaki SSL approximation (Figure 4b, Zheng and Wang, 1995).

Transitions between the rods-at-lamellae, balls-at-lamellae and perforated-lamellae are somewhat subtler than the instability of the triple-lamellae morphology. In Figure 4.12, the balls-at-lamellae structure is optimal when $f_B < 0.045$, the rods-at-lamellae structure is favored for $0.045 < f_B < 0.135$ and the free energy of the perforated B-lamellae structure is always a little larger than either the rods-at-lamellae or triple-lamellae structures. This sequence of phases (balls-at-lamellae $\rightarrow$ rods-at-lamellae $\rightarrow$ triple-lamellae with increasing f_B) appears to be quite general, provided the free energy of the balls-at-lamellae, rods-at-lamellae and perforated lamellae structures are calculated using the same type of estimate of chain stretching (low, intermediate or high) and shape for domain interfaces (elliptical, parabolic or rectangular). As is illustrated Figure 4.14, increasing $\gamma_{AC}/(\gamma_{AB}+\gamma_{BC})$ shifts the rods-at-lamellae $\rightarrow$ balls-at-lamellae transition shifts to smaller values of f_B.

The phase behavior of the balls-at-lamellae, rods-at-lamellae and perforated-lamellae structures appear to be analogous to the SSL behavior of the corresponding AB or ABA block copolymer phases (spheres, cylinders and perforated-lamellae). In

AB diblock copolymers, the sphere phase is stable at low volume fractions ($f_B < 0.1$) and the cylinder phase at intermediate volume fractions ($0.1 < f_B < 0.3$) while the free energy of the AB perforated-B-lamellae structure is always larger than either the cylinder or lamellar phases (Fredrickson, 1991). Relative to the inner B domain thickness, the spheres structure has a smaller outer A domain thickness. At low B domain volume fractions (f_B) the fraction of chain stretching energy from the outer A block is smaller in the sphere phase and this plays a significant role in the transition between the sphere and cylinder phases.

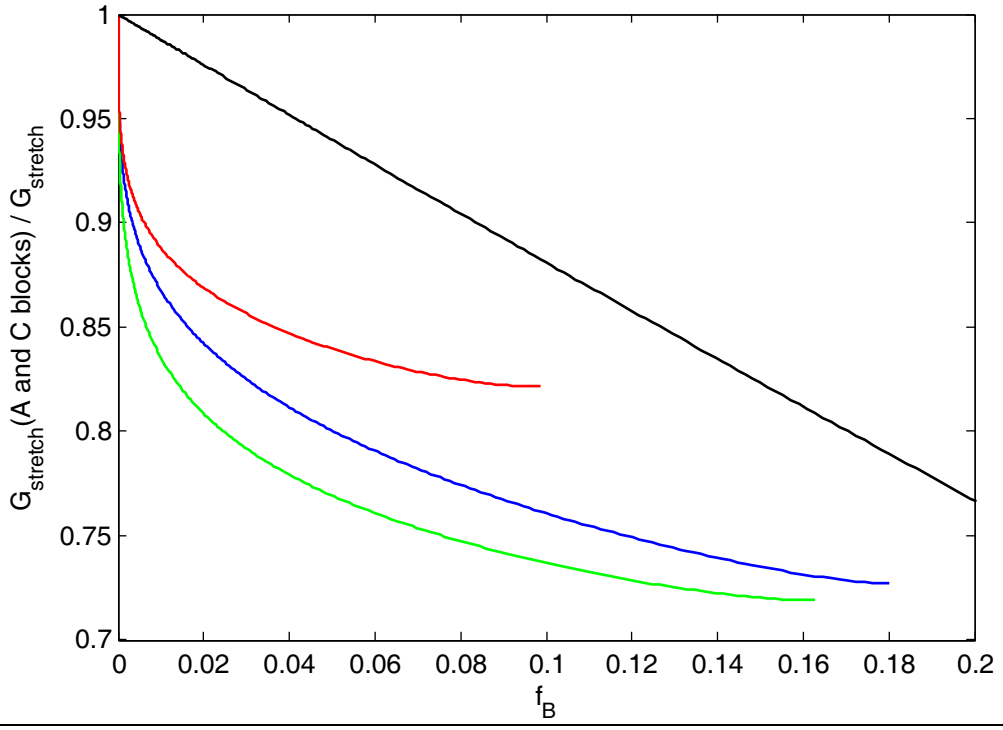

Figure 4.15 –Fraction of chain stretching energy per copolymer in the A and C blocks ($G_{stretch}$(A and C domains) / $G_{stretch}$) as a function of B block volume fraction (f_B) for the triple-lamellae (black), perforated-lamellae (red), rods-at-lamellae (blue) and balls-at-lamellae (green) structures ($f_A = f_C$; $p = p_A = p_B = p_C$; $\gamma = \gamma_{AB} = \gamma_{BC} = \gamma_{AC}$; elliptical AB and BC interfaces; intermediate estimate of chain stretching). For clarity, the stretching energy is only plotted for the region where $\phi_a < 1$.

For the A and C domains of the rods-at-lamellae and balls-at-lamellae structures, chain stretching along the lamellar axis is not too different. However, lateral chain stretching is proportional to $(1-\phi_a)^2$ (Equation 4-52) in the rods-at-lamellae structure and goes as $(1-\phi_a^{1/2})^2$ in the balls-at-lamellae structure (Equation 4-67). Thus, when the B domains occupy a smaller fraction of the in-plane interface (ϕ_A and f_B smaller) the balls-at-lamellae structure is likely to have less chain stretching in the A and C blocks.

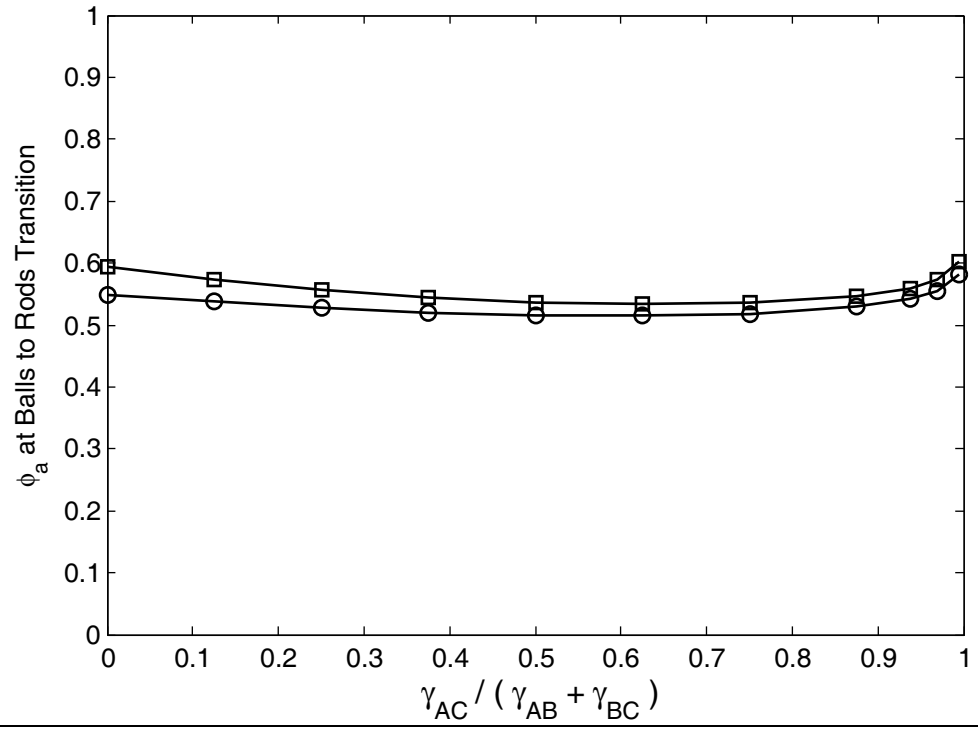

Figure 4.16 – Fraction of plane of AC interface occupied by B domains (ϕ_a) in the balls-at-lamellae (circles) and rods-at-lamellae (squares) structures (at the rods-at-lamellae→balls-at-lamellae transition) as a function of $\gamma_{AC}/(\gamma_{AB}+\gamma_{BC})$. As before, the A and C blocks were equivalent ($f_A = f_C$; $\gamma_{AB} = \gamma_{BC}$; $p_A = p_B = p_C$) and f_B was set to the transition value shown in Figure 4.14. The AB and BC domain interfaces were assumed to be elliptical in shape and the intermediate estimate of chain stretching was employed (Equations 4-52 and 4-67).

Figure 4.15 shows that the fraction of chain stretching energy in the outer A and C blocks ($G_{stretch}$(A and C blocks)/$G_{stretch}$) is indeed smaller in the balls-at-lamellae structure than the rods-at-lamellae structure, especially when B domain volume fraction (f_B) is small. Furthermore, as shown in Figure 4.16, the transition between balls-at-lamellae and rods-at-lamellae structures is strongly correlated with ϕ_a, the fractional in-plane area of the B domains. Thus, at small values for the B domain volume fraction (f_B), the A and C domain chain stretching energy appears to favor the balls-at-lamellae structure.

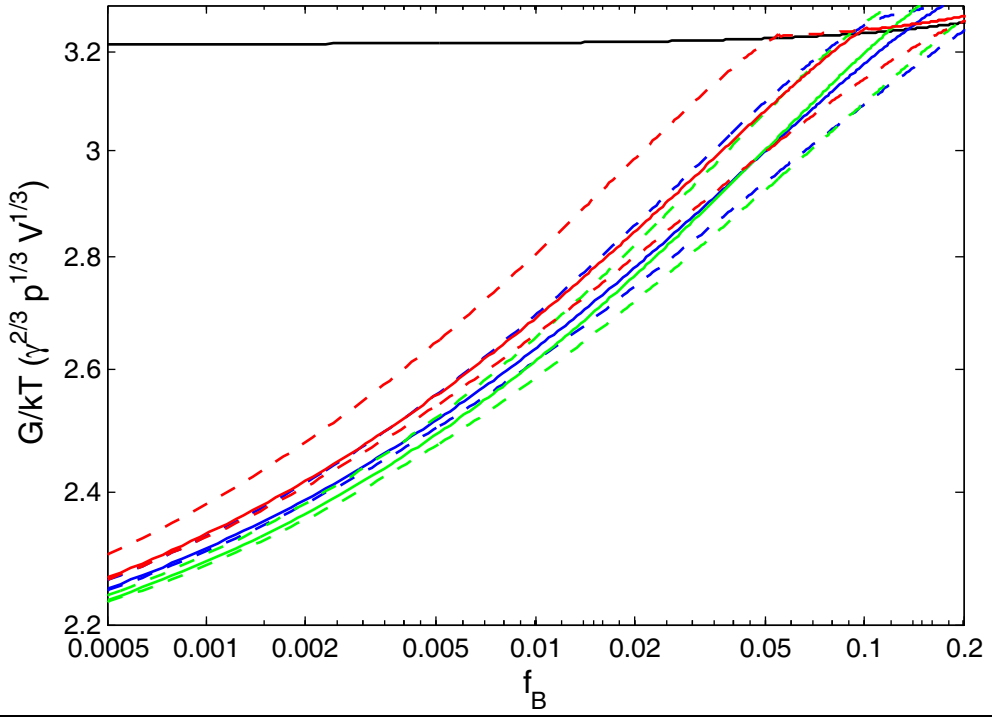

Figure 4.17 – Gibbs free energy per copolymer (G) as a function of B-block volume fraction (f_B) for the triple-lamellae (black), perforated lamellae (red), rods-at-lamellae (blue) and balls-at-lamellae (green) structures when the A and C blocks have equal volume (f_A=f_C) and block packing lengths (p=p_A=p_B=p_C) and interfacial tensions are equal (γ=γ_{AB}=γ_{BC}=γ_{AC}). AB and BC domain interfaces were assumed to be elliptical. For the perforated lamellae, rods-at-lamellae and balls-at-lamellae structures, G was estimated using the low (dashed), intermediate (solid) and high (dashed) estimates of chain stretching.

However, this interpretation requires a significant caveat. As is illustrated in Figure 4.17, the manner in which the chain stretching energy of the A and C domains is estimated can have significant effects on the apparent stability of the balls-at-lamellae, rods-at-lamellae and spheres-at-lamellae structures. For example, if the actual free energy per copolymer of the perforated-lamellae structure were close to the "low" estimate while that for the balls-at-lamellae structure and rods-at-lamellae structure were close to the "high" estimate, the perforated-lamellae structure would be stable over a wide range of compositions ($0.01 < f_B < 0.18$). Thus, a rigorous SSL phase diagram will require more exact upper and lower bounds on free energy per copolymer for each of the morphologies. However, the approximate approach used in this chapter still provides insight into the thermodynamics of these structures.

Finally, the prediction of these SSL models can be compared to PEP-b-PEO-PHMA copolymers described in Chapter 3. The composition and properties of the PEP-b-PEO-b-PHMA copolymers are summarized in Tables 3.1, 3.2 and 3.3. Using these values and SSL models for each morphology (Sections 4.2.1, 4.3.1 and 4.3.2), free energy per copolymer and unit cell parameters were computed for copolymers **1**, **2** and **3** and are the results are presented in Table 4.3. For these calculations, the AB/BC domain boundaries were assumed to have an elliptical profile while the intermediate estimate of chain stretching was employed. Figure 4.18 shows the predicted free energy for the triple-lamellae, rods-at-lamellae and balls-at-lamellae structures for a series of volume fractions similar to those of copolymers **1**, **2** and **3**.

Unfortunately, the predicted unit cell dimensions satisfy neither the "narrow interface" nor the "strong-stretching" approximations of the SSL. These failings are particularly severe for the B-domains in copolymers **2** and **3** where the domain thickness, $d_x \approx 6$nm, is less than 3 times the thickness of the combined AB and BC

interfaces (t_{AB} = 0.88nm, t_{BC} = 1.21 nm, Table 3.2) and approximately equal to the un-extended RMS length of the B block (L_B is 6.0nm for copolymer **2** and 4.5nm for copolymer **3**, Table 3.3). Thus, the primary use of the SSL models discussed here is to provide a conceptual framework to understand of the stability of A/C lamellar structures. With this consistent SSL model, further understanding of these structures with lamellar A and C domains can be most rapidly obtained via a three-dimensional self-consistent field theory calculation.

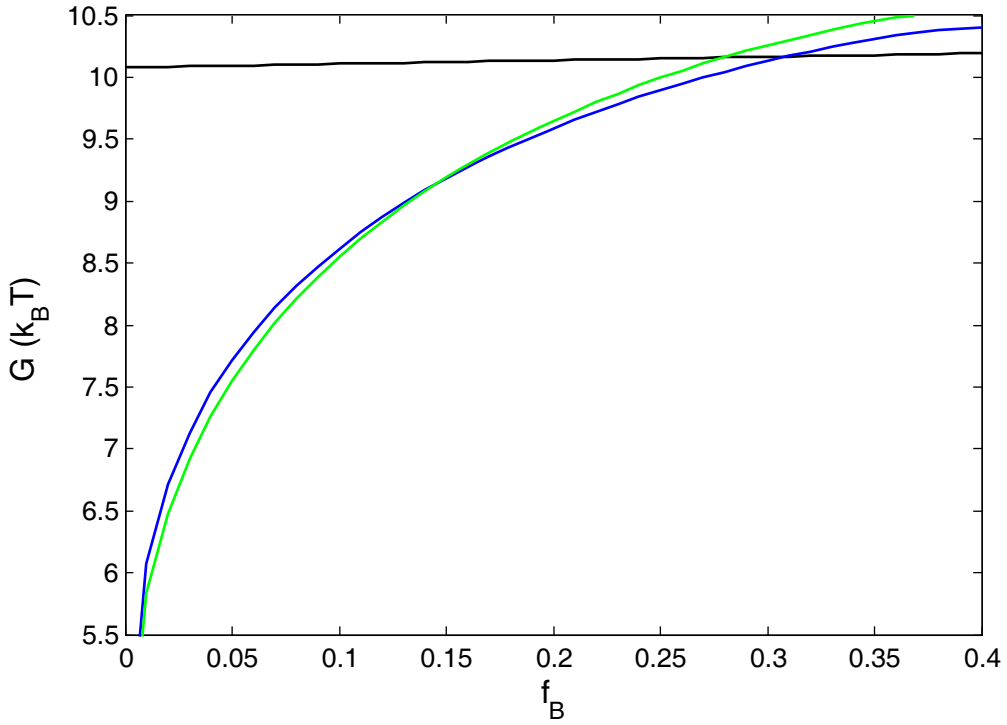

*Figure 4.18 – Gibbs free energy per copolymer (G) for the triple-lamellae (black), rods-at-lamellae (blue) and balls-at-lamellae (green) structures for volume fractions f_A=0.6-f_B and f_C=0.4 which approximate those of copolymers **1**, **2** and **3**. Block packing lengths and interfacial tensions are given in Tables 3.1 and 3.2 while the copolymer volume matches that of copolymer **2** (V_p =47.4 nm^3).*

*Table 4.3 - Gibbs free energy (G) per copolymer and unit cell parameters for Copolymers **1**, **2** and **3**. (Composition and properties in Tables 3.1, 3.2 and 3.3)*

	Triple-Lamellae	**Rods-at-Lamellae**	**Balls-at-Lamellae**
Copolymer 1			
G (k_BT)	10.92	10.63	10.74
d_l (nm)	46.1	42.7	41.8
d_i (nm)	-	31.6	47.7
d_y (nm)	-	24.2	41.4
d_x (nm)	-	8.9	10.4
ϕ_A	-	0.22	0.23
Copolymer 2			
G (k_BT)	10.15	9.191	9.195
d_l (nm)	40.2	35.2	34.1
d_i (nm)	-	18.8	26.4
d_y (nm)	-	11.5	20.1
d_x (nm)	-	5.5	6.6
ϕ_A	-	0.18	0.20
Copolymer 3			
G (k_BT)	9.59	8.710	8.712
d_l (nm)	35.6	31.2	30.2
d_i (nm)	-	16.8	23.5
d_y (nm)	-	10.3	18.0
d_x (nm)	-	4.8	5.8
ϕ_A	-	0.20	0.21

4.5 Conclusion

In this chapter, the thermodynamic properties of the triple-lamellae, perforated-lamellae, rods-at-lamellae and balls-at-lamellae ABC block copolymer morphologies have been studied using the SSL approach of Semenov (Semenov, 1985; Matsen, 2002). In the SSL, the stability of ABC block copolymer structures depends upon both the block volume fractions (f_A, f_B, f_C) and the interfacial tension between the AB, BC and AC interfaces ($\gamma_{AB}, \gamma_{BC}, \gamma_{AC}$). This chapter has focused upon ABC block copolymers in which the volume of the B domain is not dominant ($f_B < 0.5$) and the A and C blocks have equivalent properties ($f_A = f_C$; $\gamma_{AB} = \gamma_{BC}$; $p_A \approx p_C$).

When $\gamma_{AC} > \gamma_{AB} + \gamma_{BC}$, the B domain acts as a buffer between the more incompatible A and C blocks and the triple-lamellar structure is stable for all $f_B < 0.5$. In contrast, when $\gamma_{AC} < \gamma_{AB} + \gamma_{BC}$, the lamellar B domain of the triple-lamellae structure becomes unstable at low values of f_B. From estimates of the free energy per copolymer for each morphology, decreasing f_B causes a transition from the triple-lamellae structure to rods-at-lamellae structure, and further reduction of f_B drives a second transition to the balls-at-lamellae structure. This sequence of transitions (triple-lamellae $\rightarrow$ rods-at-lamellae $\rightarrow$ balls-at-lamellae) agrees with the earlier analysis of Zheng and Wang (Zheng and Wang, 1995).

Chapter Five - ABC Block Copolymer/ Aluminosilicate Patterned Sheets

5.1 Introduction

The use of block copolymers to direct the assembly of inorganic precursors into nanometer-scale structures (Thompson et. al., 2001; Bockstaller, et. al. 2005; Shenhar et. al., 2005) is of interest for applications such as catalysts, selective membranes and low dielectric insulators (Kresge, et. al. 1992; Soler-Illia, et. al. 2002). Compared to two-domain AB or ABA architectures, ABC triblock copolymers promise several potential advantages for use as structure-directing agents. Firstly, ABC copolymers form a much larger range of structures (Matsushita, et. al. 1980; Zheng and Wang, 1995; Bates and Fredrickson, 1999) and may provide access to several network structures (Mogi, et. al. 1992; Epps, et. al. 2004) as well as non-centrosymmetric (Goldacker, et. al. 1999) and chiral (Krappe, et. al. 1995) morphologies. Furthermore, because ABC copolymers can form three chemically distinct types of domain, ABC copolymers may permit the independent structuring of two or three types of inorganic precursor (Bockstaller, et. al. 2005; Chiu, et. al. 2005). However, harnessing the complex phase behavior of ABC triblock copolymers has been challenging.

This chapter describes the characterization of a hexagonally patterned lamellar morphology found in a set of PEP-b-PEO-b-PHMA (ABC) triblock copolymer/ aluminosilicate materials. In these materials, the volume fraction of the PEP block ($0.09 \leq f_{PEP} \leq 0.12$) was much smaller than the PEO-aluminosilicate ($0.28 \leq f_{PEO+Aluminosilicate} \leq 0.44$) and PHMA ($0.47 \leq f_{PHMA} \leq 0.60$) domains.

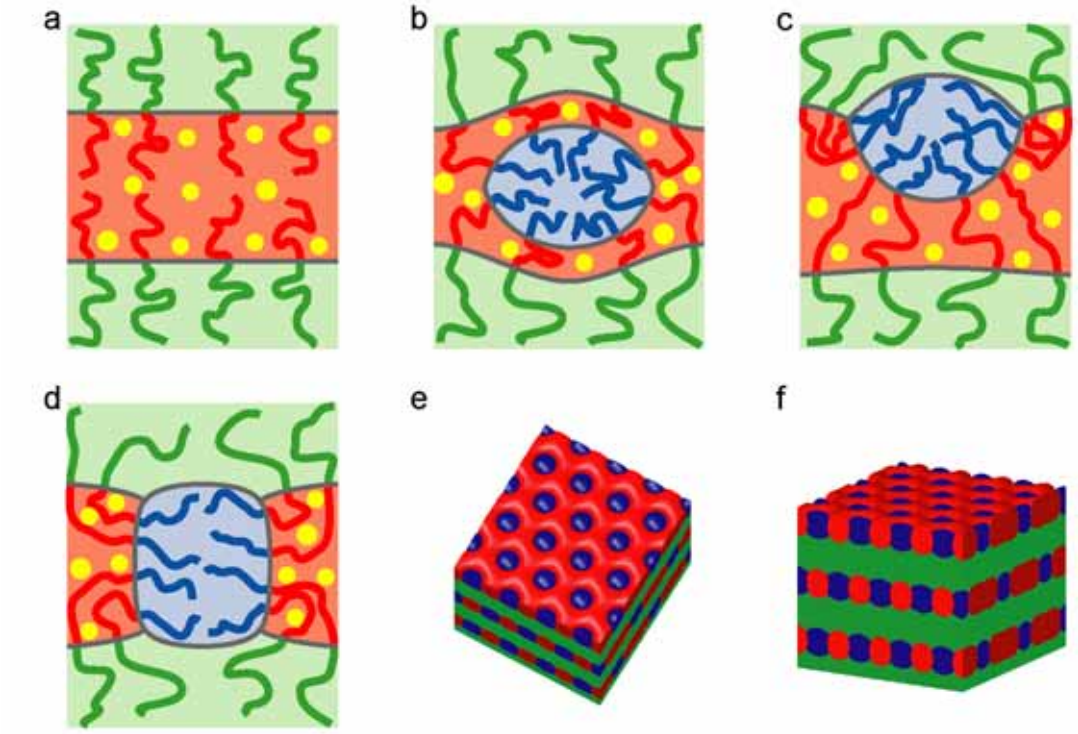

*Figure 5.1 - Structural models for PEP-b-PEO-b-PHMA block copolymer/aluminosilicate lamellar morphologies with a small PEP block. In the absence of the PEP block, the PEO (red) and PHMA (green) chains stretch into their respective domains while the aluminosilicate particles (yellow) partition into the hydrophilic PEO domain (**a**). Possible domain structures discussed in the text are illustrated as follows: In the "balls-in-lamellae" structure the small PEP block (blue) forms round micellar domains (**b**). Dimple structure with PEP micelles at the PHMA/PEO-aluminosilicate interface (**c**). In the "pillared-lamellae" structure the PEP domain form pillars spanning across the PEO-aluminosilicate domain (**d**). Top (**e**) and side (**f**) views of the "pillared-lamellae" structure. (n.b. In an ABC copolymer, the curvature of AC domain interfaces depends on a number of considerations and the shape of PEP domains shown are only approximate.)*

These compositions ($f_A << f_B, f_C$) correspond to the small end-block regime of interest for studying the transition from two-domain diblock to three-domain triblock morphologies (Bailey, et. al. 2001). In a diblock PEO-b-PHMA copolymer /aluminosilicate material (Renker, et. al. 2004), the PHMA and PEO-aluminosilicate

phases can form a simple lamellar morphology as illustrated in Figure 5.1a. However, in the triblock copolymer, the enthalpic cost for the PEP block mixing in the PEO-aluminosilicate domain is very large ($\chi_{PEP/PEO}N \approx 346 > \chi_{PEP/PHMA}N \approx 50$). This unfavorable interaction can be reduced by the formation of micellar PEP domains as in the "balls-in-lamellae" (Figure 5.1b; Zheng and Wang, 1995), "cylinders-in-lamellae" (Ludwigs, et. al. 2003), dimple (Figure 5.1c) and "pillared-lamellae" (Figures 5.1d-f; Bailey et. al. 2001) structures.

For these hybrid materials, Small Angle X-ray Scattering (SAXS) and electron microscopy data indicated both the PHMA and PEO-aluminosilicate phases formed lamellar sheets aligned parallel to the surface of the film. Scanning Transmission Electron Microsopy (STEM) images of individual layers of the material showed a hexagonal mesh structure within each PEO-aluminosilicate layer consistent with the presence of round, micellar PEP domains. These results establish that ABC copolymers can be used to direct silica-type materials into well-ordered morphologies.

5.2 Experimental Methods

5.2.1 Materials Synthesis

The materials described in this chapter were synthesized by Dr Surbhi Mahajan. The poly(ethylene-alt-propylene-block-ethylene oxide-block-n-hexyl methacrylate) (PEP-b-PEO-b-PHMA) copolymer was prepared via stepwise anionic polymerization, catalytic hydrogenation and atom transfer radical polymerization (Mahajan, et. al. 2004). The properties of the parent ABC copolymer are summarized in Table 5.1. The molecular weight (M_n = 48520 g/mol) and polydispersity (M_w/M_n = 1.13) were determined via NMR and GPC. Block volume fractions (f_{PEP}=0.15,

f_{PEO}=0.11 and f_{PHMA} = 0.74) and Root Mean Square end-to-end lengths (L_A = 7.6 nm, L_B = 6.7nm, L_C = 11.2 nm) were calculated using the block densities and packing lengths of the corresponding homopolymers. The Flory-Huggins interaction parameters were estimated using the approximation of Hildebrand and Scott (Madkour, 2001).

Table 5.1- Properties of parent ABC block copolymer[a]

[b]f_A	0.15
f_B	0.11
f_C	0.74
V	48600 cm^3/mol (80.7 nm^3/molecule)
M_n	48520 g/mol
M_w/M_n	1.13
[c]$\chi_{AB}N$	350
$\chi_{BC}N$	130
$\chi_{AC}N$	50
[d]L_A	7.6 nm
L_B	6.7 nm
L_C	11.2 nm

[a]*The parent copolymer corresponds to copolymer EPOM2 in Chapter Five (Table 5.1, page 85) of Surbhi Mahajan's thesis (Mahajan, 2005).*
[b]*Block Volume fractions for room temperature homopolymer densities (Table 3.1)*
[c]*Flory-Huggins Interaction parameters given in (Table 3.2)*
[d]*RMS end-to-end block lengths computed with packing lengths from (Table 3.1)*

ABC copolymer-aluminosilicate composites were prepared following a general procedure described previously (Templin, et. al. 1997; Jain and Wiesner, 2004).

Briefly, the ABC copolymer was dissolved in a 50-50 mixture of tetrahydrofuran and chloroform to form a 2% solution by weight. In a second vial, a sol of 3-(glycidyloxypropyl) trimethoxysilane (GLYMO) and aluminum *sec*-butoxide (mole ratio of 8:2) was prepared following a two-step acid catalyzed hydrolysis procedure described previously (Templin, et. al. 1997). For each hybrid material, appropriate volumes of the copolymer solution and this sol were combined and the resulting solution stirred for one hour. Films were then cast by evaporation of solvents and byproducts on a hot-plate at 50°C. The resulting clear films (~1 mm thick) were then annealed for 1 hour at 130°C in a vacuum oven to remove residual solvent. For each film, volume fractions for the PEO-aluminosilicate domain ($f_{PEO+aluminosilicate}$) were calculated assuming a density of 1.4 g/cm^3 for the PEO-aluminosilicate phase (Jain and Wiesner, 2004); compositions are reported in Table 5-2.

Table 5-2 : Composition of ABC Copolymer/aluminosilicate compounds.

Compound	f_{PEP}	$f_{PEO+aluminosilicate}$	f_{PHMA}
H28	0.12	0.28	0.60
H34	0.11	0.34	0.55
H39	0.10	0.39	0.51
H44	0.09	0.44	0.47

Domain volume fractions were calculated assuming room temperature densities of ρ_{PEP} = 0.855 g/cm^3 (Fetters, et. al. 1994), $\rho_{PEO+aluminosilicate}$ = 1.4 g/cm^3 (Jain and Wiesner, 2004), ρ_{PHMA} = 1.007 g/cm^3 (Rodger and Mandelkern, 1957).

5.2.2 X-ray Scattering

Small and Wide-angle X-ray scattering data were gathered using a laboratory source. Briefly, CuK$_\alpha$ x-rays (λ=1.54Å) were generated with a rotating anode Rigaku

RU-3HR generator (Voltage = 42kV, Current = 56mA, 2mm×0.2mm point focus on the copper anode), filtered by a nickel foil (thickness = 10 μm; Goodfellow, PA) and focused and further monochromatized with a pair of Franks mirrors (Hajduk, 1994). The flux at the sample was ~4×10^7 X-ray photons per second in a ~1mm×1mm beam. Small Angle X-ray Scattering (SAXS) data was gathered using 60cm or 100cm flight tubes while Wide Angle X-ray Scattering (WAXS) was measured using a 1.5cm flight tube. A small circle of lead tape (typical diameter of 2-3mm) at the end of the flight tube blocked the transmitted X-ray beam while the scattered X-rays were imaged with a home-built 2-D X-ray area detector (Tate, et. al. 1995). The distance from the sample to detector and position of the beam center were determined using silver behenate (d_l = 5.8376nm; Blanton, et. al. 1995)and silver stearate (d_l = 4.868nm; Vand and Aitken, 1949) calibrants. Scattering lengths in text are given as $s = 2\ sin\ (\theta)/\lambda$, where 2θ is the total scattering angle.

Samples of the hybrid material were cut to size (~1mm thick × 1mm wide × 5mm long) and positioned using a mechanical rotation stage. To study the effect of solvent on the hybrid material, samples were placed in a standard glass X-ray capillary (d = 1.5mm, Charles Supper, MA) and a small amount (5-15 microlitres) of cyclohexane added. The capillary was sealed with Parafilm M (Alcan Packaging, WI) to slow the escape of the solvent, and SAXS data gathered as the solvent slowly evaporated.

Oriented samples of the parent ABC block copolymer were prepared using a small, home-built shear cell. Specimens (~ 7mm long × 4mm wide × 1.5mm deep) were pressed into the shear cell. Under rough vacuum, the sample was heated to 75°C and then sheared (~150% shear at ~0.5 Hertz) for 5 minutes. The shear cell was then

cooled back to room temperature (~1°C/minute) and the polymer removed and studied via SAXS.

Solvent annealed samples of the parent ABC copolymer were prepared by heating the copolymer to T=100°C before exposing it to a cyclohexane vapor (~ 0.5MPa pressure). After 30 minutes annealing in the cyclohexane vapor, the sample was dried out using a rough vacuum (2 hours) before cooling the sample back to room temperature (~1°C/minute).

The structure of the hybrid materials was modeled in MATLAB using level set functions (Wohlgemueth, et. al. 2001) consistent with block volume fractions and unit cell dimensions determined from SAXS, AFM and STEM data. Fourier coefficients of the structural models were evaluated numerically and compared to the measured SAXS structure factors.

5.2.3 Microscopy

Cross-sections of the hybrid materials were prepared by freeze-fracture. Small (6mm × 2mm × 1mm) samples of the hybrid material were held with tweezers and frozen by dipping into liquid nitrogen. While under the liquid nitrogen, the end of the sample was snapped off to expose a fresh cross-section perpendicular to the surface of the film. After thawing, samples were imaged at room temperature with a LEO 1550 Field Emission Scanning Electron Microscope (FE-SEM) using the secondary electron signal and an accelerating voltage of 2 kV. For Transmission Electron Microscopy (TEM), thin sections (50-100nm thick) of the hybrid material were cut using a Leica Ultracut UCT microtome at 210K and transferred to copper mesh TEM grid with a thin carbon layer. Bright-field TEM was performed using a JEOL 1200EX microscope operating at 120kV.

Individual layers of the hybrid material were isolated by dispersing the hybrid material in an organic solvent (1mg hybrid/1g of toluene) for 12 hours followed by mild sonication of the resulting solution (Ulrich, et. al. 1999). Single drops of this solution were then placed onto a copper mesh TEM grid with a thin carbon layer and the solvent was allowed to evaporate. High resolution annular dark-field imaging and parallel electron energy loss spectroscopy (PEELS) of these samples were performed using the Cornell VG-HB501UX 100-keV UHV-STEM (Muller, et. al. 1998). Additional STEM was performed using a LEO 1550 FE-SEM microscope fitted with a 4-quadrant solid-state STEM detector (accelerating voltage 30 kV). Malcolm Thomas in the Cornell Center for Materials Science performed most of the electron microscopy reported in this chapter.

The individual sheets were also examined via Atomic Force Microscopy (AFM) by drop-coating the dispersed solution onto a silicon substrate (1cm × 1cm) and allowing the solvent to evaporate. The samples were imaged using a Veeco Nanoscope III Multimode scanning probe microscope employing tapping mode etched silicon tips. These measurements were performed by Dr Phong Du.

5.3 Results

All four compounds (Table 5-2) shared a common morphology of hexagonally patterned aluminosilicate sheets aligned parallel to the film surface (Figures 5.1e, 5.1f). For clarity, structural data for compound **H34** is used to summarize the common features of the morphology before then considering small variations in structure between the four compounds.

5.3.1 SAXS

Figure 5.2 shows 2-dimensional SAXS from compound **H34** in which the film surface normal is directed along the vertical axis.

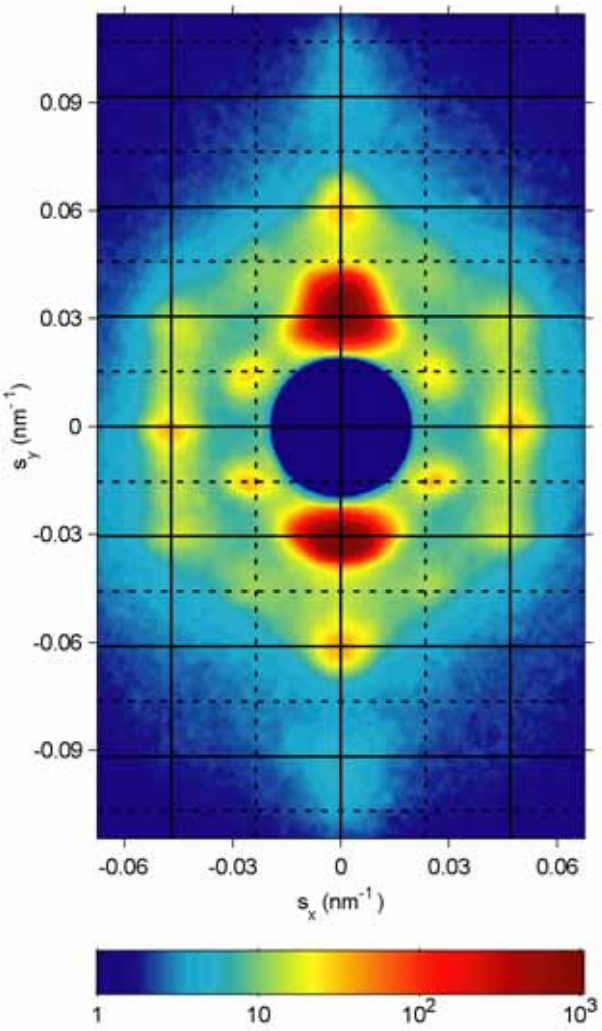

*Figure 5.2 - 2-D SAXS (logarithmic scale) from compound **H34** with the sample's surface normal directed along the vertical axis. The solid layer (horizontal) and row (vertical) lines mark repeat spacings of $d_l = 33.0 \pm 3.3$nm ($\Delta s_y = 0.030 \pm 0.003$ nm^{-1}) and $d_r = 21.7 \pm 1.9$ nm ($\Delta s_x = 0.046 \pm 0.004$ nm^{-1}) respectively as reported in Table 5-3. Dotted layer and row lines correspond to a doubled unit cell.*

The scattering pattern did not change when the sample was rotated about the film normal, indicating simple fiber-type alignment of the structure with respect to the film surface (Finkenstadt and Millane, 1998). The position and intensity of scattering along the horizontal layer and vertical row lines is summarized in Table 5-3.

*Table 5-3 : Parameters from 2-D SAXS from **H34** (Figure 5.2).*

Line	**s_y (nm^{-1})**	**D_y (nm)**	**s_x (nm^{-1})**	**D_x (nm)**	**[a]Integrated Intensity**
1st Layer	0.030±0.003	33.0±3.3	0±0.005	-	100
2nd Layer	0.059±0.003	16.8±0.9	0±0.006	-	1.9±0.2
Outer Row	-0.03 to 0.03	-	0.046±0.004	21.7±1.9	76.7±0.9
Inner Row	0.014±0.003	71±14	0.025±0.003	39.2±4.5	11.0±0.4

[a]Scaled relative to intensity of first order lamellar peaks. Errors include only the standard deviation of the least squares fitting.

Several features of the structure can be clearly resolved in the SAXS pattern. Firstly, the three orders of Bragg spots along the vertical axis ($\Delta s_y = 0.030 \pm 0.003$ nm^{-1}) correspond to the lamellar stacking ($d_l = 33.0 \pm 3.3$nm) of the aluminosilicate sheets. The narrow angular width of these spots (FWHM = 11°) confirms the lamellae are strongly aligned during the solvent-casting process (Coulon, et. al. 1989; Fukunaga, et. al. 2000). Secondly, the intense, in-plane scattering along the vertical row lines at $|s_x| = 0.046 \pm 0.004$ nm^{-1} indicates periodic structure within the sheets with a repeat spacing of $d_r = 21.7 \pm 1.9$ nm. The integrated scattering intensity along these row lines is quite strong (~ 75 % of the intensity of the first lamellar peak).

This strong scattering reflects the presence of large in-plane modulations of the PEO-aluminosilicate density, as is evident from structure factors calculated for the

pillared-lamellae model shown in Figures 5.1e-f. In this structure the cylindrical PEP domains (f_{PEP} = 0.11) form pillars running through each PEO-aluminosilicate sheet ($f_{PEO+aluminosilicate}$ = 0.34) in a 2-layer ABAB type stacking. Assuming room temperature densities for the PEP, PHMA and PEO+aluminosilicate domains, the outer row lines ($|s_x| = 0.046 \pm 0.004$ nm^{-1}) have an integrated intensity of 90% to 110% of the intensity of the first order lamellar Bragg peaks ($s_x = 0$nm^{-1}, $|s_y| = 0.030 \pm 0.003$ nm^{-1}). Thus, the observed intensity for the outer row lines is largely consistent with the intensity expected for a pillared lamellae structure.

However, in the actual material the sheets cannot be stacked with long-range, periodic order or the scattering along the row lines would form Bragg Spots rather than the observed Bragg Rods. Such stacking disorder is frequently observed in hexagonal layered structures when the two-layer (ABABA...) stacking and three-layer (ABCABCA...) stacking are nearly degenerate (Ahn and Zin, 2000; Zhu et. al., 2003). Finally, as discussed in later sections, a unit cell doubling is suggested by the inner Bragg spots marked by the dotted row and layer lines ($|s_x| = 0.025 \pm 0.003$ nm^{-1}, $|s_y| = 0.014 \pm 0.003$ nm^{-1}).

The response of the hybrid materials to changes in temperature and solvent content provide further support for this interpretation of the SAXS data. A lamellar block copolymer/aluminosilicate material should preferentially deform along its lamellar axis because the covalent bonding network within each PEO-aluminosilicate layer constrains in-plane deformations. Because the middle PEO block of each chain is embedded within the covalent aluminosilicate network, shape changes in the sample should be directly reflected in the unit cell dimensions. Thus, following thermal expansion or swelling due to solvent uptake, the layer lines (lamellar ordering) should shift while the row lines (in-plane ordering) should remain fixed.

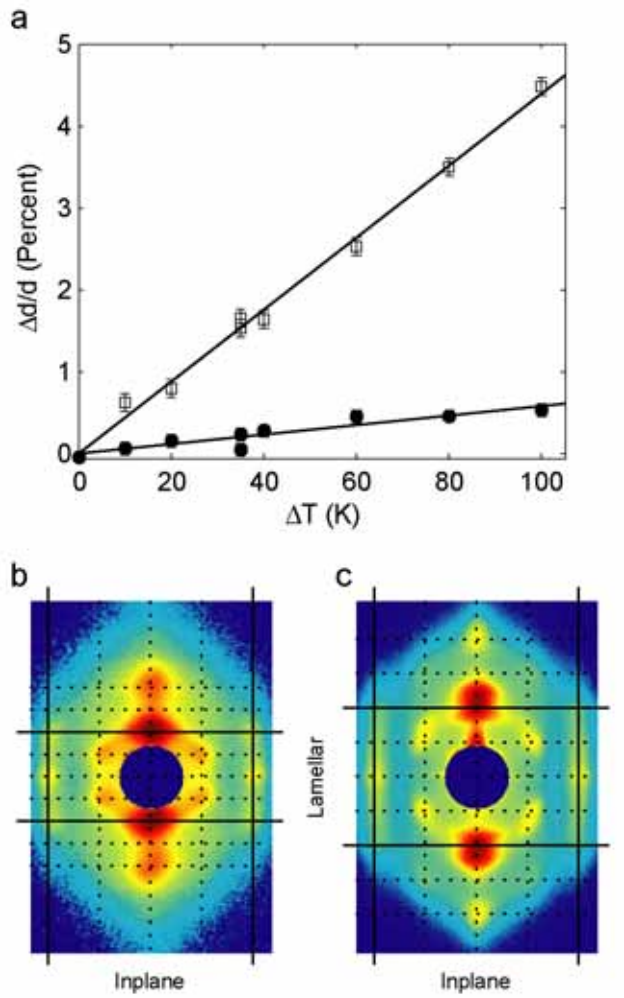

*Figure 5.3 - Hybrid Material Anisotropy. Percent change in lamellar (open squares) and in-plane (closed circles) repeat spacings of compound **H34** as a function of temperature (263K to 363K) (**a**). Along the lamellar direction the linear thermal expansion coefficient ($4.33 \pm 0.11 \times 10^{-4}$ K^{-1}) is 7.5±1 times the expansion coefficient in the in-plane direction ($5.8 \pm 0.8 \times 10^{-5}$ K^{-1}). 2-D SAXS (logarithmic scale) from compound **H34** swollen by cyclohexane ($d_l = 50 \pm 1$ nm) (**b**) and following re-evaporation of solvent ($d_l = 32.8 \pm 0.5$nm) (**c**). Although cyclohexane changes the lamellar repeat spacing, the in-plane row spacing ($d_r = 21.7 \pm 1.9$ nm) remains essentially constant.*

Figure 5.3a shows the change in lamellar and in-plane cell dimensions as a function of temperature. The linear thermal expansion coefficient ($4.33 \pm 0.11 \times 10^{-4}$ K^{-1}) along the lamellar direction was 7.5 ± 1 times the expansion coefficient in the in-plane direction ($5.8 \pm 0.8 \times 10^{-5}$ K^{-1}), confirming the anisotropic thermal expansion of the structure along the lamellar axis. Similarly, when **H34** was exposed to a non-polar solvent (cyclohexane) the structure within the sheets remained essentially unchanged ($d_r = 21.7 \pm 1.9$ nm) while the adjoining PHMA domains swelled, as illustrated by the 50 ± 3 % increase in lamellar spacing shown in Figure 5.3b. Remarkably, following evaporation of the solvent, the structure relaxed to the initial state as shown in Figure 5.3c (compare to Figure 5.2). The extreme anisotropy of the hybrid materials provides strong support for a hexagonally patterned lamellar structure.

5.3.2 Microscopy

Real-space images of the hybrid material were obtained from the bulk material, thin sections, and individual sheets isolated by solvent dispersal. An SEM image of a cross-section perpendicular to the film surface (surface normal vertical) is shown in Figure 5.4a. The bright regions in the image correspond to the aluminosilicate phase, although the Secondary Electron (SE) signal is also sensitive to surface topography. The aluminosilicate layers run parallel to the surface of the film and the interlayer spacing has a range of 31 ± 5 nm, in agreement with the SAXS data ($d_l = 33.0 \pm$ 3.3nm). The SEM images also show structure along each aluminosilicate layer with a mean repeat spacing of 23.6 ± 3 nm as determined by the Fourier transforms (FT) of several images. Although some of the sheets appear to have polymer (dark) channels running through them, these features along the edge of each sheet must be interpreted with caution, as the SE signal is sensitive to both composition and topography of the freeze-fractured surface.

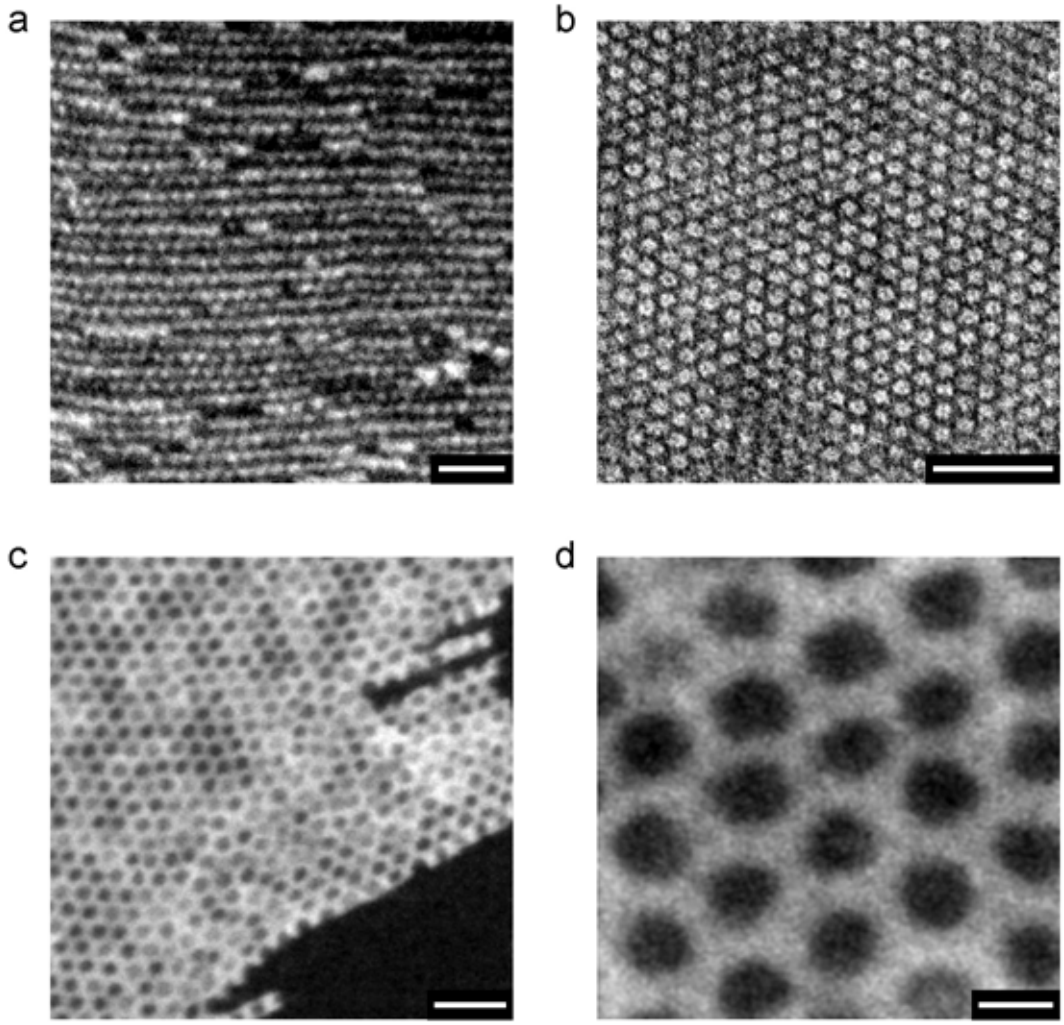

*Figure 5.4 - Electron Micrographs of compound **H34**. SEM image (aluminosilicate bright) of the bulk material for a cross-section perpendicular to the surface (surface normal vertical) (**a**, 100nm scale bar). Bright-field TEM (aluminosilicate dark) of a thin (~50nm) section cut parallel to the surface (**b**, 100nm scale bar). Dark-field STEM image (aluminosilicate bright) of an individual sheet isolated by dispersion in solvent (**c**, 100nm scale bar) and a higher magnification image of the 2-D mesh structure (**d**, 20nm scale bar).*

The in-plane structure of the sheets was imaged via Bright-Field TEM of thin sections (50 to 100 nm) cut parallel to the film surface. As shown in Figure 5.4b, the aluminosilicate phase (dark) formed a well-ordered 2-D hexagonal mesh with a "hole" spacing of 21.2 ± 1.8 nm (row spacing 18.3 ± 1.6 nm). These 2-D modulations of aluminosilicate density within each layer agree well with the strong in-plane ordering seen in the SAXS pattern (d_r = 21.7 ± 1.9 nm). These structural features were also evident in individual layers isolated by solvent-dispersal of the hybrid material.

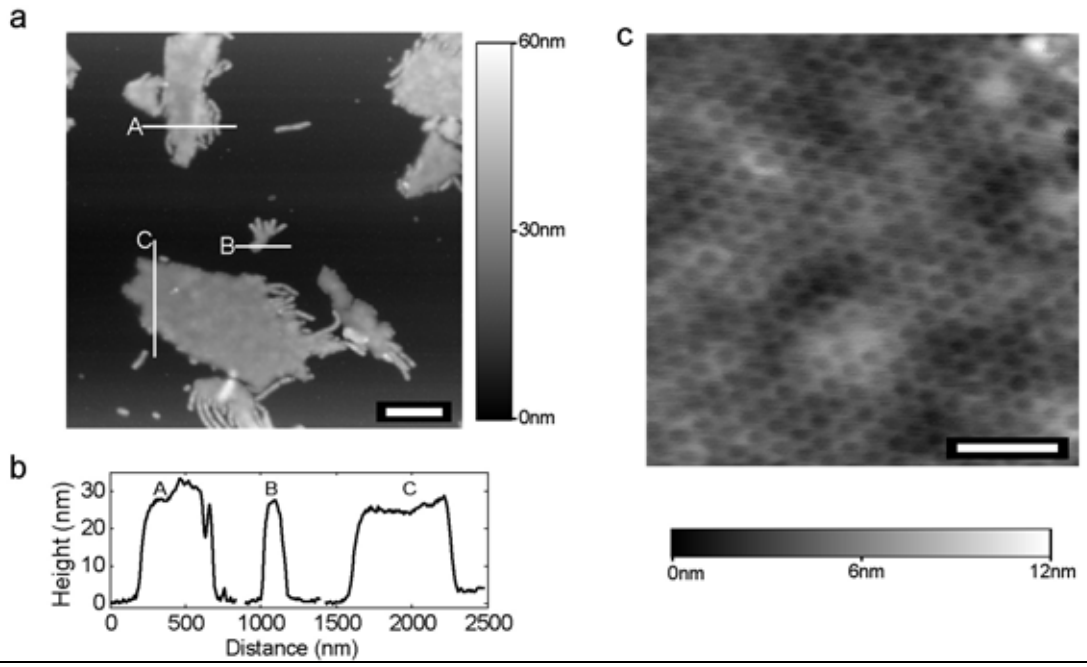

*Figure 5.5 - AFM image of solvent-dispersed sheets of compound **H34** supported a silicon substrate (**a**, scale bar 500nm). Sections across three sheets (A,B,C) have a mean height of 26.3 ± 3.0nm (**b**). Higher magnification image of single sheet showing the hexagonal pattern (row spacing 23.5 ± 1.0nm) observed for large amplitude tapping (**c**, scale bar 100nm).*

As shown in the Figure 5.5, AFM images of individual sheets were quite flat and the average height (26.3 ± 3.0nm) was consistent with the SAXS layer spacing

(d_I=33.0 ± 3.3nm). Using a higher magnification and large tapping-mode amplitude, a hexagonal pattern with a row spacing of 23.5 ± 1.0nm could just be resolved (Figure 5.5c).

The structure of the PEO-aluminosilicate domain within individual sheets was examined using the atomic number sensitivity of annular dark-field STEM imaging. In Figures 5.4c and 5.4d (aluminosilicate bright), the 2-D hexagonal pattern is readily apparent and the enrichment of silicon within the mesh framework was confirmed using Parallel Electron Energy Loss Spectroscopy (PEELS; Spence, 2006; Thomas and Midgley, 2004). The dark regions in the hexagonal mesh could correspond to dimples in the PEO-aluminosilicate domain (Figure 5.1c), or holes where the PEO-aluminosilicate phase was completely excluded (Figure 5.1d). In Figure 5.4c, some of the spots are considerably darker than others. This variation is readily accounted for if the darker spots correspond to holes through the PEO-aluminosilicate and the brighter spots correspond to dimples in the PEO-aluminosilicate layer.

To test this idea, isolated sheets of compounds **H34** and **H44** were imaged in a field emission SEM using both dark-field (STEM) and Secondary Electron (SE) signals as shown in Figure 5.6. If each sheet has a mixture of dimples and holes, compound **H34** should have more holes because it has a smaller PEO-aluminosilicate volume fraction. The SE imaging mode may also distinguish between holes and dimples as the appearance of individual dimples could differ depending on whether they are on the top or the bottom of the PEO-aluminosilicate domain. In contrast, dimples on the top or bottom of the sheet should appear the same in STEM mode because the electrons pass through the sheet and are sensitive to the integrated scattering intensity along their path.

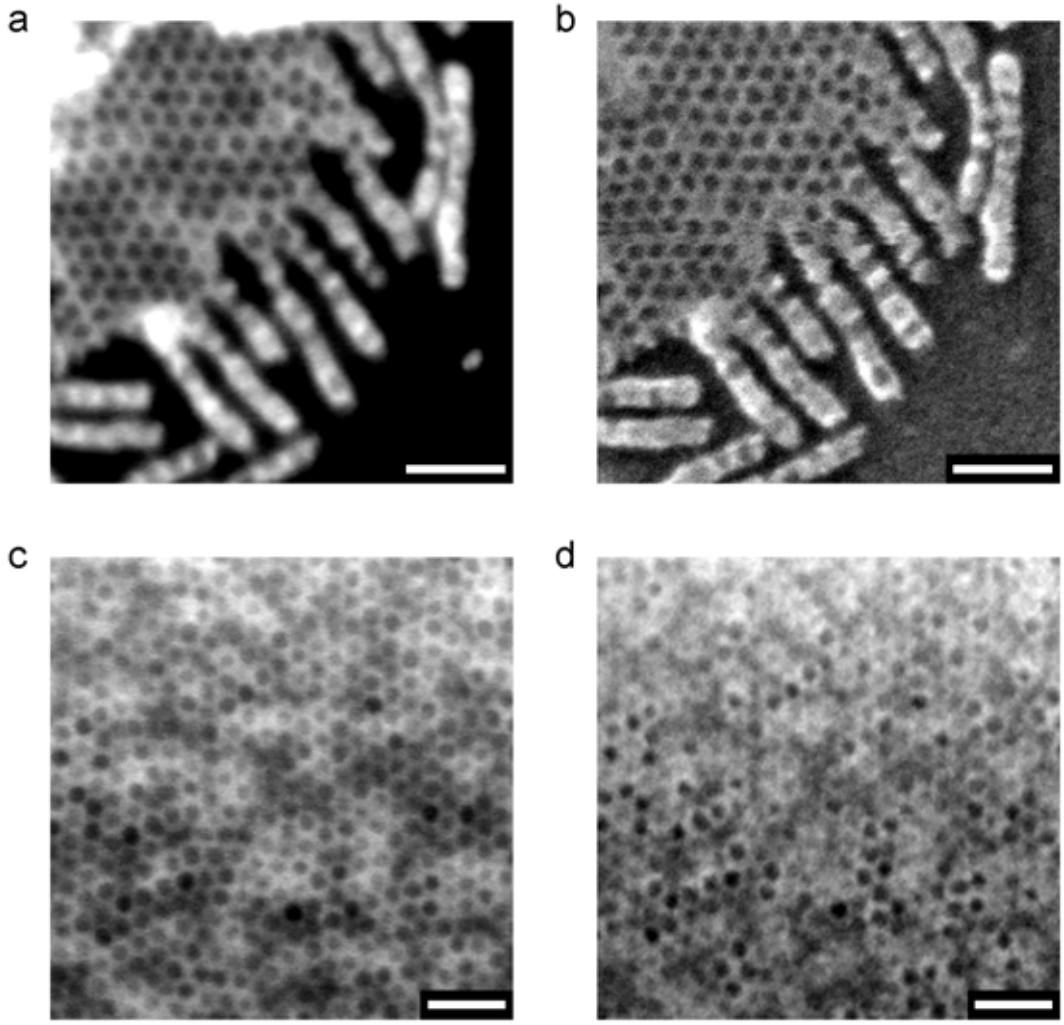

*Figure 5.6 - Solvent-dispersed sheets of compounds **H34** (**a**, **b**) and **H44** (**c**, **d**) imaged via dark-field STEM (**a**, **c**) and the secondary electron SEM signal (**b**, **d**). In all images the scale bar is 100nm and the aluminosilicate phase is bright.*

For compound **H34**, most spots are dark in the STEM image (Figure 5.6a) and clear in the SE image (Figure 5.6b), consistent with holes in the PEO-aluminosilicate sheet. In contrast, in the STEM image of compound **H44** (Figure 5.6c) only a small number of the spots are dark. Furthermore, a sizeable fraction of the spots evident in the STEM image (Figure 5.6c) cannot be resolved in the SE image (Figure 5.6d), consistent with having dimples on the top and bottom of the sheet. These results

suggest the hexagonal pattern in the PEO-aluminosilicate domains consists of mixture of dimples and holes.

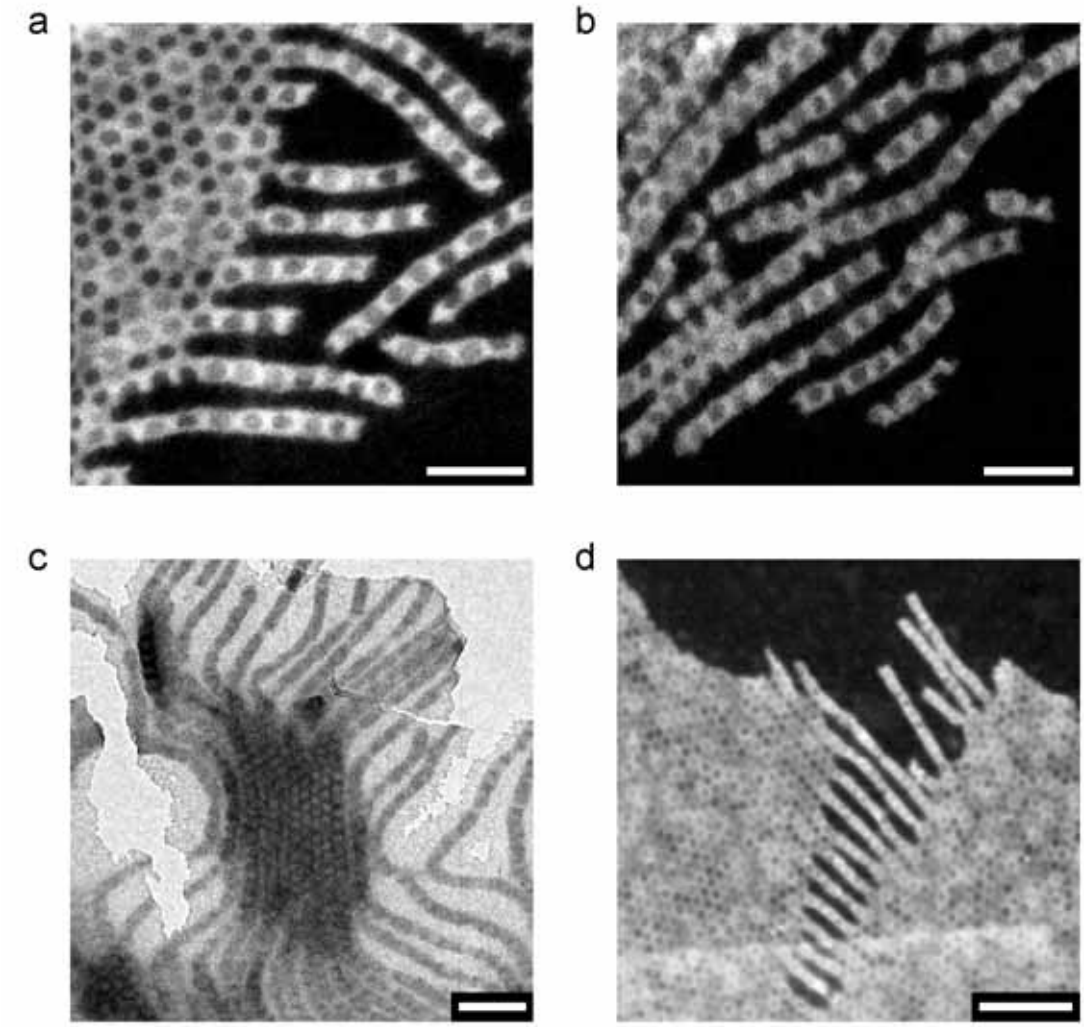

*Figure 5.7 - Dark-field STEM image of the edge of a single sheet of compound **H34** isolated by solvent dispersal shows how alternating rows terminate while the remaining rows continue as individual strands (**a**, aluminosilicate bright, 100nm scale bar). Dark-field STEM image of individual strands of compound **H34** (**b**, aluminosilicate bright, 100nm scale bar). Bright-field TEM of the edge of a thin (~ 50nm) section of the bulk material (compound **H34**) cut parallel to the sample surface (**c**, aluminosilicate dark, 100nm scale bar). Dark-field STEM image of a single sheet of compound **H44** isolated by solvent dispersal showing strand formation within the middle of a sheet (**d**, aluminosilicate bright, 200nm scale bar).*

Finally, despite the apparent hexagonal symmetry of the sheet structure, a curious feature was frequently seen at the edges of sheets. Frequently, as shown in Figure 5.7a, alternating rows of the meshwork terminated while the remaining rows continued as individual strands. Isolated strands were also present (Figure 5.7b) and were more prevalent for the thinner aluminosilicate sheets of compounds **H28** and **H33** and for solutions that had been sonicated longer, suggesting the strands formed by breaking from sheets (Warren et. al., 2007). As shown in Figure 5.7c, the sheet structure also broke up into strands at the edges of microtomed sections. In a few of instances, alternating strands were observed within isolated sheets as shown in Figure 5.7d. Thus, the sheets appear to possess a direction along which they preferentially form strands.

5.3.3 Internal Domain Structure

Wide-Angle X-ray Scattering from these hybrid materials showed the presence of several types of structural correlation. In Figure 5.8a, the outer-most peak (d_{CC} = 0.48 ± 0.01 nm, s = 2.08 ± 0.04 nm^{-1}) corresponds to chain-chain correlations within the PEP and PEO blocks as well as correlations between the alkyl side-chains within the PHMA block. Within the PHMA block, the difference in polarizability and flexibility between the methacrylate backbone and alkyl side chains leads to a structure where rows of aligned polymer backbones are spaced apart by their alkyl side chains (Beiner, et. al. 2002) as illustrated in Figure 5.8b. These correlations between polymer backbones within the PHMA block gives rise to the intermediate peak (d_{BB} = 1.38 ± 0.03 nm, s = 0.72 ± 0.02 nm^{-1}) that agrees with the reported WAXS from PHMA homopolymers (d_{BB} = 1.40 nm; Beiner, et. al. 2002). The innermost peak (d_{SOL} = 2.4 ± 0.3 nm, s = 0.416 ± 0.05 nm^{-1}) is present only in the hybrid materials and reflects correlations between the densely packed aluminosilicate sol

particles within the PEO-aluminosilicate domain (Jain and Wiesner, 2004; Warren, et. al. 2007). This structure is also apparent in high magnification dark-field STEM images (Figure 5.8c) of individual PEO-aluminosilicate domains.

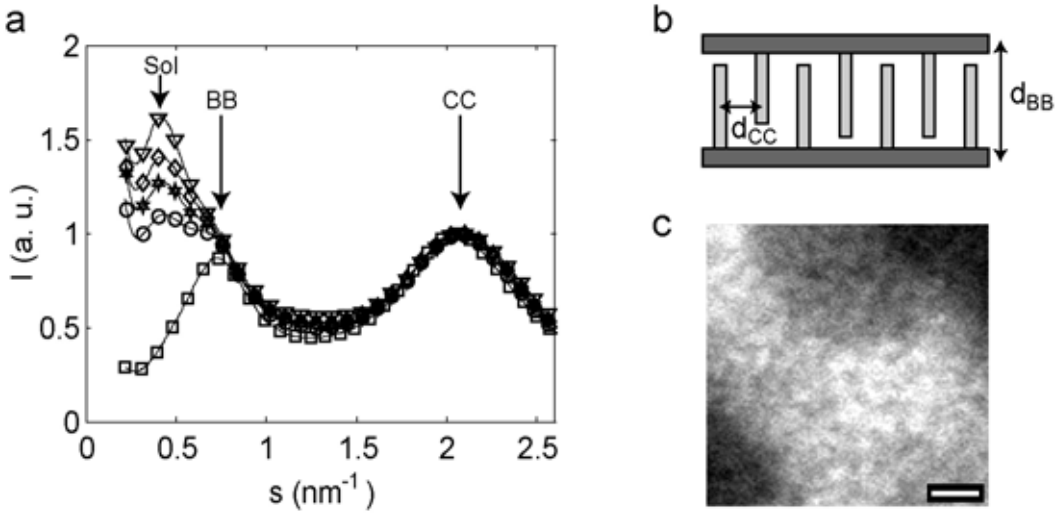

*Figure 5.8 - Wide Angle X-ray Scattering (WAXS) data from the parent ABC copolymer (squares), **H28** (circles), **H34** (hexagram), **H39** (diamonds) and **H44** (triangles) hybrid materials show correlations between the alkyl chains (d_{CC} = 0.48 ± 0.01 nm) in all three domains, the polymer backbones within the PHMA domains (d_{BB} = 1.38 ± 0.03 nm), and the aluminosilicate sol particles in the PEO-aluminosilicate domains (d_{SOL} = 2.4 ± 0.3 nm) (**a**). Schematic of PHMA structure where parallel backbones (dark, horizontal) are spaced apart by their side-chains (light, vertical) (**b**). Dark-field TEM (aluminosilicate bright, 5nm scale bar) showing structure within the PEO-aluminosilicate domain (**c**).*

5.3.4 Parent Copolymer Structure

In the parent PEP-b-PEO-b-PHMA copolymer, the large volume fraction of the PHMA domain (f_{PHMA} = 0.74 > f_{PEP}=0.15, f_{PEO}=0.11) should favor morphologies in which the PEP and PEO blocks form micellar or cylindrical domains (Zheng and Wang, 1995) surrounded by a matrix of PHMA. Since the mixing enthalpy of the A and C blocks is relatively small ($\chi_{PEP/PHMA}N \approx 50 < \chi_{PEP/PEO}N \approx 350$, $\chi_{PEO/PHMA}N \approx$

130), morphologies with optional PEP/PHMA domain interfaces should be favored. Earlier experimental studies of ABC copolymers in this regime have reported a number of morphologies including the "spheres-on-spheres" (Breiner et. al., 1998), "core-shell" cylinders, "rings-at-cylinders" and "helices-around-cylinders" structures (Breiner, et. al. 1997; Krappe, et. al. 1995).

Casting from solvent did not align the parent ABC copolymer morphology so samples were aligned using reciprocating shear (Keller, et. al. 1970; Kannan and Kornfield, 1994; Stangler and Abetz, 2003). 2-D SAXS from these samples were consistent with a hexagonal structure aligned with the shear axis. This alignment is evident in SAXS data taken with the X-ray beam directed perpendicular to the shear axis (horizontal) as shown in Figure 5.9a. The integrated angular intensity of the inner peak (Figure 5.9c) had a FWHM of ~33° concentrated perpendicular to the shear axis. In contrast, SAXS data taken with the X-ray beam parallel to the shear axis (Figure 5.9d, 9f) exhibited 6-fold symmetry, consistent with a hexagonal lattice. The individual scattering peaks were quite broad as is evident in the plots of radial averaged scattering intensity in Figures 5.9b and 5.9e. The bright inner ring (s_0 = $(2.63 \pm 0.05) \times 10^{-2}$ nm^{-1}) corresponded to a repeat spacing of 38.0 ± 0.7 nm while the broad second peak at $3^{½} \times s_0$ and shoulder at $7^{½} \times s_0$ are consistent with the allowed reflections for a hexagonal unit cell. Thus, morphologies in which the PEP and PEO domains form a cylindrical core are consistent with SAXS from shear-aligned samples.

However, a different morphology formed in samples prepared by annealing in a cyclohexane atmosphere. Figure 5.10 shows a powder average of scattering from a solvent-annealed sample.

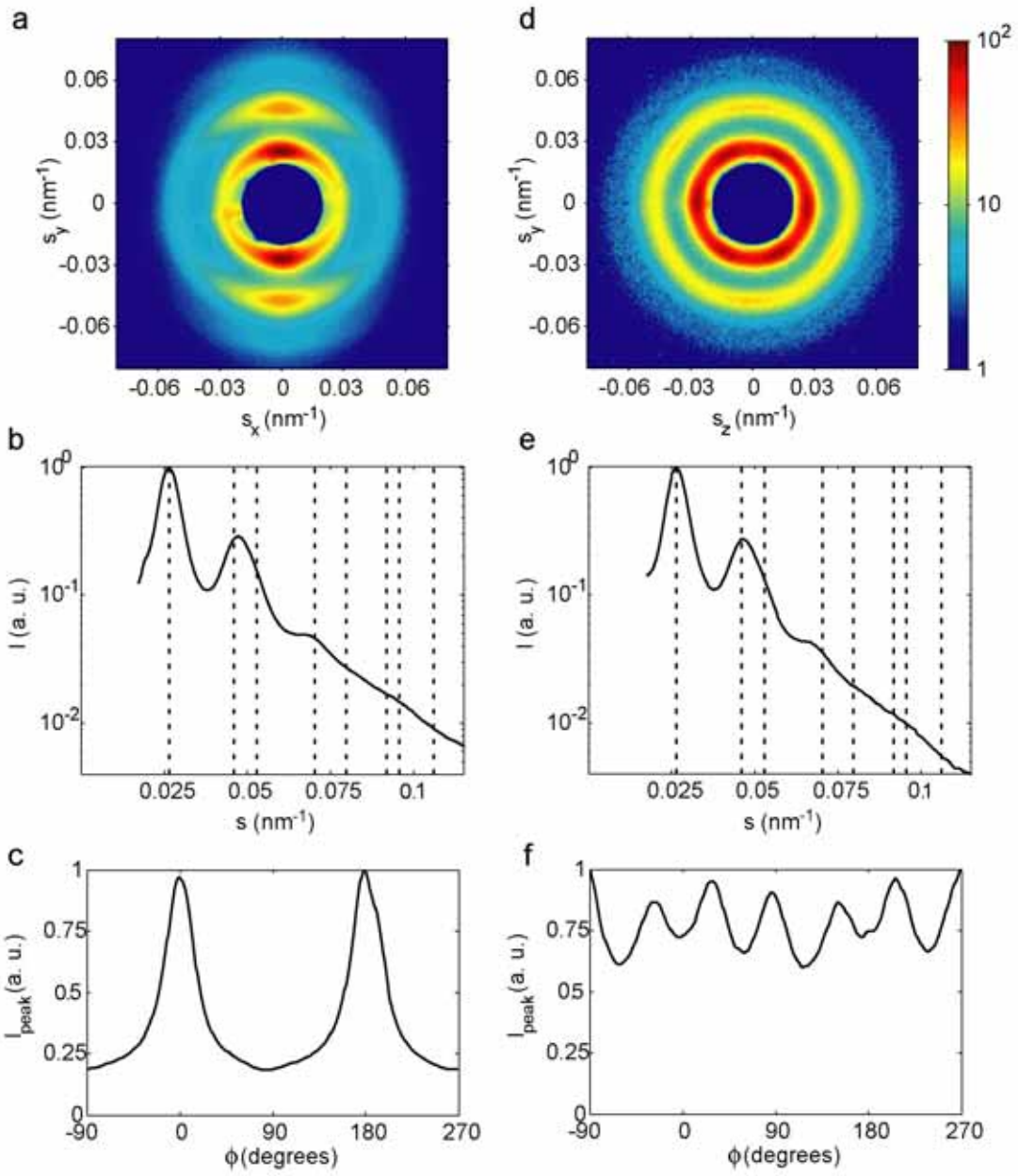

*Figure 5.9 - . 2-D SAXS (logarithmic scale) from a shear-aligned specimen of the parent ABC block copolymer (**a**, **d**). The shear direction is horizontal in (**a**) and along the x-ray beam direction in (**d**), while the surface normal of the sample is vertical in both images. Radial averages (**b**,**e**) in both cases show a main peak at s = (2.63 ± 0.05) × 10^{-2} nm^{-1} (repeat spacing of 38.0 ± 0.7 nm) and the dotted vertical lines indicate the allowed reflections for a hexagonal lattice. The angular dependence of the main peak intensity shows alignment perpendicular to the shear direction (**c**) with some 6-fold (**f**) symmetry within this plane.*

Surprisingly, the observed scattering peaks could be indexed to a simple cubic lattice (s_0 = 0.0322 ± 0.0003 nm^{-1}, repeat spacing of 31.1 ± 0.3 nm) with peaks position at relative positions of s/s_0= 1, $2^{½}$, $3^{½}$, $4^{½}$, $5^{½}$, $6^{½}$, $8^{½}$ and $9^{½}$. Heating or cooling the sample changed the lattice size, but not the relative position of the peaks.

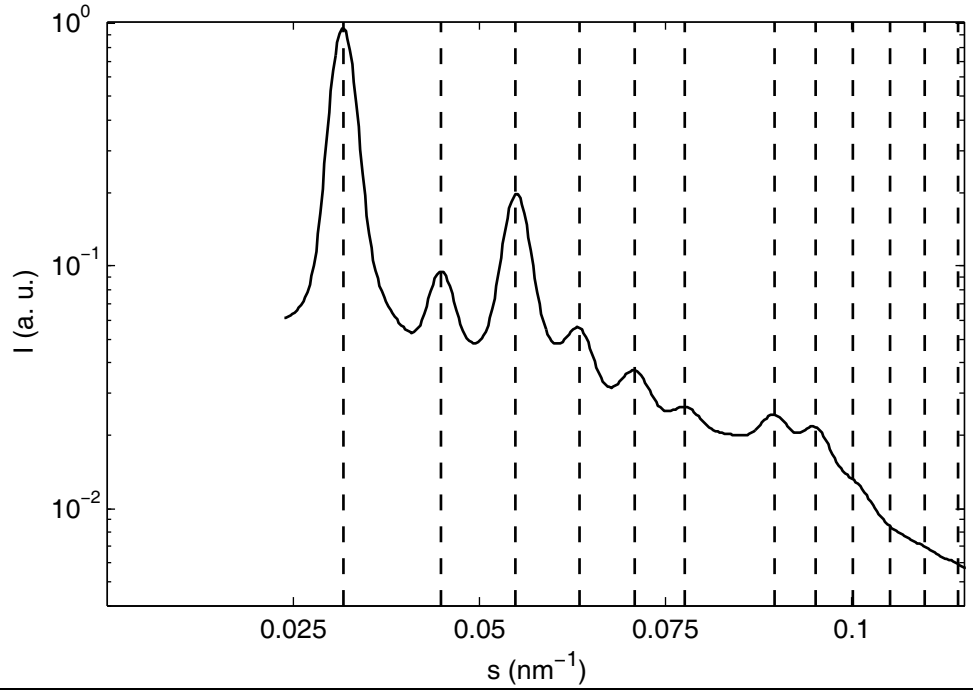

Figure 5.10 - Powder-averaged SAXS from the parent ABC block copolymer following annealing at 100C in a saturated vapor of cyclohexane. The dashed lines correspond to a simple cubic unit cell with a lattice size of 31.1 ± 0.3 nm.

After annealing at elevated temperature (200°C), neither the cubic or hexagonal morphologies changed significantly and higher temperatures caused thermal breakdown of the polymer. However, the hexagonal morphology could be transformed into the cubic morphology by annealing at 100°C in a cyclohexane vapor while shearing the cubic morphology at ~75°C converted it to the hexagonal

morphology. Thus, it appears the copolymer can be kinetically trapped in distinct, metastable structures as has been previously reported for other block copolymer systems (Ott et. al., 2001; Huang et. al., 2003). Unfortunately, the low glass temperature of all three blocks made EM imaging of the parent polymer challenging, since the structure of thin sections is only preserved at cryogenic temperatures and a cryo-EM stage was not available. Although SAXS from the parent ABC block copolymer is consistent with micellar or cylindrical PEP and PEO domains, further work will be required to determine the equilibrium morphology of the copolymer.

5.4 Discussion

SAXS and microscopy data from these hybrid materials show a lamellar morphology ($d_l \sim 33$ nm) in which each PEO-aluminosilicate domain is hexagonally patterned ($d_r \sim 23$ nm) with holes and/or dimples. The structure of the PEO-aluminosilicate domains has some similarities to the minority phase in the Hexagonally Perforated Lamellae (HPL) morphology observed in diblock copolymers (Hamley, et. al. 1993). However, the HPL morphology is believed to be metastable in diblock copolymers and is only found in a small region of the phase diagram (Hadjuk, et. al. 1997). Indeed, the HPL morphology was not observed in earlier studies of diblock PEO-b-PHMA copolymer/ aluminosilicate copolymers (Renker, et. al. 2004). In contrast, the present ABC copolymer/aluminosilicate morphology forms over quite a wide range of volume fractions ($f_{PEO+aluminosilicate} = 0.28$ to at least 0.44) suggesting the small PEP block has an important influence on the morphology.

The PEP block should form distinct domains because the enthalpy for mixing with the PEO-aluminosilicate domain is truly prohibitive ($\chi_{PEP/PEO\text{-}aluminosilicate}N > \chi_{PEP/PEO}N \approx 350$) while the enthalpy for mixing with the PHMA block is also large

($\chi_{PEP/PHMA}N \approx 50$). Because the volume fraction of the PEP block is small ($f_{PEP} \sim 0.1$), round micellar PEP domains have the smallest contact area per unit volume. Within each sheet, the best packing for these micellar PEP domains is a 2-D hexagonal array (Figures 5.1e-f). The optimal position and shape of PEP domains depends upon a trade-off between chain stretching and interfacial area. In the "balls-in-lamellae" structure (Figure 5.1b; Zheng and Wang, 1995), the burial of the PEP domain within the PEO-aluminosilicate layer incurs a large enthalpic penalty because the surface tension of the PEP/PEO-aluminosilicate interface is larger than that of a PEP/PHMA interface.

As shown in Figure 5.1c, moving the PEP micelle to one side of the PEO-aluminosilicate sheet reduces the area of the PEP/PEO-aluminosilicate interface at the cost of forming a PEP/PHMA interface. Alternatively, as proposed by Bailey and colleagues (Bailey, et. al. 2001), the PEP domain can form a pillars spanning the PEO-aluminosilicate domain as shown in Figure 5.1d. Although both structures reduce the PEP/PEO-aluminosilicate interface, the dimple structure is likely to be favored for smaller PEP micelles while the pillared structure may suit larger PEP micelles. Thus, the hexagonal structure observed within each sheet is likely to reflect the presence of an array of round PEP micelles forming dimples and pillars in the PEO-aluminosilicate domains.

These hexagonally patterned sheets are the main structural element in the hybrid materials. However, the curious strand features in Figure 5.7 and inner Bragg reflections in Figure 5.2 ($|s_x| = 0.025 \pm 0.003$ nm^{-1}, $|s_y| = 0.014 \pm 0.003$ nm^{-1}) suggest the presence of periodic ordering at longer length-scales (larger unit cell). The inner Bragg reflections share the fiber-type alignment of the lamellar structure and their position relative to the lamellar and outer row lines is consistent with a "doubled" unit

cell (Height = $2\times d_l$, In-plane Period = $2\times d_r$) even after changes to the lamellar lattice following heating or solvent uptake. Consequently, these reflections are likely to result from the hexagonally patterned sheet morphology itself or a structure commensurate with it.

Given the individual strands observed by electron microscopy (Figure 5.7), one possibility is that in some parts of the sample, layers of sheets transform into alternating layers of strands (Figures 5.11a,b). Such a change of the PEO-aluminosilicate domains from 2-D sheets to 1-D strands could be favored in regions with a lower PEO-aluminosilicate volume fraction and then be kinetically trapped during the solvent-casting process. As shown in Figures 5.11a and 5.11b, this structure naturally forms a unit cell in which both the unit cell height ($2\times d_l$) and row spacing ($2\times d_r$) are doubled relative to the lamellar structure. Depending on exact structure of strands, roughly 6% to 15% of the volume of compound **H34** would need to have this morphology to account for the intensity of the inner Bragg Reflections (Table 5-3).

However, the strands need not be present in the bulk material and the inner Bragg reflections could reflect broken hexagonal symmetry within the sheet structure. For example, even though every row appears identical in the EM projections, out-of-plane modulations such as those shown in Figures 5.11c and 5.11d cannot be excluded. Lamellar structures are unstable to undulatory modes (Rosedale, et. al. 1995; Cohen et. al. 2001) and the gentle undulations (2.2nm RMS amplitude) illustrated in Figures 5.11c and 5.11d are sufficient to account for the intensity of the inner Bragg Reflections (Table 5-3). Although it seems more probably there are alternating layers of strands within the bulk material, further study will be required to understand whether the strands are a structural intermediate formed during solvent

casting or predominantly a product of the solvent isolation procedure (Warren, et. al. 2007).

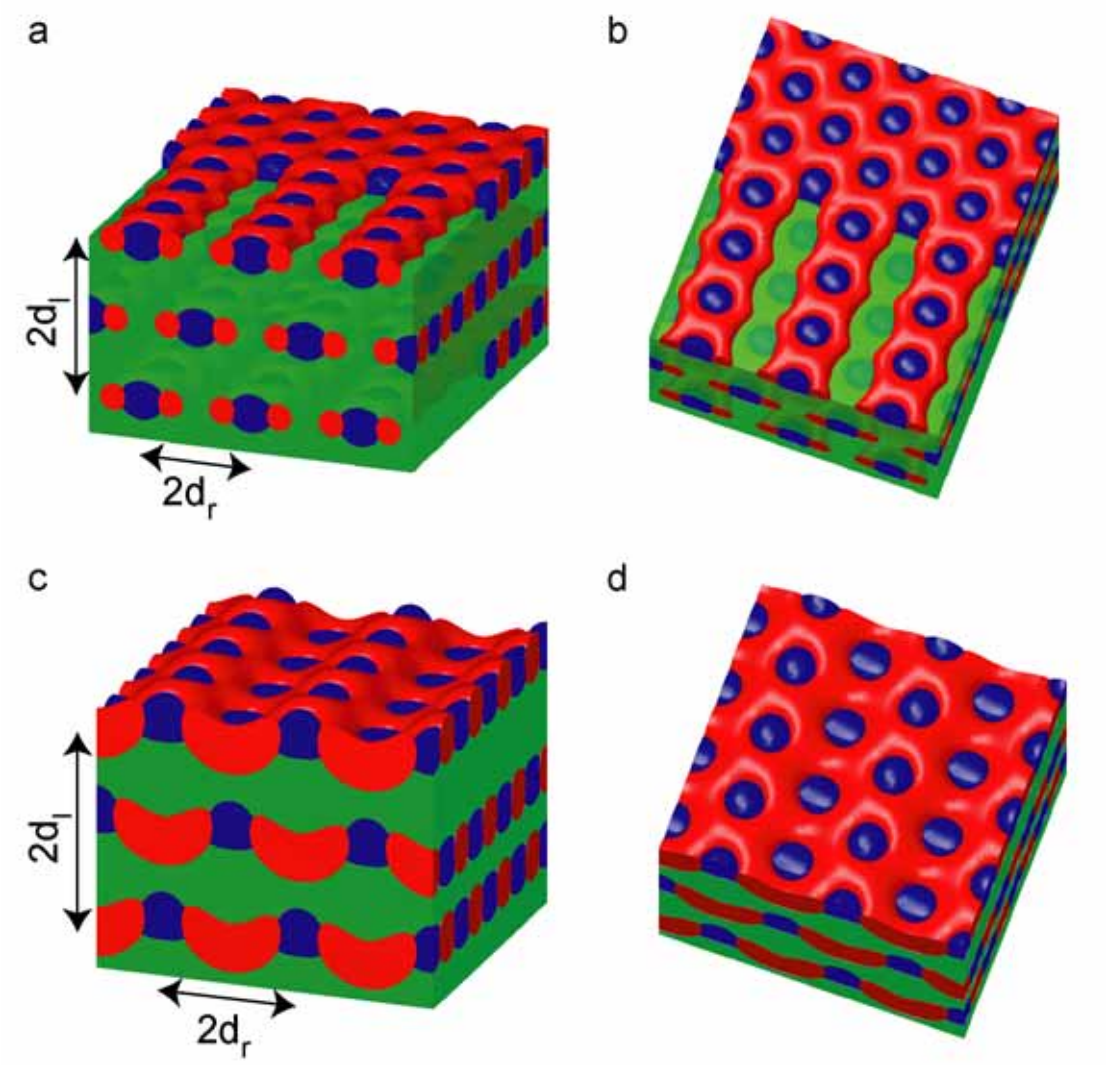

*Figure 5.11 - Structural Models of Unit-Cell Doubling. If strand formation is correlated between successive sheets (**a, b**) the strands form a unit cell doubled along two lattice directions (Height = 2×d_l, Width =2×d_r). To account for the intensity of inner row in Figure 2, approximately 6% to 15% of the sample would need to consist of the strand structure. Alternatively, the symmetry of the unit cell could be broken by anti-correlated undulations in sheets in successive. Undulations with a RMS magnitude of ~2.2nm are consistent with the observed inner row lines (**c,d**).*

5.5 Conclusion

PEP-b-PEO-b-PHMA triblock copolymer/aluminosilicate compounds were prepared in which the PEP volume fraction ($0.09 \leq f_{PEP} \leq 0.12$) was much smaller than that of the PEO-aluminosilicate ($0.28 \leq f_{PEO+Aluminosilicate} \leq 0.44$) and PHMA ($0.47 \leq f_{PHMA} \leq 0.60$) domains. X-ray scattering and electron microscopy data indicate that the PEO-aluminosilicate phase forms hexagonally patterned layers oriented parallel to the surface of the film. The structural data from the hybrid materials is largely consistent with the proposed "pillared-lamellae" structure (Bailey, et. al. 2001) in which micellar PEP domains form a hexagonal array of pillars within each PEO-aluminosilicate sheet.

Chapter Six – Woodpile Structure

6.1 Introduction

This chapter describes a woodpile structure (Figure 6.1; Sozuer and Dowling, 1994) found in a PEP-b-PEO-b-PHMA triblock copolymer/aluminosilicate material with domain volume fractions of $f_{PEP} = 0.19$, $f_{PEO+Aluminosilicate} = 0.32$ and $f_{PHMA} = 0.49$. Elucidation of this complex morphology required the use of scanning transmission electron tomography (Midgley and Weyland, 2003) to obtain three-dimensional images of the material structure. The individual PEO/aluminosilicate domains formed wiggly, zigzag shaped strands (concertinas). In the bulk material, these PEO/aluminosilicate strands were arranged in a four-layer woodpile (Sozuer and Dowling, 1994) structure in which strands in successive layers ran in alternate directions (ϕ ~75°) and the third and fourth layers of strands were offset.

Although examples of the woodpile structure are known in molecular scale systems (O'Keefe and Andersen, 1977; Meille et. al. 1990; Rosi et. al. 2005), structures with a non-parallel rod stacking have not previously been reported in block copolymers. Thus, unlike the hexagonally patterned lamellae structure described in Chapter 5, this woodpile structure cannot be thought of as a simple modification or variation of existing two-domain block copolymer morphologies. Structural modeling suggests this unusual structure may be stabilized by the presence of both PEP and PHMA domains on the outside of each PEO/aluminosilicate strand.

These results confirm that ABC block copolymers can be used to direct the assembly of inorganic precursors into complex structures not previously achieved using two-domain AB or ABA block copolymers.

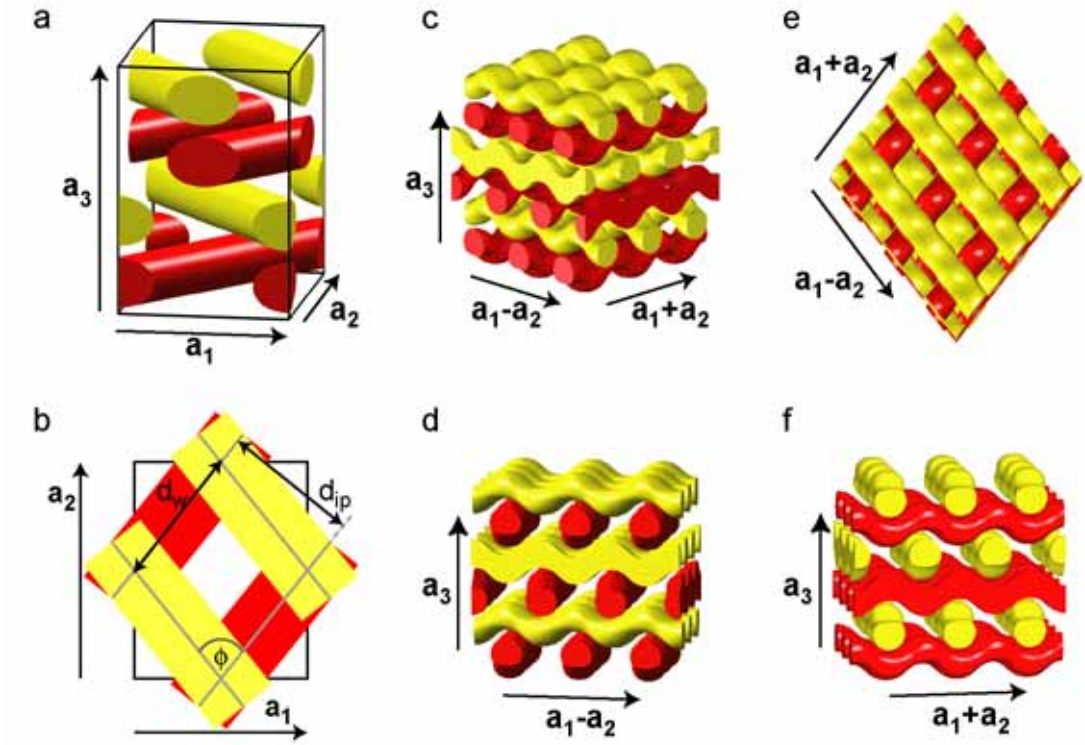

*Figure 6.1 - Four-layer woodpile structure. In the face-centered orthorhombic unit cell (side view **a,** top view **b**), strands in odd/even layers (red/yellow) are directed along the ($\mathbf{a_1} + \mathbf{a_2}$)/($\mathbf{a_1} - \mathbf{a_2}$) diagonals while the third and fourth layers are offset by ($\mathbf{a_1}+\mathbf{a_3}$)/2. The angle between the two strand directions ($\phi \approx 75°$), spacing between strands within each plane (d_{ip}) and period of wiggles along each strand (d_w) are indicated in the overhead view (**b**). Models of the undulating structure viewed from the front (**c**), overhead (**e**) and both strand directions (**d, f**). For the material described in this chapter the lattice constants are $|\mathbf{a_1}| = 29.4 \pm 0.8$ nm, $|\mathbf{a_2}| = 38.3 \pm 1.0$ nm and $|\mathbf{a_3}| = 42.8 \pm 1.5$nm.*

6.2 Experimental Methods

6.2.1 Materials Synthesis

Dr Surbhi Mahajan synthesized the materials described in this chapter. Poly(ethylene-alt-propylene-block-ethylene oxide-block-n-hexyl methacrylate) (PEP-b-PEO-b-PHMA) was prepared via stepwise anionic polymerization, catalytic hydrogenation and atom transfer radical polymerization as described earlier (Mahajan

et. al., 2004). The properties of the parent ABC copolymer are summarized in Table 6.1. The molecular weight (M_n=25100 g/mol) and polydispersity (M_w/M_n=1.08) were determined via a combination of NMR and GPC. Block volume fractions (f_{PEP} = 0.22, f_{PEO} = 0.20 and f_{PHMA} = 0.58) and Root Mean Square end-to-end lengths were calculated using the density and packing lengths of the corresponding homopolymers. The Flory-Huggins interaction parameters were estimated using the approximation of Hildebrand and Scott (Madkour, 2001).

Table 6.1- Properties of parent ABC block copolymer[a]

[b]f_A	0.22
f_B	0.20
f_C	0.58
V	25100 cm^3/mol (41.7nm^3/molecule)
M_n	25100 g/mol
M_w/M_n	1.08
[c]$\chi_{AB}N$	180
$\chi_{BC}N$	70
$\chi_{AC}N$	25
[d]L_A	6.6 nm
L_B	6.5 nm
L_C	7.2 nm

[a]*The parent copolymer corresponds to copolymer EPOM2 in Chapter Five (Table 5.1, page 85) of Surbhi Mahajan's thesis (Mahajan, 2005).*
[b]*Block Volume fractions for room temperature homopolymer densities (Table 3.1)*
[c]*Flory-Huggins Interaction parameters given in (Table 3.2)*
[d]*RMS end-to-end block lengths computed with packing lengths from (Table 3.1)*

The hybrid material was prepared following a general procedure described earlier (Templin, et. al. 1997; Jain and Wiesner, 2004). A 2% (by weight) solution of the ABC copolymer in a 50-50 mixture of tetrahydrofuran and chloroform was combined with a pre-hydrolyzed sol of 3-(glycidyloxypropyl) trimethoxysilane (GLYMO) and aluminum sec-butoxide. After stirring the solution for one hour, films were cast by evaporation on a hotplate at 50°C. The clear film (~0.5mm thick) was annealed for 1 hour at 130°C in a vacuum oven to remove residual solvent. Assuming a density of 1.4 g/cm^3 for the PEO+inorganic phase (Jain and Wiesner, 2004), the domain volume fractions of the hybrid material were $f_{PEP} = 0.19$, $f_{PEO+aluminosilicate} = 0.32$ and $f_{PHMA} = 0.49$.

6.2.2 X-ray Scattering

Small and wide-angle X-ray scattering data were gathered using a laboratory source. Briefly, CuK$_\alpha$ x-rays (λ=0.154nm) were generated with a Rigaku RU-3HR generator (Tube Voltage = 42kV, Tube Current = 56mA, 2mm×0.2mm point focus on a Copper Anode), filtered by a nickel foil (thickness = 10 μm; Goodfellow, PA) and focused and further monochromatized with a pair of Franks mirrors (Hadjuk, 1994). The flux at the sample was ~4×10^7 X-ray photons per second in a 1mm×1mm diameter beam. Small Angle X-ray Scattering (SAXS) data was gathered using a 60cm or 80cm flight tube while Wide Angle X-ray Scattering (WAXS) was measured using a 1.5cm flight tube. At the end of the flight tube, the transmitted x-ray beam was blocked with a small (typical diameter of 2-3mm) circle of lead tape while the scattered x-rays were imaged with a home-built 2-D X-ray area detector consisting of a phosphor screen, fiber-optic coupler and 1024×1024 pixel CCD (Tate, et. al. 1995). The distance from the sample to detector and position of the beam center were determined using silver

behenate (d_1 = 5.8376nm; Blanton, et. al. 1995) and silver stearate (d_1 = 4.868nm; Vand and Aitken, 1949) calibrants.

Samples of the ABC copolymer were placed in glass x-ray capillaries (1mm diameter, Charles Supper, MA) and annealed in a vacuum (150^{o}C for 2 hours) before data collection. Samples of the hybrid material were cut to size (1mm wide by 5mm thick) and positioned using a mechanical rotation stage. For unoriented samples, X-ray scattering was azimuthally averaged about the incident beam direction and reported as a function of the magnitude of the scattering vector, $s = 2 \times \sin(\theta) / \lambda$, where 2θ is the angle between incident and scattered radiation.

6.2.3 TEM

Transmission Electron Microscopy images of the hybrid material were obtained by Dr Surbhi Mahajan. Thin sections (50-100nm thickness) of the hybrid material were cut at 210K using a Leica Ultracut UCT microtome and transferred to copper TEM grids. To isolate individual strands, the hybrid material was dispersed in toluene overnight (1mg hybrid/1g toluene) and the solution then sonicated briefly (Ulrich, et. al. 1999). Approximately 10μL of this solution was evaporated onto a holey carbon film supported on a 200 mesh copper TEM grid. Dark-field Energy-Filtered Transmission Electron Microscopy was performed using a LEO 922 Omega EF-TEM (tungsten filament) microscope at 200kV and objective aperture angle of 3.6 mrad. Using a slow-scan CCD (2K*2K), images were acquired for inelastic scattering at the silicon L-edge (120-145eV).

6.2.4 STEM Tomography

Dr Matthew Weyland performed Scanning Transmission Electron Microscopy Tomography on the hybrid materials. All tomography was carried out using an FEI

Tecnai F20-ST field emission gun scanning transmission electron microscope (FEG-(S)TEM). The STEM probe size, and nominal resolution, at the used settings is ~1.6 Å. Images were acquired using a Fischione high angle annular dark field (HAADF) detector with the detector inner radius setting of ~30 milli-radians. Tilt series were acquired automatically using FEI Xplore3D tomography acquisition software. The tilt series of the isolated strand specimen was acquired from ±72° with a 2° increment, a total of 73 images, at a magnification of 320,000x, corresponding to a pixel size of 0.35 nm in a 1024x1024 pixel image. The tilt series of the bulk specimen was acquired from ±72° with a 2° increment, a total of 73 images, at a magnification of 115,000x, corresponding to a pixel size of 0.99 nm in a 1024x1024 pixel image. Due to the limited tilt range, imposed by the need to clamp the specimen in the holder, the resolution in tomographic reconstructions is inhomogeneous: the resolution is highest in x, along the tilt axis, intermediate along y, perpendicular to the tilt axis, and lowest in z, depth direction.

Tomographic data processing was performed using custom software (Midgely and Weyland, 2003) designed in IDL (Interactive Data Language) V6.0. Alignment of tilt series, to a common tilt axis, was achieved by sequential cross-correlation and manual adjustment. Tomographic reconstruction of the bulk series was carried out by r-weighted backprojection (Radermacher, 1992), while the strand series was reconstructed by simultaneous iterative reconstruction (Gilbert, 1972) (SIRT), in a multiplicative mode with 30 iterations.

All three dimensional visualization of both strand and bulk reconstructions were carried out using Amira V3. Surface renders were generated using an isosurface value at the measured surface intensity of the aluminosilicate in the reconstruction. There is a small error in this value due to the non-homogeneity of the reconstruction

intensity in the three volume directions. Voxel projections of the bulk specimens were generated using modified optical absorption values in order to mask the effect of the high intensity contaminants and highlight the aluminosilicate structure.

6.2.5 Structural Modeling

Block domains were modeled in MATLAB using level set functions (Wohlgemuth, et. al., 2001). Briefly, the density of each phase was represented by periodic functions consistent with the lattice symmetry and dimensions determined from the STEM tomographic reconstruction. The interfaces between domains lie on isosurfaces (level sets) of these density functions. For the PEO/ aluminosilicate domains, Fourier coefficients were matched to the volume fraction and structure of the isolated strand reconstruction. Functions for the distance to the nearest strand and next nearest strand were used to generate level sets for the generalized Voronoi cell as well as the PEP and PHMA domains.

6.3 Results

6.3.1 ABC Copolymer Structure

For this PEP-b-PEO-b-PHMA copolymer, the relatively small mixing enthalpy of the A and C blocks ($\chi_{AC}N \approx 25 < \chi_{AB}N \approx 180$, $\chi_{BC}N \approx 70$) favors optional AC domain interfaces over the obligatory AB and BC interfaces. Theoretical (Zheng and Wang, 1995) and experimental (Breiner, et. al. 1997) studies in this regime reported structures with a cylindrical A/B core surrounded by the outer C block for block volume fractions corresponding to this ABC copolymer ($f_A \approx f_B \approx 0.2 < f_C \approx 0.6$). Within the cylindrical A/B core, several B-domain structures have been observed including a

cylindrical shell, perforated cylinder, cylindrical rods, helical rods and cylindrical rings (Breiner, et. al. 1997; Krappe et. al., 1995).

Long-range ordering within the parent ABC copolymer is evident from the SAXS data shown in Figure 6.2. All but one of the peaks could be indexed to the first seven reflections of a hexagonal lattice (repeat spacing of 29.08 ± 0.15nm), while the additional peak at $s = 8.06 \pm 0.05 * 10^{-2}$ nm^{-1} (12.4 ± 0.1nm d-spacing) requires the structure to have a third crystallographic axis.

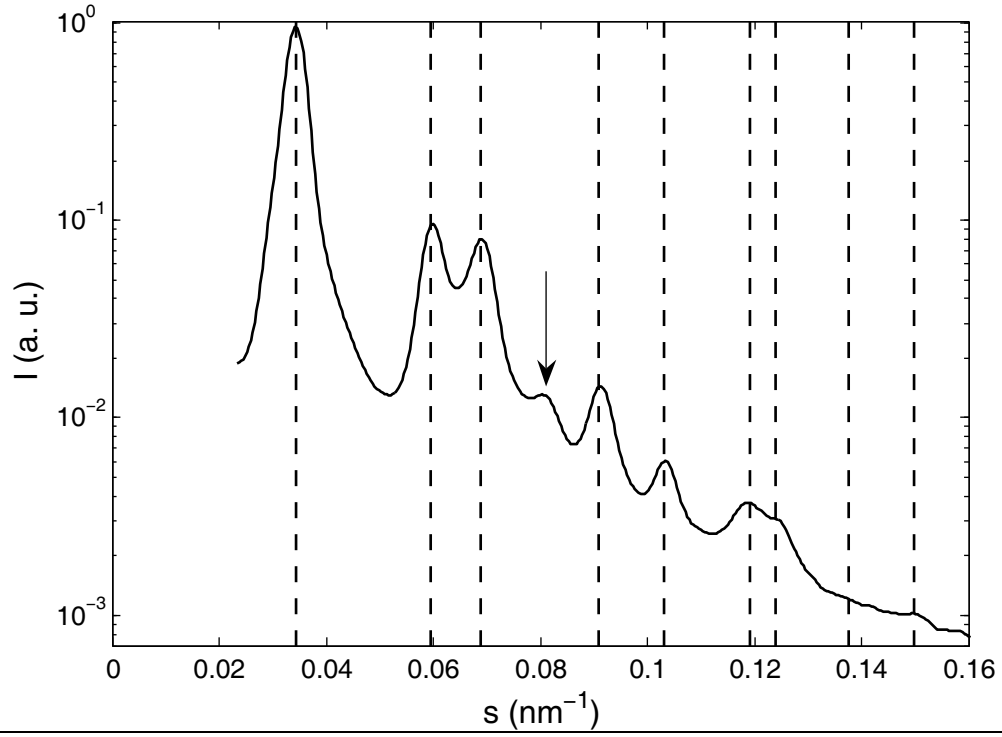

Figure 6.2- SAXS from the parent ABC block copolymer at 100°C. The vertical dashed lines indicate the allowed reflections for a hexagonal unit cell (repeat spacing 29.08 ± 0.15 nm). The peak at $s = (8.06 \pm 0.05) \times 10^{-2}$ nm^{-1} (arrow) does not index to this hexagonal lattice.

Unfortunately, transmission electron microscopy of the ABC copolymer was challenging. Firstly, because the glass temperature of all three blocks is below room

temperature, samples must be both microtomed and imaged at cryogenic temperatures and a cryo-EM stage was not available. Furthermore, PEP-b-PEO-b-PHMA cannot readily be stained with RuO_4 or OsO_4 and contrast between the unstained blocks is low.

Although the SAXS data is consistent with the anticipated structure of cylindrical A/B domains arranged in a hexagonal array, additional information is required to determine the actual structure of the ABC copolymer.

6.3.2 Hybrid Structure

SAXS from the hybrid material is shown in Figure 6.3. The elongation of the main diffraction ring along the film normal (vertical) reflects a modest, unidirectional shrinkage ($\varepsilon = 9.0 \pm 1.5\%$) common for solvent-cast materials (Klotz, et. al. 2002). Rotating the sample about the film normal left the distinct diffraction spots in Figure 6.3a unaltered, indicating a partial fiber-type orientation (Finkenstadt and Millane, 1998) of the structure.

The four Bragg spots on the main ring ($|s_x| = 0.047 \pm 0.001$ nm^{-1}, $|s_y| = 0.020 \pm 0.002$ nm^{-1}, $23.0 \pm 2.5°$ from horizontal) have the largest integrated scattering intensity when the fiber alignment is accounted for. Figure 6.3b shows the pseudo fiber-average for the sample computed using the expression,

$$I_{AVG}(s) = \int_{\varphi=0}^{\varphi=2\pi} I\left(s\sin\varphi, \frac{s\cos\varphi}{1-\varepsilon}\right) \times \frac{|\sin\varphi| d\varphi}{4} \qquad (6.1)$$

where $I(s_x,s_y)$ is the 2-D scattering intensity and ε is the unidirectional shrinkage of the sample along the film normal. The center of the diffraction ring had a repeat spacing of 19.4 ± 0.5nm with shoulders at 22.8 ± 0.5nm and 17.4 ± 0.5nm. The lack of a unique lattice orientation and/or higher order reflections prevented a direct

determination of the crystal lattice from SAXS data. However, the SAXS data clearly indicated that the hybrid material and parent ABC copolymer had different structures.

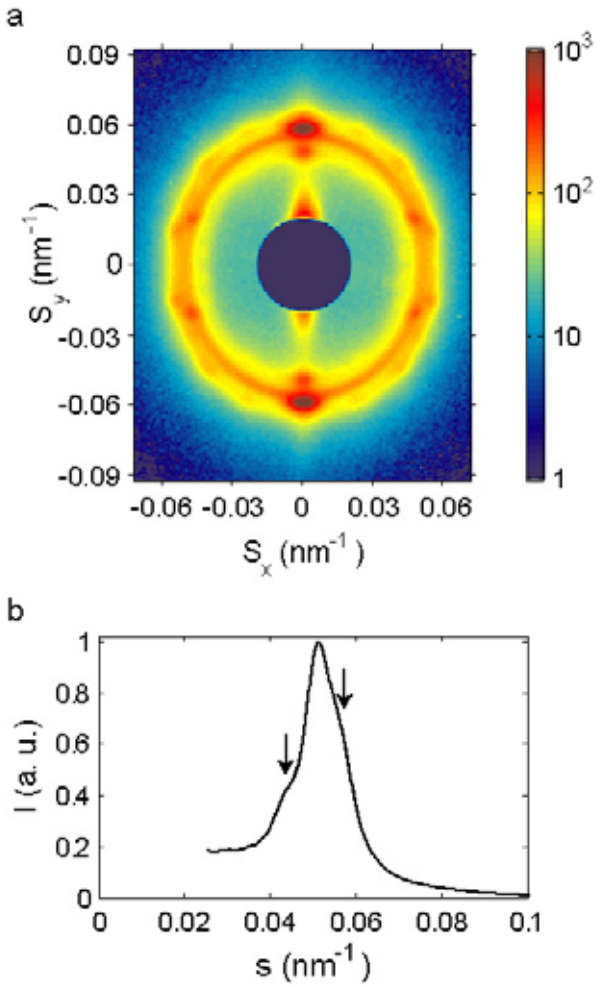

*Figure 6.3 - 2-D SAXS pattern (logarithmic scale) from the hybrid material (surface normal vertical) (**a**). The majority of scattering is unoriented although the Bragg spots indicate some fiber-type alignment along the surface normal. The main ring has a repeat spacing of 19.4 ± 0.5 nm and is slightly elliptical (9.0 ±1.5%) because of anisotropic shrinkage along the surface normal. Fiber-averaged integrated scattering intensity SAXS pattern from the hybrid material (**b**). In addition to the main peak at 19.4 ± 0.5nm (s = 5.15±0.13 × 10^{-2} nm^{-1}), arrows mark the shoulders evident at repeat spacings of 22.8 ± 0.5nm (s= 4.39 ± 0.09 × 10^{-2} nm^{-1}) and 17.4 ± 0.5nm (s= 5.75 ± 0.16 × 10^{-2} nm^{-1}).*

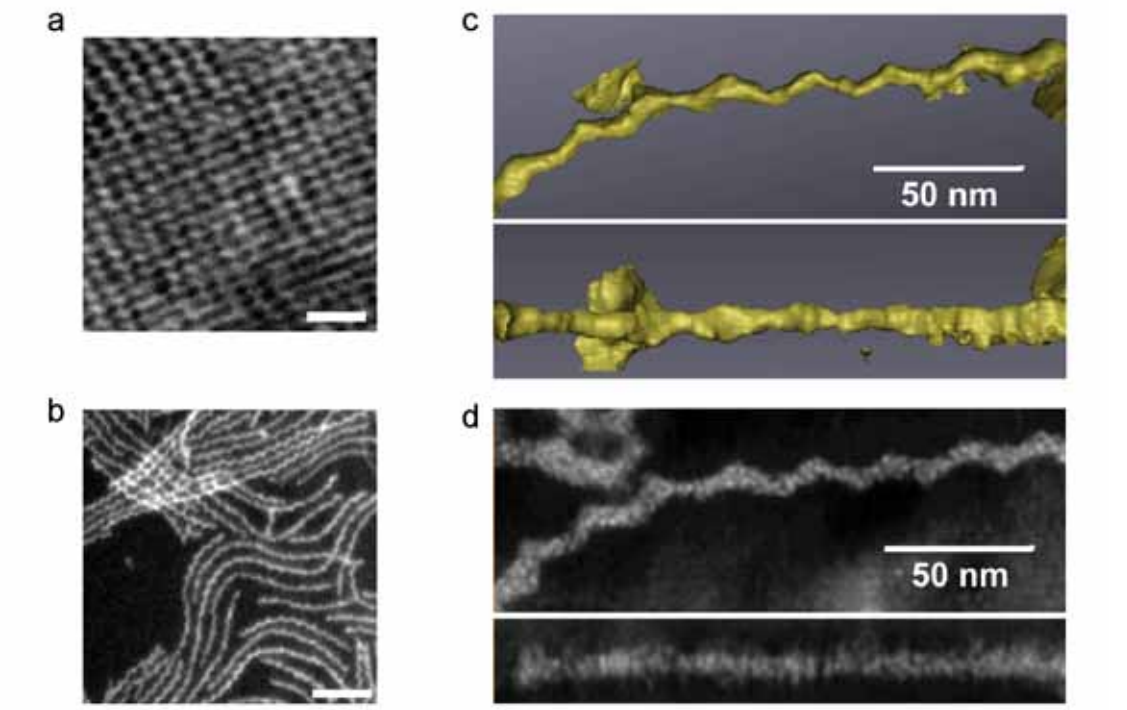

*Figure 6.4 - Dark-field TEM of a thin section of bulk material (aluminosilicate bright) (**a,** scale bar 100nm) and individual aluminosilicate strands (**b**, scale bar 200nm). These images were obtained by Dr Surbhi Mahajan. Two iso-surface renders showing the surface of the aluminosilicate strand from top and edge on obtained from the tomographic reconstruction of an individual hybrid strand (see also Supplementary Movie1). The strand shows a clear "concertina" structure (**c**). The thickness of strands is approximately 10nm, while the wiggles along each strand have a period of d_w ~ 24 nm and a peak-to-peak amplitude of ~ 5nm (**c**). Corresponding slices through the center of the reconstruction shows individual sol particles (diameter ~ 2nm) within the body of the concertina (**d**). These images were obtained by Dr Matthew Weyland.*

Thin sections (~60nm) of the bulk material were examined via Dark-Field Transmission Electron Microscopy. Figure 6.4a confirms the periodic character of the aluminosilicate (bright) structure but differs from projections of hexagonally packed cylinders. However, individual aluminosilicate domains isolated by solvent dispersal and sonication are clearly one-dimensional strands (Figure 6.4b) with a curious zigzag character. The projection in Figure 6.4a gives the appearance of layers of strands

running in two almost perpendicular directions, but the detailed structure of the strands and their arrangement within the bulk material remain unclear from these TEM micrographs.

To resolve the ambiguity of SAXS and TEM micrographs, Dr Matthew Weyland performed electron tomography (Frank, 1992) in which a real space three-dimensional reconstruction is determined using a tilt series of electron micrographs. While conventional bright field electron tomography is classically used for the examination of biological macromolecules it has also been successfully applied to analyze the 3D morphology of block-copolymer systems (Spontak et. al. 1996; Kaneko et. al., 2006) and porous inorganic materials (Ziese et. al., 2003). Recent adaptation of the technique to work with STEM imaging (Midgley and Weyland, 2003) has made it ideal for studying materials with differing atomic numbers and densities.

The tomographic reconstruction of an isolated strand (Figure 6.4c and 6.4d) revealed a complex structure. In one direction, the individual aluminosilicate strands showed a zigzag shape with a wiggle period of $d_w \approx$24nm and peak-to-peak wiggle amplitude of ~5nm. In the perpendicular direction, the strands were almost flat leading to an overall structure of a stretched "concertina". The cross-section of the concertina was approximately 5nm wide by 10nm thick although variations were evident along its length.

The resolution of the reconstruction was also sufficient to resolve the internal structure of the concertina. Sections through the reconstruction shown in Figure 6.4d reveal a distinctly bi-modal distribution of intensity with bright and dark regions approximately 1-3nm in size. The bright regions correspond to aluminosilicate rich sol particles (high atomic number, e.g., high-Z) while the polymer rich regions (low-

Z) are darker. This internal structure within the PEO-aluminosilicate domains is also evident in the Wide Angle X-ray Scattering data shown in Figure 6.5. WAXS from the parent ABC copolymer has two distinct peaks corresponding to the alkyl chain-chain distance (d_{CC} = 0.48 ± 0.01 nm) and mean spacing between methacrylate backbones (d_{BB} = 1.35 ± 0.03 nm) within the PHMA block (Beiner, et. al. 2002). For the hybrid material, a third peak is present arising from correlations between the densely packed sol particles (Jain and Wiesner, 2004) within the PEO-aluminosilicate domain (d_{SOL} = 2.5±0.3nm).

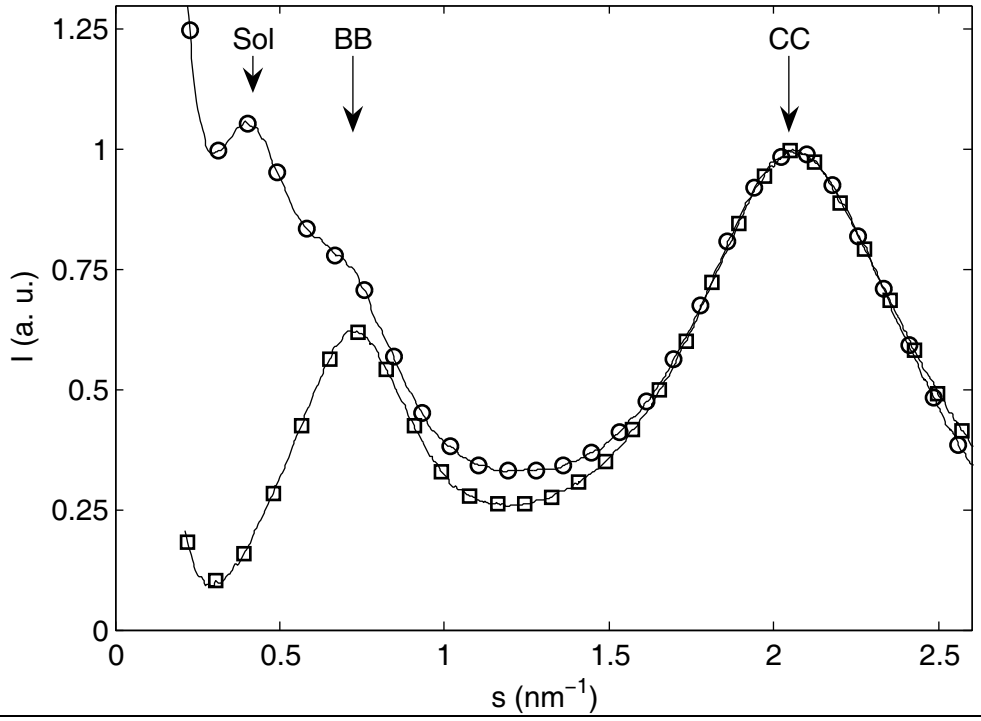

Figure 6.5- Wide Angle X-ray Scattering data from the parent ABC copolymer (squares) and hybrid material (circles) show correlations between the aluminosilicate sol particles in the PEO-aluminosilicate domains (d_{SOL} = 2.5 ± 0.3 nm), the polymer backbones within the PHMA domains (d_{BB} = 1.35 ± 0.03 nm) and the alkyl chains (d_{CC} = 0.48 ± 0.01 nm) in all three domains.

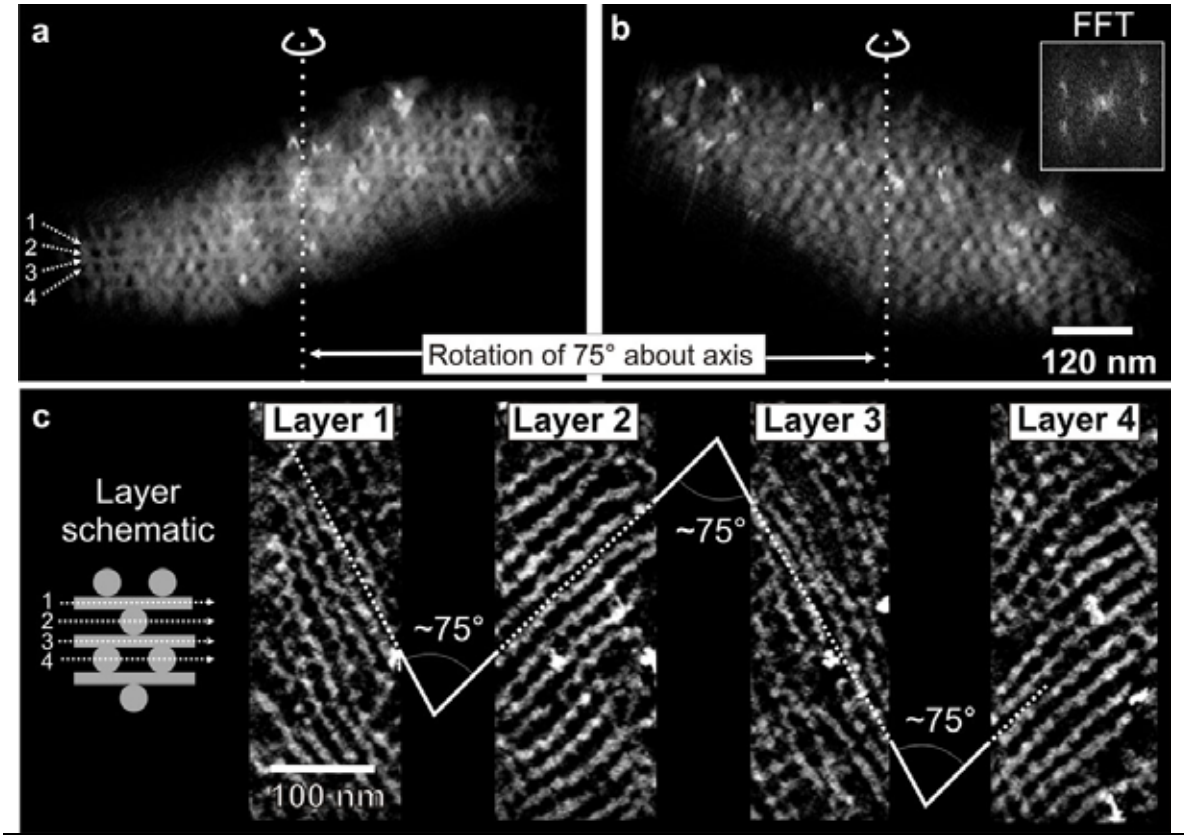

*Figure 6.6 - STEM tomographic reconstruction of the bulk specimen (aluminosilicate bright). Voxel projections through volume separated by 75 degrees (**a**, **b**). Scale bar is 120nm in both cases. Inset in (**b**) shows the 2-D Fourier transform of the density projection. Both projections show layers of strands end-on in a staggered configuration and in addition, strands running across each projection are also just visible. Sections taken through the strand layers at depths of 0nm, 11nm, 22nm and 33 nm respectively show successive layers of strands running in alternate directions (**c**). The spacing between strands within each layer is $d_{ip} \approx 23.3$ nm while the angle between the direction of strands in successive layers is $\phi \approx 75°$. (Figure courtesy of Dr Matthew Weyland.)*

To determine the arrangement of individual concertinas, a tomographic reconstruction was performed upon a thin section of the bulk material as shown in Figure 6.6. Strikingly, the unit cell consisted of a four layer woodpile (Sozuer and Dowling, 1994; Figure 6.1) in which the direction of concertinas in successive layers alternated. The first and third layers of concertinas were directed along the [110]

diagonal while the second and fourth layers ran along the [1$\underline{1}$0] diagonal. Furthermore, layers were staggered with the third and fourth layers offset by $(\mathbf{a_1}+\mathbf{a_3})/2$.

For a projection along the [110] direction (Figure 6.6a and 6.1d), concertinas in the even layers were end on and had the appearance of staggered rows of dots, while concertinas in the odd layers ran horizontally across the projection. Rotating by ~75° to the [1$\underline{1}$0] direction (Figure 6.6b and 6.1f), the odd layers of the lattice were then end on and formed a staggered dot pattern. The lack of homogeneity in the reconstruction resolution may account for why the side-on layers are clearer in Figure 6.6a than Figure 6.6b. The alternating direction of concertinas was most evident in slices taken through consecutive layers in the sequence. In Figure 6.6c the strands ran in alternate directions ($\mathbf{a_1}+\mathbf{a_2}$, $\mathbf{a_1}-\mathbf{a_2}$, $\mathbf{a_1}+\mathbf{a_2}$, ...) in successive layers. Within each layer the average distance between strands was $d_{ip} \approx 23.3$nm while the distance between layers was approximately 11nm. Because strands in successive layers crossed at $\phi \approx 75°$, the maximum possible symmetry of the unit cell was the orthorhombic Fddd space group (No. 70, IUCr Tables; Hahn, T. 2002) with lattice constants $|\mathbf{a_1}| = 29.4 \pm 0.8$ nm, $|\mathbf{a_2}| = 38.3 \pm 1.0$ nm and $|\mathbf{a_3}| = 42.8 \pm 1.5$nm.

Comparison of this structure to the SAXS data shows a number of similarities. For the level-set model shown in Figure 6.1c-f, the {111} reflections have the largest structure factor and the repeat spacing of these reflections (20.5 ± 0.4 nm) is similar to that of the main ring in the SAXS data (19.4 ± 0.5nm). Given the bending and twisting of concertinas evident even within the small field of view of the tomographic reconstruction, the absence of higher order reflections in the SAXS pattern is not surprising. It is difficult to predict the preferred alignment of the structure, but orienting the layers of strands parallel to the film surface ($\mathbf{a_3}$-axis along film normal) is likely to be favorable. For this orientation, the intense {111} reflections should appear

at ($|s_x|$ = 0.043 ± 0.002 nm^{-1}, $|s_y|$= 0.023 ± 0.001 nm^{-1}, 28.6° ± 1.4° from horizontal) which is close to the position of the four bright Bragg spots on the main SAXs ring (Figure 6.3a). Finally, it should be noted that the scattering features at 22.8 ± 0.5nm and 17.4 ± 0.5nm are not consistent with Fddd symmetry. The present data is insufficient to determine if this is because the structure has a lower symmetry, the lattice is skewed or a small fraction of strands in the sample are packed with a different symmetry.

6.4 Discussion

Two striking features of this material are the zigzag, concertina shape of the aluminosilicate strands and the alternating direction of strands within the woodpile lattice. At the molecular scale, the woodpile structure has been observed in several systems including zeolites (O'Keefe and Andersen, 1997), metal-organic frameworks (Rosi, et. al. 2005) and γ-isotactic polypropylene (Meille, et. al. 1990). In liquid crystal systems, a non-parallel rod packing has been proposed to describe the structure of a counter-ion condensed F-actin phase (Wong, et. al. 2003). However, structures involving the non-parallel packing of rods are quite unusual.

Rods formed in AB/ABA block copolymers (Bates and Fredrickson, 1999) and copolymer/silica materials (Renker, et. al. 2004) have a uniform cross-section and pack into a parallel, hexagonal array. Thus, the more complicated self-assembly behavior of ABC triblock copolymers is probably responsible for the structure of this material. Previous studies of ABC copolymer systems have reported both strands with non-uniform cross-sections (Krappe et. al., 1995; Breiner et. al., 1997) and strands packed in non-hexagonal (but parallel) arrays (Mogi et. al. 1992; Brinkmann et. al., 1998). However, structures with non-parallel stackings of rods, such as the woodpile lattice, have not previously been reported for ABC block copolymers.

To better understand this structure, it is important to consider the PEP and PHMA domains surrounding the PEO/aluminosilicate core of each concertina. Because chain stretching is energetically costly (Thomas, et. al. 1987; Grason, 2006), PEP and PHMA chains tend to stretch to the nearest PEO/aluminosilicate domain. Thus, the shape of the polymer sheath is approximately the region of space closest to the core of the concertina (a generalized Voronoi cell). Figure 6.7 shows the generalized Voronoi cell for straight rods arranged in a four-layer woodpile lattice. The region of space closest to the central rod wiggles under the rods in the layer above and over the rods in the layer below leading to an overall concertina-shape. The shape of the Voronoi cell accounts for several aspects of the material's structure.

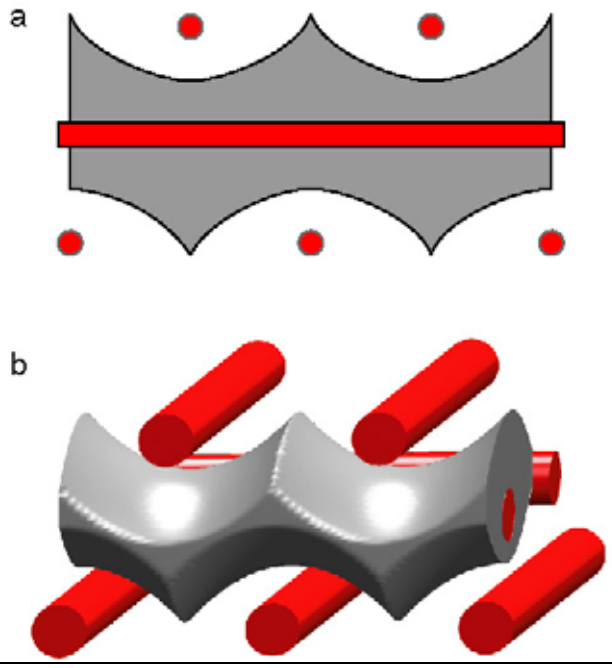

*Figure 6.7 - Generalized Voronoi Cell for the four-layer woodpile structure. The region of space closest to the central rod is marked in gray in both the two-dimensional section (**a**) and 3-D view (**b**). The Voronoi Cell wiggles under the rods in the layer above and over the rods in the layer below leading to a zigzag, concertina shape. The distance from the rod to the cell surface is smallest where strands cross and largest between crossings.*

Firstly, the zigzag shape of the PEO/aluminosilicate core probably reflects the concertina shape of Voronoi cell. The effect of Voronoi cell shape on inner domain shape has previously been observed in an ABC block copolymer core-shell hexagonal morphology (Gido et. al., 1993). For straight rods arranged in a woodpile lattice, the surrounding sheath (Figure 6.7 a) is thinnest where rods cross and thickest between rods. These variations in thickness increase the chain stretching energy of the outer PEP and PHMA domains. The thickness of the outer sheath becomes more uniform if the core wiggles under the strands in the layer above and over the strands in the layer beneath it as shown in Figure 6.8a. Thus, wiggling of the inner domain can lower the chain-stretching energy of the outer domains at the cost of a larger interfacial area. If this mechanism caused the wiggling of the strands, the zigzag period of isolated concertinas ($d_w \approx$24nm) should match the distance between strand crossings within the woodpile lattice ($d_{ip}/\sin(\phi) \approx$ 24nm) as is indeed the case. Unfortunately, though, the orientation of wiggles along each concertina is not resolved in the tomographic reconstruction.

A second feature of the woodpile lattice is the relative offset of the layers above and below any given layer (Figures 6.6a-b and 6.1d,f). Even though these layers are not in direct contact, their relative position affects the shape of the Voronoi cell of the layer of strands sandwiched between them. When the strands in the layers above and below a layer are offset, as in the four-layer woodpile lattice, the variations in Voronoi cell cross-section (and chain-stretching energy) are smallest.

Despite the zigzag shape of the PEO/aluminosilicate core, the thickness of the outer polymer layer still varies along its length. If the outer layer consisted of a single component, these variations in chain stretching would be prohibitive when compared to those in the traditional (parallel) hexagonal lattice. However, the optimal thickness

of the PEP and PHMA domains on the outside of the concertinas may be different, and the best arrangement of strands should accommodate these differences while also ensuring the PEP and PHMA domains align with those of neighboring strands.

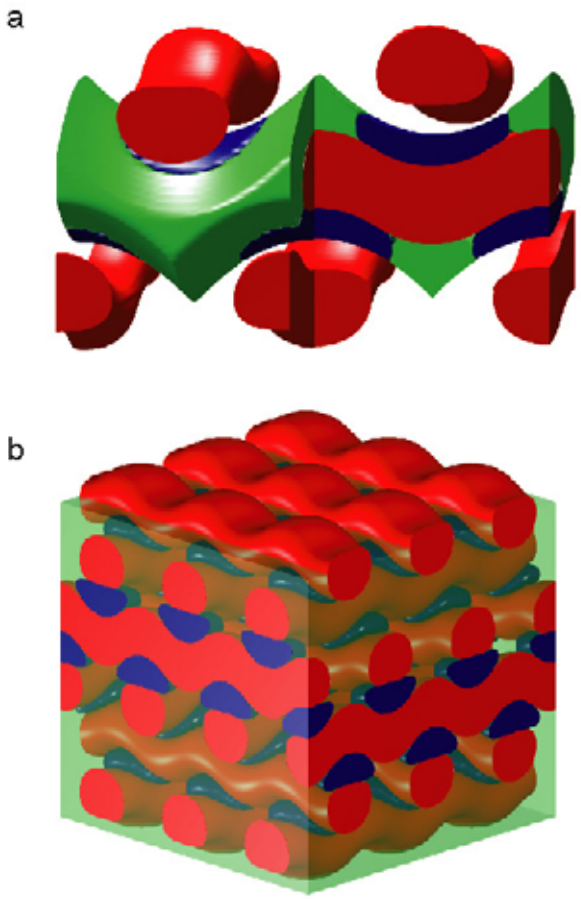

*Figure 6.8 - Model distribution of PHMA (green) and PEP domains (blue) surrounding the central PEO/aluminosilicate (red) core of the concertina. The smaller PEP domains are positioned where concertinas cross as shown in both the cut-away view of a single strand (**a**) and for the full structure (**b**).*

Figure 6.8 shows a plausible arrangement of the PEP (blue) and PHMA (green) domains consistent with the block volume fractions and Voronoi cell shape. The smaller PEP block forms micellar domains bridging the short gaps where

concertinas cross. For this model, the optimum distance between concertinas in each layer (d_{ip}) and distance between PEP domains along the top or bottom of the concertina (d_w) determine the angle at which the layers of concertinas cross (ϕ, Figure 6.1b). This may account for the observed crossing angle of $\phi \sim 75°$ although shrinkage during solvent casting and distortion during microtoming should also be considered.

In structures with a non-parallel packing of rods, the individual rods frequently have a commensurate periodic structure. For example, the helical backbone of γ-isotactic polypropylene (Meille, et. al. 1990) is accommodated by an orthorhombic woodpile structure ($\phi \approx 81°$). Similarly, the double-twist tubes in cholesteric blue phases (Wright and Mermin, 1989; Cao et. al., 2002) cannot pack closely when they are parallel. This general mechanism could also stabilize non-parallel rod morphologies in ABC triblock copolymers as indicated by the model in Figure 6.8.

The present work confirms that the complex phase behavior of ABC copolymers provides access to new organic/inorganic material structures. New structures may be important for applications such as self-assembled photonic band-gap materials (Vukusic and Sambles, 2003; Yoon, et. al. 2005). Although the lattice of the present material is too small for optical wavelengths, the incorporation of inorganic material allows high dielectric contrast within the material (Yoon, et. al. 2005) and the four-layer woodpile structure has a full three-dimensional photonic band-gap (Sozuer and Dowling, 1994; Ho et. al., 1994; Kopperschmidt, 2003), unlike existing diblock copolymer morphologies (Maldovan, et. al. 2002).

6.5 Conclusion

The morphology of a PEP-b-PEO-b-PHMA triblock copolymer/ aluminosilicate material was determined using Scanning Transmission Electron

Tomography. The middle PEO-aluminosilicate phase formed zigzag concertina-shaped strands surrounded by a polymer sheath formed from the outer PEP and PHMA blocks. In the bulk material, the PEO-aluminosilicate strands were arranged in layers with strands in successive layers alternating in direction. This four-layer woodpile structure is quite unusual and it is not yet known which interactions favor this structure. However, the zigzag shape of the strand strongly suggests the PEP and PHMA domains are arranged periodically along the outside of each PEO-aluminosilicate strand. Such a periodic structure could prevent efficient, parallel stacking of the strands, thereby favoring the observed four-layer woodpile structure. The results described in this chapter confirm that ABC triblock copolymers can direct the assembly of silica-type materials into structures not previously achieved using two-domain AB or ABA block copolymers.

Chapter Seven – Conclusion

This thesis has described experimental and thermodynamic studies of block copolymer and block copolymer/aluminosilicate materials. This final chapter summarizes the results of these studies, outlines potential experimental and theoretical work building on these studies and also relates these results to current research in block copolymer physics. Section 7.1 reviews the experimental work on network structures and suggests several new experiments. The transition between two domain and three domain structures in symmetric ABC triblock copolymers is discussed in Section 7.2 and further experiments and calculations are outlined. Section 7.3 summarizes the features of the new ABC triblock copolymer/aluminosilicate morphologies reported in Chapters 5 and 6 and suggests new experiments building on these results. Finally, Section 7.4 relates the most significant findings of this work to current challenges in block copolymer science.

7.1 Network Structures

Bicontinuous network structures have many applications leading to considerable interest in their reliable syntheses. In block copolymers, networks with 3-fold coordinated nodes appear to be favored by the requirement that chains in the minority domain to stretch into center of each node. Chapter 2 described the characterization of a bicontinuous, network structure formed in a solvent-cast PI-b-PEO block copolymer/aluminosilicate material. A previous study had concluded the structure of this material was consistent with the Plumber's Nightmare morphology in which the minority (PI) network has 6-fold coordinated nodes (Finnefrock, et. al. 2001; Finnefrock, et. al. 2003). However, SAXS and TEM data from the material are more consistent with a distorted double gyroid structure in which the minority PI

network has 3-fold coordinated nodes. This new result suggests the constraints favoring 3-fold coordinated nodes in block copolymer structures may also be important in copolymer/inorganic materials.

Future experiments building on this work are described below.

7.1.1 EM Tomography

The identification of network structures from SAXS and TEM data is quite challenging and the SAXS and TEM from this material may be consistent with a structure not considered in the present analysis. Consequently, it will be very important to directly measure the structure of the pores via an EM tomographic reconstruction (Spontak et. al. 1996; Kaneko et. al. 2006; Jinnai et. al. 2006). The calcined material is well suited to EM tomography as it can be sliced into thin sections and has excellent electron density contrast. Ideally, a tomographic reconstruction would directly measure both the structure of the network and the distortion caused by solvent casting.

7.1.2 Must networks have 3-fold nodes?

Do network structures formed in block copolymer systems have to have 3-fold coordinated nodes? Both SCMFT (Matsen, 1995; Matsen and Bates, 1996) and SSL calculations (Likhtman and Semenov, 1997) suggest that the addition of a homopolymer can stabilize network structures with 4-fold coordinated nodes. Experimental verification of this result would be very interesting. The PI-b-PS block copolymer system in which the double gyroid structure was first characterized (Hadjuk et. al. 1994; Forster et. al. 1994) should be a good system for these experiments. PI-b-PS block copolymers are well suited for electron microscopy and at moderate molecular weights (e.g. 30,000 g/mol) can be cooled from the disordered

state to allow the formation of "equilibrium" structures. Short-chain PI and PS homopolymers would mix in with the blocks (Lescanec et. al., 1998) to allow adjustment of block volume fractions, while longer PI and PS homopolymers can be added to relieve packing stress (Lescanec et. al. 1998). Provided appropriate sample mixing and annealing procedures can be established, predictions that relief of packing stress in the majority/minority phase stabilizes the perforated-lamellar/double diamond structure could be directly tested. These experiments would be especially interesting given the recent identification of an Fddd network structure in AB diblock copolymers (Tyler and Morse, 2005; Takenaka et. al., 2007).

7.1.3 ABC triblock copolymer/inorganic networks

Robust synthetic methods are required for practical applications of network structures. In AB diblock copolymers, the double gyroid morphology only forms within a small window of compositions (Matsen and Bates, 1996; Floudas, et. al. 2001). It is not surprising, then, that in AB diblock copolymer/inorganic composites the formation of bicontinuous network structures is quite sensitive to experimental conditions (Urade et. al., 2007). However, continuous network structures occupy a much larger region of ABC copolymer phase space (Bailey et. al., 2004) and present a promising route to the robust synthesis of copolymer/inorganic network structures. Although the addition of aluminosilicates may destabilize these network structure (Bailey et. al., 2003; Ch 5 Mahajan, 2005), these experiments are well worth attempting.

The three experiments outlined in this section should contribute to a better understanding of how additives such as homopolymers and inorganic particles affect the formation of networks structures in block copolymer systems. Given the potential applications for these materials, finding robust synthetic procedures is of the highest

importance and attempts to synthesize network structures in ABC copolymer/inorganic materials will be very significant.

7.2 Symmetric ABC Lamellar Structures

The addition of a third block in an ABC triblock copolymer greatly increases the complexity of its phase behavior and understanding this behavior has been the major focus of the research described in this thesis. On approach for understanding this complexity is to use ABC block copolymers with one small block to examine the transition from two to three domain structures. Chapters 3 and 4 described experimental and theoretical studies of ABC block copolymers with a small ($f_B < 0.5$), incompatible ($\gamma_{AC}N < \gamma_{AB}N, \gamma_{BC}N$) middle B block and approximately equivalent A and C domains ($f_A \approx f_C > f_B$; $p_A \approx p_B \approx p_C$). The SSL analysis presented in Chapter 4 suggests the A and C domains form lamellae while reducing the volume fraction of the middle block (f_B) causes the B domains to transform from lamellae to rods and from rods to balls. Chapter 3 reported experimental studies consistent with this sequence of transitions. This research establishes one way in which the influence of a third domain on phase behavior varies with the size of that domain.

However, the experimental work was restricted by the small quantities of the individual copolymers (~50 mg) and the difficulty of performing electron microscopy. The synthesis of new copolymers would permit a number of interesting experiments outlined below and opportunities for theoretical calculations are also described.

7.2.1 Ordered Balls-at-Lamellae Structure

In the rods-at-lamellae and balls-at-lamellae structures, periodic ordering can occur both along the AC lamellae direction and within the plane of the AC interfaces. For the copolymers studied in Chapter 3, long-range periodic order along the AC

interface was not observed for a balls-at-lamellae structure. Interestingly, when copolymer **3** was doped with Li-triflate above the concentration used for ionic conductivity measurements (1 Li^+ : 50 PEO monomers), additional SAXS scattering peaks were observed. These peaks could have come from an ordered balls-at-lamellae structure, but the conductivity of these samples was not measured to confirm the PEO domains were indeed micellar balls. In future work, it should be possible to form an ordered balls-at-lamellae structure either by synthesizing a polymer with a higher molecular weight or by using lithium triflate to increase the block interaction parameters. This experiment would be helpful for understanding the ordering of B domains at each AC interface.

7.2.2 Shear-Aligned Structures

Studies of ordering of B domains at AC interfaces could also benefit from experiments using shear-aligned samples. Although solvent casting aligned the lamellae parallel to the sample surface, shear alignment should permit alignment of both the lamellae and the structure at the AC interfaces. Shear alignment worked fairly well for the ABC copolymer described in Chapter 5 (Epom41, p85, Ch5, Mahajan, 2005) but the amount of copolymers **1**, **2** and **3** was insufficient to use this shear cell. Shear-aligned samples of the rods-at-lamellae structure should be especially interesting. As described in Chapter 3, increasing the temperature changed the packing of rods in the rods-at-lamellae structure. This effect was also seen in two other ABC copolymers with similar compositions (EPOM30, f_B = 0.12; EPOM36, f_B = 0.13; p28, LB15, GEST; p85, Ch5, Mahajan 2005). In powder or fiber-aligned samples, the strong scattering from the lamellar reflections dominates the diffraction pattern but in a shear-aligned sample, directing the x-ray beam along the rod axis should give much stronger non-lamellar scattering. Thus, aligned samples should be

very helpful for studying the ordering of B domains in the rods-at-lamellae and balls-at-lamellae structures.

7.2.3 Doping and Blending

Mapping the phase diagram of this system would permit better comparison of theory and experiment. Such a mapping would require a large number of samples with different compositions and interaction parameters. In other ABC copolymer systems, this fine sampling has been achieving by blending homopolymers with a set of ABC copolymers (Sugiyama et. al., 2001; Suzuki et. al., 2002; Epps et. al., 2005). Preliminary experiments blending homo-PEO into copolymers **2** and **3** were encouraging, but in future work it may be better to blend into the end blocks (Suzuki et. al. 2002). Tuning of the block-block interaction parameters should also be possible by doping the PEO block with lithium triflate. Finally, it should be possible to study these structures using a cryo-EM stage. Iodine staining may improve contrast for the PHMA block (Kaneko et. al. 2006) and doping the PEO block with silver triflate would be one way to obtain contrast for this phase. Using doping and blending, it should be possible to determine an accurate phase diagram for this system.

7.2.4 SCMFT

The analysis in Chapter 4 provides a description of the triple-lamellae, rods-at-lamellae and balls-at-lamellae structures in the limit of strong segregation. However, the segregation of blocks in actual ABC triblock copolymers is rarely this strong, especially when one of the blocks is small. Thus, it is important to see how intermediate levels of segregation effects the free energy of these morphologies. Although some 2-D Self-Consistent Mean-Field Theory (SCFMT) calculations have been made (Bohbot-Raviv and Wang, 2000; Tang, et. al. 2004), 3-D SCMFT calculations are needed to examine the transition to the balls-at-lamellae structure.

Furthermore, SCFMT calculations would permit direct observation of the transition from a two-domain lamellar structure to structure with distinct A, B and C domains.

The experiments and SCMFT outlined in this section would contribute to the understanding of the transition between two domain and three domain morphologies. The highest priority should probably be given to SCFMT calculations as these can provide a comprehensive description of the effects of a small, thermodynamically incompatible block.

7.3 ABC Block Copolymer/Aluminosilicate Structures

Harnessing the complex phase behavior of ABC triblock copolymers to structure inorganic materials remains an important and exciting challenge in block copolymer science. Chapter 5 and 6 described steps in this direction through the characterization of two morphologies found in PEP-b-PEO-b-PHMA copolymer/aluminosilicate compounds. The hexagonally patterned morphology described in Chapter 5 was consistent with the proposed "pillared-lamellae" morphology (Bailey, et. al. 2001). In contrast, the 4-layer woodpile structure reported in Chapter 6 has not previously been observed in block copolymer systems.

Although these represent significant progress within the field, understanding and controlling structure formation in ABC copolymer/ inorganic materials will require much additional work. Three important steps are outlined below.

7.3.1 Resolving all three domains

A very obvious but important step will be to directly measure the structure of all three types of domain within ABC block copolymer/aluminosilicate materials. In

the present work, the structure of the electron-density PEO-aluminosilicate phase could be directly measured while modeling was used to infer the likely position of the PHMA and PEP blocks. With a selective stain to provide contrast between the PEP and PHMA blocks, electron tomography could be used to measure the position of all three domains. Iodine vapor has been used to preferentially stain the poly(methyl methacrylate) (PMMA) block in a PS-b-PEP-b-PMMA triblock copolymer (Kaneko et. al. 2006) and this may also work for the PHMA block. Assuming a stain can be found, it will be especially interesting to examine the wiggly strands from the woodpile morphology to determine the actual structure of PEP and PHMA domains. Direct measurement of the position of all three blocks will represent a significant advance in the characterization and understanding of ABC triblock copolymer/inorganic materials.

7.3.2 Hybrid Phase Diagram

An important result of the present work was to establish that well-ordered structures can form in ABC copolymer/aluminosilicate materials. A next, significant step will be to systematically explore how morphology depends upon block volume fractions and interactions. For example, one would anticipate that increasing the middle-block volume fraction (e.g. $f_{PEP} \approx 0.1, f_{PEO+aluminosilicate} \approx 0.65, f_{PHMA} \approx 0.25$) should transform the PHMA domains into cylinders but it isn't as easy to predict the position of the small PEP block within such a structure. Similarly, hybrid materials with a smaller middle block volume fraction (e.g. $f_{PEP} \approx 0.07, f_{PEO+aluminosilicate} \approx 0.2$, $f_{PHMA} \approx 0.73$) would useful for determining how PEO+aluminosilicate cylinders adjust to accommodate a small PEP block. Finally, compositions along the line,

$$f_{PEP} = 0.10 + x, \qquad f_{PEO+Aluminosilicate} = 0.32 \qquad f_{PHMA} = 0.58 - x, \tag{7.1}$$

would be very helpful for understanding the transition between the patterned sheet and woodpile structures. Because the structures form via a non-equilibrium process and parameters other than the block volume fractions (e.g. ratio of PEO to aluminosilicate) may be significant, these experiments are likely to be quite difficult. However, this systematic exploration will be an essential to understanding and controlling the morphology of ABC copolymer/aluminosilicate materials.

7.3.3 Woodpile Lattice

The woodpile structure described in Chapter 6 is quite unusual and its identification suggests several new experiments. Firstly, it will be very important to repeat the synthesis of this material to establish the conditions under which it can form. The formation of the ABC copolymer "knitting-pattern" morphology depends upon the solution from which the film is cast (Ott et. al. 2001) and the woodpile structure may also be quite sensitive to synthetic conditions. In addition to repeating the synthesis, it will be informative to see what structure forms at the corresponding composition ($f_A \approx 0.2, f_B \approx 0.3\, f_C \approx 0.5$) in pure ABC block copolymers. This region of phase space has not been extensively studied as the A block volume fraction is smaller than the "knitting pattern" (Ott et. al. 2001) while the B block volume fraction is larger than reported parallel cylinder morphologies (Breiner et. al. 1997). Finally, it will be important to identify which interactions favor the non-parallel rod stacking of the woodpile lattice. In Chapter 6, a mechanism was proposed in which the periodic arrangement of A and C domains along each strand prevented efficient parallel packing of the strands. This idea can be tested by calculating the preferred position of the A and C domains with SCMFT.

The experiments and calculations outlined in this section should further contribute to the understanding of structure formation in ABC copolymer/inorganic

materials. Measuring the position of all three blocks via electron tomography should be given a high priority as this information is essential for a deeper understanding of these structures.

7.4 Conclusion

The preceding three sections suggested experimental and theoretical work to build upon the results described in this thesis. This final section relates the work reported in this thesis to current challenges in block copolymer physics.

After many years of experimental and theoretical work, the equilibrium phase behavior of two domain AB and ABA block copolymers is fairly well understood. In contrast, the systems with three or more types of domain, such as the linear ABC block copolymers studied in this thesis, show much more complex behavior and are not nearly as well understood. While this complexity offers many new opportunities, progress in modeling, predicting and controlling the behavior of these multi-domain systems also presents a number of challenges. The increased number of relevant parameters complicates experimental studies of phase behavior while theoretical studies are challenging because of the tremendous number of candidate structures. For example, the four-layer woodpile structure described in Chapter 6 has not been mentioned in any published theoretical study of ABC copolymer phases. Finally, the dynamics of structure formation are not well understood for AB diblock copolymers, and non-equilibrium kinetics are likely to be even more important for structure formation in ABC triblock copolymers.

Understanding the process of structure formation in multi-domain and multi-component polymeric systems is likely to require many years of research. This thesis has contributed to this ultimate goal by confirming new, complex and well-ordered structures can be formed within such multi-domain, multi-component systems.

REFERENCES

Abetz, V.; Stadler, R.; Leibler, L. 1996. "Order-disorder and order-order transitions in AB and ABC block copolymers: Description by a simple model." Polymer Bulletin, Volume 37(1), p135-142.

Abetz, V; Simon, P.F.W. 2005. "Phase Behavior and Morphologies of Block Copolymers." Advances in Polymer Science, Volume 189, p125-212.

Ahn, J.H.; Zin, W.C. 2000. "Structure of Shear-Induced Perforated Layer Phase in Styrene-Isoprene Diblock Copolymer Melts." Macromolecules, Volume 33, p641-644.

Aizenberg, J.; Weaver, J.C.; Thanawala, Monica S.; Sundar, V.C.; Morse, D.E.; Fratzl, P. 2005. "Skeleton of Euplectella sp.: Structural Hierarchy from the Nanoscale to the Macroscale." Science, Volume 309, p275-278.

Als-Nielsen, J.; McMorrow, D. 2001. "Elements of Modern X-ray Physics." John Wiley and Sons Ltd., New York.

Anderson, D.M.; Gruner, S.M.; Leibler, S. 1988. "Geometrical Aspects of the Frustration in the Cubic Phases of Lyotropic Liquid Crystals." Proceedings of the National Academy of Sciences, Volume 85, p5364-5368.

Anderson, D.H.; Bellare, J.; Hoffman, J.T. ; Hoffman, D.; Gunther, J.; Thomas, E.L. 1992. "Algorithms for the Computer Simulation of Two-Dimensional Projections from Structures Determined by Dividing Surfaces." Journal of Colloid and Interface Science, Volume 148(2), p398-414.

Anderson, D.M.; Davis, H.T.; Scriven, L.E.; Nitsche, J.C.C. 1990. "Periodic Surfaces of Prescribed Mean Curvature." p337-396 in "Advances in Chemical Physics", Edited by I. Prigogine and S.A.Rice, Volume LXXVII, John Wiley and Sons, New York.

Anderson, D.; Wennerstrom, H.; Olsson, U. 1989. "Isotropic bicontinuous solutions in surfactant-solvent systems: the L_3 phase." Journal of Chemical Physics, Volume 93, p4243-4253.

Angelescu, D.E.; Harrison, C.K.; Trawick, M.L.; Register, R.A.; Chaikin, P.M. 2005. "Two-Dimensional Melting Transition Observed in a Block Copolymer." Physical Review Letters, Volume 95, 025702.

Argyros, A.; Manos, S.; Large, M. C. J.; McKenzie, D. R.; Cox, G. C.; Dwarte, D. M. 2002. "Electron tomography and computer visualization of a three-dimensional 'photonic' crystal in a butterfly wing-scale." Micron, Volume 33, p483-487.

Auschra, C.; Stadler, R. 1993. "New Ordered Morphologies in ABC Triblock Copolymers." Macromolecules, Volume 26, p2171-2174.

Bagshaw, S.A.; Prouzet, E.; Pinnavaia, T.J. 1995. "Templating of Mesoporous Molecular Sieves by Nonionic Polyethylene Oxide Surfactants." Science, Volume 269, p1242-1244.

Bailey, F. E. 1990. "Alkylene Oxides and their Polymers." Dekker, New York.

Bailey, T.S.; Pham, H.D.; Bates, F.S. 2001. "Morphological Behavior Bridging the Symmetric AB and ABC States in the Poly(styrene-b-isoprene-b-ethylene oxide) Triblock Copolymer System." Macromolecules, Volume 34, p6994-7008.

Bailey, T.S.; Hardy, C.M.; Epps III, T.H.; Bates, F.S. 2002. “A Non-cubic Triply Periodic Network Morphology in Poly(isoprene-*b*-styrene-*b*-ethylene oxide) Triblock Copolymers.” Macromolecules, Volume 35, p7007-7017.

Ball, R.C.; Marko, J.F.; Milner, S.T.; Witten, T.A. 1991. “Polymers Grafted to a Convex Surface.” Macromolecules, Volume 24, p693-703.

Balsamo, V.; Gil, G.; Urbina de Navarro, C.; Hamley, I.W.; von Gyldenfeldt, F.; Abetz, V.; Canizales, E. 2003. "Morphological Behavior of Thermally Treated Polystyrene-b-polybutadiene-b-poly(ε-capralactone) ABC Triblock Copolymers." Macromolecules, Volume 36, p4515-4525.

Bang, J.; Kim, S. H.; Drockenmuller, E.; Misner, M.J.; Russell, T.P.; Hawkes, C.J. 2006. "Defect-Free Nanoporous Thin Films from ABC Triblock Copolymers." Journal of American Chemical Society, Volume 128, p7622-7629.

Bates, F.; Fredrickson, G.H. 1990. “Block Copolymer Thermodynamics: Theory and Experiment.” Annual Reviews of Physical Chemistry, Volume 41, p525-557.

Bates, F.; Fredrickson, G.H. 1999. "Block Copolymers - Designer Soft Materials." Physics Today, Volume 52, February, p32-38.

Beckmann, J.; Auschra, C.; Stadler, R. 1994. "Ball at the wall - A new lamellar multiphase morphology in a polystyrene-block-polybutadiene-block-

poly(methylmethacrylate) triblock copolymer." Macromolecular Rapid Communications, Volume 15, p67-72.

Beiner, M.; Kabisch, O.; Reichl, S.; Huth, H. 2002. "Structural and dynamic nanoheterogeneities in higher poly(alkyl methacrylate)s." Journal of Non-Crystalline Solids, Volume 307-310, p658-666.

Beiner, M.; Huth, H. 2003. "Nanophase separation and hindered glass transition in side-chain polymers." Nature Materials, Volume 2, p595-599.

Benedicto, A. D.; O'Brien, D. F. 1997. "Bicontinuous Cubic Morphologies in Block Copolymers and Amphiphile/Water Systems: Mathematical Description through the Minimal Surfaces." Macromolecules, Volume 30, p3395-3402.

Blanton, T.N.; Huang, T.C.; Toraya, H.; Hubbard, C.R.; Robie, S.B.; Louër, D.; Göbel, H.E.; Will, G.; Gilles, R.; Raftery, T. 1995. "JCPDS-International Center for Diffraction Data round robin study of silver behenate. A possible low-angle X-ray diffraction calibration standard." Powder Diffraction, Volume 10(2), p91-95.

Bockstaller, M. R.; Mickiewicz, R. A.; Thomas, E. L. 2005. " Block Copolymer Nanocomposites: Perspectives for Tailored Functional Materials." Advanced Materials, Volume 17, p1331-1349.

Bohbot-Raviv, Y.; Wang, Z.G. 2000. "Discovering new ordered phases of block copolymers." Physical Review Letters, Volume 85(16), p3428-3431.

Boker, A.; Knoll, A.; Elbs, H.; Abetz, R.; Muller, A.H.E.; Krausch, G. 2002. "Large Scale Domain Alignment of a Block Copolymer from Solution using Electric Fields." Macromolecules, Volume 35, p1319-1325.

Brakke, K. 1992. "The Surface Evolver." Experimental Mathematics, Volume 1(2), p141-165.

Brakke, K. A. 1996. "The Surface Evolver and the Stability of Liquid Surfaces." Philosophical Transactions : Mathematical, Physical and Engineering Sciences, Volume 354, p2143-2157.

Brakke, K. A. 2005. "The Surface Evolver Manual – Version 2.26." http://www.susqu.edu/brakke.

Brandrup, J.; Immergut, E. H. 1989. "Polymer Handbook." 3rd edition, J. Wiley and Sons, New York, Chapter VII, p554-555

Breiner, U.; Krappe, U.; Abetz, V.; Stadler, R. 1997. "Cylindrical morphologies in asymmetric ABC triblock copolymers." Macromolecular Chemistry and Physics, Volume 198(4), p1051-1083.

Breiner, U.; Krappe, U.; Jakob, T.; Abetz, V.; Stadler, R. 1998a. "Spheres on spheres - a novel spherical multiphase morphology in polystyrene-block-polybutadiene-block-poly(methyl methacrylate) triblock copolymers." Polymer Bulletin, Volume 40(2-3), p219-226.

Breiner, U.; Krappe, U.; Thomas, E.L.; Stadler, R. 1998b. "Structural Characterization of the 'Knitting Pattern' in Polystyrene-block-poly(ethylene-co-butylene)-block-poly(methyl methacrylate) Triblock Copolymers." Macromolecules, Volume 31, p135-141.

Brinkmann, S.; Stadler, R.; Thomas, E.L. 1998. "New structural motif in hexagonally ordered cylindrical ternary (ABC) block copolymer microdomains." Macromolecules, Volume 31(19), p6566-6572.

Bronstein, L.; Seregina, M.; Valetsky, P.; Breiner, U.; Abetz, V.; Stadler, R. 1997. "Transition metal complex induced morphology change in an ABC-triblock copolymer." Polymer Bulletin, Volume 39(3), p361-368.

Brunauer, S.; Demming, L.; Demings, W.E.; Teller, E. 1940. “On a Theory of the van der Waals Adsorption of Gases.” Journal of the American Chemical Society, Volume 62, p1723-1732.

Callen, H.B. 1985. “Thermodynamics and an Introduction to Thermostatistics.” 2nd Edition, John Wiley and Sons, Brisbane.

Caruso, T.; Capoleoni, S.; Cazzanelli, E.; Agostino, R.G.; Villano, P.; Passerini, S. 2002. "Characterization of PEO-Lithium Triflate Polymer Electrolytes : Conductivity, DSC and Raman Investigations." Ionics, Volume 8, p36-43.

Cao, W.; Munoz, A.; Palffy-Muhoray, P.; Taher, B. 2002. "Lasing in a three-dimensional photonic crystal of the liquid crystal blue phase II." Nature Materials, Volume 1, p111-113.

Coulon, G.; Russell, T.P.; Deline, V.R.; Green, P.F. 1989. "Surface-Induced Orientation of Symmetric, Diblock Copolymers: A Secondary Ion Mass Spectrometry Study." Macromolecules, Volume 22, p2581-2589.

Chan, V.Z.H.; Hoffman, J.; Lee, V. Y.; Iatrou, H.; Avgeropoulos, A.; Hadjichristidis, N.; Miller, R. D.; Thomas, E.L. 1998. "Ordered Bicontinuous Nanoporous and Nanorelief Ceramic Films from Self Assembling Polymer Precursors." Science, Volume 286, p1716-1719.

Chiu, J. J.; Kim, B. J.; Kramer, E. J.; Pine, D. J. 2005. "Control of Nanoparticle Location in Block Copolymers", Journal of American Chemical Society, Volume 127, p5036-5037.

Cho, B. K.; Jain, A.; Gruner, S.; Wiesner, U. 2004. "Mesophase Structure-Mechanical and Ionic Transport Correlations in Extended Amphiphilic Dendrons." Science, Volume 305, p1598-1601.

Chopp, D. L. 1993. "Computing Minimal Surfaces via Level Set Curvature Flow." Journal of Computational Physics, Volume 106, p77-91.

Chu, B.; Hsiao, B.S. 2001. “Small-Angle X-ray Scattering of Polymers.” Chemical Reviews, Volume 101, p1727-1761.

Cochran, E.; Bates, F.S. 2004. “Shear-Induced Network-to-Network Transition in a Block Copolymer Melt.” Physical Review Letters, Volume 93(8), 087802-1.

Cochran, E.; Garcia-Cervera, C.; Fredrickson, G.H. 2006. "Stability of the Gyroid Phase in Diblock Copolymers at Strong Segregation." Macromolecules, Volume 39, page 2449-2451.

Cohen, Y.; Brinkmann, M.; Thomas, E.L. 2000. "Undulation, dilation and folding of a layered block copolymer. " Volume 114, p984-992.

Cooke, D.M.; Shi, A.C. 2006. “Effects of polydispersity on phase behavior of diblock copolymers.” Macromolecules, Volume 39(19), p6661-6671.

Coulon, G.; Russell, T.P.; Deline, V.R.; Green, P.F. 1989. "Surface-Induced Orientation of Symmetric, Diblock Copolymers: A Secondary Ion Mass Spectrometry Study." Macromolecules, Volume 22, p2581-2589.

Dair, B.J.; Avgeropoulos, A.; Hadjichristidis, N.; Thomas, E.L. 2000. “Mechanical properties of the double gyroid phase in oriented thermoplastic elastomers.” Journal of Materials Science, Volume 35(20), p5207-5213.

Dash, J.G. 2002. "Melting from one to two to three dimensions." Contemporary Physics, Volume 43(6), p427-436.

David, W.I.F. 1986. "Powder diffraction peak shapes. Parameterization of pseudo-Voigt as a Voigt function." Journal of Applied Crystallography, Volume 19, p63-64.

Dormindontova, E.E.; Lodge, T.P. 2001. "The Order-Disorder Transition and the Disordered Micelle Regime in Sphere-Forming Block Copolymer Melts." Macromolecules, Volume 34, p9143-9155.

Dotera, T. 2002. "Tricontinuous Cubic Structures in ABC/A/C copolymer and Homopolymer Blends." Physical Review Letters, Volume 89, 205502.

Enlow, J.D.; Enlow, R.L.; McGrath, K.M.; Tate, M.W. 2004. "Modeling liquid crystal bilayer structures with minimal surfaces." Journal of Chemical Physics, Volume 120, p1981-1989.

Epps, T.H.; Bailey, T.S.; Waletzko, R.; Bates, F.S. 2003. "Phase Behavior and Block Sequence Effects in Lithium Perchlorate-Doped Poly(isoprene-b-styrene-b-ethylene oxide) and Poly(styrene-b-isoprene-b-ethylene oxide) Triblock Copolymers." Macromolecules, Volume 36, p2873-2881.

Epps, T. H.; Cochran, E. W.; Bailey, T. S.; Waletzko, R. S.; Hardy, C. M.; Bates, F. S. 2004. "Ordered Network Phases in Linear Poly (isoprene-b-styrene-b-ethylene oxide) Triblock Copolymers." Macromolecules, Volume 37, p7085-7088.

Epps, T. H.; Chatterjee, J.; Bates, F. S. 2005. "Phase Transformations Involving Network Phases in ISO Triblock Copolymer-Homopolymer Blends." Macromolecules, Volume 38, p8775-8784.

Erhardt R.; Boker, A.; Zettl, H.; Kaya, H.; Pyckhout-Hintzen, W.; Krausch, G.; Abetz, V.; Mueller, A.H.E. 2001. "Janus Micelles." Macromolecules, Volume 34(4), p1069-1075.

Fetters, L.J.; Lohse, D.J.; Richter, D.; Witten, T.A.; Zirkel, A. 1994. "Connection between Polymer Molecular Weight, Density, Chain Dimensions and Melt Viscoelastic Properties." Macromolecules, Volume 27, p4639-4647.

Fetters, L.J.; Lohse, D.J.; Graessley, W.W. 1999. "Chain Dimensions and Entanglement Spacing in Dense Macromolecular Systems." Journal of Polymer Science Part B : Polymer Physics, Volume 37, p1023-1033.

Feynman, R.P.; Leighton, R.B.; Sands, M. 1977. "The Feyman Lectures on Physics." Addison-Wesley Publishing Company, Sydney.

Finkenstadt, V.L.; Millane, R.P. 1998. "Fiber Diffraction Patterns from General Unit Cells : the Cylindrically Projected Reciprocal Lattice." Acta Crystallographica A, Volume 54, p240-248.

Finnefrock, A.C.; Ulrich, R.; Du Chesne, A.; Honeker, C.C.; Schumacher, K.; Unger, K.K.; Gruner, S.M.; Wiesner, U. 2001. "Metal Oxide Containing Mesoporous Silica with Bicontinuous 'Plumber's Nightmare' Morphology from a Block Copolymer - Hybrid Mesophase". Angewante Chemie International Edition, Volume 40(7), p1207-1211.

Finnefrock, A.C.; Ulrich, R.; Toombes, G.E.S.; Gruner, S.M.; Wiesner, U. 2003. "The Plumber's Nightmare: A New Morphology in Block Copolymer-Ceramic Nanocomposites and Mesoporous Aluminosilicates." Journal of the American Chemical Society, Volume 125(43), p13084-13093.

Flory, P.J. 1942. "Thermodynamics of high polymer solutions." Journal of Chemical Physics, Volume 10, p51-61

Flory, P. 1949. "The Configuration of Real Polymer Chains." Journal of Chemical Physics, Volume 17(3), p303.

Floudas, G.; Vazaiou, B.; Schipper, F.; Ulrich, R.; Wiesner, U.; Iatrou, H.; Hadjichristidis, N. 2001. "Poly(ethylene oxide-*b*-isoprene) Diblock Copolymer Phase Diagram." Macromolecules, Volume 34(9), p2947-2957.

Fogden, A.; Hyde, S. 1999. "Continuous Transformations of Cubic Minimal Surfaces." European Physical Journal B, Volume 7, p91-104.

Forster, S.; Khanpur, A.K.; Zhao, J.; Bates, F.S.; Hamley, I.W.; Ryan, A.J.; Bras, W. 1994. "Complex Phase Behavior of Polyisoprene-Polystyrene Diblock Copolymers Near the Order-Disorder Transition." Macromolecules, Volume 27, p6922-6935.

Fraaije, J.G.E.M.; van Vlimmeren, B.A.C.; Maurits, N.M.; Postma, M.; Evers, O.A.; Hoffman, C.; Altevogt, P.; Goldbeck-Wood, G. 1997. "The dynamic mean-field density functional method and its application to the mesoscopic dynamics of quenched block copolymer melts." Journal of Chemical Physics, Volume 106, p4260.

Frank, J. 1992. "Electron Tomography: Three-dimensional imaging with the Transmission Electron Microscope." Plenum Press, New York.

Fredrickson, G.H. 1991. "Stability of a Catenoid-Lamellar Phase for Strongly Stretched Block Copolymers." Macromolecules, Volume 24, p3456-3458.

Fredrickson, G.H.; Ganesan, V.; Drolet. F. 2002. "Field-Theoretic Computer Simulation Methods for Polymers and Complex Fluids." Macromolecules, Volume 35, p16-39.

Fukunaga, K.; Elbs, H.; Magerle, R.; Krausch, G. 2000. "Large-scale alignment of ABC block copolymer microdomains via solvent vapor treatment." Macromolecules, Volume 33, p947-953.

Gao, C.; Sakamoto, Y.; Sakamoto, K.; Terasaki, O.; Che, S. 2006. "Synthesis and Characterization of Mesoporous Silica AMS-10 with Bicontinuous Cubic Pnm Symmetry." Angewandte Chemie, International Edition, Volume 45(26), p4295-4298.

Garcia, C.B.W.; Zhang, Y.; Mahajan, S.; DiSalvo, F.; Wiesner, U. 2003. "Self-Assembly Approach toward Magnetic Silica-Type Nanoparticles of Different Shapes from Reverse Block Copolymer Mesophases." Journal of the American Chemical Society, Volume 125(4), p13310-13311.

Garstecki, P.; Holyst, R. 2000. "Scattering on triply periodic minimal surfaces - the effect of the topology, Debye-Waller, and molecular form factors." Journal of Chemical Physics, Volume 113(9), p3772-3779.

Garstecki, P.; Holyst, R. 2001. "Scattering patterns of self-assembled gyroid cubic phases in amphiphilic systems." Journal of Chemical Physics, Volume 115(2), p1095-1099.

Garstecki, P.; Holyst, R. 2002. "Scattering Patterns of Self-Assembled Cubic Phases. 1. The Model." Langmuir, Volume 18, p2519-2528.

Garstecki, P.; Holyst, R. 2002b. "Scattering Patterns of Self-Assembled Cubic Phases. 2. Analysis of Experimental Spectra." Langmuir, Volume 18, p2529-2537.

Garstecki, P.; Holyst, R. 2003. "Scattering Patterns of Multiply Continuous Cubic Phases in Block Copolymers. I. The Model." Macromolecules, Volume 36, p9181-9190.

Garstecki, P.; Holyst, R. 2003b. “Scattering Patterns of Multiply Continuous Cubic Phases in Block Copolymers. II. Applications to Various Triply Periodic Architectures.” Macromolecules, Volume 36, p9191-9198.

Gido, S.P.; Schwark, D.W.; Thomas, E.L.; do Carmo Goncalves, M. 1993. "Observation of a non-constant mean curvature interface in an ABC triblock copolymer." Macromolecules, Volume 26, p2636-2640.

Gilbert, P. 1972. "Iterative Methods for the Three-dimensional Reconstruction of an Object from Projections." Journal of Theoretical Biology, Volume 36, p105.

Glatter, O.; Kratky, O. 1982. "Small angle x-ray scattering." Academic Press, New York.

Goldacker T.; Abetz, V.; Stadler, R.; Erukhimovich, I.; Leibler, L. 1999. " Non-centrosymmetric superlattices in block copolymer blends." Nature, Volume 398 (6723), p137-139.

Grason, G.M. 2006. "The packing of soft materials: Molecular asymmetry, geometric frustration and optimal lattices in block copolymer melts." Physics Reports, Volume 433, p1-64.

Grubbs, R. B. 2005. "Multiblock Copolymers: PEO Stuck in the Middle." Macromolecular Chemistry and Physics, Volume 206, p625-627.

Guinier, A.; Fournet, G. 1955. "Small-Angle Scattering of X-rays." John Wiley and Sons, New York.

Hahn, Th. editor. 2002. "International Tables for Crystallography Volume A : Space-group symmetry." Kluwer Academic Publishers, Boston.

Hajduk, Damian Andrew. 1994. "Morphological Transitions in Block Copolymers." Ph.D. Thesis, Princeton University, p45-54.

Hajduk, D.A.; Harper, P. E.; Gruner, S. M.; Honeker, C.C.; Kim, G.; Thomas, E.L.; Fetters, L.J. 1994. "The Gyroid : A New Equilibrium Morphology in Weakly Segregated Diblock Copolymers." Macromolecules, Volume 27, p4063-4075.

Hajduk, D. A.; Harper, P. E.; Gruner, S. M.; Honeker, C.C., Kim, G.; Thomas, E.L.; Fetters, L.J. 1995. "A reevaluation of Bicontinuous Cubic Phases in Starblock Copolymers." Macromolecules, Volume 28, p2507-2573.

Hajduk, D. A.; Takenouchi, H.; Hillmyer, M. A.; Bates, F. S.; Vigild, M. E.; Almdal, K. 1997. "Stability of the Perforated Layer (PL) Phase in Diblock Copolymer Melts." Macromolecules, Volume 30, p3788-3795.

Halperin, A. 1990. "Rod-coil copolymers: their aggregation behavior." Macromolecules, Volume 23, p2724.

Hamley, I.W.; Koppi, K.A.; Rosedale, J.H.; Bates, F.S.; Almdal, K.; Mortensen, K. 1993. "Hexagonal mesophases between lamellar and cylinders in a diblock copolymer melt." Macromolecules, Volume 26, p5959-5970.

Hamley, I. W. 1998. "The Physics of Block Copolymers." Oxford University Press, New York.

Harper, Paul Ellsworth. 1996. “Structural Studies of Surfactant and Polymer Systems.” Ph.D. Thesis, Princeton University.

Harper, P.E.; Gruner, S.M. 2000. "Electron Density modeling and reconstruction of infinite periodic minimal surfaces (IPMS) based phases in lipid water systems. I. Modeling IPMS-based Phases." European Physical Journal E, Volume 2, p217-228.

Harper, P.E., Gruner, S.M. 2000. "Electron Density modeling and reconstruction of infinite periodic minimal surfaces (IPMS) based phases in lipid-water systems. II. Reconstruction of D surface based phases." European Physical Journal E, Volume 2, p229-245.

Hayward, R.C.; Alberius, P.C.A.; Kramer, E.J.; Chmelka, B.F. 2004. "Thin Films of Bicontinuous Cubic Mesostructured Silica Templated by a Nonionic Surfactant." Langmuir, Volume 20, p5998-6004.

Hayward, R.C.; Chmelka, B. F.; Kramer, E.J. 2005. "Template Cross-Linking Effects on Morphologies of Swellable Block Copolymer and Mesostructured Silica Thin Films." Volume 38, p7768-7783.

Helfand, E. 1975. "Theory of inhomogeneous polymers: Fundamentals of the Gaussian random-walk model." Journal of Chemical Physics, Volume 62(3), p999-1005.

Helfand, E.; Sapse, A.M. 1975. "Theory of unsymmetric polymer-polymer interfaces." Journal of Chemical Physics, Volume 62(4), p1327-1331.

Helfand, E.; Wasserman, Z.R.; 1976. "Block Copolymer Theory : 4: Narrow Interphase Approximateion." Macromolecules, Volume 9, p879.

Helfand, E.; Wasserman, Z.R. 1978. "Block Copolymer Theory : 5: Spherical Domains." Macromolecules, Volume 11(5), p960-966.

Helfand, E.; Wasserman, Z.R. 1980. "Block Copolymer Theory : 6: Cylindrical Domains." Macromolecules, Volume 13, p994.

Ho, K.M.; Chan, C.T.; Soukoulis, C.M.; Biswas, R.; Sigalas, M. 1994. Solid State Communications. Volume 89, p413-416.

Honeker, C.C.; Thomas, E.L.; Albalak, R.J.; Hajduk, D.A.; Gruner, S.M.; Capel, M.C. 2000. "Perpendicular Deformation of a Near-Single-Crystal Triblock Copolymer with a Cylindrical Morphology. 1. Synchrotron SAXS." Macromolecules, Volume 33(25), p9395-9406.

Huang, T.C.; Toraya, H.; Blanton, T.N.; Wu, Y. 1993. "X-ray Powder Diffraction Analysis of Silver Behenate, a Possible Low-Angle Diffraction Standard." Journal of Applied Crystallography, Volume 26, p180-184.

Huang, H.; Zhang, F.; Hu, Z.; Du, B.; He, T.; Lee, F.K.; Wang, Y.; Tsui, O.K.C. 2003. "Study on the Origin of Inverted Phase in Drying Solution-Cast Block Copolymer Films." Macromolecules, Volume 36, p4084-4092.

Huckstadt, H.; Gopfert, A.; Abetz, V. 2000. "Influence of the block sequence on the morphological behavior of ABC triblock copolymers." Polymer, Volume 41(26), p9089-9094.

Huggins, M. 1941. "Solutions of Long Chain Compounds." Journal of Chemical Physics, 1941, Volume 9(5), p440.

Humlicek, J. 1982. "Optimized Computation of Voigt and Complex Probability Functions." Journal of Quantitative Spectroscopy and Radiative Transfer, Volume 27(4), p437-444.

Huse, D.A.; Leibler, S. 1988. Journal de Physique (France),Volume 49, p605-620.

Hyde, S.T. 1996. "Bicontinuous Structures in lyotropic liquid crystals and crystalline hyperbolic surfaces." Current Opinion in Solid State and Materials Science, Volume 1, p653-662.

Ikkala, O.; ten Brinke, G. 2002. "Functional Materials Based on Self-Assembly of Polymeric Supramolecules." Science, Volume 295, p2407-2409.

Jain, A.; Wiesner, U. 2004. "Silica-Type Mesostructures from Block Copolymer Phases: Formation Mechanism and Generalization to the Dense Nanoparticle Regime." Macromolecules, Volume 37, p5665-5670.

Jain, A.; Toombes, G. E. S.; Hall, L. M.; Mahajan, S.; Garcia, C. B. W.; Probst, W.; Gruner, S. M.; Wiesner, U. 2005. "Direct Access to Bicontinuous Skeletal Inorganic

Plumber's Nightmare Networks from Block Copolymers." Angewandte Chemie International Edition. Volume 44, p1226-1229.

Janssen, A. H.; Yang, C. M.; Wang, Y.; Schuth, F.; Koster, A. J.; de Jong, K. P. 2003. "Localization of Small Metal (Oxide) Particles in SBA-15 Using Bright-Field Electron Tomography." Journal of Physical Chemistry B, Volume 107, p10552-10556.

Jinnai, H.; Hasegawa, H.; Nishikawa, Y.; Sevink, G.; Braunfeld, M.; Agard, D.; Spontak, R. 2006. "3D Nanometre-Scale Study of Coexisting Bicontinuous Morphologies in a Block Copolymer/Homopolymer Blend." Macromolecular Rapid Communications, Volume 27, p1424-1429.

Jinnai, H.; Nishikawa, Y.; Spontak, R.; Smith, S.; Agard, D.; Hashimoto, T. 2000. "Direct Measurement of Interfacial Curvature Distributions in a Bicontinuous Block Copolymer Morphology." Physical Review Letters, Volume 84, p518-521.

Kamperman, M.; Garcia, C.; Du, P.; Ow, H.; Wiesner, U. 2004. "Ordered Mesoporous Ceramics Stable up to 1500°C from Diblock Copolymer Mesophases." Journal of the American Chemical Society, Volume 126(45), p14708-14709.

Kane, L.; Spontak, R. 1994. "Microstructural Characteristics of Strongly-Segregated AXB Triblock Terpolymers Possessing the Lamellar Morphology." Macromolecules, Volume 27, p1267-1273.

Kaneko, T.; Suda, K.; Satoh, K.; Kamigaito, M.; Kato, T.; Ono, T.; Nakamura, E.; Nishi, T.; Jinnai, H. 2006. "A Ladder Morphology in an ABC Triblock Copolymer." Macromolecular Symposia, Volume 242, p80-86.

Kannan, R.M.; Kornfield, J.A. 1994. "Evolution of Microstructure and Viscoelasticity during Flow Alignment of a Lamellar Diblock Copolymer." Macromolecules, Volume 27, p1177-1186.

Karcher, H.; Polthier, K. 1996. “Construction of Triply Periodic Minimal Surfaces.” Philosophical Transactions : Mathematical, Physical and Engineering Sciences, Volume 354, p2077-2104.

Keller, A.; Pedemonte, E.; Willmouth, F.N. 1970. "Macro-lattice from Segregated Amorphous Phases of a Three Block Copolymer." Nature, Volume 225, p538-539.

Kinning, D.J.; Thomas, E.L.; Ottino, J.M. 1987. "Effect of morphology on the transport of gases in block copolymers." Macromolecules, Volume 20, p1129.

Klotz, M.; Albouy, P.; Ayral, A.; Menager, C.; Grosso, D.; Van der Lee, A.; Cabuil, V.; Babonneau, F.; Guizard, C. 2000. "The True Structure of Hexagonal Mesophase-Templated Silica Films As Revealed by X-ray Scattering: Effects of Thermal Treatments and of Nanoparticle Seeding." Chemistry of Materials, Volume 12, p1721-1728.

Kopperschmidt, P. 2003. "Tetragonal photonic woodpile structures." Applied Physics B, Volume 76, p729-734.

Kosonen, H. et al. 2002. "Mesomorphic Structure of Poly(styrene)-block-poly(4-vinylpyridine) with Oligo (ethylene oxide) sulfonic Acid Side Chains as a Model for Molecularly Reinforced Polymer Electrolyte." Macromolecules Volume 35, p10149-10154.

Kossuth, M.B.; Morse, D.C.; Bates, F.S. 1999. "Visco-eleastic behavior of cubic phases in block copolymer melts." Journal of Rheology, Volume 43, p167-196.

Krappe, U.; Stadler, R.; Voigt-Martin, I.; 1995. "Chiral Assembly in Amorphous ABC Triblock Copolymers. Formation of a Helical Morphology in Polystyrene-block-polybutadiene-block-poly (methyl methacrylate) Block Copolymers." Macromolecules, Volume 28, p4558-4561.

Kresge, C.; Leonwicz, M.; Roth, W.; Vartuli, J.; Beck, J. 1992. "Ordered mesoporous molecular sieves synthesized by a liquid-crystal template mechanism." Nature, Volume 359, p710.

Kroger, N.; Deutzmann, R.; Sumper, M. 1999. "Polycationic Peptides from Diatom Biosilica that Direct Silica Nanosphere Formation." Science, Volume 286, p1129-1132.

Lai, C.; Loo, Y.L., Register, R.A.; Adamson, D.H. 2005. "Dynamics of a Thermoreversible Transition between Cylindrical and Hexagonally Perforated Lamellar Mesophases." Macromolecules, Volume 38, p7098-7104.

Lambert, C. A.; Radzilowski, L. H.; Thomas, E. L. 1996. "Triply Periodic Level Surfaces as Models for Cubic Tricontinuous Block Copolymer Morphologies." Philosophical Transactions: Mathematical, Physical and Engineering Sciences, Volume 354(1715), p2009-2023.

Lee, M.; Cho, B.K.; Ihn, K.J.; Lee, W.K.; Oh, N.K.; Zin, W.C. 2001. "Supramolecular Honeycomb by Self-Assembly of Molecular Rods in Rod-Coil Molecule." Journal of the American Chemical Society, Volume 123, p4647-4648.

Lee, B.; Park, I.; Yoon, J.; Park, S.; Kim, J.; Kim, K.W.; Chang, T.; Ree, M. 2005. "Structural Analysis of Block Copolymer Thin Films with Grazing Incidence Small-Angle X-ray Scattering." Macromolecules, Volume 38, p4311-4323.

Leibler, L. 1980. "Theory of Microphase Separation in Block Copolymers." Macromolecules, Volume 13, p1602-1617.

Lescanec, R.L.; Fetters, L.J.; Thomas, E.L. 1998. "Assessing homopolymer distribution in ABC triblock copolymer/homopolymer blends through a transition in interfacial geometry." Macromolecules, Volume 31(5), p1680-1685.

Li, Z. B.; Kesselman, E.; Talmon, Y.; Hillmyer, M. A.; Lodge, T. P. 2004. "Multicompartment Micelles from ABC Miktoarm Stars in Water." Science, Volume 306, p98-101.

Lidin, S.; Hyde, S.T.; Ninham, B.W. 1990. "Exact Construction of Periodic Minimal Surfaces : the I-WP surface and its isometries." Journal de Physique (France), Volume 51, p801-813.

Lifshitz, I.M.; Grosbert, A.; Khokhlov, A.R. 1978. "Some problems of the statistical physics of polymer chains with volume interaction." Reviews of Modern Physics, Volume 50, p683-713.

Likhtman, A.E.; Semenov, A.N. 1994. "Stability of the OBDD Structure for Diblock Copolymer Melts in the Strong Segregation Limit." Macromolecules, Volume 27, p3103-3106.

Likhtman, A.E.; Semenov, A.N. 1997. "Theory of Microphase Separation in Block Copolymer/Homopolymer Mixtures." Macromolecules, Volume 30, p7273-7278.

Liu, Y.; Abetz, V.; Muller, A.H.E. 2003. "Janus Cylinders." Macromolecules, Volume 36, p7894-7898.

Lodge, T.P. 2003. "Block Copolymers: Past Success and Future Challenges." Macromolecular Chemistry and Physics, Volume 204(2), p265-273.

Longley, W.; McIntosh, T.J. 1983. "A bicontinuous tetrahedral structure in a liquid-crystalline lipid." Nature, Volume 303(5918), p612-614.

Loo, Y.L.; Register, R.A.; Adamson, D.H.; Ryan, A.J. 2005. "A Highly Regular Hexagonally Perforated Lamellar Structure in a Quiescent Diblock Copolymer." Macromolecules, Volume 38, p4947-4949.

Ludwigs, S.; Boker, A.; Voronov, A.J.; Rehse, N.; Magerle, R.; Krausch, G. 2003. "Self-assembly of functional nanostructures from ABC triblock copolymers." Nature Materials, Volume 2, p744-747.

Ludwigs, S.; Boker, A.; Abetz, V.; Muller, A.H.E.; Krausch, G. 2003b. "Phase behavior of linear polystyrene-block-poly(2-vinylpyridine)-block-poly(tert-butyl methacrylate) triblock terpolymers." Polymer, Volume 44, p6815-6823.

Ludwigs, S.; Schmidt, K.; Krausch, G. 2005. "One-Dimensional Swelling of a pH-Dependent Nanostructure Based on ABC Triblock Terpolymers." Macromolecules, Volume 38, p2376-2382.

Luzzati, V. and P.A. Spegt. 1967. "Polymorphism of Lipids." Nature, Vol 21, p701-704.

Lyaskaya, Y.V.; Birshtein, T.M. 1995. "Triblock copolymers : the role of interfacial tension coefficients at two interfaces." Polymer, Volume 36, Issue 5, p975-980.

Lynd, N.A.; Hillmyer, M.A. 2005. "Influence of polydispersity on the self-assembly of diblock copolymers." Macromolecules, Volume 38, Issue 21, p8803-8810.

Maddaford, P.J.; Trokcioglu, C. 1993. "Structure of Cubic Phases in the Ternary System Didodecyldimethylammonium Bromide/Water/Hydrocarbon." Langmuir, Volume 9, p2868-2878.

Madkour, T.M. 2001. "A combined statistical mechanics and molecular dynamics approach for the evaluation of the miscibility of polymers in good, poor and non-solvents." Chemical Physics, Volume 274, p187-198.

Mahajan, S.; Renker, S.; Simon, P.F.W.; Gutmann, J.S.; Jain, A.; Gruner, S.M.; Coates, G.W.; Wiesner, U. 2003. "Synthesis and Characterization of Amphiphilic Poly (ethylene oxide)-block-poly(hexyl methacrylate) Copolymers." Macromolecular Chemistry and Physics, Volume 204, p1047-1055.

Mahajan, S.; Cho, B. K.; Allgaier, J.; Fetters, L. J.; Coates, G. W.; Wiesner, U. 2004. "Synthesis of Amphiphilic ABC Triblock Copolymers with PEO as the Middle Block." Macromolecular Rapid Communications, Volume 25, p1889-1894.

Mahajan, Surbhi. 2005. "Novel Amphiphilic AB Diblock and ABC Triblock Copolymers as Structure Directing Agents for Nanostructured Silica-Type Materials." Ph.D. Thesis, Cornell University.

Maldovan, M.; Urbas, A.M.; Yufa, N.; Carter, W.C.; Thomas, E.L. 2002. " Photonic properties of bicontinuous cubic microphases." Physical Review B, Volume 65, 165123.

Maldovan, M.; Thomas, E.L. 2005. "Diamond-structured photonic crystals." Nature Materials, Volume 3, p593-600.

Maniadis, P. ;Thompson, R.B.; Rasmussen, K.O.; Lookman, T. 2004. “Ordering mechanisms in triblock copolymers.” Physical Review E, Volume 69, 031801.

Marko, J.F.; Siggia, E.D. 1995. "Stretching DNA." Macromolecules, Volume 28, p8759-8770.

Martinez-Veracoechea, F.; Escebedo, F. 2006. "Simulation of the gyroid phase in off-lattice models of pure diblock copolymer melts." Journal of Chemical Physics, Volume 125, 104907.

Matsen, M.W.; Schick, M. 1994. "Stable and Unstable Phases of a Diblock Copolymer Melt." Physical Review Letters, Volume 72(16), p2660-2663.

Matsen, M.W. 1995. "Phase Behavior of Block Copolymer/Homopolymer Blends." Macromolecules, Volume 28, p5765-5773.

Matsen, M.W.; Bates, F.S. 1996. "Unifying weak- and strong-segregation block copolymer theories." Macromolecules, Volume 29, p1091-1098.

Matsen, M.W.; Bates, F.S. 1996b. "Origins of Complex Self-Assembly in Block Copolymers." Macromolecules, Volume 29, p7641-7644.

Matsen, M.W. 1998. "Gyroid versus double-diamond in ABC triblock copolymer melts." Journal of Chemical Physics, Volume 108(2), p785-796.

Matsen, M.W. 2002. "The Standard Gaussian Model for Block Copolymer Melts." Journal of Physics : Condensed Matter, Volume 14, p21-47.

Matsen, M.W. 2003. "Comment on 'Cylindrical phase of block copolymers : Stability of circular configuration to elliptical distortions and thin film morphologies.'" Physical Review E. Volume 67, 023801.

Matsushita, Y.; Choshi, H.; Fujimoto, T.; Nagasawa, M. 1980. "Preparation and Morphological Properties of a Triblock Copolymer of the ABC Type." Macromolecules, Volume 13, p1053-1058.

Matsushita, Y.; Suzuki, J.; Seki, M. 1998. "Surfaces of tricontinuous structure formed by an ABC triblock copolymer in bulk." Physica B, Volume 248, p238-242.

Meille, S.V.; Bruckner, S.; Porzio, W. 1990. "Gamma-Isotactic Polypropylene. A Structure with Non-Parallel Chain Axes." Macromolecules, Volume 23, p4114-4121.

Midgley, P.A.; Weyland, M. 2003. "3D electron microscopy in the physical sciences: the development of Z-contrast and EFTEM tomography." Ultramicroscopy, 96(3-4), p413.

Milner, S.T.; Witten, T.A.; Cates, M.E. 1988. "Theory of the Grafted Polymer Brush." Macromolecules, Volume 21, p2610-2619.

Mogi, Y.; Kotsuji, H.; Kaneko, Y.; Mori, K.; Matsushita, Y.; Noda, I. 1992. "Preparation and morphology of triblock copolymers of the ABC type." Macromolecules, Volume 25, p5408-5411.

Mogi, Y.; Kotsuji, H.; Kaneko, Y.; Mori, K.; Matsushita, Y.; Noda, I. 1992b. "Tricontinuous Morphology of Triblock Copolymers of the ABC Type." Macromolecules, Volume 25, p5412-5415.

Mogi, Y.; Nomura, M.; Kotsuji, H.; Ohnishi, K.; Matsushita, Y.; Noda, I. 1994. "Superlattice Structures in Morphologies of the ABC Triblock Copolymers." Macromolecules, Volume 27(23), p6755 - 6760.

Monnier, A.; Schuth, F.; Huo, Q.; Kumar, D.; Marolese, D.; Maxwell, R.S.; Stucky, G.D.; Krishnamurty, M.; Petroff, P.; Firouzi, A.; Janicke, M.; Chmelka, B.F. 1993. "Cooperative Formation of Inorganic-Organic Interfaces in Synthesis of Silicate Mesostructures." Science, Volume 261, p1299-1303

Morkved, T.L.; Lu, M.; Urbas, A.M.; Ehrichs, E.E.; Jaeger, H.M.; Mansky, P.; Russell, T.P. 1996. "Local control of microdomain orientation in diblock copolymer thin films with electric fields." Science, Volume 273, p931-933.

Muller, D. A; Singh, D.J.; Silcox, J. 1998. Physical Review B, Volume 57, p8181–8202.

Muthukumar, M.; C.K. Ober; E.L. Thomas. 1997. "Competing Interactions and Levels of Ordering in Self-Organizing Polymeric Materials." Science, Volume 277, p1225-1232.

Nakazawa, H., Ohta, T. 1993. "Microphase Separation of ABC-Type Triblock Copolymers." Macromolecules, Volume 26, p5503-5511.

Neumann, C.; Abetz, V.; Stadler, R. 1996. "Indication of an order-order-transition by a partial disordering in ABC triblock copolymers." Polymer Bulletin, Volume 36, Issue 1, p43-50.

Neumann, C.; Loveday, D.R.; Abetz, V.; Stadler, R. 1998. "Morphology, Dynamic Mechanical Properties, and Phase Behavior of ABC-Triblock Copolymers with Two Semicompatible Elastomer Blocks." Macromolecules, Volume 31, p2493-2500.

Noda, S.; Tomoda, K.; Yamamoto, N.; Chutinan, A. 2000. "Full Three-Dimensional Photonic Bandgap Crystals at Near-Infrared Wavelengths." Science, Volume 289, p604-606.

Noro, A.; Cho, D.; Takano, A.; Matsushita, Y. 2005. "Effect of molecular weight distribution on microphase-separated structures from block copolymers." Macromolecules, Volume 38(10), p371-4376.

Ogawa, S.; Imada, M.; Yoshimoto, S.; Okano, M.; Noda, S. 2004. "Control of Light Emission by 3D Photonic Crystals." Science, Volume 305, p227-229.

O'Keefe, M.; Andersson, S. 1977. "Rod Packings and Crystal Chemistry." Acta Crystallographica A, Volume 33, p914-923.

Olmsted, P.D.; Milner, S.T. 1998. "Strong Segregation Theory of Bicontinuous Phases in Block Copolymers." Macromolecules, Volume 31, p4011-4022.

Ott, H.; Abetz, V.; Aldstadt, V. 2001. "Morphological studies of poly(styrene)-block-poly(ethylene-co-butylene)-block-poly(methyl methacrylate) in the composition region of the "knitting pattern" morphology." Macromolecules, Volume 34(7), p2121-2128.

Petschek, R.G.; Wiefling, K.M. 1987. "Novel Ferroelectric Fluids." Physical Review Letters, Volume 39(3), p343-346.

Phan, S.; Fredrickson, G.H. 1998. "Morphology of Symmetric ABC Triblock Copolymers in the Strong Segregation Limit." Macromolecules, Volume 31, p59-63.

Press, W.; Teukolsky, S.A.; Vetterling, W.T.; Flannery, B.P. 1986. "Numerical recipes: the art of scientific computing." Cambridge University Press, New York.

Radermacher, M. 1992. "Electron tomography: three-dimensional imaging with the transmission electron microscope." Frank, J. Editor, Plenum Press, London, p91.

Radiman, S.; Toprakcioglu, C.; Faruqi, A.R. 1990. "Symmetry transition in the cubic phase of a ternary surfactant system." Journal de Physique, Volume 51, p1501–1508.

Renker, S.; Mahajan, S.; Babski, D. T.; Schnell, I.; Jain, A.; Gutmann, J.; Zhang, Y.; Gruner, S. M.; Spiess, H. W.; Wiesner, U. 2004. "Nanostructure and Shape Control in Polymer-Ceramic Hybrids from Poly (ethylene oxide)-block-Poly (hexyl methacrylate) and Aluminosilicates Derived from Them." Macromolecular Chemistry and Physics, Volume 205, p1021-1030.

Rodgers, S.S.; Mandelkern, L. 1957. "Glass Formation in Polymers. I. The Glass Transitions of the Poly-(n-alkyl Methacrylates)." Journal of Physical Chemistry, Volume 61(7), p985-991.

Rosedale, J.H.; Bates, F.S.; Almdal, K.; Mortensen, K.; Wignall, G.D. 1995. "Order and Disorder in Symmetric Diblock Copolymer Melts." Macromolecules, Volume 28, p1429-1443.

Rosi, N. L.; Kim, J.; Eddaoudi, M.; Chen, B.; O'Keeffe, M.; Yaghi, O. M. 2005. "Rod Packings and Metal-Organic Frameworks Constructed from Rod-Shaped Secondary Building Units." Journal of the American Chemical Society, Volume 127, p1504-1518.

Ruokolainen, J.; Makinen, R.; Torkkeli, M.; Makela, T.; Serimaa, R.; ten Brinke, G.; Ikkala, O. 1998. "Switching Supramolecular Polymeric Materials with Multiple Length Scales." Science, Volume 280, p557-560.

Ruzette, A.; Soo, P.P.; Sadoway, D.R. ; Mayes, A.M. 2001. "Melt-Formable Block Copolymer Electrolytes for Lithium Rechargeable Batteries." Journal of the Electrochemical Society, Volume 148(6), A537-A543.

Ruzette, A.; Leibler, L. 2005. "Block Copolymers in tomorrow's plastics." Nature Materials, Volume 4, p19-31.

Sakamoto, Y.; Kaneda, M.; Terasaki, O.; Zhao, D.Y.; Kim, J. M.; Stucky, G.; Shin H.; Ryoo, R. 2000. "Direct imaging of the pores and cages of three-dimensional mesoporous materials." Nature, Volume 408, p449-453.

Sakurai, S.; Umeda, H.; Furukawa, C.; Irie, H.; Nomura, S.; Lee, H.H.; Kim, J.K. 1998. "Thermally induced morphological transition from lamella to gyroid in a binary

blend of diblock copolymers." Journal of Chemical Physics, Volume 108, p4333-4339.

Sakurai, S.; Isobe, D.; Okamoto, S.; Yao, T.; Nomura, S. 2001. "Collapse of the Ia3d cubic symmetry by uniaxial stretching of a double-gyroid block copolymer." Physical Review E., Volume 63, 061803

Sayar, M.; Olvera de la Cruz, M.; Stupp, S.I. 2003. "Polar order in nanostructured organic materials." Europhysical Letters, Volume 61(3), p334.

Schmidt, S.C.; Hillmyer, M. A. 2002. "Morphological Behavior of Model Poly(ethylene-*alt*-propylene)-b-polylactide Diblock Copolymers." Journal of Polymer Science Part B: Polymer Physics, Volume 40, p2364-2376.

Schoen, A.H. 1970. "Infinite Periodic Minimal Surfaces without Self-Intersections." NASA Technical Note, TN D-5541.

Schroeder, G.E.; Hyde, S.T.; Iatrou, H.; Hadjichristidis, N.; Akasaka, S.; Hasegawa, H. 2006. " Electron tomography of a novel non-cubic network phase in ABC copolymers." American Physical Society, APS March Meeting, March 13-17, Abstract N30.0003.

Schulz, M.F., Bates, F.S.; Almdal, K.; Mortensen, K. 1994. "Epitaxial Relationship for Hexagonal-to-Cubic Phase Transition in a Block Copolymer Mixture." Physical Review Letters, Volume 73, p86–89.

Schuth, F.; Schmidt, W. 2002. "Microporous and Mesoporous Materials." Advanced Materials, Volume 14, p629-638.

Schwarz, H.A. 1890. "Gesammelte Mathematische Abhandlungen", Springer, Berlin.

Schwarz, U.S.; Gompper, G. 1999. "Systematic Approach to Bicontinuous cubic phases in ternary amphiphilic systems." Physical Review E, Volume 59, p5528-5541.

Schwarz, U.S.; Gompper, G. 2001. "Bending Frustration of Lipid-Water Mesophases Based on Cubic Minimal Surfaces." Langmuir, Volume 17, p2084-2096.

Scriven, L.E. 1976. Nature, Volume 263, p123-124.

Semenov, A.N. 1985. "Contribution to the theory of microphase layering in block-copolymer melts." Soviet Physics JETP. Volume 61(4), p733-742.

Shenhar, R.; Norsten, T.B.; Rotello, V.M. 2005. " Polymer-Mediated Nanoparticle Assembly : Structural Control and Applications." Advanced Materials, Volume 17, p657-669.

Shimizu, K.; Cha, J.; Stucky, G.; Morse, D. E. 1998. " Silicatein alpha : Cathepsin L-like protein in sponge biosilica." Proceedings of the National Academy of Sciences USA, Volume 95, p6234-6238.

Sides, S.W.; Fredrickson, G.H. 2004. "Continuous polydispersity in a self-consistent field theory for diblock copolymers." Journal of Chemical Physics, Volume 121(10), p4974-4986.

Simon, P.F.W.; Ulrich, R.; Spiess, H.W.;Wiesner, U. 2001. "Block Copolymer-Ceramic Hybrid Materials from Organically Modified Ceramic Precursors." Chemistry of Materials, Volume 13, p3464-3486.

Soler-Illia, G. J. D.; Sanchez, C.; Lebeau, B.; Patarin, J. 2002. "Chemical Strategies to Design Textured Materials." Chemical Reviews, Volume 102, p4093-4138.

Soo, P.P. et al. 1999. "Rubbery Block Copolymer Electrolytes for Solid-State Rechargeable Lithium Batteries." Journal of the Electrochemical Society, Volume 146, p32-37.

Sozuer, H.S.; Dowling, J.P. 1994. "Photonic band calculations for woodpile structures", Journal of Modern Optics, Volume 41, p231-239.

Spence, J. C. H. 2006. "Absorption Spectroscopy with sub-angstrom beams: ELS in STEM." Reports on Progress in Physics, Volume 69(3), p725-758.

Spontak, R.J. et. al. Macromolecules. 1996, 29, 4494-4507.

Stadler, R.; Auschra, C.; Beckmann, J.; Krappe, U.; Voigt-Martin, I.; Leibler, L. 1995. "Morphology and Thermodynamics of Symmetric Poly(A-block-B-block-C) Triblock Copolymers." Macromolecules, Volume 28, p3080-3097.

Stangler, S.; Abetz, V. 2003. "Orientation behavior of AB and ABC block copolymers under large amplitude oscillatory shear flow." Rheological Acta, Volume 42, p569-577.

Steele, B.C.H.; Heinzel, A. 2001. "Materials for fuel-cell technologies." Nature Volume 414, p345-352.

Stewart, S.; Liu, G. 2000. "Block Copolymer Nanotubes." Angewandte Chemie International Edition, Volume 39, p340-344.

Strom, P.; Anderson, D.M. 1992. "The Cubic Phase Region in the System Didodecyldimethylammonium Bromide Water Styrene." Langmuir, Volume 8(2), p691-709.

Sugiyama, M.; Shefelbine, T.; Vigild, M.; Bates, F. 2001. "Phase Behavior of an ABC Triblock Copolymer Blended with A and C Homopolymers." Journal of Physical Chemistry B, Volume 105, p12448-12460.

Suzuki, J.; Furuya, M.; Inuma, M.; Takano, A.; Matsushita, Y. 2002. "Morphology of ABC Triblock Copolymer/Homopolymer Blend Systems." Volume 49, p1135-1141.

Takano, A.; Soga, K.; Suzuki, J.; Matsushita, Y. 2003. "Noncentrosymmetric Structure from a Tetrablock Quarterpolymer of the ABCA Type." Macromolecules, Volume 26, p9288-9291.

Takenaka, M., Wakada, T.; Akasaka, S.; Nishitusi, S.; Saijo, K.; Shimizu, H.; Hasegawa, H. 2007. "Orthorhombic Fddd Network in Diblock Copolymer Melts." Macromolecules, Volume 40, p4399-4402.

Tang, Ping; Qiu, F.; Zhang, H.; Yang, Y.. 2004. “Morphology and Phase Diagram of Complex Block Copolymers : ABC linear triblock copolymers.” Physical Review E, Volume 69, 031803.

Tate, M.W.; Eikenberry, E.F.; Barna, S.L.; Wall, M.E.; Lowrance, J.L.; Gruner, S.M. 1995. "A large-format, high-resolution area x-ray detector based on a fiber-optically bonded charge-coupled device (CCD)." Journal of Applied Crystallography, Volume 28, p196-205.

Tate, M.W., Gruner, S.M.; Eikenberry, E. 1997. "Coupling format variations in x-ray detectors based on charge coupled devices." Reviews of Scientific Instruments, Volume 68, p47-54.

Templin, M.; Franck, A.; Du Chesene, A.; Leist, H.; Zhang, Y.; Ulrich, R.; Schadler, V.; Wiesner, U. 1997. "Organically Modified Aluminosilicate Mesostructures from Block Copolymer Phases." Science, Volume 278, p1795-1798.

Thomas, E.L.; Kinning, D.J.; Alward, D.B.; Henkee, C.S. 1987. "Ordered Packing Arrangments of Spherical Micelles of Biblock Copolymers in Two and Three Dimensions." Macromolecules, Volume 20, p2934-2939.

Thomas, E.L.; Anderson, D.M.; Henkee, C.S.; Hoffman, D. 1988. "Periodic area-minimizing surfaces in block copolymers." Nature, Volume 334, p598-601.

Thomas, J.M.; Midgley, P.A. 2004. "High-resolution transmission electron microscopy: the ultimate nanoanalytical technique." Chemical Communications, Volume 11, p1253-1267.

Thompson, R. B.; Ginzburg, V. V.; Matsen, M. W.; Balazs, A. C. 2001. " Predicting the Mesophases of Copolymer-Nanoparticle Composites." Science, Volume 292, p2469-2472.

Tyler, C.; Morse, D. 2005. "The orthorhombic Fddd network in triblock and diblock copolymer melts." Physical Review Letters Volume 94, 208302.

Ulrich, R.; Du Chesne, A.; Templin, M.; Wiesner, U. 1999. "Nano-Objects with Controlled Shape, Size, and Composition from Block Copolymer Mesophases." Advanced Materials, Volume 11, p141-146.

Ulrich, Ralph. 2000. "Morphologien and Eigenschaften strukturierter organisch-anorganisher Hybridmaterialien." Ph.D. Dissertation, Johannes-Gutenberg University, Mainz.

Urade, V. N.; Wei, T.; Tate, M. P.; Kowalski, J.D.; Hillhouse, H.W. 2007. "Nanofabrication of Double-Gyroid Thin Films." Chemical Materials, Volume 19, p768-777.

Urbas, A.M.; Maldovan, M.; DeRege, P.; Thomas, E.L. 2002. "Bicontinuous Cubic Block Copolymer Photonic Crystals." Advanced Materials, Volume 14, p1850-1853.

Vand, V.; Aitken, A.; Campbell, R.K. 1949. "Crystal Structure of Silver Salts of Fatty Acids." Acta Crystallographica, Volume 2, p398-403.

Volcani, B. E. 1981. "Silicon and Siliceous Structures in Biological Systems." Simpson, T. L.; Volcani B. E. Editors; Springer, New York, p157-200.

von Schnering, H.G.; Nesper, R. 1991. "Nodal surface of Fourier series : fundamental invariants of structured matter." Zeitschrift fur Physik B - Condensed Matter, p408-412.

Vukusic, P.; Sambles, J. 2003. "Photonic structures in biology." Nature, Volume 424, p852-855.

Wang, X.; Dormidontova, E.E.; Lodge, T.P. 2002. "The Order-Disorder Transition and the Disordered Micelle Regime for Poly(ethylenepropylene-b-dimethylsiloxane) Spheres." Macromolecules, Volume 35, p9687-9697.

Warren, B.E. "X-ray Diffraction." Dover Publications Inc., New York City, 1969.

Warren, S.C.; Disalvo, F.J.; Wiesner, U. 2007. "Nanoparticle-tuned assembly and disassembly of mesostructured silica hybrids." Nature Materials, Volume 6, p156-161.

Wind, M.; Graf, R.; Heuer, A.; Spiess, H. W. 2003. "Structural Relaxation of Polymers at the Glass Transition: Conformational Memory in Poly (n-alkylmethacrylates)." Physical Review Letters, Volume 91, 155702-1.

Wind, M.; Graf, R.; Renker, S.; Spiess, H. W.; Steffen, W. 2005. "Structure of amorphous poly-(ethylmethacrylate): A wide-angle x-ray scattering study." Journal of Chemical Physics, Volume 122, 014906.

Winey, K.I.; Thomas, E.L.; Fetters, L.J. 1992. "The Ordered Bicontinuous Double-Diamond Morphology in Diblock Copolymer/Homopolymer Blends." Macromolecules, Volume 25, p422-428.

Wohlgemuth, M.; Yufa, N.; Hoffman, J.; Thomas, E.L. 2001. "Triply Periodic Bicontinuous Microdomain Morphologies by Symmetries." Macromolecules, Volume 34, p6083-6089.

Wong, G.C.L.; Lin, A.; Tang, J.X.; Li, Y.; Janmey, P.A.; Safinya, C.R. 2003. "Lamellar Phase of Stacked Two-Dimensional Rafts of Actin Filaments." Physical Review Letters, Volume 91(1), 018103-1.

Wright, D.C.; Mermin, N.D. 1989. "Crystalline Liquids: the blue phases." Reviews of Modern Physics, Volume 61(2), p385-432.

Wright, P.V.; Zheng, Y.; Bhatt, D.; Richardson, T.; Ungar, G. 1998. "Supramolecular Order in New Polymer Electrolytes." Polymer International, Volume 47, p34-42.

Xi, Haowen; Milner, S.T. 1996. “Bicontinuous Phase in Diblock Copolymer Melts with Added Homopolymer.” Macromolecules, Volume 29, p2404-2411.

Yamauchi, K.; Hasegawa, H.; Hashimoto, T.; Nagao, M. 2003. "Complex microphase separation and microdomain structures in poly(isoprene)-block-poly(D-styrene)-block-poly(vinyl methyl ether) triblock copolymer." Journal of Applied Crystallography, Volume 36, p708-712.

Yoon, J.; Lee, W.; Thomas, E.L. 2005. "Self-assembly of block copolymers for photonic-bandgap materials." MRS Bulletin, Volume 30, p721-726.

Yoshizawa, M.; Mukai, T.;Ohtake, T.; Kanie, K.; Kato, T.; Ohno, H. 2002. "Ion-conductive mechanism in liquid crystalline molecules having polyether segment." Solid State Ionics, Volume 154-155, p779-787.

Young, R.A.; Wiles, D.B. 1982. "Profile Shape Functions in Rietveld Refinements." Journal of Applied Crystallography, Volume 15, p430-438.

Young, R.J. 1983. "Introduction to Polymers." Chapman and Hall Limited, New York.

Zhao, D.; Huo, Q.; Feng, J.; Chmelka. B.F.; Stucky, G.D. 1998. "Nonionic Triblock and Star Diblock Copolymer and Oligomeric Surfactant Syntheses of Highly Ordered, Hydrothermally Stable, Mesoporous Silica Structures." Journal of the American Chemical Association, Volume 120, p6024-6036.

Zheng, W.; Wang, Z.G. 1995. "Morphology of ABC Triblock Copolymers." Macromolecules, Volume 28, p7215-7223.

Zhu, L.; Cheng, S.Z.D.; Calhoun, B.H.; Ge, Q.; Quirk, R.P.; Thomas, E.L.; Hsiao, B.S.; Yeh, F.; Lotz, B. 2001. "Phase structures and morphologies determined by self-organization, vitrification, and crystallization : confined crystallization in an ordered lamellar phase of PEO-b-PS diblock copolymer." Polymer, Volume 42, p5829-5839.

Zhu, L.; Huang, P.; Chen, W.Y.; Weng X; Cheng, S.Z.D.; Ge, Q.; Quirk, R.P.; Senador, T.; Shaw, M.T.; Thomas, E.L.; Lotz, B.; Hsiao, B.S.; Yeh, F.; Liu, L. 2003. "Plastic Deformation" Mechanism and Phase Transformations in a Shear-Induced Metastable Hexagonally Perforated Layer Phase of a Polystyrene-b-poly(ethylene oxide) Diblock Copolymer." Macromolecules, Volume 36, p3180-3188.

Zhu, L.; Sun, L.; Miao, J.; Cui, L.; Ge, Q.; Quirk, R. P.; Xue, C.; Cheng, S. Z. D.; Hsiao, B. S.; Avila-Orta, C. A.; Sics, I.; Cantino, M. E. 2005. "Epitaxial Phase Transformation between Cylindrical and Double Gyroid Mesophases." Materials Research Society Symposium Proceedings, Volume 856E, BB2.3.1-2.3.6.

Ziese, U.; de Jong, K.P.; Koster, A.J. 2003. "Electron Tomography: a tool for 3D structural probing of heterogenous catalysts at the nanometer scale." Applied Catalysis A : General, Volume 260, p71-74.